IMPLEMENTATION OF NO LIF DIAGNOSTICS TO CHARACTERIZE THE ROLE OF THERMAL NON-EQUILIBRIUM WITHIN A HYPERSONIC TURBULENT BOUNDARY LAYER

A Dissertation

by

ZACHARY DANIEL BUEN

Submitted to the Graduate and Professional School of
Texas A&M University
in partial fulfillment of the requirements for the degree of

DOCTOR OF PHILOSOPHY

Chair of Committee,	Simon W. North
Committee Members,	Rodney D. W. Bowersox
	Dong Hee Son
	Matthew Sheldon
Head of Department,	Simon W. North

December 2021

Major Subject: Chemistry

ABSTRACT

A flat plate wedge with a DC glow-discharge plasma along the leading edge was designed to introduce thermal non-equlibrium (TNE) directly into a turbulent boundary layer. Various NO laser induced fluorescence (LIF) techniques were introduced into the hypersonic Actively Controlled Expansion (ACE) wind tunnel facility to quantify the potential role of TNE. The NO was continuously seeded into the settling region upstream of the flow conditioners to mitigate the downstream perturbations within the test section. The NO spatial distribution was relatively localized within the test section core to provide an upper limit concentration of 1%. Following the excitation of the $A^2\Sigma^+$ ($v' = 0$) $\leftarrow$ $X^2\Pi_{1/2}$ ($v'' = 0$) transition, the resulting ground state $NO_{v=1}$ population was 16% of the total excited state population with the O_2 accounting for a majority of the collisional quenching. Freestream rotational thermometry measurements suggested the observed fluctuations were on the order of 4% within the test section core. The flat plate rotational thermometry campaign successfully characterized the temperature profile for a range of laminar and turbulent boundary layers. The rotational thermometry measurements concluded the TNE introduced by the plasma did not have an effect on the downstream turbulent behavior. A vibrational thermometry study concluded the nascent $NO_{v=1}$ population introduced by the plasma slowly diffused for the laminar case; however, the mechanically tripped turbulent boundary layer experienced a significant degree of mixing. The freestream velocity fluctuations were 1% and agreed well with previous ACE measurements. The flat plate velocimetry results did not find any evidence of TNE effecting the downstream turbulence. Spanwise velocimetry on the flat plate determined the laminar flow was relatively uniform across the plate and illustrated break down in response to the mechanical trips.

DEDICATION

I dedicate this dissertation to the person who was with me during my time in Texas, my love Corrie Kamigaki. She moved with me to Texas in the summer of 2016 to build a new a life. Her love and support for me was unconditional and unrelenting. I am forever grateful because she was always there for the highs and lows of graduate school. The stress these past five years was daunting at times, but she was an outlet to enjoy life outside of work. Having her in my life gave me perspective on what was important and reminded me of my goals after school. She kept me honest and pushed me to improve myself daily. She is one of the most thoughtful and caring people I have had in my life. I loved her humor and her willingness to go on my partially planned adventures. I could not imagine my time in Texas without her or our two dogs, Louie and Maleah. I am not sure how to thank her for all the sacrifices she made these past years, but I think I owe her a puppy at the very least. I look forward to growing old with you babe.

ACKNOWLEDGMENTS

I would like to thank my advisor Dr. Simon North for his guidance and mentorship during my Ph.D. career. His attitude and approach to science instilled the confidence in me to perform the following experiments. He taught me the importance of self-reliance and how it should be used to improve yourself as a scientist. His ability to push you to be a better researcher is unparalleled. In times of adversity I will always remember his of advice of 'you just got to get it done and that's it.'

I would like to thank all of my North group members over the years. Thank you to Nic West for teaching me the fundamentals of laser diagnostics and how to design experiments. Thank you to Josh Winner for his mentorship, endless sports banter, and being the person out of Kentucky since Abraham Lincoln. I would like to thank Wei-Wei for his comedic gold and good-natured personality. Thank you to Colin Wallace for his friendship, support, and his ability to correct my outlandish claims. Special thanks to his wife Emma (Pace) Wallace for her audacious attitude towards life. Also special thanks to their son Ben Wallace for being you and his efforts in the '05 championship run. Shout-out to Carolyn Gunthardt for being an awesome friend and for having one of the best sense of humors. Thank you to Jason Kuszynski for being a solid undergraduate and for redesigning the roots blower. Thank you to Madeline Smotzer for her diligence, perseverance, and patience in implementing the NO LIF experiments. Her chipper Ohio attitude helped me push through all of the lab difficulties over the years. She is a fantastic friend and I would not want another junior student...besides Ashley (Britt) Moran. Thank you Ashley for all of the work and hours you dedicated to expanding the ability of NO LIF diagnostics. Her New Jersey swagger helped me push the experiments to where they are today. I am indebted to these two women and they will do fantastic things in their scientific careers. Thank you to Scott Moran for his service, friendship, and hospitality. Thank you to Megan Aardema for teaching me the ways of a Michigander and knowing that you don't choose the shorts life, but the shorts life chooses you. To Nick Shuber, my brother on two wheels, thank you carrying the big motivating energy you have and wearing black for all the poor and beaten down. Thank you to Naa-Kwarley Quartey for her

sunny disposition and for cooking pizza in a toaster oven.

Additionally I would like to take the time to thank all of my engineer friends from the NAL. First I would like to thank Dr. Rodney Bowersox for letting me work in his magnificent laboratory. He has been incredibly helpful, insightful, and patient over the years. Thank you to Casey Broslawski for the immense of amount of effort you poured into making this project succeed. I recall our early days of Lazarus and it reminds me of how much we have progressed. Our camaraderie was crucial to the project's success and I know he will make a superb NASA engineer. Thank you to Ian Neel and Andrew Leidy for being excellent senior students and for teaching me how to maintain the NAL facility. Thank you to Farhan Siddiqui for his brute strength, can-do attitude, and check engine code reader. I wish I could capture the essence of Heather Kostak's sigh because it sums up the day-to-day feeling of graduate school, but she truly is a joy to have in lab. Thank you to Tyler Dean for showing me I could always have a tougher project *i.e.* HXT and I will miss his fresh golf graduate school attire. I wish Trevor Blair the best of luck in his aerospace career and I will miss his basketball knowledge. I would like to thank Mckenna Roberts for her laugh, it helped break up my concentration during data analysis. Thank you to John Wirth for his service and showing us how to cram five years worth of work into three...good luck. Thank you to all of the NAL undergraduate students because you were there to do the work that I did not have time to do. Thank you to Maddie Hetlage and Hayden Morgan for showing me that engineers can also have the same everlasting passion for laser diagnostics.

A special thanks to Cecil Rhodes who maintained and improved the NAL. He was a godsend and was imperative to the facility operations. Thank you to John Kochan for his dialogue and his willingness to help out with any task. Thank you to Will Seward for his invaluable machining skills, my Ph.D. work would be very different without his efforts. Thank you to Tim Pehl of the electronics shop, he was always there to help and provided key recommendations on electrical problems that I little experience with. Thank you to Sandy Horton for doing all the behind the scene efforts and keeping the chemistry department going.

I would also like to thank the people at the University of the Pacific that helped get me to Texas

A&M. First I would like to thank Dr. Silvio Rodriguez for seeing the potential in me and pushing me to apply to graduate school. I would like to thank Dr. Ren for the opportunity to perform research within her lab. My time in her lab grew into a passion for science. Finally, thank you Dr. Tsai for convincing me to apply and attend Texas A&M, it was one of the best decisions I have made in my life thus far.

Thank you to my parents for all of their love and instilling a solid work ethic to push through adversity. Thank you to all my siblings for their continuous support of their oddball brother. Thank you to all my grandparents, aunties, uncles, cousins, nieces, nephews because you all have shaped me into the person I am today. Thank you to all my friends for having an ear for me and bringing humor to my life. Big shout-out to my homie Vlad Roytman for all the BBQ and cigar sessions, they made the stresses of graduate school go away.

CONTRIBUTORS AND FUNDING SOURCES

Contributors

This work was supported by dissertation committee consisting of my committee chair Simon North, Professor Dong Hee Son of the Department of Chemistry Department, Professor Matthew Sheldon of the Chemistry Department, and Professor Rodney Bowersox of the Aerospace Engineering Department.

The laser diagnostics were lead by Zachary Buen. Madeline Smotzer and Ashley Britt have contributed significantly to the development and advancement of the NO LIF diagnostics within the ACE facility. Dr. Joshua Winner initiated the implementation of the NO LIF techniques. Jason Kuszynski also contributed to the development of the NO LIF diagnostics within ACE.

The model design, development, and characterization outside of the laser diagnostics was performed by Casey Broslawski. He additionally contributed to preliminary MTV analysis.

Funding Sources

Graduate study was supported by a fellowship from Texas A&M University and a dissertation research fellowship from the Vannevar Bush Faculty Fellowship (VBFF).

NOMENCLATURE

VENOM	Vibrationally Excited Nitric Oxide Monitoring
LIF	Laser Induced Fluorescence
PLIF	Planar Laser Induced Fluorescence
MTV	Molecular Tagging Velocimetry
PIV	Particle Imaging Velocimetry
SREF	Stimulated Raman Excited Fluorescence
NO	Nitric Oxide
SFM	Sum-Frequency Mixing
FCU	Frequency Conversion Unit
DIF	Dual Image Feature
ICCD	Intensified Charge Coupled Device
MCP	Micro Channel Plate
PMT	Photomultiplier Tube
P_T	Stagnation Pressure
ACE	Actively Controlled Expansion Tunnel
U	Axial Velocity
U'	Axial Velocity Fluctuation
U_∞	Freestream Axial Velocity Fluctuation
V	Transversal Velocity
V'	Transversal Velocity Fluctuation
T	Temperature
T'	Temperature Fluctuation

$U'T'$	Axial Heat Flux
$V'T'$	Transversal Heat Flux
$U'V'$	Reynolds Shear Stress
P_T	Stagnation Pressure
P_∞	Freestream Pressure
T_T	Stagnation Temperature
T_∞	Freestream Temperature
Re	Reynolds Number
FFT	Fast Fourier Transform
ROI	Region of Interest
C_{12}	Empirical Correction Constant
ΔE_{21}	Energy Difference between ro-vibronic states
$\frac{S_1}{S_2}$	Image Ratio
T_{rot}	Rotational Temperature
k_B	Boltzmann Constant
∂T	Temperature Uncertainty
∂R_{12}	Ratio Uncertainty
PEEK	Polyether ether ketone
TNE	Thermal Non-Equilibrium
CNE	Chemical Non-Equilibrium
V-T	Vibration to Translation Energy Transfer
V-V	Vibration to Vibration Energy Transfer
CFD	Computational Fluid Dynamics
DNS	Direct Numerical Simulations
LES	Large Eddy Simulations

DC	Direct Current
RF	Radio Frequency
PID	Proportional Integral Derivative

TABLE OF CONTENTS

Page

LIST OF FIGURES

FIGURE Page

LIST OF TABLES

TABLE Page

1. INTRODUCTION AND BACKGROUND

1.1 General Motivation

Aircrafts traveling faster than the speed of sound experience a jarring environment. The speed of the vehicle speed, stability, and durability are dependent on the interactive aerodynamic forces exerted on the body. As vehicles approach supersonic and hypersonic velocities, the air along the surface becomes more compressed and the aerodynamic forces scale with velocity. The air compression leads to adiabatic heating along the surface of the vehicle, causing high degrees of thermal loading. The calculated stagnation temperatures for a commercial airliner traveling at 575 mph or a Mach 3 SR-71 Blackbird traveling at 2,000 mph are 33 °C and 399 °C using the ram rise equation,

$$RR_{total} = \frac{V^2}{2C_P}e, \tag{1.1}$$

where V is the aircraft velocity, C_p heat capacity at constant pressure, and *e* is the recovery factor. This equation illustrates how the surface temperatures rise dramatically for vehicles traveling at supersonic velocities. The heat generated along the vehicle diffuses normal to the surface through collisional molecular energy exchange processes. As the fluid heats, the viscosity changes causing frictional forces to develop in the fluid near the surface. These frictional forces are referred to as the skin friction of the vehicle and is proportional to the square of the velocity. The skin friction contributes to the overall drag profile and ultimately decelerates the vehicle.

Thermal loading and drag become significant at high velocities posing difficulties for designing robust, fast vehicles. Ongoing design efforts rely on computational fluid dynamics (CFD) simulations to predict the flow environment and vehicle performance. In particular the models must accurately predict the behavior of the boundary layer, the thin layer of fluid just above the surface. The mass, momentum, and energy exchange along the surface give rise to a considerable portion of the large-scale fluid dynamics experienced by the vehicle. The boundary layer can be described as laminar, an ordered energy exchange, or turbulent, statistically random energy exchange. Due

to the steady behavior of a laminar flow, the exchange processes are simple and can be readily modeled. Turbulent flows contain swirl-like structures that randomly mix the elements within the boundary layer. Current theoretical models have difficulty in accurately describing this turbulent mixing behavior for supersonic and hypersonic vehicles. Modeling becomes more difficult when considering the effects of chemical non-equilibrium (CNE) and thermal non-equilibrium (TNE) in the flow. CNE and TNE occur in regions where the surface temperature is high *i.e.* several thousands of Kelvin. As the gas above the surface reaches these temperatures, diatomic molecules dissociate and initiate a chain of chemical reactions. In addition the differing relaxation rates of translational, rotational, and vibrational modes introduce TNE among the internal modes. TNE also occurs across shock structures because the shock thickness is a few mean free paths which limits the number of molecular collisions. TNE can lead to a dampening or amplification of boundary layer turbulence. Directly solving for turbulent flows with CNE or TNE is computationally expensive when using direct numerical simulations (DNS). This has lead to several models being developed to reduce the computational demand needed to resolve turbulence. These models require experimental validation, however the amount of available turbulent empirical data is limited. The database is even further reduced in regards to experiments studying the role of TNE within turbulent flows. The data is limited because many techniques have difficulty in spatially resolving the fluctuating flow parameters without perturbing the flow. In recent years, non-intrusive optical diagnostic techniques have emerged as promising candidates to quantify turbulence. Minimizing the perturbations to the flow is critical in evaluating the fundamental driving forces within the boundary layer. The following work expands on the current turbulent empirical database by directly measuring the temperature and velocity fluctuations within a hypersonic turbulent boundary layer. The effect of TNE will also be examined by introducing vibrationally excited N_2 into the flow through the operation of a DC glow-discharge plasma.

1.2 Turbulent Boundary Layer Research Goals

The first goal of the presented work was to implement novel laser diagnostics into a conventional hypersonic blow-down wind tunnel for the characterization of a turbulent boundary layer.

The second goal was to introduce vibrationally excited N_2 into the flow and measure the downstream turbulent temperature and velocity profiles. Turbulent boundary layers have a high degree of mass, momentum, and heat exchange compared to the laminar counterpart. Experimentally quantifying turbulence in a hypersonic flow is not trivial which has lead to the current limited empirical database for turbulent boundary layers. The database is further reduced when considering experiments directly quantifying the effects of TNE within a hypersonic turbulent flow. Boundary layers for vehicles traveling at hypersonic velocities or greater have non uniform CNE and TNE distributions normal to the surface. It is then crucial for turbulent models to contain terms accounting for the effects of non-equilibrium in the flow. The following measurements presented demonstrate the ability to directly measure the individual fluctuating components of velocity, U, and temperature, T. The results demonstrate the viability of NO laser induced fluoresce (LIF) techniques within the ACE facility. The following expands on the merits of these fluctuating parameters and their ability to quantify turbulence.

1.2.1 Boundary Layer Fundamentals

The large scale fluid mechanics of the flow are influenced by the underlying molecular kinetic processes. Molecular exchange of momentum and energy within the boundary layer are diffusion driven processes causing gradients to form normal to the surface. The molecular transport of these phenomena give rise to the bulk properties of the flow i.e. viscosity and thermal conduction. The boundary layer is defined as the thin layer of fluid near the surface where viscous effects need to be considered in the flow modeling. Changes in the viscosity of the fluid are due to the kinetic energy of the flow frictionally dissipating along the surface. The internal energy of the fluid nearest the surface begins to increase and diffuse in the normal direction. The molecular internal energy distribution can be described with a temperature, *T*, assuming a temperature-dependent Boltzmann weighted internal energy distribution. The thermal gradient normal to the surface produces a viscosity gradient due to its temperature dependence. Viscosity gradients in a flow introduce frictional forces between adjacent fluid layers where these layers can now exchange momentum between one another. This diffusion of momentum through the boundary layer yields a velocity gradient where

the average flow velocity at the surface is zero under the no-slip condition. The no-slip condition assumes the average velocity of the fluid relative to the surface is equal to zero. The velocity boundary layer thickness is defined as the viscous fluid velocity being 99% of the bulk freestream velocity. The velocity profile of a boundary layer can be used to understand the transport of momentum through the boundary layer. Consider figure 1.1, a one dimensional flow moving in the horizontal direction *i* with gradients in the *j* direction velocity, *∂u/∂j*, and *j* direction temperature, *∂T/∂j*. These gradients cause the flow to experience a plane of shear stress between adjacent hor-

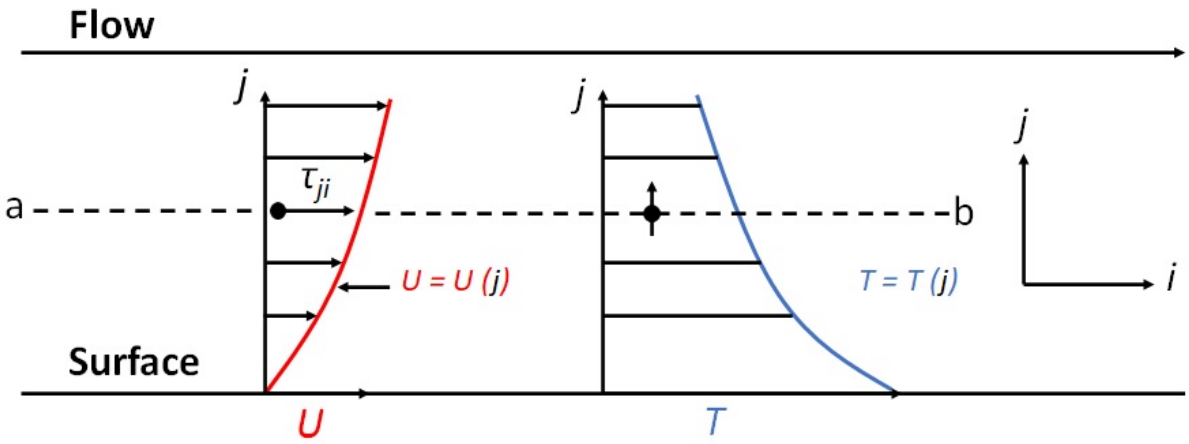

Figure 1.1: 1-D flow depicting the relationships of shear stress and thermal conduction to the velocity and temperature gradients.

izontal planes of the flow. The molecular shear stress, τ_{ij}, is proportional to the velocity gradient seen here in the equation:

$$\tau_{ji} = \mu \frac{\partial u}{\partial j} \tag{1.2}$$

where the viscosity coefficient, μ, is a proportionality constant.

Again the molecular momentum exchange is dependent on the internal energy gradient where the energy gradient is dependent on the thermal conduction of the flow. The internal energy of the flow is highest near the wall where the kinetic dissipation is large and gradually approaches

the freestream temperature. The boundary layer heat transfer can be related to the boundary layer thermal gradients using the thermal conductivity of the fluid. Consider $\dot{q}_i$ to be the heat transferred in a fluid in the direction *i* per second per unit area. The temperature gradient in the same direction, ∂T/∂i can be related to the molecular heat transfer

$$\dot{q}_i = -k(\frac{\partial T}{\partial i}) \tag{1.3}$$

where the thermal conductivity of the fluid, *k*, is a proportionality constant.

The momentum and energy transport are coupled because μ and *k* are temperature-dependent molecular properties of the flow. The molecular viscosity coefficient is defined using Sutherland's law

$$\frac{\mu}{\mu_0} = (\frac{T}{T_0})^{\frac{3}{2}}(\frac{T_0 + 110}{T + 110}) \tag{1.4}$$

where μ_0 and T_0 are the respective viscosity and temperature references for the fluid. The thermal conductivity is proportional to the viscosity of the fluid with the expression

$$k \propto \mu c_p \tag{1.5}$$

where c_p is the heat capacity at constant pressure.

The content presented thus far only considers one-dimensional flows, but real flows are three-dimensional which complicate the equations describing these flows. Numerous derivations and examples detailing the 3-D shear stress dilatations can be seen in a several textbooks.[1][2][3] To this point the momentum and energy transfer have been discussed as molecular driven diffusion processes with the coefficient of transport μ and *k*, respectively. Figure 1.2 provides a sketch for the ordered laminar boundary layer where exchange processes only occur between adjacent fluid layers. The steadiness of the laminar flow allows for accurate prediction of the coefficients used to solve for the transport of momentum and energy.[4][5][6] For laminar boundary layers these coefficients can be sufficient when describing the fluid behavior. However, for a turbulent boundary layer

the random mixing of momentum and energy is not accounted for by the molecular coefficients of transport. Large whirl-like or eddy structures randomly exchange momentum and energy through the height of the boundary layer. The size, velocity, and timescales of these eddy structures significantly impact the degree of turbulent mixing within the boundary layer. The onset, formation, and growth of these turbulent structures is random making it difficult to explicitly solve or model. The exchange of momentum and energy through the eddy structures is determined using the bulk flow terms of turbulent viscosity and turbulent thermal conductivity, ϵ and κ respectively. Theses turbulent flow exchange coefficients are far larger than the molecular coefficients of transport for the fluid. Turbulent coefficients again rely on the evolving bulk flow properties of temperature and velocity. Correctly predicting turbulent boundary layer behavior requires accurately calculating the relative magnitude of the turbulent eddy mixing compared to the molecular energy exchange mechanisms of momentum and energy. This balancing feat has been the subject of interest for many computational fluid dynamicist for decades.

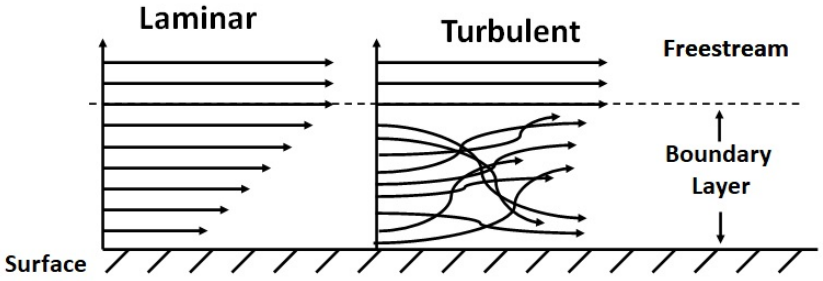

Figure 1.2: Rudimentary sketch of a laminar and turbulent boundary layer behavior.

1.2.2 Turbulent Modeling Approaches

Modeling the flow requires accurate predictions of the evolving viscous forces in the boundary layer. Changes in fluid viscosity directly impact the transport of momentum and energy throughout the boundary layer. The Euler equations are a set of coupled differential equations characterizing the relationships of velocity, pressure, and density of an inviscid fluid in motion. The equations

conserve mass transfer and balance the exchange of momentum and energy within the fluid. The Euler equations are the governing equations for adiabatic inviscid flows. With viscous effects accounted for, the Navier-Stokes equations can be derived from the Euler equations. These new equations describe how the moving velocity, pressure, density, and temperature of the fluid are related. The Navier-Stokes equation derivations are beyond the scope of this work, but can be referenced to in various literature sources.[7][8] They will be described here with a qualitative approach. The set of time-dependent equations consist of a mass continuity equation, three conservation of momentum equations,and a conservation of energy equation. The independent variables of the equations are the *i, j*, and *k* coordinates in three-dimensional space and time *t*. The dependent variables within the equations are the three dimensional velocity components, local pressure, local density, and local temperature. In a simple sense the three momentum equations describe the total convective gains/losses relative to the total diffusive losses/gains within the boundary layer.

Many representations of the Navier-Stokes equations contain terms derived from similarity parameters. This means the forces within the boundary layer can be solved to scale which reduces the boundary layer analysis in a non-dimensional approach. Forces within the boundary layer are influenced by the flow velocity, temperature, density, and other higher order parameters such as the viscosity and thermal conduction of the fluid. To capture the variable relations, ratios of these flow parameters are used to solve for turbulent flow behavior. This is helpful in predicting turbulence because it simplifies the derivations by introducing non-dimensionalized terms. Similarity parameters also make it feasible for researchers to relatively compare experimental data from various facilities and models. The governing similarity parameters for compressible, viscous flows are

$$\text{Ratio of Specific Heat} \qquad \gamma = \frac{c_p}{c_v} \qquad \frac{\text{Constant Pressure Heat Capacity}}{\text{Constant Volume Heat Capacity}} \tag{1.6}$$

$$\text{Mach Number} \qquad M_\infty = \frac{V_\infty}{a_\infty} \qquad M_\infty^2 \propto \frac{\text{Flow Kinetic Energy}}{\text{Flow Internal Energy}} \tag{1.7}$$

$$\text{Reynolds Number} \qquad Re = \frac{\rho_\infty V_\infty L}{\mu_\infty} \qquad Re \propto \frac{\text{Inertial Forces}}{\text{Viscous Forces}} \tag{1.8}$$

$$\text{Prandtl Number} \qquad Pr = \frac{\mu c_p}{k} \qquad Pr \propto \frac{\text{Frictional Dissipation}}{\text{Thermal Conduction}} \tag{1.9}$$

and provide insight to the competing forces driving turbulence. Solutions to the Navier-Stokes equations requires simultaneously solving all five of the equations due to the coupled relationship of the dependent variables. Solving these equations analytically is not practical due the lack of mathematical tools capable of explicitly solving non-linear partial differential equations. High fidelity numerical simulations can be computationally expensive if similarity parameters are not used, numerical approximations are minimized, and the relative temporal and spatial scales are small enough to resolve all scales of turbulence. However, similarity parameters and approximations are employed to reduce the overall computational demand, but they can introduce large errors. Also the finite scale of the computational grid may not resolve the smallest scale of turbulence which can cause errors in the final result. High fidelity direct numerical simulations (DNS) solve the Navier-Stokes equation explicitly for all turbulence length scales. DNS calculations are expensive because they must resolve the entire range of turbulent spatial scales within the defined computational grid. The scales range from the Kolmogorov microscales to the integral scale of the larger eddies. Kolmogorov scales describe the smallest dissipative turbulent structures in which molecular viscosity begins to dissipate the kinetic energy of the turbulent flow into the internal energy modes of the fluid. The Kolmogorov scale equations,

$$\eta = (\frac{\nu}{\varepsilon})^{\frac{1}{4}} \qquad \text{Length Scale} \qquad (1.10)$$

$$\tau_\eta = (\frac{\nu}{\varepsilon})^{\frac{1}{2}} \qquad \text{Time Scale} \qquad (1.11)$$

$$u_\eta = (\nu\varepsilon)^{\frac{1}{4}} \qquad \text{Velocity Scale} \qquad (1.12)$$

where ν is the kinematic viscosity of the fluid and ε is the average rate of turbulent kinetic energy dissipation. The analysis assumes the dissipative structures below the Kolmogorov length scale, η, are statistically isotropic within the fluid. It is also assumed at small scales the directionality of the turbulent structures is lost as the energy dissipates from larger to smaller scales. The small scale structures in high Re turbulent flows are independent of the mean flow velocity or the initial boundary layer conditions. Instead they depend on the viscous to turbulent kinetic energy dissi-

pation ratio. The number of DNS mesh points required to fully resolve all scales of turbulence is proportional to Re^3. Real hypersonic flight conditions have a Reynolds number on the order of 10^6-10^7, so the needed computational memory for DNS grows rapidly. Therefore many full DNS treatments are often performed on low-speed flows.[9] To reduce the computational demand, large Eddy simulations (LES) assume small turbulence length scales are isotropic so they can be modeled with a relatively simple turbulence term and the larger length scales are solved explicitly with the Navier-Stokes equations. The computational demand remains large because the time steps must be small enough to obtain statistically significant turbulent behavior predictions. LES are often used for moderate Re flows, but remain computationally expensive for supersonic and hypersonic flows. The Reynolds-averaged Navier Stokes (RANS) equations further reduce the computational demand by introducing time-averaging integrals written as

$$\bar{X} = \lim_{T\to\infty} \frac{1}{T} \int_{t_0+T}^{t_0} x dt \tag{1.13}$$

directly into the analysis. This mathematical treatment assumes the fluctuating quantity was collected for a sufficient amount of time T resulting in a statistically significant mean quantity with minimal error. With time-averaging, the instantaneous flow quantities such as velocity are decomposed into their respective time-averaged mean and fluctuating components using Reynolds decomposition.[10] The momentum transport equation for incompressible stationary flows,

$$\underbrace{\rho \bar{u}_j \frac{\partial \bar{u}_j}{\partial x_j}}_{\text{Momentum Change}} = \underbrace{\rho \bar{f}_i}_{\text{Total Force}} + \frac{\partial}{\partial x_j}\Big(\overbrace{-p\delta_{ij}}^{\text{Total Stresses}} + \overbrace{\mu \frac{\partial \bar{u}_\text{i}}{\partial x_j} + \frac{\bar{u}_\text{j}}{\partial x_i}}^{\text{Viscous Stresses}} - \overbrace{\rho \overline{u_i' u_j'}}^{\text{Reynolds Stresses}} \Big) \tag{1.14}$$

shows the introduction of a new term, Reynolds stresses. The Reynolds stresses can be equated to the momentum transferred by a molecule traveling in *i* direction with velocity U_i to a molecule in the *j* direction. The equation contains a coupled relationship between the fluctuating parameters of density, pressure, and temperature. Favre averaging introduces mass-averaging techniques where

the boundary layer is assumed to have constant pressure. The Favre time-averaged energy transport equation can be written as

$$\vartheta_i^T = \overline{\rho e'' u_i''} \tag{1.15}$$

where ϑ_i^T is the turbulent energy flux, *e* is the mass-weighted time-weighted internal energy distribution, and *u* is the mass-average time-average velocity vector.[11] Equation 1.15 ignores pressure dependent terms. It is assumed the local internal energy populations within the flow can be described with a single temperature value. The development of turbulence models using the mentioned mathematical approaches can be found in a variety of literature sources.[12][13][14][15][16]

It is difficult to accurately model turbulence with explicit numerical approaches or with truncated algebraic models; however, the lack of comparable empirical data exacerbates the uncertainty error of the prediction. The development of techniques capable of characterizing the velocity, temperature, pressure, and density of the flow are critical in model validation. The presented work will demonstrate the ability to directly measure the fluctuating temperature and velocity profiles of a hypersonic turbulent boundary layer. The work to follow in the coming years will directly measure the turbulent heat flux, $\mathrm{U'T'}$ and $\mathrm{V'T'}$, using the Vibrationallly Excited Nitric Oxide Monitoring (VENOM) technique. Additionally, VENOM can also provide measurements related to Reynolds shear stress, $\mathrm{U'V'}$, within in the turbulent boundary layer. These higher order flow metrics can be used in the iterative development of reduced fidelity turbulence modeling.

1.2.3 Thermal Non-Equilibrium Perturbations in Turbulent Flows

In hypersonic flows, disturbances in the laminar boundary layer can amplify along the surface and initiate turbulent transition. The dominant disturbances, the first and second modes, are a function of the bulk flow and initial boundary layer conditions. First mode instabilities are vortical disturbances originating from a combination of freestream disturbances and bulk flow interactions with the surface geometry. Second modes are similar to acoustic waves confined between the surface and the sonic line of the boundary layer. At high velocities the second mode disturbances are assumed to be dominant. The boundary layer height can amplify a set range of acoustic waves

along the surface. The primary and secondary disturbances can interact with each other to trigger the boundary to transition. It is known acoustic waves are damped by viscous thermal conductive losses when propagating through air. As viscosity increases the dampening mechanisms grow stronger within the flow. Higher Reynolds number flows often correlate to turbulent flows due to the large ratio between the inertial and viscous forces. Therefore an increase in the local velocity can lead to turbulent dampening. This was demonstrated by Fuller *et al.* within a slow flow facility containing a radio frequency (RF) plasma.[17] A mesh was used to mechanically introduce freestream turbulence where it then passed through an RF plasma. The RF plasma was used to introduce TNE in the form of vibrationally excited N_2 *i.e.* $N_{2,v=1}$. The N_2 vibrational temperature was measured using Coherent Anti-Stokes Spectroscopy (CARS) and they observed a gradual decrease in the N_2 vibrational temperature. Using particle imaging velocimetry (PIV) they determined the axial Reynolds shear stress decreased downstream of the plasma. Using a kinetic model they determined the TNE *i.e.* $N_{2,v=1}$ coupled into the flow through collisions with H_2O present in the ambient air. The rotational bath gas temperature was measured using NO planar laser induced fluorescence (PLIF) and they observed a temperature increase as the nascent $N_{2,v=1}$ population vibrationally relaxed. The freestream temperature rise correlated to an increase in the fluid viscosity which increased the degree of turbulent dampening. This method turbulent dampening is explained in *Surveys in Mechanics* where it states the bulk viscosity of the flow is related to the rotational temperature.[18] The rotational internal energy distribution for diatomic species under these conditions thermalizes in 0.1-10 $\times$ $10^{-}8$ s. Therefore, if the V-V and V-T energy exchange mechanisms such occur on a similar timescale then it may be a source of turbulent dampening. Leonov *et al.* also observed a dampening of flow instabilities within a transonic wind tunnel.[19] They employed a series of RF surface plasma discharge elements upstream of an adverse pressure gradient. Downstream of the plasma thy measured a decrease in the pressure fluctuations using a spanwise transducer array. They attributed the increased flow stability to bulk flow thermal perturbations resulting from the RF plasma operation. Merriman *et al.* have observed a shock flow perturbation resulting from plasma thermal effects. A Schlieren imaging campaign demonstrated

the weakening of an oblique shock during the operation of a 230 W RF plasma within a Mach 2 wind tunnel.[20] They determined the rapid relaxation of electronically excited N_2 caused a temperature increase within the thermal boundary layer and altered the shock angle by 14 degrees.

Samimy *et al.* performed a cohesive study investigating the correlation of between low Reynolds jet structures and RF plasma actuator parameters.[21] They forced select jet azimuthal modes by changing the actuator location with respect to the jet and by also varying the operating actuator RF frequency. They determined the acoustic modes were extremely sensitive to the location of the actuator suggesting a potential spatial frequency matching of the plasma to the free jet. Additionally they optimized the standing waves structures by matching the plasma frequency to the Strouhal number. Another study probed the onset of turbulence on a series of swept cylinder models within a hypersonic shock tunnel.[22] Pitot probe pressure transducer measured the acoustic pressure fluctuations at a fixed location as the shock heated gas moved over the test article. The onset of turbulence was delayed when CO_2 was used as the test gas. They concluded the timescale of the CO_2 vibrational relaxation was coupled to the acoustic modes present within the boundary layer causing a delay in turbulent transition. The bulk influence of TNE has been well studied within multiple facilities with varying geometries; however, a majority of the presented studies were unable to directly quantify and model how the TNE coupled into the flow instabilities. The goal of this dissertation was to carefully characterize the initial conditions along a flat plate geometry and to seed a known quantity of TNE, vibrationally excited N_2, directly into the boundary layer. Due to the timescales of V-T and V-V energy transfer, the vibrationally excited N_2 was assumed to relax only through collisions with the model surface. This implies the TNE is coupled into the flow through surface interactions which may produce a TNE gradient normal to the wall. At the downstream location of the fully turbulent boundary layer, laser diagnostics were employed to directly measure any potential effect of the seeded TNE.

1.3 Laser Diagnostics in Fluids

The introductory work thus far has focused on the driving aerodynamic forces within a turbulent hypersonic boundary layer. The fluid mechanics occurring within the boundary layer is

fascinating, but difficult to model due to the evolving 3-dimensional complexity of the boundary layer. Within in this relatively thin layer of fluid there are large amounts of momentum and energy exchange. Several existing models aim to statistically predict the the turbulent behavior. Accurately modeling the transport phenomena is a trade-off between the computational demand and the fidelity of the model. Many researches approximate certain physical flow phenomena to reduce the computational load. Common approximation approaches employ Reynolds decomposition which separates the mean and fluctuating components of a quantity of interest. As discussed, the Bowersox truncated algebraic model contains terms describing the mean temperature and velocity profiles for a turbulent boundary layer as well as the corresponding fluctuations. The heat fluctuation profile of the boundary layer can be related to the coupled relationship of U′ and T′, the fluctuating axial velocity and fluctuating temperature, respectively. The Reynolds shear stress in a plane, τ_{ij}, of the boundary layer is proportional to $u_i' u_j'$. The fluctuations of the boundary layer are related to the transport of momentum and energy throughout the boundary layer. The greater the fluctuations relative to the mean implies a greater degree of turbulent mixing. These fluctuating flow parameters can be described as a turbulence gauge. The accuracy of the model requires validation because of the approximations within the derivation. Validation can be performed by comparing the results of the model to a benchmarked computational prediction or against empirical data. The experimental database related to direct off-body temperature and velocity measurements within a hypersonic boundary layer are limited. Measurements of this nature are intriguing, but require extensive infrastructure and specialized instrumentation. In the following section multiple experimental techniques will be presented and discussed; however, they focus will focus on the merits of velocimetry and thermometry using NO laser based diagnostics.

1.3.1 Thermometry Techniques

Non-intrusive temperature measurements are ideal in hypersonic flows. Filtered Rayleigh Scattering (FRS) is a non-intrusive method used for the past three decades.[23][24][25] A narrow linewidth beam is sent into a flow where the light is scattered by the windows, walls, and gas molecules in the flow. A spatially resolvable CCD camera measures the scatter; however, an ab-

sorbance cell is placed between the camera and region of interest. The specie within the cell will absorb the narrow bandwidth light, but variations in the linewidth profile due to molecular interactions are acquired by the camera. The perturbed linewidth can then be modeled to determine the temperature of the flow; however the temperature fluctuates with pressure which makes the modeling difficult.[26] Due to the intensity of the Rayleigh scattering, the filtered spectrum signal is weak but still measurable. Another technique capable of measuring the instantaneous temperature of a flow is broadband N_2 CARS. It has been used extensively in measuring single-shot temperatures within combustion flames and hypersonic flows.[27][28][29] A pump beam, broadband stokes beam, and a probe beam interact simultaneously in a finite space to coherently produce a broadband out beam. The output beam passes through a shortpass filter into a spectrometer coupled to a spatially resolvable CCD camera. The measurement provides instantaneous vibrational and rotational temperatures by fitting the acquired spectrum. Temperature uncertainty and spatial resolution are a function of the incident beam geometries because the output CARS signal is generated by the spatial overlap of the three beams. A large beam overlap may sample low and high temperature regions and the resulting CARS signal would have a convoluted temperature spectrum. BOXCARS allows for sub-mm resolution which decreases the potential of measuring regions where temperature gradients exist. All three beams must be phase matched in space by optimizing the phase-matching angles detailed by Eckbreth.[30] Fraval *et al.* performed BOXCARS measurements in a free piston shock tunnel providing vibrationally and rotationally resolved spectra .[31] The facility produced a high enthalpy shock which propagated through a converging diverging nozzle. The geometry of the nozzle allowed for hypersonic expansion and due to the rotational and vibrational relaxation timescales the resulting flow was a two temperature system. They used CARS to characterize the TNE flow at the nozzle exit and to measure the vibrational temperature at various points downstream.

PLIF is a widely used technique capable of characterizing the velocity, pressure, molecular density, and temperature of the flow. The technique provides spatially resolved images by collecting the fluorescence following the excitation of a select molecular transition using a laser sheet ($\sim$

300 - 800 μm). Several studies have demonstrated its ability in determining the pressure and velocity in combustion and supersonic flow fields.[32][33][34] Determination of pressure and velocity is dependent on collecting the broadband emission and separating the individual spectroscopic signatures. Algorithms fit these select spectral signatures to determine the pressure broadening and the Doppler shift to determine the pressure and velocity of the flow. Typically in these experiments the laser was scanned to collect a large set of spectral signatures to minimize empirical error. Therefore the technique may not be sensitive to high-frequency pressure and velocity fluctuations. However over four decades ago, NO PLIF was shown to measure instantaneous temperature fluctuations in a combustion flow environment in a study by Seitzman *et. al.*[35] They measured the total broadband emission following the excitation of the NO $Q_1(22)$ $A^2\Sigma^+$ $(v' = 0) \leftarrow X^2\Pi$ $(v'' = 0)$ transition. Each image provided a two-dimensional temperature map, assuming the maximum signal in the image equated to 740 K. A temperature dependent Boltzmann distribution model was used to determined the temperature in which the $Q_1(22)$ 'internal-calibration' configuration suffered from large uncertainties in regions where the fluorescence signal was low. Building on the techniques of Seitzman, Palmer et al. developed a two-laser/two-camera approach to reduce the degree of uncertainty.[36] The new approach measured the instantaneous vibrational and frame averaged rotational temperature map of an underexpanded jet. Two successive images were taken following the excitation of a select ro-vibronic $A^2\Sigma^+ \leftarrow X^2\Pi$ transition either in (0,0) or (0,1) band. A two-dimensional instantaneous vibrational temperature map was determined from the relative fluorescence ratio between the two signals.

1.3.2 Velocimetry Techniques

Non-intrusive measurements are ideal when performing high flow velocity measurements because any instrument mounted within the flow has the potential introduce perturbations. Various laser diagnostic techniques are capable of extracting temperature and velocity components in a flow. A common velocimetry technique is particle imaging velocimetry (PIV) where metal oxides on the order of 300 nm are seeded into a flow and probed by two time delayed lasers. Scattered light from the seeded particles are imaged with a CCD camera and the velocity is determined by

cross-correlation of two images to track the displacement of a single particle in time. PIV does have some limitations in regards to the flow fields it is capable of characterizing. In *PIV Measurements in Shock Tunnels and Shock Tubes*, the author details the inability of the PIV particles to accurately track the velocity profile across a shock.[37] The velocity discontinuity is to large and the particles have difficulty in decelerating at the rate of the small diatomic molecules. The viability of the PIV technique in low number density flows, such as the Actively Controlled Expansion (ACE) tunnel, decreases due to the increase in the Knudsen number, Kn. This Knudsen number equation,

$$Kn = \frac{\lambda}{L} \tag{1.16}$$

where λ is the mean free path across and L is the diameter of the seeded particle provides a dimensionless parameter which describes the limitations of the PIV technique. Typically flows with a Kn > 0.01 demonstrate some degree of velocity slip. Lastly PIV suffers from non-uniform seeding and these inhomogeneities have difficulty in resolving 2-D velocity flow fields.

The molecular tagging velocimetry (MTV) technique has been performed within a variety of flow fields. A trace gaseous species is seeded into a flow and molecularly tagged by photo-initiating a chemical process or by producing a nascent ro-vibronic state of the seeded gas. In a photodissociation scheme the first beam is referred to as the write beam and it photodissociates the seeded gas species. Following the write beam, a second beam probes a select ro-vibronic transition of the photo products. A portion of the broadband emission is collected with a spatially resolvable CCD camera. The tagged species displaces within the flow and is probed later in time by a second read laser beam tuned to excite a select ro-vibronic transition. The emission is again acquired with spatially resolvable CCD camera and the flow velocity is determined using the equation,

$$U = \frac{x}{t} \tag{1.17}$$

where U is the velocity, x is the displacement, and t is the relative time delay between the acquired

images. The other MTV method requires two lasers separated by a single time delay. The first laser or the write beam, electronically excites a select ro-vibronic transition and portion of the fluorescence is collected with a CCD camera. Following the electronic relaxation of the seeded species a nascent ground state population is produced. The nascent ground state population reduces ambiguity with the background gas and is probed later in time with a single read beam. Following the second laser a portion of the broadband emission is acquired. MTV measurements often have improved seeding and more accurate flow tracking capabilities compared to the PIV technique. Sakurai *et al.* compared MTV and PIV velocity profiles using acetone and dioctyl sebacate, respectively, within a pulsed underexpanded jet facility.[38] The PIV acquired velocity profile exhibited a gradual deceleration following the Mach disk which is in accurate because it is known to have a sharp discontinuity. They determined the acetone MTV tracked the velocity discontinuity across the underexpanded Mach disk more accurately. Hsu *et.al* performed MTV measurements of an underexpanded jet using the photodissociation reaction,

$$\mathrm{NO_2} + 355\ \mathrm{nm} \rightarrow \mathrm{NO_{v=0}} + \mathrm{O(^1D)} \tag{1.18}$$

$$\rightarrow \mathrm{NO_{v=1}} + \mathrm{O(^1D)} \tag{1.19}$$

where the 40% of the nascent NO is in the NO $X^2\Pi$ (v = 1) state.[39] They probed both the nascent $NO_{v=0}$ and $NO_{v=1}$ states in two different MTV excitation scheme.[40][41] Their study was the first to probe the nascent $NO_{v=1}$ state within a hypersonic flow field. They argued the $NO_{v=1}$ profile provided a better S/N ratio compared to the images collected following the excitation of the NO $X^2\Pi$ (v = 0) state.

1.3.3 Vibrationally Excited Nitric Oxide Monitoring

Prior to discussing the VENOM technique, it is important to briefly discuss NO spectroscopy. NO has an unpaired electron that results in electron orbit, electron spin, and molecular rotation interactions. These interactions cause two types of splitting of the degenerate electronic levels in the NO $X^2\Pi$ ground state. The first comes from spin-orbit coupling which is due to the electron

orbit coupled to the electron spin which yields the NO $X^2\Pi_{1/2}$ and NO $X^2\Pi_{3/2}$ ground state. The second splitting is the interaction of the electron orbit with the molecular rotation. This splitting is referred to as the lambda-doubling and it becomes more pronounced at larger rotational energies. The spin-orbit coupling results in a much larger splitting relative to the lambda-doubling. The excited NO $A^2\Sigma^+$ state, does not exhibit spin-orbit coupling nor lambda-doubling, but instead has an electron spin and molecular rotation interaction which causes splitting as the rotational energy increases. The combination of all these splittings produces 12 possible branches in the $A^2\Sigma^+$ ($v' = 0$) $\leftarrow$ $X^2\Pi$ transition. Branches that only differ in the final excited state overlap with one another, so only 8 of the branches are resolvable. The thesis by Dr.Sanchez-Gonzalez provides an excellent depiction ground and excited state spiltting as well as the 8 possible branches.[42]

The final goal for the NO LIF diagnostics is to fully implement the VENOM technique to obtain simultaneous 2D temperature and velocity profiles. The application of the technique will be first discussed in the ACE tunnel. Freestream temperatures following the isotropic expansion were assumed to be $\sim$60 K, so the diatomic molecules were assumed to be in the ground vibronic state. Following the seeding of NO into the ACE facility, they will be molecularly tagged using two sheeted 226 nm beams overlapped in space. These initial beams are referred to as the "write" beams. The 226 beams will be modulated by a microcylindrical lens array to form gridlines; the effective image is composed of light and dark regions which allow for 2D velocity analysis. The 226 nm beam will electronically excite the NO γ band to undergoes the $A^2\Sigma^+$ ($v' = 0$) $\leftarrow$ $X^2\Pi$ transition. Electronically excited NO relaxes back down to the ground state through a convolution of fluorescence and collisional quenching. In the absence of collisional quenching, the $NO_{v=1}$ population should be $\sim$26%; however, if NO relaxes exclusively by quenching then the NO $X^2\Pi$ ($v = 1$) population is assumed to be $\sim$10%. Collisional O_2 quenching and NO self-quenching have similar quenching cross sections, however O_2 quenching will have a greater impact in the ACE facility due to the relative O_2 concentration. Collisional quenching by N_2 is negligible due to the quenching cross section being $\sim$5000 times smaller. Producing a nascent NO $X^2\Pi$ ($v = 1$) population tags the flow because the NO $X^2\Pi$ ($v = 1$) population will be frozen during the timescale

of the experiment. The inefficiency of V-V and V-T energy transfer under the ACE flow conditions allows the NO $X^2\Pi$ (v = 1) to remain relatively constant. A time delay between the write and first read beam allows for translational/rotational thermalization following the relaxation of the NO $A^2\Sigma^+$ (v = 1) state. The first read beam propagates into the test section to probe the nascent NO $X^2\Pi$ (v = 1) population. The read beam is tuned to a low *J* state based on the expected temperature range of the flow. The ICCD camera is gated to acquire a portion of the broadband NO $A^2\Sigma^+$ ($v'' = 1$) emission. The image gates are minimized to mitigate image blurring effects due to flow field displacement. The second read beam is tuned to a high *J* state, followed by a second ICCD gate to collect the broadband emission. Figure 1.3 illustrates the NO electronic excitation scheme and the timing related to the lasers, NO fluorescence, and camera gating. The resulting images undergoes post-image processing to improve the flow displacement analysis. The displacement among the molecularly tagged grid lines is determined and the second read image is de-warped onto the first read image to accurately determine the image fluorescence ratio. Velocity is found by dividing the total net displacement by the known time delay between the two read images. The resulting 2-D velocity map provides information related to the axial velocity as well as potential local structures present within the flow. The temperature is determined using the fluorescence ratio and the equation,

$$\frac{S_1}{S_2} = C_{12} e^{(-\frac{\Delta E_{21}}{k_B T_{rot}})} \tag{1.20}$$

where S_1/S_2 is the fluourescent signalratio, ΔE_{21} was energy difference calculated using the Dunham expansion, and T_{rot} was the known temperature. The VENOM technique was first demonstrated by Sanchez-Gonzalez *et al.* within an underexpanded jet facility. They probed the nascent $NO_{v=1}$ population shown in equation 1.19. Their resulting 2-D velocity map agreed well with CFD predictions and tracked the velocity accurately across the Mach disk. However, they concluded their temperature map overestimated the true temperature in low density regions. In these regions the flow had inadequate collisional thermalization during the time delay following the photodissociation of NO_2.[43] A VENOM variant, 'invisible ink', electronically excited the $A^2\Sigma^+$ ($v' = 0$) $\leftarrow$ $X^2\Pi_{1/2}$ ($v'' = 0$) transition within an underexpanded jet facility.[44] Following the relaxation

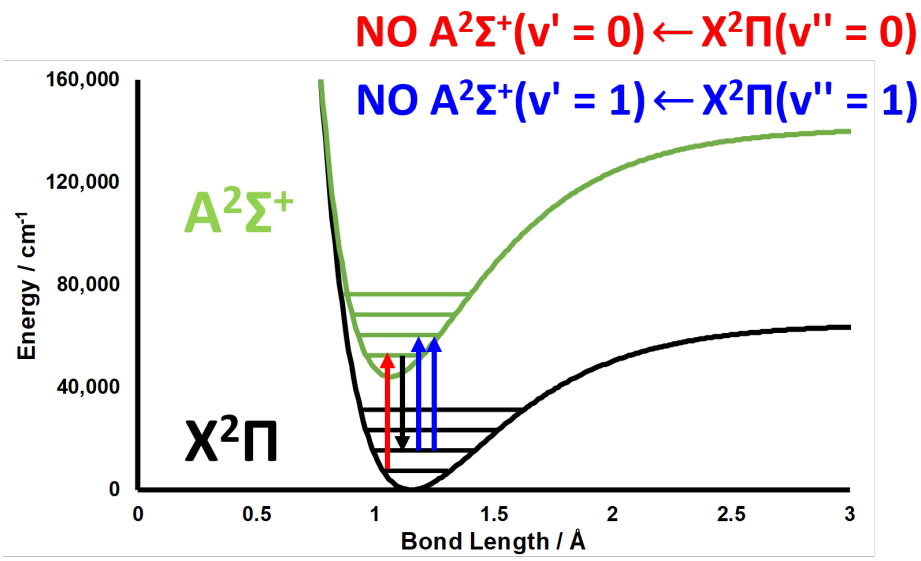

(a)

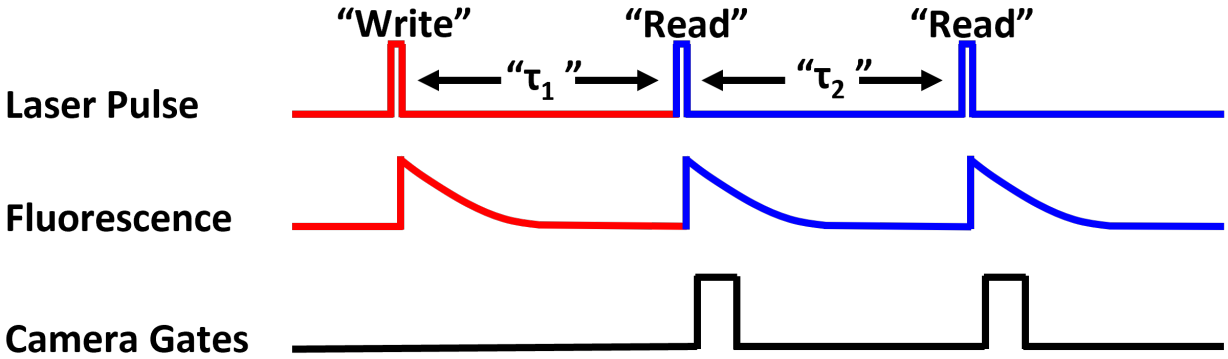

(b)

Figure 1.3: Figure a depicts the excitation schemes related to the NO $X^2\Pi$ ground state. Figure b is the timing sequence related to the lasers, NO fluorescence, and camera gating.

of the NO $A^2\Sigma^+$ ($v' = 0$) state through a convolution of fluorescence and collisional quenching a nascent NO $X^2\Pi$ ($v = 1$) population was produced. The resulting $NO_{v=1}$ population was then used as the tracer species to obtain 2-D temperature and velocity maps. The resulting velocity curves agreed well with CFD predictions and there was also an improvement in the observed temperature profiles. Therefore the invisible ink VENOM variant has proven to be a better alternative to obtain simultaneous measurements of temperature and velocity.

2. EXPERIMENTAL METHODS

2.1 General Experimental Overview

A flat plate hypersonic turbulent boundary layer was characterized using an array of instrumentation with a focus on laser based diagnostic techniques. The most significant infrastructure component was the hypersonic Actively Controlled Expansion (ACE) blow-down wind tunnel. The facility generated repeatable hypersonic conditions for a multitude of test matrix runs. A 2.75° half-angle flat plate model was mounted within the ACE test section with a 36 cm $\times$ 18 cm cross-sectional plane. The leading edge of the model contained an insert for diamond-shaped trips to generate a turbulent boundary layer. Directly downstream of the trips were two copper electrode inserts which produced a DC glow-discharge plasma. The goal of the plasma was to introduce TNE directly into the boundary layer via production of N_2 (v=1). The resulting laminar and turbulent boundary layers were characterized with NO LIF optical diagnostic techniques to understand the TNE influence. Significant work was required to safely introduce NO/N_2 gas mixtures into the facility with minimal flow perturbations. A digital delay generator was utilized to synchronize the NO introduction with multiple UV laser beams tuned to discrete NO transitions. Data acquisition of the images, laser power traces, and tunnel pressure traces were collected in real-time with an in-house written LabVIEW program. The collected images were analyzed to quantify the turbulent behavior along the flat plate.

2.2 Actively Controlled Expansion (ACE) Tunnel

The experiments discussed in this body of work were performed within the ACE blow-down wind tunnel facility. A brief explanation will be discussed, however a more detailed description on the design and performance can be found in Semper *et al.*[45][46] The ACE facility is a conventional wind tunnel with a variable Mach number from 5 to 8 and a Reynolds number sweep range of 0.5 $\times$ 10^6 m^{-1} to 8 $\times 10^6$ m^{-1}. A 23.2 m^3 tank was pressurized to 2500 PSIG with dried air. A Fox Two-Stage Ejector pulls vacuum onto the ACE facility through the diffuser. The maximum run

time is limited to 40 seconds due to the ejector's mass flow rate of 25 kg s^{-1}. The mass flow rate through the ACE facility is 1.0 to 1.5 kg s^{-1}. The air passes through a Chromalox heater to convectively pre-heat the ACE facility infrastructure to 430 K in order to avoid O_2 liquefaction during the expansion. A thermocouple and pitot probe are used to measure the stagnation conditions within the pre-expansion region *i.e.* the ACE settling region. Freestream disturbances are reduced through a series of flow conditioners upstream the converging section of the 2-D symmetric de Laval nozzle. A separate pressure transducer is mounted near the exit of the nozzle to measure the static pressure within the test section. The ACE test section contains multiple optical ports fitted with UV grade fused silica windows. At Mach 6, the measured RMS pressure fluctuations are $\sim 1\%$ and the RMS Mach number fluctuations are $\sim 0.5\%$ in the exit plane of the core flow.[45][46] The air then moves to the diffuser which gradually decelerates the flow from hypersonic to subsonic conditions. The diffuser throat height is adjustable to accommodate a range of blockage model ratios.

2.3 Flat Plate Wedge Model

The model used for the NO LIF ACE campaign was a 2.75° half-angle flat plate wedge designed by Casey Broslawski of the Aerospace Engineering Department at Texas A & M University. A detailed description of the model can be found in the paper by Buen *et al.* however, a brief description is presented as follows.[47] The model was designed to have a zero pressure gradient along the length of the plate. An insert can be added 6 cm downstream from the leading edge. The trips insert contained diamond-shaped geometries with a height of 3.4 mm with a spacing of 6 mm between each trip center. Directly downstream of the trips insert were two copper electrodes where a 46 W DC glow discharge plasma was produced. A 3.8 cm $\times$ 6.6 cm anti-reflective fused silica window insert was located 10 cm downstream of the leading edge. A 25.5 cm $\times$ 6.6 cm anti-reflective fused silica window insert was located 23.5 cm downstream of the leading edge. The window inserts reduced laser scatter during off-body measurements normal to the plate's surface. In Figure 2.1 a cutaway view of the flat plate wedge is mounted within the ACE test section. The variations relating to the individual experiments are a function of the measurement location and

plate configuration (Table 2.1).

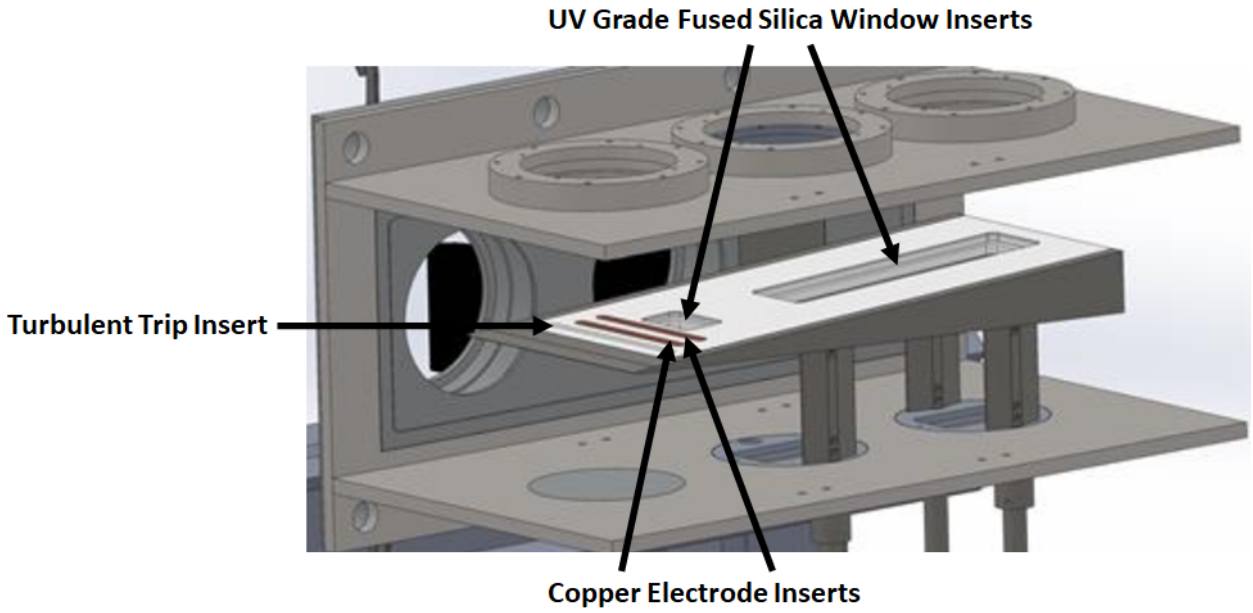

Figure 2.1: Cutaway of the flat plate wedge mounted within the ACE test section.

The first location, 120 mm downstream the leading edge, was selected with the assumption that any thermal perturbations from the plasma will be the most sensitive directly downstream of the copper electrodes. The third location was selected based on Schlieren experiments performed by Casey Broslawski. Schlieren imaging identified an expansion interacting with the plate at ∼450 mm downstream of the leading edge. In an effort to avoid any shock wave boundary layer interactions (SWBLI), the NO LIF experiments were performed at 405 mm downstream of the leading edge where the expansion wave was ∼32 mm normal to the surface. The second location at 260 mm was selected because it was halfway between the first and third locations. Experiments characterizing the turbulent behavior of the boundary layer have been separated into two additional categories. Previous measurements suggest that the boundary layer behavior may differ when measuring directly downstream of a trip structure (wake) or in between two trip structures (trough).[48] Therefore, measurements were performed downstream of a wake or a trough.

Location	Laminar (No Trips)		Turbulent (Trips)			
	Plasma Off	Plasma On	Wake		Trough	
			Plasma Off	Plasma On	Plasma Off	Plasma On
1st (120 mm)	L1	LP1	TW1	TWP1	TT1	TTP1
2nd (260 mm)	L2	LP2	TW2	TWP2	TT2	TTP2
3rd (405 mm)	L3	LP3	TW3	TWP3	TT3	TTP3

Table 2.1: Variable flat plate wedge operational conditions.

2.4 Laser Systems

2.4.1 System Specifications

The work presented here employed two laser configurations to generate UV beams in the 223 to 227 nm range. The UV output allows for NO LIF using the $A^2\Sigma^+$ ($v' = 0$) $\leftarrow$ $X^2\Pi$ ($v'' = 0$) and $A^2\Sigma^+$ ($v' = 1$) $\leftarrow$ $X^2\Pi$ ($v'' = 1$) transitions. One configuration frequency doubles the output from a Sirah CBR-G-18 pulsed dye laser using Coumarin 450 in methanol. The 355 nm third harmonic of a Spectra-Physics Lab 150-10 Nd:YAG laser was used to pump a Sirah Cobra dye laser. The UV beam produced by frequency doubling yielded $\sim$800 μJ per pulse with a range of 225 to 227 nm. The second laser configuration used the 532 nm second harmonic of a Spectra-Physics Pro-290-10 Nd:YAG to pump a Sirah Cobra Stretch pulsed dye laser. The tunable output range of the dye laser was from 600 to 630 nm depending on the dye solution. For the $A^2\Sigma^+$ ($v' = 0$) $\leftarrow$ $X^2\Pi$ ($v'' = 0$) transition the dye solution consisted of Rhodamine 640 dissolved into ethanol. The dye solution was changed to a mixture of Rhodamine 610 and Rhodamine 640 dissolved into methanol to probe the $A^2\Sigma^+$ ($v' = 1$) $\leftarrow$ $X^2\Pi$ ($v'' = 1$) transition. Residual 355 nm from the Pro-290-10 Nd:YAG laser was mixed with the tunable output in a SFM-355-frequency mixing unit to produce 10 to 12 mJ per pulse in a range of 223 to 227 nm. Both laser configurations produced linewidths of $\sim$0.08 cm^{-1}. The linewidths are limited by the resonator resolution of the pulsed dye lasers.

2.4.2 Laser Calibration

The laser systems were calibrated regularly to ensure precise on-resonant NO transitions. The calibration setup for the frequency doubled configuration will be discussed first. It was only used to excite the transitions within the $A^2\Sigma^+$ ($v' = 0$) $\leftarrow$ $X^2\Pi$ ($v'' = 0$) regime. The calibration cell used for this configuration can be seen in Figure 2.2. The cell was fitted with entry and exit fused silica windows for the propagation of the UV beam. The middle of the cell contained a 1 inch fused silica window for optical access and a 5 mm port for a custom made Taylor cone used to reduce laser scattering. The cell was evacuated with a Leybold D65B backing vacuum pump and the pressure was continuously monitored by a vacuum transducer (Baratron MKS type 622). The gas line on the bottom of the cell connected to an in-house made mixture of 5% NO in N_2 fitted with a low pressure regulator. The gas source and vacuum lines both contained needle valves for the user to tune the calibration cell pressure. The pressure of the cell during the wavelength calibration did not exceed 3.0 Torr. The laser output was directed through a UV grade window lens where the reflected beam from the window was collected with a fast response photodiode (Thorlabs Type DET10A). This was used to account for shot-to-shot laser power fluctuations. The laser beam then propagated into the cell through a UV grade window. A photomultiplier (PMT) tube (Hamamatsu Type H6780-03) was mounted directly in front of the 1 inch fused silica window to collect the NO fluorescence. A 12-bit Lecroy (HRO 66Zi) oscilloscope at a sampling rate of 2 GS/s digitized the collected photodiode and PMT traces. The cell was mounted on a 3-axes translational stage to reduce the degree of scatter from the entry/exit windows and the cell body.

The frequency conversion unit (FCU) was calibrated prior to wavelength calibration to ensure maximum laser power during the scan. The reflected beam from the window lens was sent to a glass vial containing 50 mg of Rhodamine-610 dissolved into 20 mL of methanol. A fast response photodiode (Thorlabs Type DET10A) was orthogonal to the beam path and collected the fluorescence. An FCU curve plot is seen in Figure 2.3. The LeCroy oscilloscope digitized the signal and a LabVIEW program integrated the area under the fluorescent decay curve. The proprietary Sirah 3.0 software calibrated the FCU crystal within a user-defined wavelength region. The user manu-

ally stepped the FCU crystal until the area under the fluorescent curve was maximized. Following the FCU calibration, the LabVIEW program then scanned through a user defined wavelength region and step spacing to calibrate the laser wavelength. A representative experimental fluorescence and a simulated fluorescence spectrum generated by LIFBASE for the $A^2\Sigma^+$ ($v' = 0$) $\leftarrow$ $X^2\Pi$ ($v'' = 0$) transition are shown in Figure 2.4. The simulated and experimental spectra were compared to identify the relative wavelength offset for the lab frame wavelength region of interest.

The sum frequency mixing configurations have a larger tunable UV output range which allowed for the excitation of the $A^2\Sigma^+$ ($v' = 0$) $\leftarrow$ $X^2\Pi$ ($v'' = 0$) and $A^2\Sigma^+$ ($v' = 1$) $\leftarrow$ $X^2\Pi$ ($v'' = 1$) transitions. The calibration cell for this configuration was similar to the cell shown in 2.2. The cell was fitted with the UV grade optical windows as mentioned before. The cell was evacuated using the Leybold backing pump and the pressure was monitored by an MKS 09XX08 vacuum transducer. The gas inlet for the cell introduced in-house made mixtures of NO/N_2 and NO_2 in ultra pure air. NO_2 was necessary for the calibrating the $A^2\Sigma^+$ ($v' = 1$) $\leftarrow$ $X^2\Pi$ ($v'' = 1$) NO transitions. In the reactions,

$$NO_2 + h\upsilon_{355nm} \rightarrow NO_{v=0} + O^3P \tag{2.1}$$

$$\rightarrow NO_{v=1} + O^3P \tag{2.2}$$

NO_2 photodissociates following the absorption of a 355 nm photon and produces a nascent NO vibrational distribution. The empirically determined branching ratio of $NO_{v=1}$:$NO_{v=0}$ is $41.2 \pm 6.2 : 58.8 \pm 8.8$.[39] A small amount of NO_2 was made by mixing a small amount of an NO/N_2 mixture and ulta-pure air (Brazos Valley Welding Supply) within a chilled (40 °F) bubbler. The NO_2 condenses within the bubbler at this temperature. The NO_2 mixture setup is shown in Figure 2.5.

The NO_2, NO, and air mixture was introduced into the calibration cell by bubbling the ultra-pure air through the bubbler where small amounts of NO_2 vapor was passed into the calibration cell. A 355 nm beam propagated through the cell to produce nascent $NO_{v=1}$ where the $A^2\Sigma^+$ ($v' = 1$) $\leftarrow$ $X^2\Pi$ ($v'' = 1$) regime was scanned by a 224 nm beam. A PMT was mounted orthogonally

to collect the subsequent fluorescence. A representative experimental scan and simulated scan are shown in Figure 2.6.

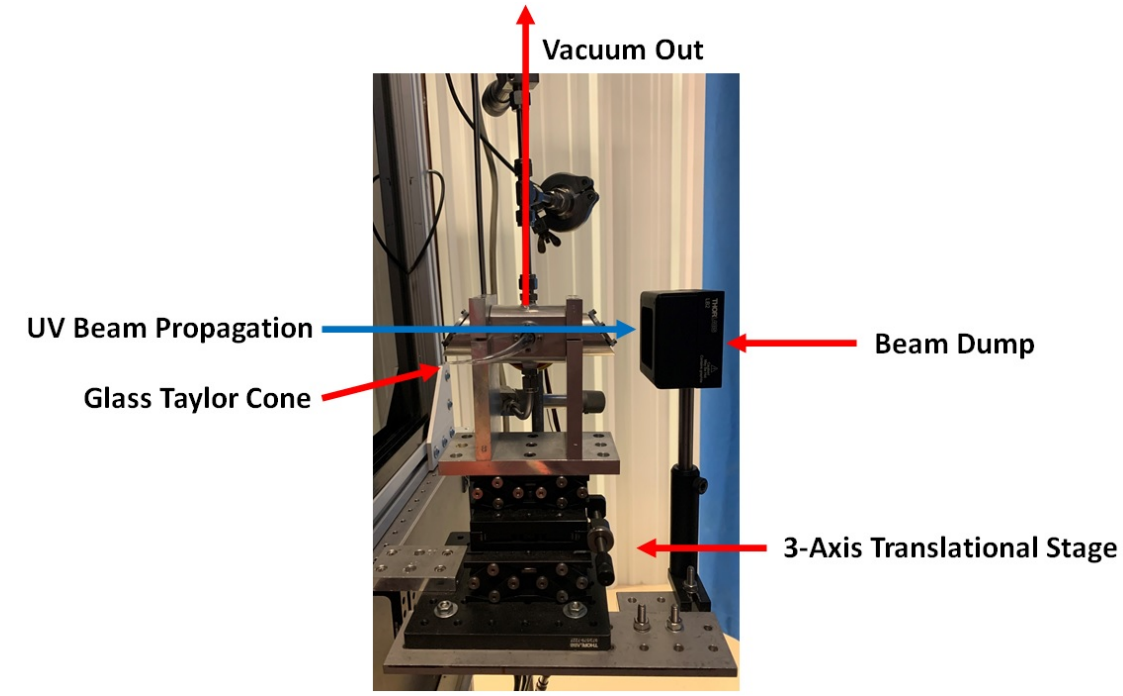

(a)

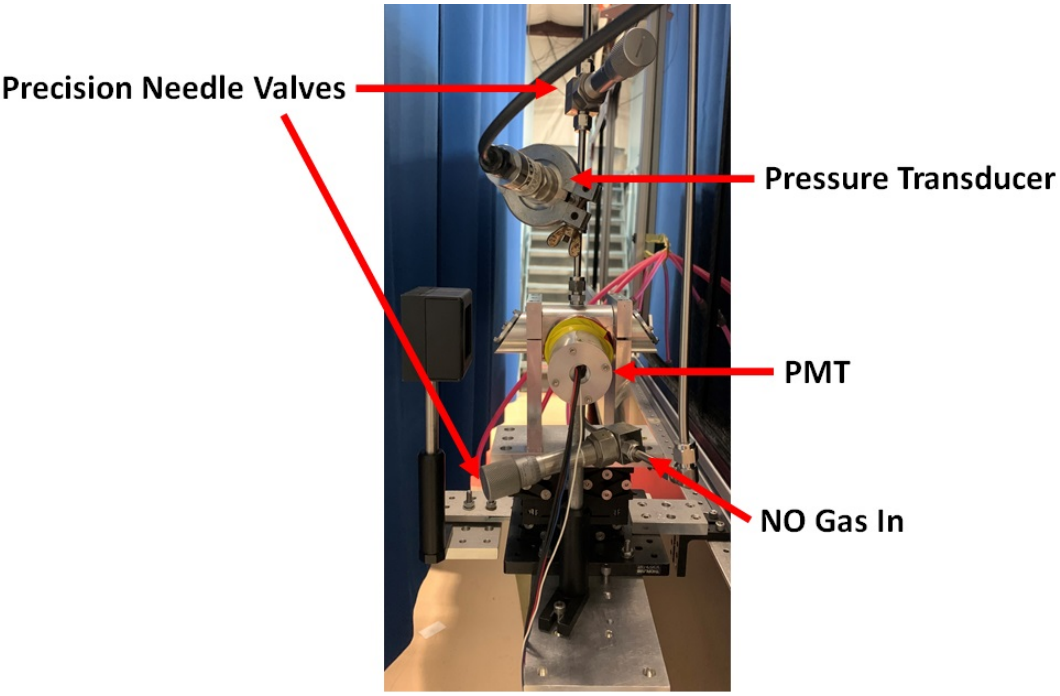

(b)

Figure 2.2: Calibration cell configuration.

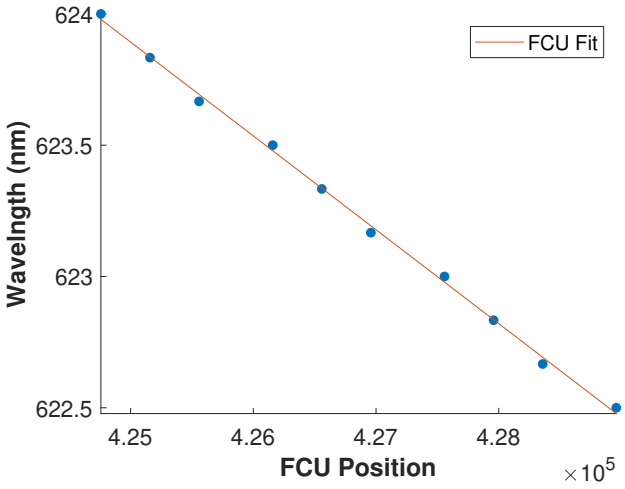

Figure 2.3: FCU calibration curve.

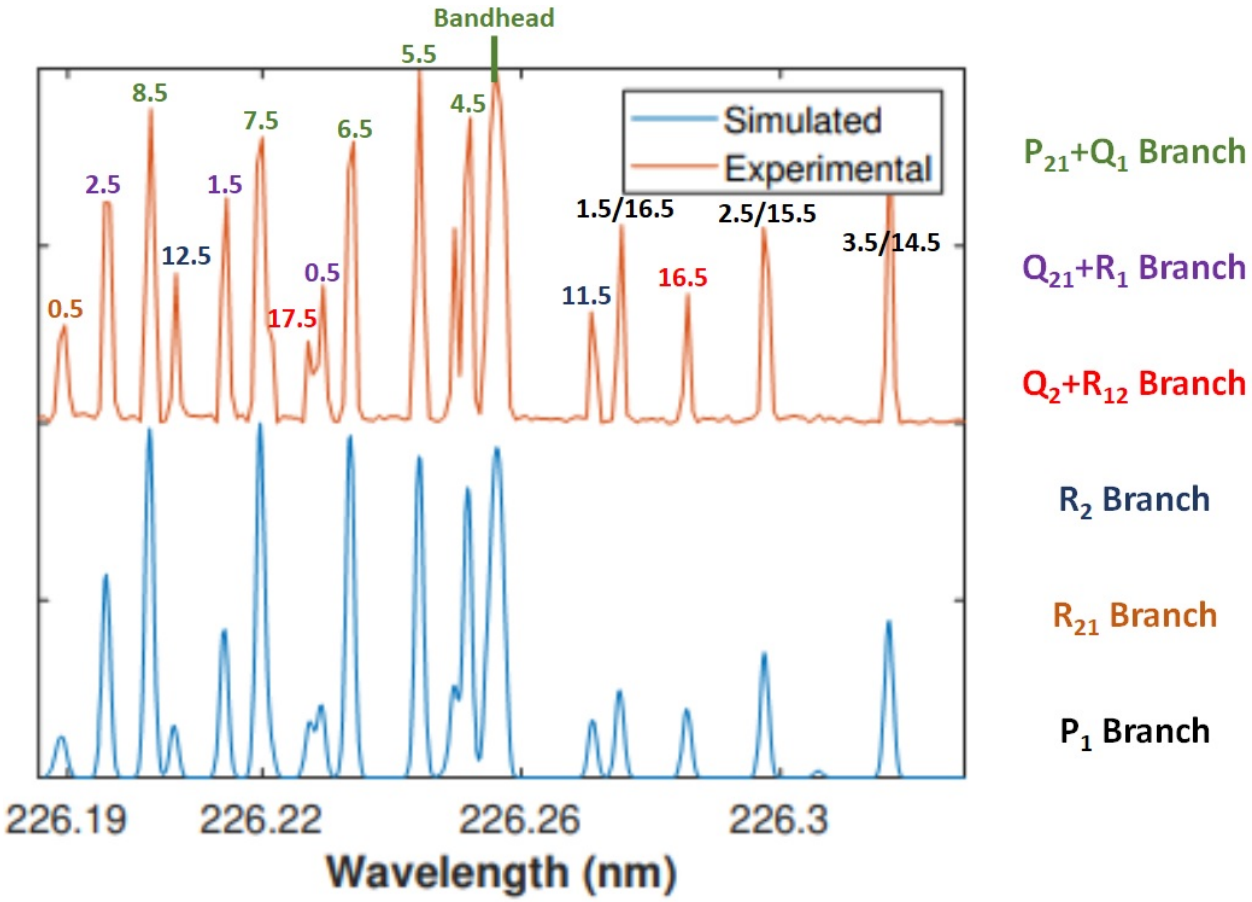

Figure 2.4: $A^2\Sigma^+$ ($v' = 0$) $\leftarrow$ $X^2\Pi$ ($v'' = 0$) spectral region.

Figure 2.5: NO_2 mixture setup.

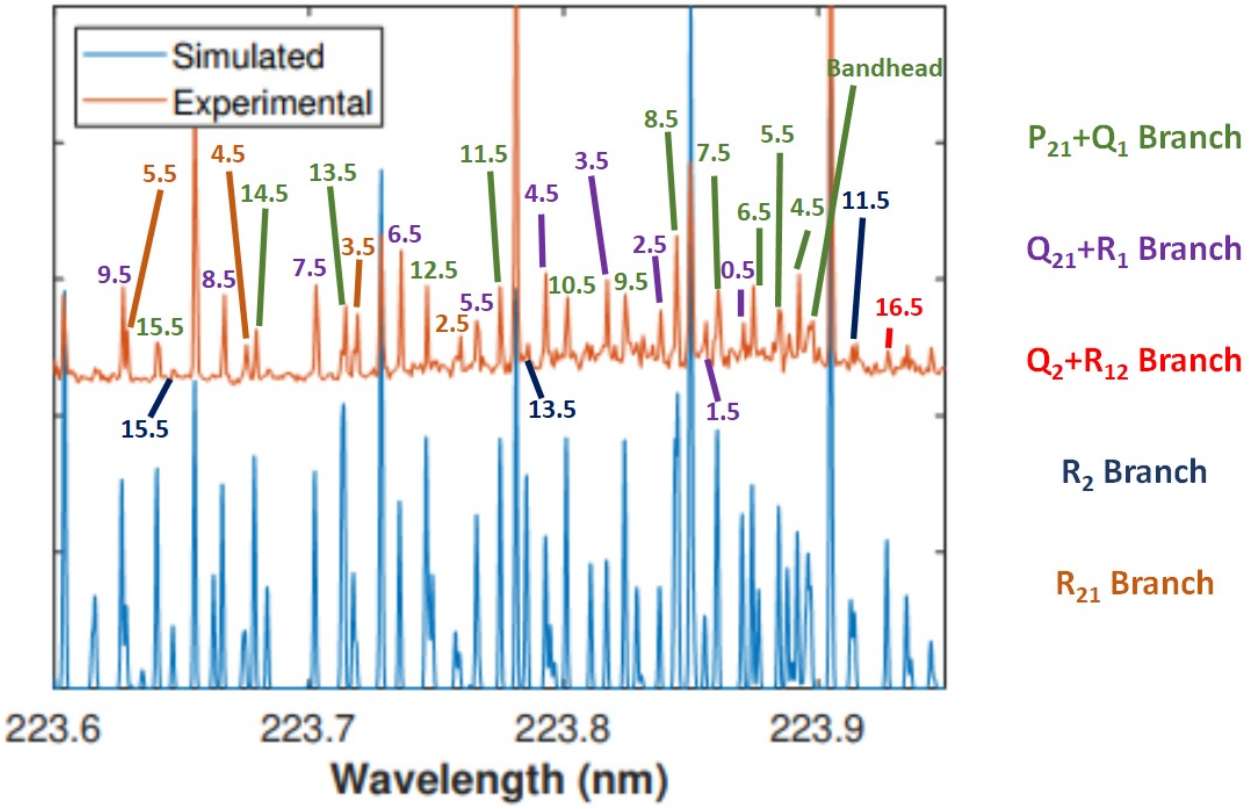

Figure 2.6: $A^2\Sigma^+$ ($v' = 1$) $\leftarrow$ $X^2\Pi$ ($v'' = 1$) spectral region.

2.5 Camera Configurations

To minimize vibrations experienced by the cameras and optics a 3' $\times$ 8' table was built to fit below the ACE infrastructure. Two 3' $\times$ 4' laser honeycomb optical breadboards were secured to the top of the table with a $^1/_4$" neoprene rubber lining inserted beneath. An aluminum T-slotted rail frame was built and secured to the table and are shown in Figure 2.7. The majority of the

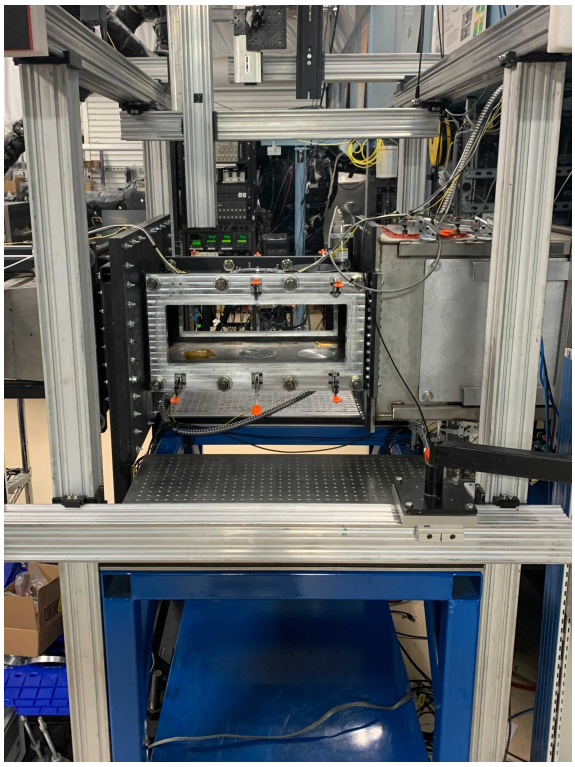

Figure 2.7: ACE table with aluminum frame.

NO LIF measurements were performed using PI-MAX4 1024 $\times$ 1024 ICCD cameras fitted with a CERCO 100 mm F/2.8 UV lens. The cameras were also fitted with 12 mm or 20 mm Kenko extension tubes to adjust the field of view. Initial NO LIF experiments required an operator to manually acquire the fluorescence images using the software interface. A LabVIEW program was written to initiate image acquisition following a set ejector pressure threshold which correlated to the onset of tunnel operation. The synchronization with the ejector pressure allowed the user

to correlate collected images with the real-time tunnel conditions such as stagnation temperature, static pressure, and Mach number. The acquisition modes for the camera were Dual Image Feature (DIF) and full frame. The DIF mode allowed the user to collect two images in rapid succession using the interline transfer function of the camera hardware. The maximum repetition rate of the camera using the DIF setting was limited to 2.5 Hz. Using the DIF mode the user defined the intensifier gain, minimum internal camera time delay, gate width minimum, and the gate delay between the two images. The full frame mode was employed to increase the image acquisition rate, although two cameras were still required for thermometry and velocimetry measurements. At full resolution the maximum acquisition rate was 5 Hz, but with 2 $\times$ 2 binning the repetition rate was increased to 10 Hz. Due to the fixed laser repetition rate it was not necessary to further increase the camera acquisition rate. The first camera received a continuous train of TTL pulses from a BNC 575 digital delay generator. An internal clock was initiated following the camera input trigger. The internal camera delay, camera gate width, and auxiliary output trigger were defined by the user. The auxiliary output trigger was transmitted to the second camera where it contained separate settings related to its internal camera delay and camera gate width. Figure 2.8 details the relative time settings during the dual camera setup.

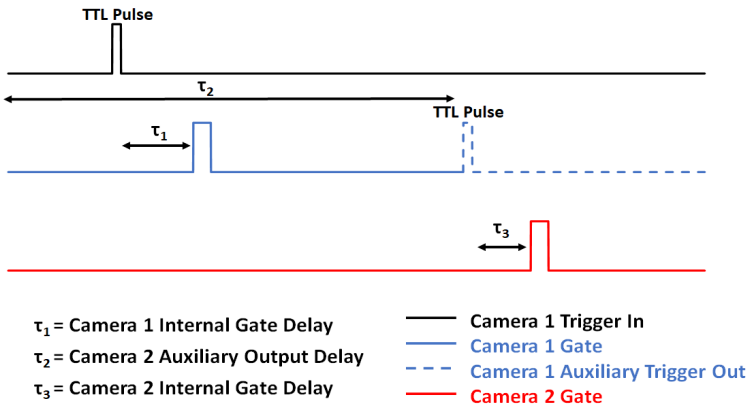

Figure 2.8: Two camera timing settings.

The images were synchronized with the ejector pressure readings of the tunnel to correlate

the acquired images with real-time tunnel conditions. The traces presented in Figure 2.9a were intentionally offset by 5 PSI to display the different ejector pressure traces collected from the two DAQ cards *i.e.* NAL DAQ and Laser DAQ. The traces in Figure 2.9b highlights the modest delay in the two traces and allowed the user to determine the offset necessary to correlate the collected images with the real-time tunnel conditions.

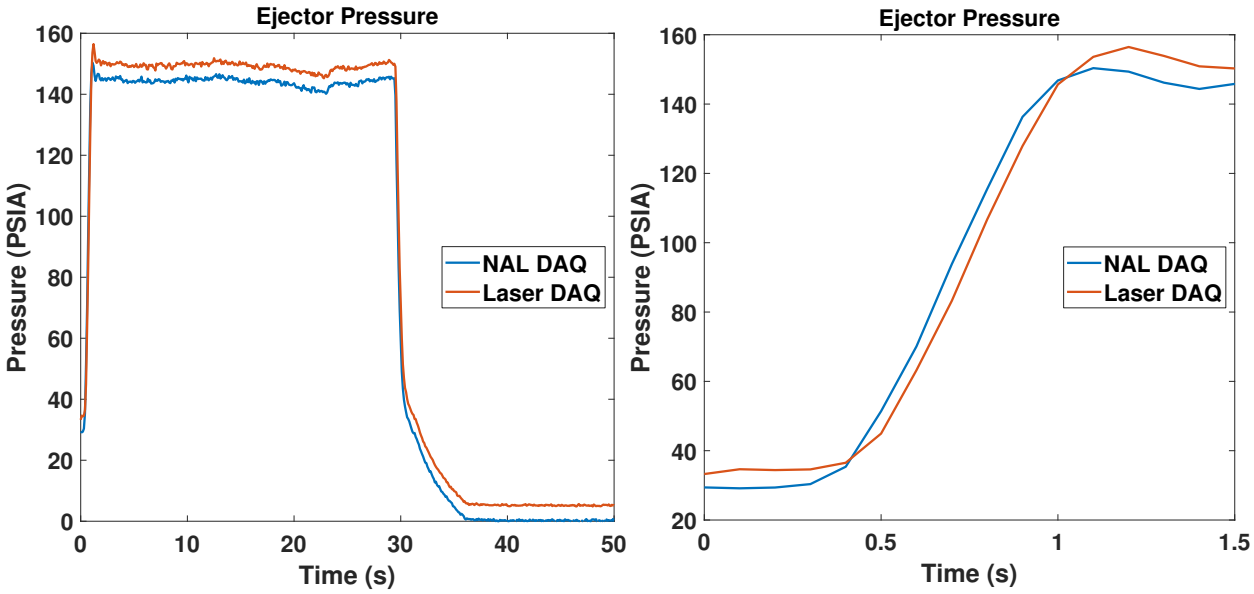

(a) (b)

Figure 2.9: Figure a is the entire ejector trace during the ACE run and Figure b is the initial 1.5 seconds of the ACE run.

2.6 Image Spatial Scaling

2.6.1 *Grid-Card Scaling*

Scaling the field of view was a critical step in the thermometry and velocimetry analysis. The length scales associated with turbulence are an important metric when comparing the empirical results to other turbulent measurements and theoretical turbulent models. The exact location of the turbulent structures on the plate was important and sub-mm errors in the spatial scaling can have a

significant impact on the calculated velocities. Additionally, the scaling was useful in identifying other flow structures such as the leading edge bow shock and the location of SWBLIs.

Each collected image was scaled using glass grid cards with known distances between the grid lines. The grid cards were placed in the camera view plane of interest. It was paramount that the grid card was parallel relative to the camera field of view *i.e.* the lens and ICCD array. To minimize any potential image aberrations, the camera was leveled and a straight edge was used to ensure the camera field of view was parallel to the streamwise plane of the model. Following the precise placement of the grid card an image was collected in full frame mode. The image resolution was the same as the images acquired in the correlating ACE run(s). Figure 2.10 displays a grid card mounted atop the model.

Figure 2.10: Grid card mounted on plate.

Scaling the pixel size to a physical length scale using the acquired grid card image was performed in LabVIEW. The grid card images were smoothed to improve the viability of the applied edge finding algorithm. The smoothing function is a Fast Fourier Transform (FFT) function,

$$X_{FFT} = FFT^{-1}(EXP(-\frac{(R_i - R_T)^2 + (C_j - C_T)^2}{w})FFT(X_{ij})) \tag{2.3}$$

where R_i is the row index, C_j is the column index, R_T is the image row resolution, C_T is the image column resolution, w is the weighting variable, and X_{ij} is the pixel value. In Figure 2.3 the only adjustable variable is w. Figure 2.11 displays the blurring effect on a single simulated grid image as a function of w . Further analysis was performed on the simulated image to quantify the blurring effect in relation to the physical space domain of the image. The simulated image was blurred several times by adjusting w from 5×10^1 to 1×10^4. A horizontal slice of a vertical grid line was Gaussian fitted to determine the width in terms of pixels. The following equation,

$$\sigma_{BX}^2 = \sigma_X^2 + \sigma_w^2 \tag{2.4}$$

where σ_{BX}^2 is the Gaussian width of the blurred image, σ_X^2 is the Gaussian width contribution of the original image, and σ_w^2 is the Gaussian width contribution from the blurring function was used to determine the FFT algorithm blurring. Figure 2.12a plots the Gaussian features from the blurred image set and Figure 2.12b shows the FFT blur width as a function of w. The FFT blur width shows a linear logarithmic trend relative to w. Following the image blurring of the grid card, the image was rotated to ensure the pixel distance between the two grid lines represented the true physical distance between the grid lines. The optimal angle of rotation was found by extracting a portion of the rotated image containing the grid line features. The rows in the extracted image were vertically binned and Gaussian fitted. Chi-square minimum analysis was performed on the two curves to find the angle producing the curve fit closest to a true Gaussian feature.

The grid line edges were identified using a LabVIEW edge finding algorithm. An edge within the image was determined by initially defining the dimensions of a kernel subspace. An applied

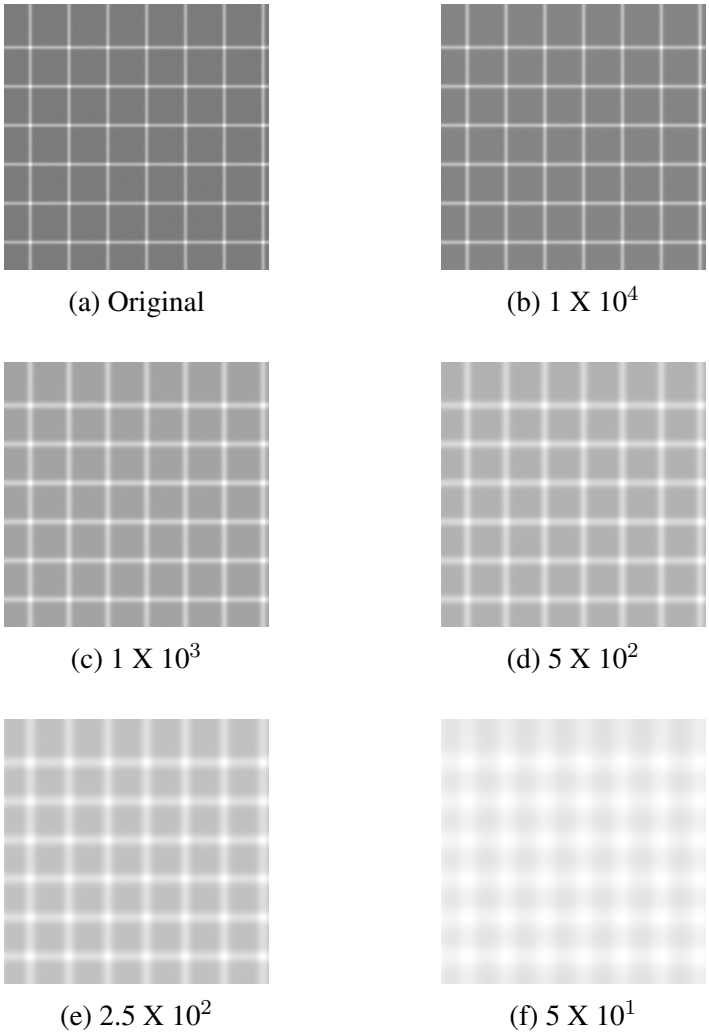

(a) Original (b) 1 X 10^4

(c) 1 X 10^3 (d) 5 X 10^2

(e) 2.5 X 10^2 (f) 5 X 10^1

Figure 2.11: Gray-scale simulated grid images with various degrees of FFT blurring.

kernel operator performed the Fourier transform of the first derivative to identify local maximum and minimum or a rising and falling edge. Sub-pixel accuracy was achieved by fitting the local maximum or minimum with a parabolic function with an estimated $1/25$ sub-pixel accuracy. The algorithm then determines the center position between the rising and falling edges. The physical image scaling was determined by dividing the known real distance by the pixel distance.

2.6.2 *Two-Camera Image Alignment*

The dual camera setup required post-processing to account for image spatial differences between the two cameras. Prior to acquiring grid card images for each camera, the cameras were

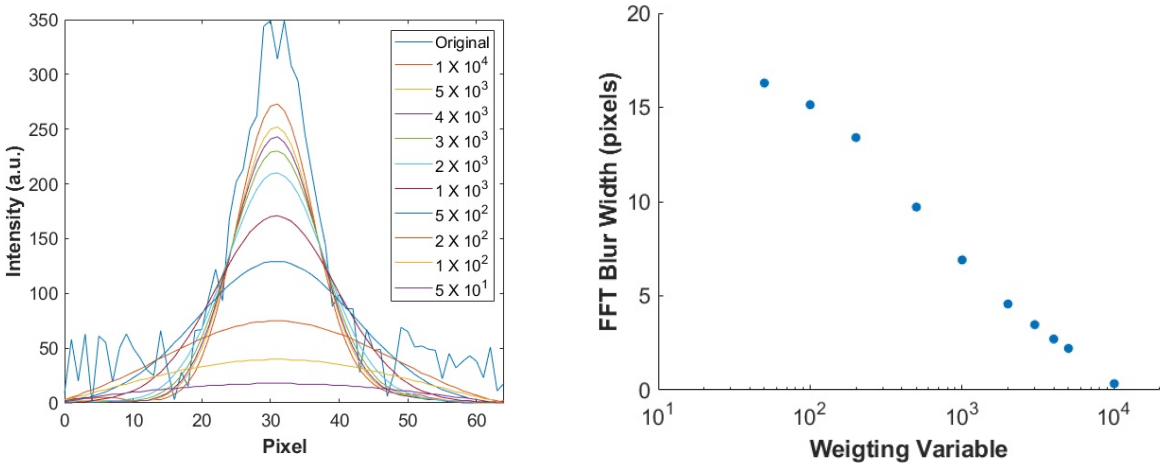

(a) Horizontal slice of grid line

(b) FFT blur width

Figure 2.12: FFT blurring image analysis.

carefully aligned in space so the spatial offset was minimized. The angle of the first acquired grid card image was optimized then the second grid card image was added to the first grid card image. Using a similar approach described previously, the rows were binned vertically and Gaussian fit. The angular and spatial offset of the second grid card image were then optimized to minimize the width of the fitted Gaussian profile. There was no correction for physical image scaling because the lens focus for both of the cameras was set to the same setting. This was verified through the image scaling process.

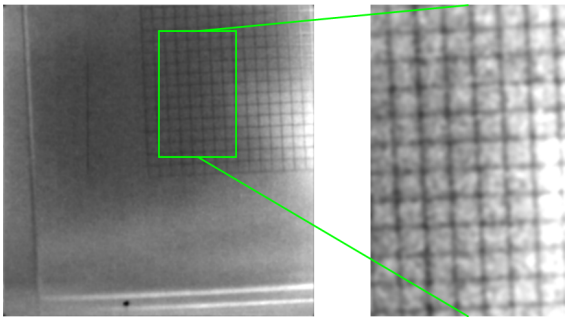

(a) Blurred extracted image

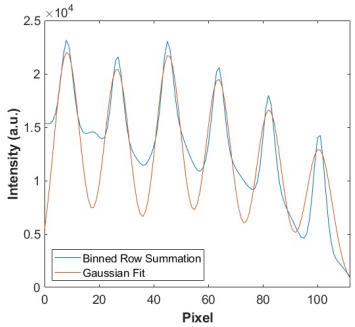

(b) Gaussian fitted curve

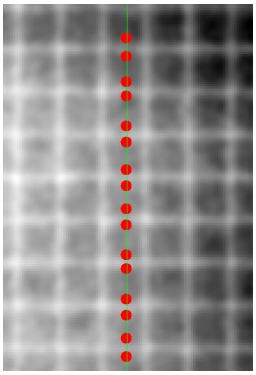

(c) Identified grid line edges

Figure 2.13: Image scaling using a grid card.

3.1 Optimization of NO Seeding

Prior to performing complex VENOM measurements, the NO LIF experiments were focused on mitigating the observed flow perturbations resulting from NO seeding. Flow visualization (PLIF) was the optical diagnostic to qualitatively characterize the observed perturbations. These experiments imaged the spanwise fluorescence profile of the seeded NO. Custom mixtures of N_2/NO were made using a constant set ratio of N_2 and NO controlled by an in-house LabVIEW PID algorithm.[49] Prior to filling the gas lines and ballast, the entire system was evacuated with the Leybold D65B backing pump. The mixture ballast was filled with N_2 (99.999% Brazos Valley Welding Supply) and NO (99.95% Praxair) until the set point pressure was reached. The ballast pressure was continuously monitored using an Omega Type PX309-300A5V pressure transducer. According to the ballast pressure, the program output a DC voltage dependent signal to control the mass flow controllers (MKS Mass-Flo 1179A) using a four channel power supply/readout (MKS 247) operating in a constant-flow ratio setting. The concentration of NO ranged from 1% to 5% during the seeding campaign. The ACE tunnel conditions during the campaign are listed in Table 3.1. The frequency doubling laser was used for the NO seeding optimization experiments. The

Mach Number	P_t (Torr)	P_∞ (Torr)	T_t (K)	T_∞ (K)	Re / m
5.9	3000	2.0	430 K	55	4.5×10^6

Table 3.1: Conditions for NO seeding optimization.

UV beam was tuned to the P_2/Q_{12} $A^2\Sigma^+$ ($v' = 0$) $\leftarrow$ $X^2\Pi_{3/2}$ ($v'' = 0$) bandhead transition. The laser beam propagated through a series of cylindrical lenses where a laser sheet ($\sim$800 μm) was focused at the center of the tunnel, 11.4 cm from the test section floor. Figure 3.1 displays the camera and

lens configuration for the NO seeding optimization experiments. The camera operated in the full

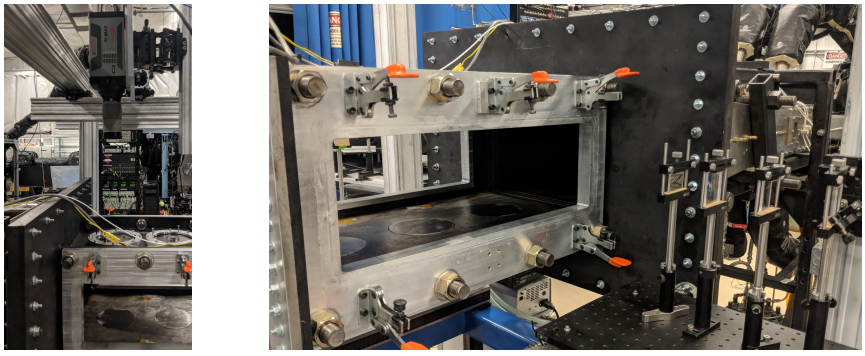

(a) (b)

Figure 3.1: Camera and lens configuration for the NO seeding optimization experiments.

frame mode at 5 Hz and was gated to image the fluorescence profile directly after the laser scatter. Following the onset of the ejector, the camera operator manually initiated image acquisition. The N_2/NO mixture was initially introduced downstream of the flow conditioners due to an existing port located on the floor of the settling region. Injecting downstream introduced perturbations into the freestream flow and will be discussed in detail later. Initial efforts to mitigate the flow perturbations were changing the seeder size, shape, and configuration. The seeders were crimped stainless steel tubes with widths of $^1/_8$", $^1/_4$", and $^3/_8$." Initial seeders were cylinders with a crimped end and were perforated with $\sim$1 mm holes along the side for the gas to exit (Figure 3.2a). The next generation of seeders contained an extended slit spanning the height of the seeder to identify the potential role of an annular gas exit. Open-slit seeders were made from the various tube sizes mentioned earlier (Figure 3.2b). The shape of the seeder was then modified to have a 90° turn where the end of the stainless steel tube was the gas exit (figure 3.2c). Again, various sized seeders were made for the 90° shape to mitigate the flow perturbations.

Initial NO LIF experiments introduced N_2/NO gas downstream of the flow conditioners within the ACE settling region. The N_2/NO mixtures were introduced through an existing 11.6 cm $\times$ 4.9 cm stainless steel port. The port contained a $^1/_2$" NPT hole allowing for the introduction of

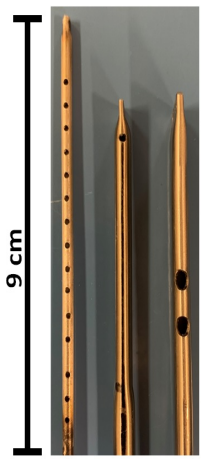

(a) Perforated Seeders

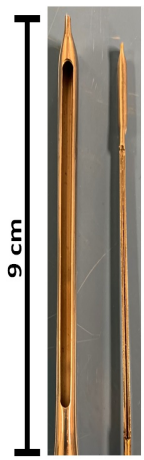

(b) Open-Slit Seeders

(c) Curved Seeders

Figure 3.2: Various seeder designs.

a stainless steel seeder. To ensure an effective seal, CONAX stainless steel compression fittings were installed to create a hermetic seal for a stainless steel tube extending into the high pressure settling region. The gas mixture was pulsed into the facility using a fuel injector housed within a pressurized chamber to minimize the risk of an NO leak. The pressure chamber is shown in Figure 3.3a and the internal fuel injector lines is shown in Figure 3.3b. The fuel injector received a 10 V 20 ms pulse at 5 Hz from a 575 Model BNC digital delay generator. The NO mixture was manually introduced into the facility using a ball valve directly under the settling region. The ball valve was closed $\sim$5 seconds prior to the end of the run to purge any residual NO within the ACE facility. The backing pressure upstream the injector was relatively constant during the entire run time.

As mentioned previously, the focus of the dissertation was to characterize the effect of TNE

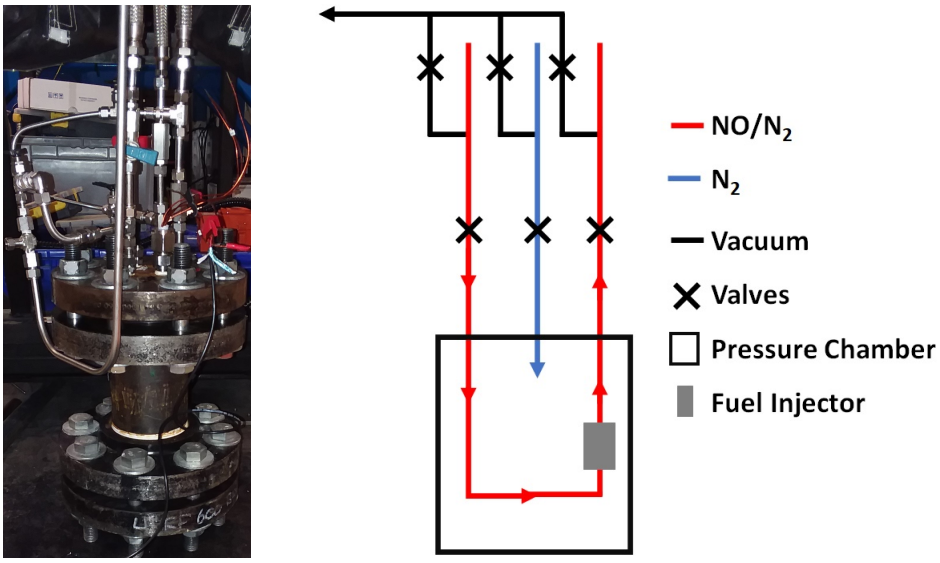

(a) (b)

Figure 3.3: Figure a is the pressure chamber housing the fuel injector and Figure b is the schematic of the gas input and output lines.

with respect to turbulence. Therefore, it was necessary to characterize the relative freestream disturbances when introducing the N_2/NO gas mixture into the ACE facility. Minimizing the degree of perturbations introduced by the seeded NO was critical. The results discussed here are the only known measurements related to the introduction of NO into the pre-expansion region of a conventional hypersonic blow-down wind tunnel. Initial experiments erred on the side of caution and reduced the amount of NO introduced into the ACE facility by pulsing N_2/NO injections. Introduction of NO downstream of the flow conditioners provided image sets with adequate freestream S/N; however, the image sets contained evidence of significant flow perturbations. The seeding configuration was assumed to perturb the flow by a combination of vortex shedding, vortex-induced vibrations, and free jet expansion through the seeding orifice. Vortex shedding is a common phenomenon where the flow develops oscillations due to the presence of an object. Vortical structures are produced on the rear of the object and periodically detach to form Kármán vortex streets. The resulting vortices become entrained within the surrounding bulk flow. Vortex shedding is a large-scale fluid effect observed in a variety of flow fields ranging from wind currents around a building

to cylindrical bodies within a supersonic flow.[50][51][52] Vortex shedding can quantified using the dimensionless Strouhal number, *St*, as shown in the equation,

$$St = \frac{f_s L}{U_\infty} \tag{3.1}$$

where f_s is the vortex shedding frequency, L is the characteristic length of the object, and U_∞ is the bulk fluid velocity; however, it was not the focus of the presented study.[53][54] Flows with a Reynolds number ranging from 2.5×10^2 to 2.0×10^5 have a *St* value of $\sim$0.2, but vary greatly for higher Reynolds number flows.[55] In a study by Ardekani, the vortical structure frequency component was directly measured using hot-wire anemometry and NO PLIF flow visualization was used to qualitatively descrive the vortex shedding process.[56] The formation of the vortical structures can be amplified in a positive feedback loop through vortex-induced vibrations. Within ACE the vortex structures detached from the seeder body and produce pressure differentials. The pressure gradients can create lift forces which lead to the seeder vibrating within the settling region. This flow effect is well characterized for cylindrical bodies in low and high speed flows and can be modeled effectively using numerical methods.[57][58][59] The final potential source of flow perturbations was from the free jet expansion process of the N_2/NO gas mixture exiting the seeder. Near the exit orifice, a laminar shear layer formed on the outer edges of the expanding jet. The instabilities in the shear layer grow rapidly and breakdown into ring vortices which are incorporated into the surrounding bulk flow. An excellent review written by List provides a detailed explanation of the turbulent free jet expansion and the effect of variable flow conditions.[60]

The perforated and open-slit seeders produced wake structures regardless of the seeder size as shown in Figure 3.4. The spatial spread of the NO LIF image sets did not display a strong dependence on the seeder width. The pressure differential across the fuel injector was varied to potentially minimize the flow perturbations, but it was determined to be insensitive. There was however an increase in the NO spatial spread when the pressure differential increased across the fuel injector as seen when comparing Figure 3.4e to Figure 3.4f . The following generation of

seeders were a curved air-foil stainless steel tubes designed to promote the Coandă effect. This flow phenomenon describes the propensity of a fluid to stay attached to a convex surface as it moves past an object.[61] As shown in Figure 3.5, the flow remained perturbed when the seeder was mounted downstream of the flow conditioners. It was apparent the NO distribution within the test section was narrower compared to the perforated and open-slit seeders. All images collected with the seeder mounted downstream of the flow conditioners had evidence of vortex shedding. The image sets collected suggested flow perturbations were present regardless of the seeder configuration. To support this, an N_2/NO gas mixture was directly injected from the ACE settling region floor without a seeder extending into the flow. The images in Figure 3.6 display a highly perturbed flow containing intricate ring vortices, but they were absent of wake-like structures. With a combination of all these findings, it was necessary to inject upstream of the flow conditioners to mitigate any flow effects from the NO seeding process. As a result, the ACE settling region was modified to inject upstream of the flow conditioners. A 1" NPT hole was drilled 17.8 cm from the side of the settling region and 2.5 cm in front of the first aero-grid. Figure 3.7 displays the side and bottom profiles of the ACE settling region. The flow perturbations were significantly minimized when injecting through the modified port. Figure 3.8 contains a series of representative images of seeding NO upstream of the flow conditioners. The flow appeared to be absent of any wake-like structures and ring vortices suggesting the aero-grids and fine meshes effectively dampened the large-scale structures. The NO spatial distribution within the test section was greater compared to injecting downstream of the flow conditioners. This was due to the increased amount of mixing at the new injection location where the air inlets for the ACE facility are directly adjacent to the seeder gas exit. The images appeared to have striations in the fluorescent profile due to non-uniform NO mixing upstream of the flow conditioners. There was no appreciable increase in the S/N when the pressure differential across the fuel injector increased.

With the flow perturbations minimized, the following goal was to maximize the observed S/N within the freestream. It was determined the amount of gas pulsed by the fuel injector was not sufficient, so the method of introducing NO transitioned from a pulse setting to a continuous seeding

setting. This was achieved by pressurizing a reservoir with a custom gas mixture then introducing the NO manually by opening a ball valve directly beneath the ACE settling region. To minimize the waste of the N_2/NO mixture and maximize the length of the ACE tunnel run several seeders were made to optimize the observed NO LIF signal. The seeder used for the subsequent thermometry and velocimetry campaigns was a $^3/_8$" crimped tube. The seeder had a single gas exit orifice 1.6 mm in diameter and the orifice was located 66.7 mm from the settling region floor (Figure 3.9. However, during continuous seeding the pressure decrease was too rapid for the mass flow controllers to maintain a constant backing pressure. Therefore the ballasts were pressurized to $\sim$200 PSIA to ensure the acquired images were repeatable and contained adequate S/N ratio. In addition, a dual ballast configuration was built to increase the length of time for image acquisition (Figure 3.10). A representative ballast trace during an ACE run is shown in Figure 3.11.

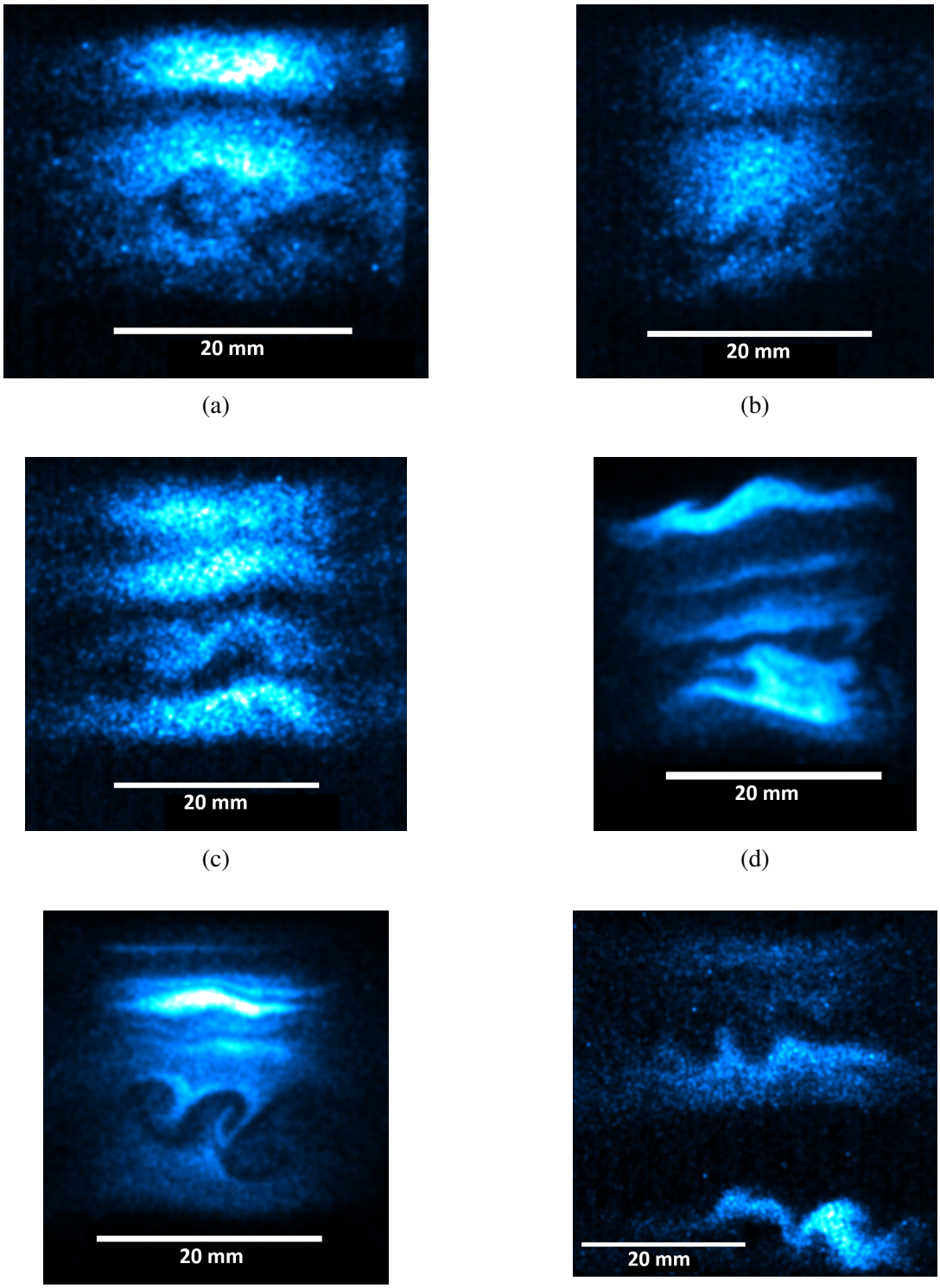

(a) (b)

(c) (d)

(e) (f)

Figure 3.4: The $^1/_8$" perforated and open-slit seeder are Figures a and b respectively. The perforated $^1/_4$" and $^3/_8$" seeder are Figures c and d respectively. A pressure differential of 30 PSIA across the fuel injector (Figure e) has a smaller NO distribution than a differential of 90 PSIA (Figure f).

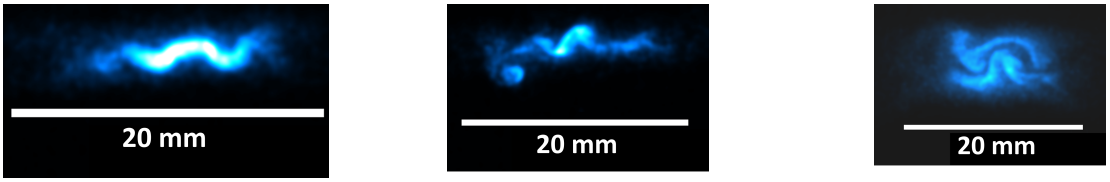

(a) (b) $^1/_4$" (c) $^3/_8$"

Figure 3.5: NO spatial distribution from the curved seeder design. Figures a, b, and c correlate to $^1/_8$", $^1/_4$", and $^3/_8$" stainless steel tube sizes.

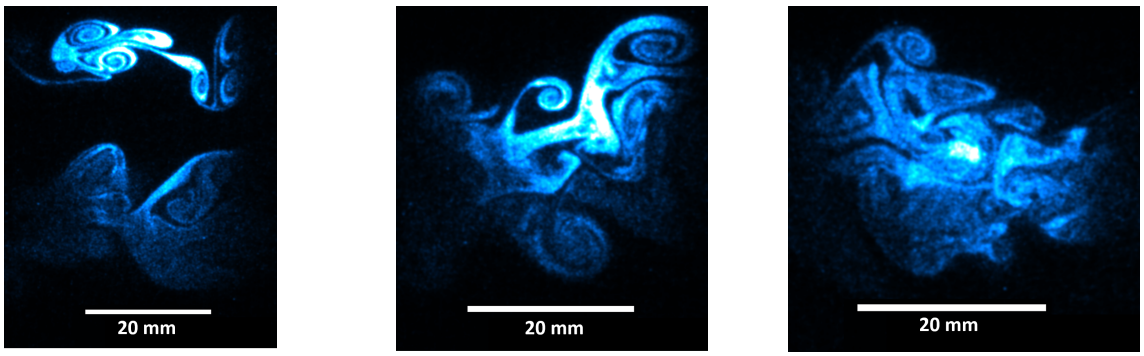

(a) (b) (c)

Figure 3.6: Distribution of injecting from ACE settling region floor.

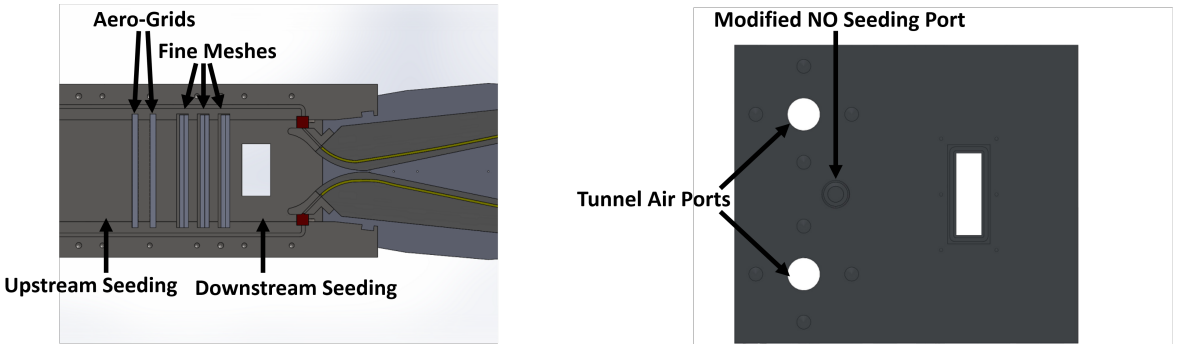

(a) (b)

Figure 3.7: Final NO introduction configuration. The side and bottom view are shown in Figures a and b, respectively.

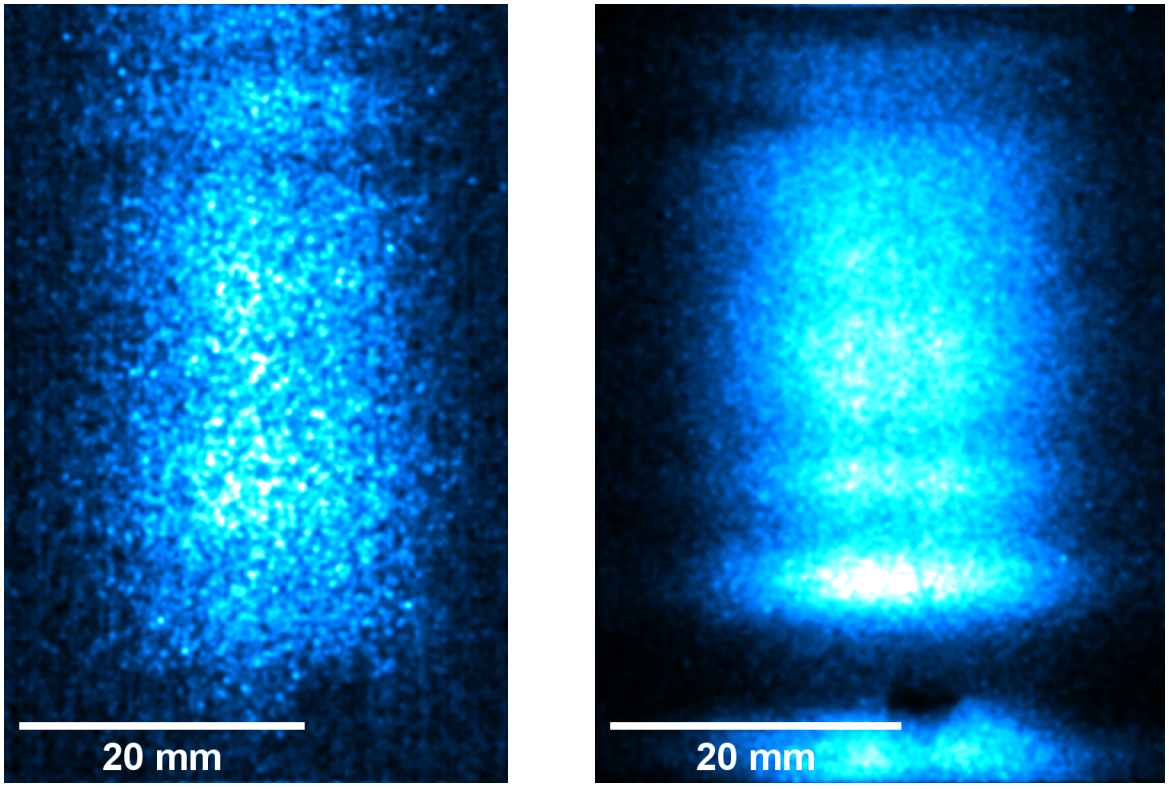

(a) (b)

Figure 3.8: NO spatial distribution from the final seeder design. Figures a and b correlate to 30 PSIA and 60 PSIA pressure differentials across the injector.

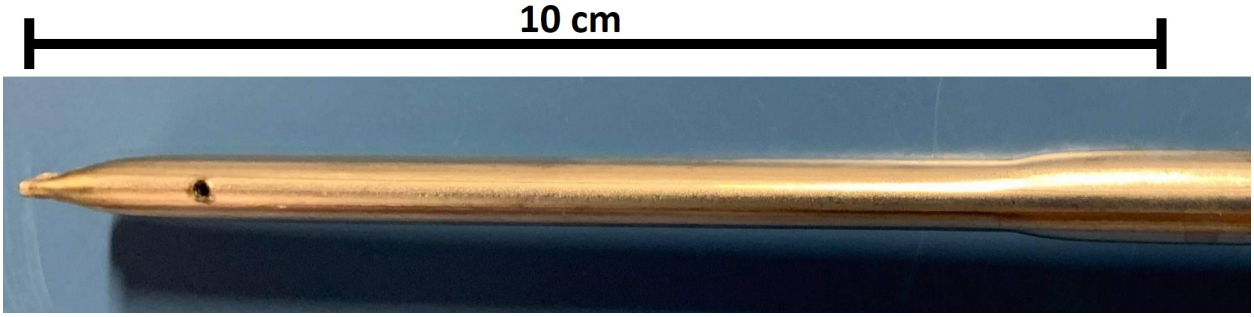

Figure 3.9: Final seeder design.

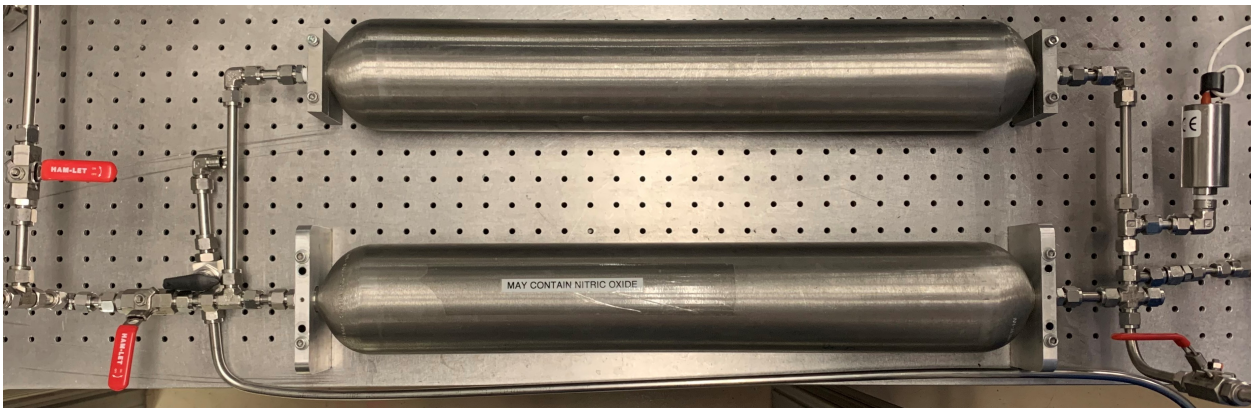

Figure 3.10: Dual ballast configuration.

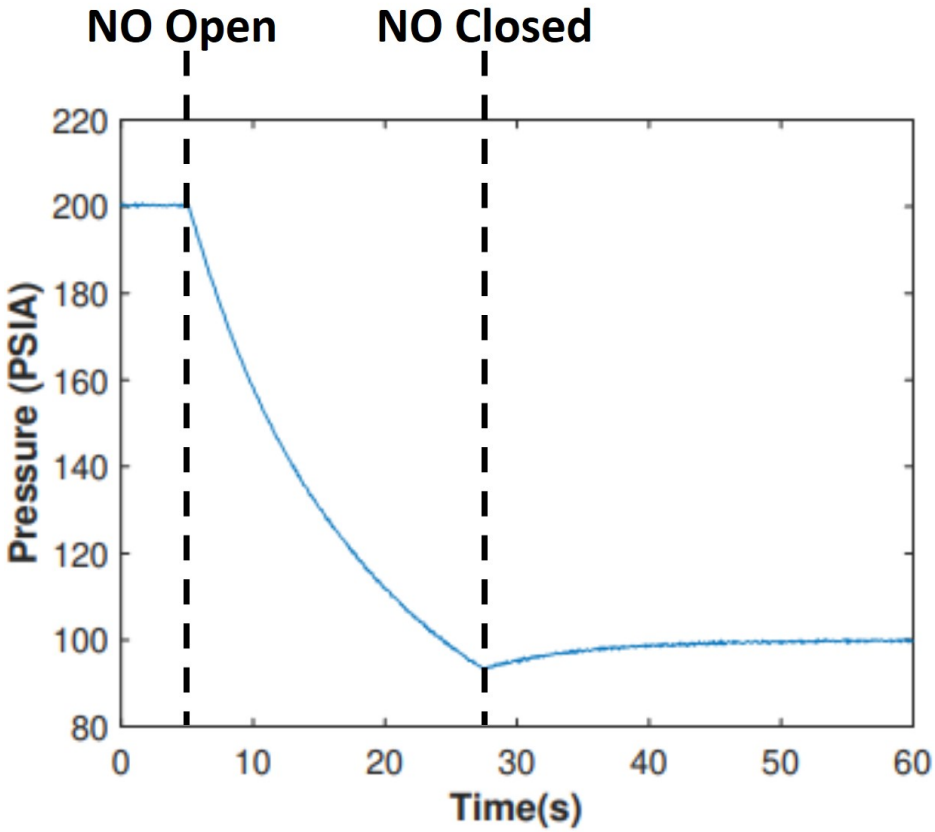

Figure 3.11: Ballast pressure trace during ACE run.

3.2 Characterization of NO Concentration

A goal of the NO LIF experiments was to characterize the relative local concentration of the NO within the ACE test section. Measuring the NO concentration in the flow was useful in designing the later experiments because it provided the limitations of the NO LIF optical based techniques. An experiment to determine the NO fluorescent lifetime within ACE was performed by measuring the total decay rate constant as a function of NO concentrations. The total decay rate constants were fit with a kinetic decay model that will be described in detail later. The ACE tunnel conditions for the campaign are listed in Table 3.2

Mach Number	P_t (Torr)	P_∞ (Torr)	T_t (K)	T_∞ (K)	Re / m
5.8	3200	2.0	430 K	56	4.8 X 10^6

Table 3.2: ACE Conditions for NO concentration campaign.

Gas mixtures of 10%, 20%, and 30% NO were made to test if the local concentration within the ACE test section was sensitive to the initial NO mixture concentration. These experiments were performed by pulsing 20 ms N_2/NO injections at 5 Hz upstream of the flow conditioners. The N_2/NO mixture was maintained at a constant pressure by the LabVIEW Proportional-Integral Derivative (PID) algorithm mentioned previously. The frequency doubling laser system was used to electronically excite the seeded NO. A BNC Model 575 digital delay generator triggered the laser pulse in relation to the fuel injector trigger. The laser beam was tuned to the P_{21}/Q_1 $A^2\Sigma^+$ ($v' = 0$) $\leftarrow$ $X^2\Pi_{1/2}$ ($v'' = 0$) bandhead transition. The laser beam propagated from the top-down region of the test section through the fused silica window ports closest to the ACE nozzle. An MCP-PMT Hamamatsu R5916U-50 was oriented 90° relative to the laser propagation. The MCP-PMT had a UG5 filter (Thorlabs) mounted in front of the PMT detector to provide a bandpass of 240 nm to 395 nm. The PMT was biased to -1.5 kV to -2 kV. The digital delay generator provided an 18 V trigger pulse to the MCP-PMT 10 ns after the laser pulse arrived in the test section to reduce the laser

scatter. The MCP-PMT had a gate width of 600 ns to ensure collection of the entire fluorescent signal along with the baseline noise after the decay. The MCP-PMT signal was digitized using a LeCroy (HRO 66Zi) oscilloscope at a sampling rate of 2 GS/s. An in-house LabVIEW program was used to collect the data.

The fluorescent lifetime was highly dependent on the concentration of the individual gas species in the system *i.e.* N_2, O_2, and NO, due to collisional quenching of the NO $A^2\Sigma^+$(v = 0) state from the mentioned species. Collisional quenching of N_2 was negligible due to the collisional quenching cross section being ∼5000 times smaller than those of O_2 and NO.[62][63][64] As described earlier the laser was tuned to excite the P_{21}/Q_1 bandhead $A^2\Sigma^+$ (v′ = 0) ← $X^2\Pi_{1/2}$ (v″ = 0) transition. There is no correlation between the collisional quenching rates and the *J* state involved during the relaxation process for the current quenching species *i.e.* N_2, O_2, and NO.[65][66][67][68] The bandhead was chosen to maximize the fluorescent signal within the low temperature freestream of ACE. The observed fluorescent signal was a product of the spontaneous emission and collisional quenching. The relaxation of the NO $A^2\Sigma^+$ state is described by

$$\mathrm{NO\ A^2\Sigma^+} \xrightarrow{k_f} \mathrm{NO\ X^2\Pi}, \tag{3.2}$$

$$\mathrm{NO\ A^2\Sigma^+ + M} \xrightarrow{k_q(T)} \mathrm{NO\ X^2\Pi + M} \tag{3.3}$$

where k_f is described as the intrinsic rate of fluorescence for NO $A^2\Sigma^+$ (v′ = 0), M a collisional quencher, and $k_{q,M}$(T) is the temperature dependent quenching rate constant for collisional quencher M. The intrinsic rate of fluorescence, k_f, is 5.19×10^{-6} s^{-1}.[65] Each averaged fluorescence decay trace was fitted using the integrated rate law

$$ln\left(\frac{I(t)}{I_0}\right) = k_{tot} = -(k_f + \sum_M k_{q,M}(T)[M])t \tag{3.4}$$

where I(t) is the measured fluorescence signal, k_{tot} is the total decay fluorescent constant, [M] is the total number density of each quenching specie with units molecules cm^{-3}, k_f has units of s^{-1}, and $k_{q,\mathrm{M}}$(T) has units of cm^3s^{-1}. The ln plots were linearly fit for each trace to find k_{tot} described

in Equation 3.4. The reciprocal of k_{tot} is equal to the fluorescence lifetime, τ. The total observed fluorescence decay constant consists of contributions from the intrinsic fluorescence rate constant, k_f, and the total collisional quenching rate $k_{q,\mathrm{M}}$(T)[M]. In the current flows the observed $k_{q,\mathrm{M}}$(T) was primarily due to collisional quenching with NO and O_2 and the total decay rate was found with

$$k_{tot} = k_f + k_{q,\mathrm{NO}}(T)[\mathrm{NO}] + k_{q,\mathrm{O_2}}(T)[\mathrm{O_2}] \tag{3.5}$$

where $k_{q,\mathrm{NO}}$(T) and $k_{q,\mathrm{O_2}}$(T) are the temperature dependent quenching rate constants for NO and O_2, respectively. The low temperature dependent collisional cross-section, $\langle\sigma_{q,\mathrm{M}}(T)\rangle$, was calculated using an inverse power-law model.[44] The temperature dependent collisional quenching rate is determined from the equation

$$k_{q,\mathrm{M}}(T) = \langle\sigma_{q,\mathrm{M}}(T)\rangle\sqrt{\frac{8k_BT}{\pi\mu_{\mathrm{NO,M}}}} \tag{3.6}$$

where $\mu_{\mathrm{NO,M}}$ is the reduced mass of the NO and the collisional quenching species.

The observed decay rates in Figure 3.12 were fitted using linear regression analysis with an R^2 exceeding 0.99. The high linearity confirms the absence of saturation effects or dimer formation due to the low temperatures. The empirical total fluorescence decay rates, averaged tunnel operating conditions, and averaged theoretical total fluorescent decay rates are seen in Table 3.3. The observed fluorescence lifetime had minimal variation with the concentration of the N_2/NO injected gas mixture. This observation implied the current fluorescent decay measurements were insensitive to changes in the concentration of NO within the injected gas mixture. Equation 3.6 was used to calculate a theoretical fluorescent decay rate to find the local concentrations of N_2, O_2, and NO. The input for the freestream number density and temperature were calculated using collected tunnel data, isentropic relations, and the ideal gas law. The input relative fractions of N_2, O_2, and NO were calculated using an algebraic expression with one adjustable parameter, the ratio of the injected mixture to the bulk flow. By adjusting this parameter, the difference between the theoretical fluorescent decay constant and the measured decay constant was minimized. Using the

model described above the upper bound limit, assuming an injection of pure NO, yielded a local concentration $\sim$1%. With this upper bound limit it was assumed that a majority, >95%, of the NO $A^2\Sigma^+$ state collisional quenching was due to O_2. Collisional O_2 quenching and NO self-quenching have similar quenching cross sections; however, O_2 quenching had a greater impact overall due to the higher O_2 concentration within the bulk flow. Figure 3.13 is a theoretical plot displaying the linear dependence of k_{tot} versus the relative freestream NO concentration. Following the relaxation from the NO $A^2\Sigma^+$ state, the relative vibrational population of the NO $X^2\Pi$ state was dependent on the fluorescent decay to collisional quenching decay ratio. The limiting cases for the NO $X^2\Pi$ (v = 1) fractional population are 0.28 for relaxation through fluorescence and 0.10 for relaxation through collisional quenching.[69][70] The $NO_{v=1}$ fractional population in the ACE test section was a product of the competing relaxation pathways. Based on the total contribution of the collisional quenching rate constants relative to the intrinsic fluorescent rate constant, 16% of the NO $A^2\Sigma^+$ ($v'' = 0$) state population relaxed to the NO $X^2\Pi$ ($v' = 1$) state. The uncertainty of the total observed fluorescence decay constant was determined by propagating standard error of linear fits. Each raw fluorescent decay trace was linearized by taking the natural log and modeled with linear regression analysis. The linear fits were averaged and fit with linear regression analysis. The upper and lower bounds of the average linear regression analysis were determined using the standard error of the points in the linear regression. The uncertainty in k_{tot} was estimated to be the averaged difference between the upper and lower bounds of k_{tot} compared to the average k_{tot}.

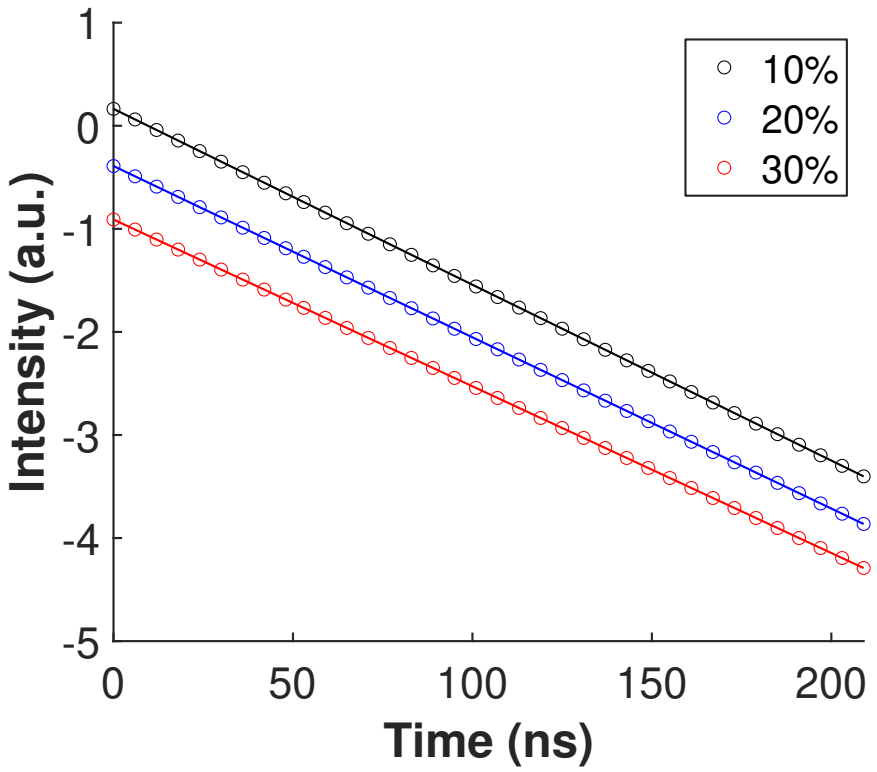

Figure 3.12: Averaged fluorescence decay traces plotted versus time for the NO mixtures with concentrations of 10%, 20%, and 30%. Only every 5th experimental point is shown. The open circles denote the averaged experimental data at each mixture concentration and the solid curves are the fits for each of the obtained averages. The 20% and 30% traces and associated fits are offset for clarity.

	Injector Gas Conc. N_2/NO	Lifetime, τ (ns)	Mach Number	Freestream Pressure (Torr)	Theoretical $k_{tot}(s^{-1})$	Measured $k_{tot}(s^{-1})$
Run 4009	10%	58.5±1.0	5.80	2.48	$1.71\times10^7\pm 1.5\times10^5$	$1.71\times10^7\pm 3.0\times10^5$
Run 4011	20%	60.4±1.1	5.81	2.38	$1.68\times10^7\pm 1.3\times10^5$	$1.66\times10^7\pm 3.0\times10^5$
Run 4012	30%	63.2±2.4	5.81	2.37	$1.69\times10^7\pm 1.6\times10^5$	$1.62\times10^7\pm 6.0\times10^5$

Table 3.3: Summary of the experimental fluorescence decay constants, tunnel run conditions, and the theoretical fluorescence decay constants.

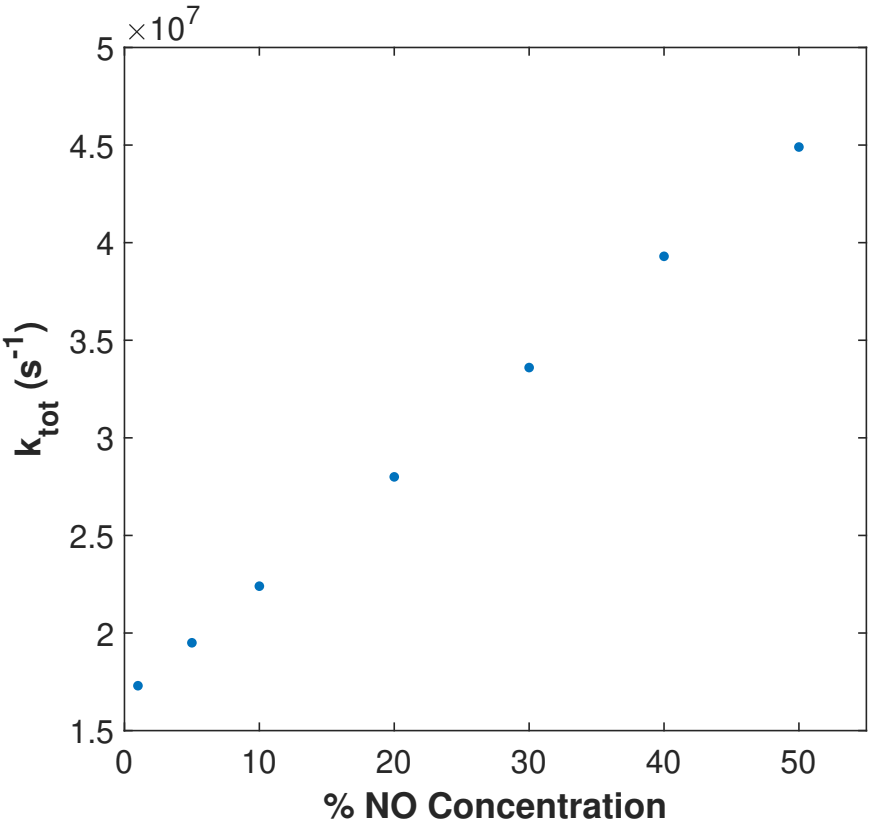

Figure 3.13: Total fluorescent decay constant (k_{tot}) vs. the NO concentration at 60 K and 2.5 Torr.

3.3 Seeded NO Distribution

Characterizing the NO distribution within the ACE test section was critical to optimizing the seeding process. The goal was to have the NO distribution span the entire optical field of view normal to the plate while minimizing the spanwise spread within the ACE test section. For the campaign, the ACE facility was continuously seeded with a 5% N_2/NO gas mixture. The top-down and spanwise distributions within the ACE tunnel were both characterized with the flat plate wedge model mounted inside the tunnel and without it. Visualizing the NO distribution profile with the model mounted within the test section was critical in understanding the large-scale flow effects. The ACE tunnel operated at a Reynolds condition of 6×10^6 m^{-1} with the model mounted within the tunnel. With the model removed, it was difficult for the ACE tunnel to reach the 6×10^6 m^{-1} Reynolds condition due to the low blockage ratio. As a result, the tunnel was swept up to 4.9 $\times$ 10^6 m^{-1} for the top-down measurements and 5.8 $\times$ 10^6 m^{-1} for the spanwise measurements. All of the other tunnel conditions for both campaigns are listed in Table 3.4.

Mach Number	P_T (Torr)	P_∞ (Torr)	T_t (K)	T_∞ (K)
5.7	3800	2.0	430 K	57

Table 3.4: ACE Conditions for NO distribution campaigns.

3.3.1 Top-down Distribution

The top-down NO distribution was measured simultaneously at two different locations within the ACE test section. Two UV laser beams from two different sum-frequency mixing laser systems were propagated in the top-down direction through UV-grade fused silica windows. For the model-out experiment the beam propagation was 17.9 cm from the test section side wall. For the model-in experiment, the plate did not have the plasma operating and the laminar insert was used. The beam was propagated through the fused silica window inserts 10.8 cm from the side of the plate. The

beams propagated through the regions of the test section correlating to the 1st and 3rd locations of the flat plate. The beams were optimized for a freestream flow of ∼57 K and tuned to the P_{21}/Q_1 $A^2\Sigma^+$ ($v' = 0$) ← $X^2\Pi_{1/2}$ ($v'' = 0$) bandhead transition. The beams did not propagate through any lenses. A ring flange mounted on top of the 152.4 cm window secured it; however, it limited the optical access to ∼14 cm. The fluorescence profiles were imaged separately using two different PI-MAX 4 cameras. The cameras were triggered using the dual camera timing scheme described earlier and were delayed 1.215 μs in time. Each camera was triggered after the laser scatter and gated for 3 ns at 10 Hz at the maximum intensifier gain. Figure 3.14 displays the experimental setup of the top-down NO distribution campaign. In the absence of the model the top-down dis-

Figure 3.14: Top-down distribution camera configuration.

tribution spanned ∼120 cm within the test section core as seen in Figures 3.15a and 3.15b. The image sets for both the model-in and model-out experiments were analyzed to characterize the fluorescence signal distribution and the temporal fluorescence signature. For the spatial analysis the images were background subtracted and horizontally binned. This provided a correlation of the fluorescence intensity relative to the top-down location within the test section. The horizontally

binned plots were averaged and normalized by the maximum for clarity resulting in the blue traces seen in Figures 3.15c and 3.15d. The blue trace was sensitive to any instantaneous changes in the fluorescence intensity. Based on the average normalized intensity it was apparent there was a local S/N minimum within the test section core. Further analysis was performed to analyze the fluorescence signal intensity during the run. The background subtracted images were integrated and normalized by the laser power to account for shot-to-shot fluctuations. The normalized temporal intensity was approximately constant, although the run time was short due to the low blockage ratio within the test section.

The decrease in S/N was attributed to a combination of the following reactions,

$$2\mathrm{NO} + \mathrm{O_2} \rightarrow 2\mathrm{NO_2} \tag{3.7}$$

$$\mathrm{NO} + \mathrm{NO} \leftrightarrow \mathrm{N_2O_2} \tag{3.8}$$

$$\mathrm{NO} + \mathrm{NO_2} + \mathrm{M} \leftrightarrow \mathrm{N_2O_3} + \mathrm{M} \tag{3.9}$$

$$\mathrm{NO_2} + \mathrm{NO_2} + \mathrm{M} \leftrightarrow \mathrm{N_2O_4} + \mathrm{M} \tag{3.10}$$

as well as the formation of higher order clusters for the NO and NO_2 species. Reaction 3.7 accounts for the nascent production of the NO_2 species formed within the ACE settling region and during the expansion process. This is a termolecular reaction where the production of NO_2 scales quadratically with the concentration of NO.[71][72][73] Decomposition of NO_2 was assumed to be negligible within the ACE facility due to its thermodynamic stability. There has been evidence of its thermal pyrolysis and bimolecular decomposition, but only within high enthalpy environments.[74][75][76][77] Reaction 3.8 represents the formation of the NO dimer where the rate of formation is 1×10^5 slower than the NO_2 formation at 300 K. At low temperatures the rate of dimerization increases due to the stability of these Van der Waals complexes being greater than the available energy. The NO dimer molecule has been studied extensively for its role in termolecular NO reactions.[73][78][79][80][81][82] The third reaction, 3.9, describes the nascent formation of N_2O_3 which has a rate constant 1×10^6 faster than the formation of NO_2 formation

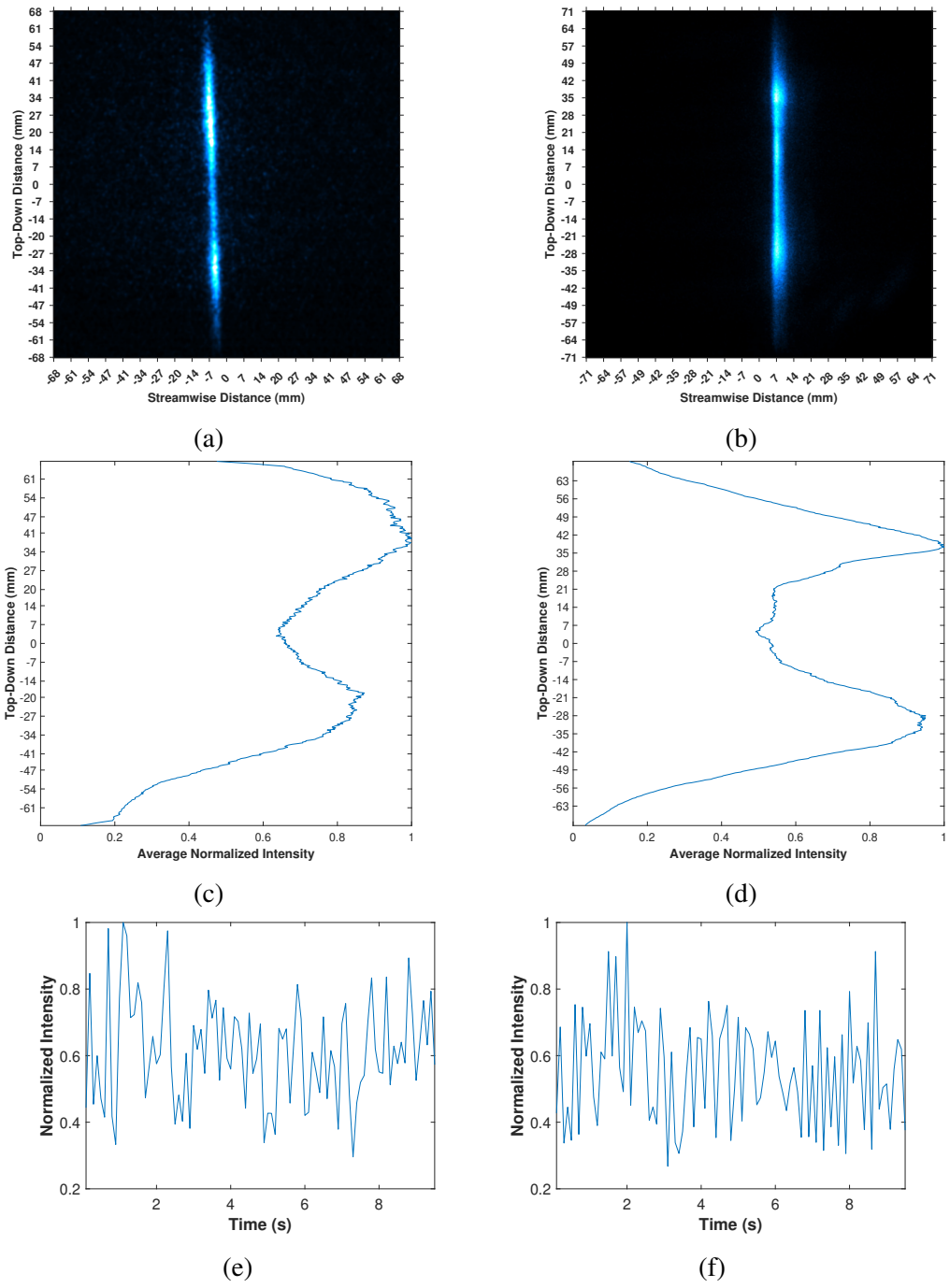

Figure 3.15: Figures a and b are the top-down distribution without the model at 1st and 3rd location, respectively. The flow is moving from left to right and the laser beam is propagating from the top of the image to the bottom. Figures c and d are the normalized spatial intensity at the 1st and 3rd location, respectively. Figures e and f are the normalized temporal intensity during the ACE run at the 1st and 3rd location, respectively.

at 300 K.[83][84][73] The last equation, 3.10, accounts for the dimerization of the nascent NO_2 species where the rate constant is the same order of magnitude as reaction 3.9.[85][73] The NO_2 dimer has been studied within various combustion and shock-tube facilities due to its kinetic role in the N_xO_y set of reactions.[86][87] [88] A kinetic model was developed to predict the number density of these nascent N_xO_y species within the ACE test section following the expansion.

The model predicted the upper and lower limits of the freestream number density as a function of the seeded NO concentration. The temperature dependent rate constants for reactions 3.7, 3.9, and 3.10 were based on the work presented in the review by Atkinson *et. al.*[73] The temperature dependent forward rate constant for reaction 3.8 was based on the work by Scott.[79] Using the theoretical ΔG value from Glendening *et al.*, the equilibrium constant was calculated to determine the backward rate constant.[82] Table 3.5 lists the forward and backward reactions used for the kinetic model. It should be noted that the rate constants for all of the mentioned reactions were extrapolated outside of the suggested temperature range for the lower temperature regime. A plot of the bimolecular rate constants is shown in Figure 3.16a. The bimolecular rate constant for reactions 3.7 and 3.9 were determined by multiplying the termolecular rate constant by the O_2 number density and total number density, respectively. The upper and lower bounds of the rate constants for reactions 3.7 and 3.9 are shown because the uncertainty was stated in the literature for those systems. The fluorescent lifetime measurements provided an upper limit NO concentration within the local ACE freestream of 1% when pure NO is seeded. The lower bound freestream NO concentration was assumed to be 5×10^{-3} % from a seeded gas mixture of 0.5% NO in N_2. The model calculated the number density fraction of N_2, O_2, NO, NO_2, N_2O_2, N_2O_3, and N_2O_4 within the ACE settling region as seen in Figures 3.16b and 3.16c. The temperature and pressure in the settling region were assumed to be constant at 430 K and 75 PSIA, respectively. Using the predicted number density fractions the final freestream number density fraction following the expansion was calculated. The temperature and pressure profiles along the centerline for a Mach 5.9 nozzle were provided by Dr. Rodney Bowersox and are shown in Figures 3.17a and 3.17b. The final predicted number density fractions for the mentioned species are shown in Figures 3.17c

and 3.17d for the seeded pure NO and 0.5% NO gas mixture, respectively. The initial NO number density within the settling region and after the expansion remained constant at both the upper and lower limit cases. The formation of the NO_2 species was the most abundant nascent species within the settling region for both the upper and lower limit case. However, following the expansion the upper limit predicted the N_2O_3 number density fraction increased $\sim$4 orders of magnitude, while the number density fraction for the NO_2 species decreased by $\sim$3 orders of magnitude. The lower limit predicted a convergence of the N_2O_3 and NO_2 densities, showing an 8 order of magnitude rise for the N_2O_3 number density. For the lower limit case, the NO_2 dimer was insignificant due to the initial NO concentration decreasing by a factor of 200.

NO_2 Formation	$k_1 = 3.3 \times 10^{-39}\ e^{\frac{530}{T}}$
N_2O_2 Formation	$k_2 = e^{-10.9+\frac{752}{T}}$
N_2O_2 Decomposition	$k_{-2} = k_2 k_{eq}$, where $k_{eq} = e^{\frac{-\Delta G}{RT}}$, $\Delta G = 38.76$ kJ mol^{-1}
N_2O_3 Formation	$k_3 = 3.1 \times 10^{-34}\ (\frac{T}{300})^{-7.7}$[M]
N_2O_3 Decomposition	$k_{-3} = 1.9 \times 10^{-7}\ (\frac{T}{300})^{-8.7}\ e^{\frac{-4880}{T}}$[M]
N_2O_4 Formation	$k_4 = 1.4 \times 10^{-33}\ (\frac{T}{300})^{-3.8}$[M]
N_2O_4 Decomposition	$k_{-3} = 1.3 \times 10^{-5}\ (\frac{T}{300})^{-3.8}\ e^{\frac{-6400}{T}}$[M]

Table 3.5: Rate equations for N_xO_y reactions where T is the temperature and [M] is the total number density.

Using the above kinetic model and the assumption that the flow from the seeder behaved as a free-expansion jet, where the seeded gas density decreased away from the exit orifice, the top-down S/N profile can be rationalized. An NO density gradient away from the seeder exit correlates to a density gradient of NO_2 and N_2O_2 where the formation of these species is quadratically dependent on the NO number density . A decrease in NO_2 corresponds to a linear decrease in the formation of N_2O_3 and N_2O_4. The NO PLIF flow visualization may be sensitive to the loss of NO near the centerline of the seeded gas exit, but it seems unlikely given the minimal change in the final

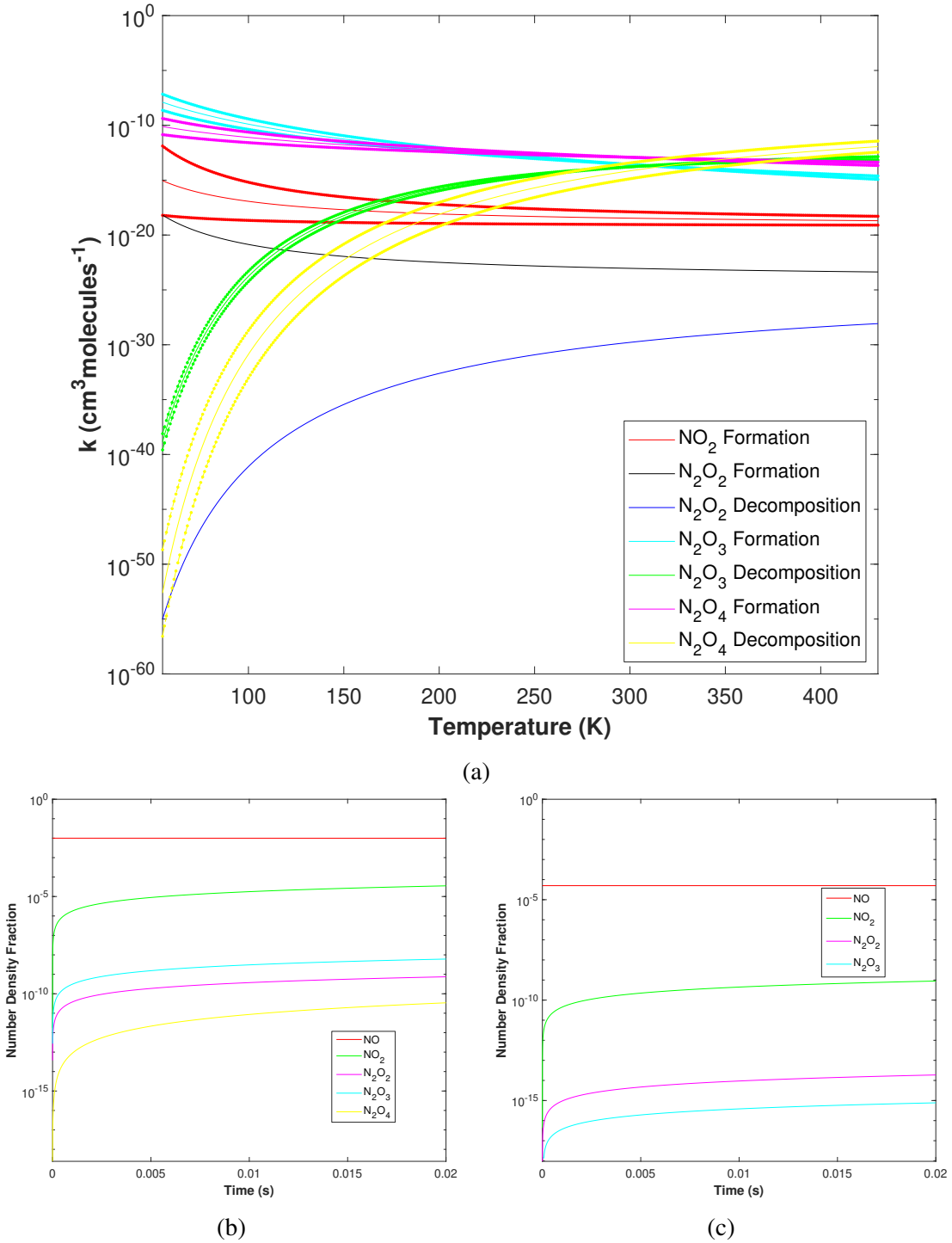

Figure 3.16: Kinetically modeled NO reactions within the ACE settling region. Figure a displays the reaction rates as a function of temperature. Figure b and c display the production of the various N_xO_y species for a seeded gas mixture of pure NO and 0.5% NO in N_2, respectively.

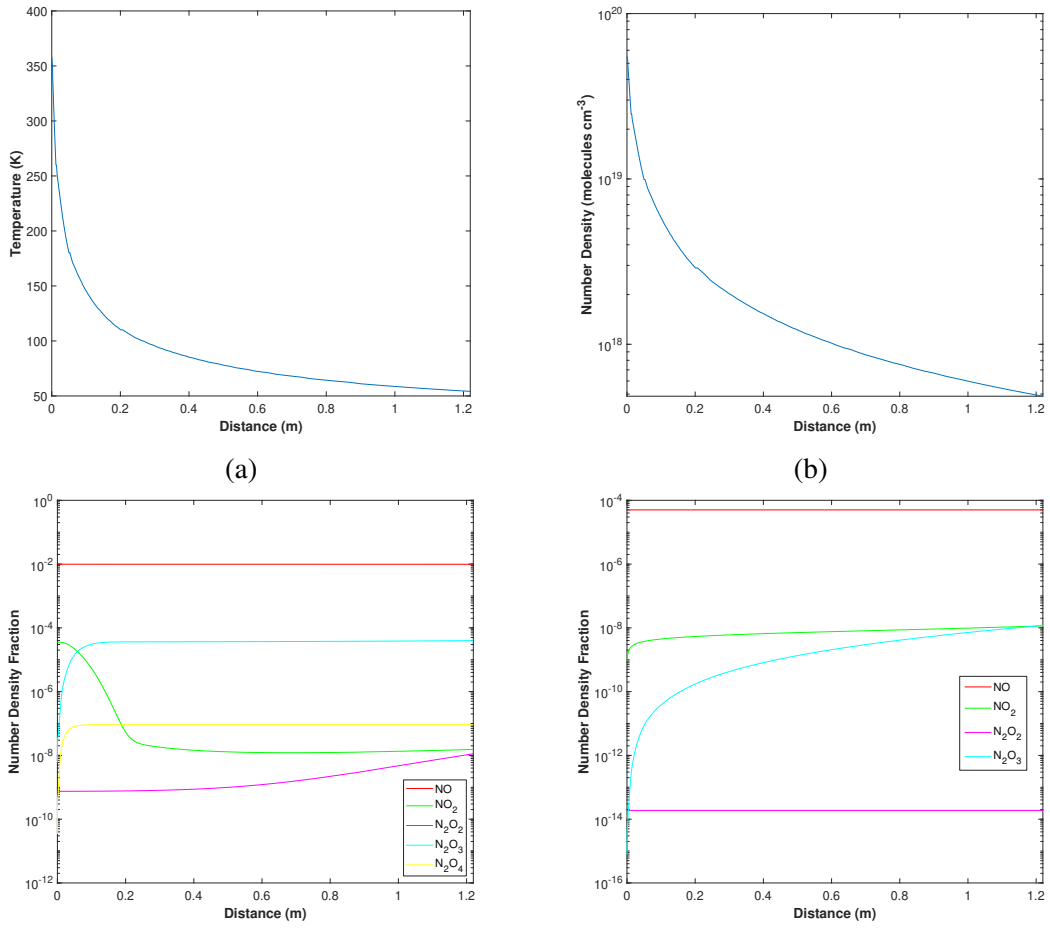

Figure 3.17: Kinetically modeled NO reactions during the hypersonic expansion. Figures a and b are the temperature and number density profiles during the expansion. Figures c and d display the production of the various N_xO_y species for a seeded gas mixture of pure NO and 0.5% NO in N_2, respectively.

predicted NO number density fraction. A more probable cause for the decrease in signal may be attributed to potentially efficient collisional quenching mechanisms of the NO $A^2\Sigma^+$ state by the nascent species. However, the literature is limited on these collisional quenching systems *e.g.* NO/NO_2, to support this claim.

With the model mounted within ACE, the NO distribution spanned the distance normal to the flat plate for the 1st location. The observed distribution was optimal because minimal NO fluorescence was observed beneath the model as shown in Figures 3.18a and 3.18b. At the 1st

location, there was a large discontinuity in the signal intensity $\sim$35 mm normal to the plate which was due to the bow shock emanating from the leading edge of the model. The large increase in the S/N ratio downstream of the shock was unexpected, but is likely due to a combination of effects. There is a known rise in the number density across a shock which would increase the observed fluorescence signal. In addition, the relatively weak binding energies of 8.5 kJ mol^{-1}, 39 kJ mol^{-1}, and 56 kJ mol^{-1} for N_2O_2, N_2O_3, and N_2O_4, respectively, may lead to dissociation across the shock and release NO into the freestream.[89][90][88] For the plate geometry there is a known 12% temperature rise across the shock using oblique shock relations. This shifts the equilibrium constant for the various N_xO_y reactions, causing NO to increase along the length of the plate. As mentioned earlier, the effect of NO $A^2\Sigma^+$ state collisional quenching by the nascent species is unknown, so a decrease in the N_xO_y species number densities may affect the observed fluorescence intensity as well. At 20 mm normal to the plate the fluorescence signal then decreases somewhat rapidly toward the surface. The Schlieren imaging campaign performed by Casey Broslawski visualized a series of weak shocks emanating from the laminar insert and two copper electrode inserts. Across these shocks were small temperature rises at an assumed constant pressure. This would gradually decrease the local number density and in turn decrease the observed fluorescence. At the top-down distance of -9 mm, there was a rapid change in the fluorescence signal. The decrease in signal is postulated to be the edge of the boundary layer because of the known density decrease. The NO distribution profile for the 3rd location was much more consistent normal to the plate relative to the 1st location. There was a slight decrease in the signal intensity 35 mm from the surface which was attributed to a weak reflected shock emanating from two potential sources. The reflected shock could either be an expansion wave from the backward facing step as the flow enters the test section or the last characteristic from the ACE nozzle. Based on the Schlieren imaging there were two shocks near the plate surface at the 3rd location. The signal intensity recovered slightly after the first shock and decayed rapidly toward the surface. The first derivative trace, Figure 3.18d, displays a sudden change in the slope at +9 mm top-down distance which was again postulated to be the edge of the boundary layer.

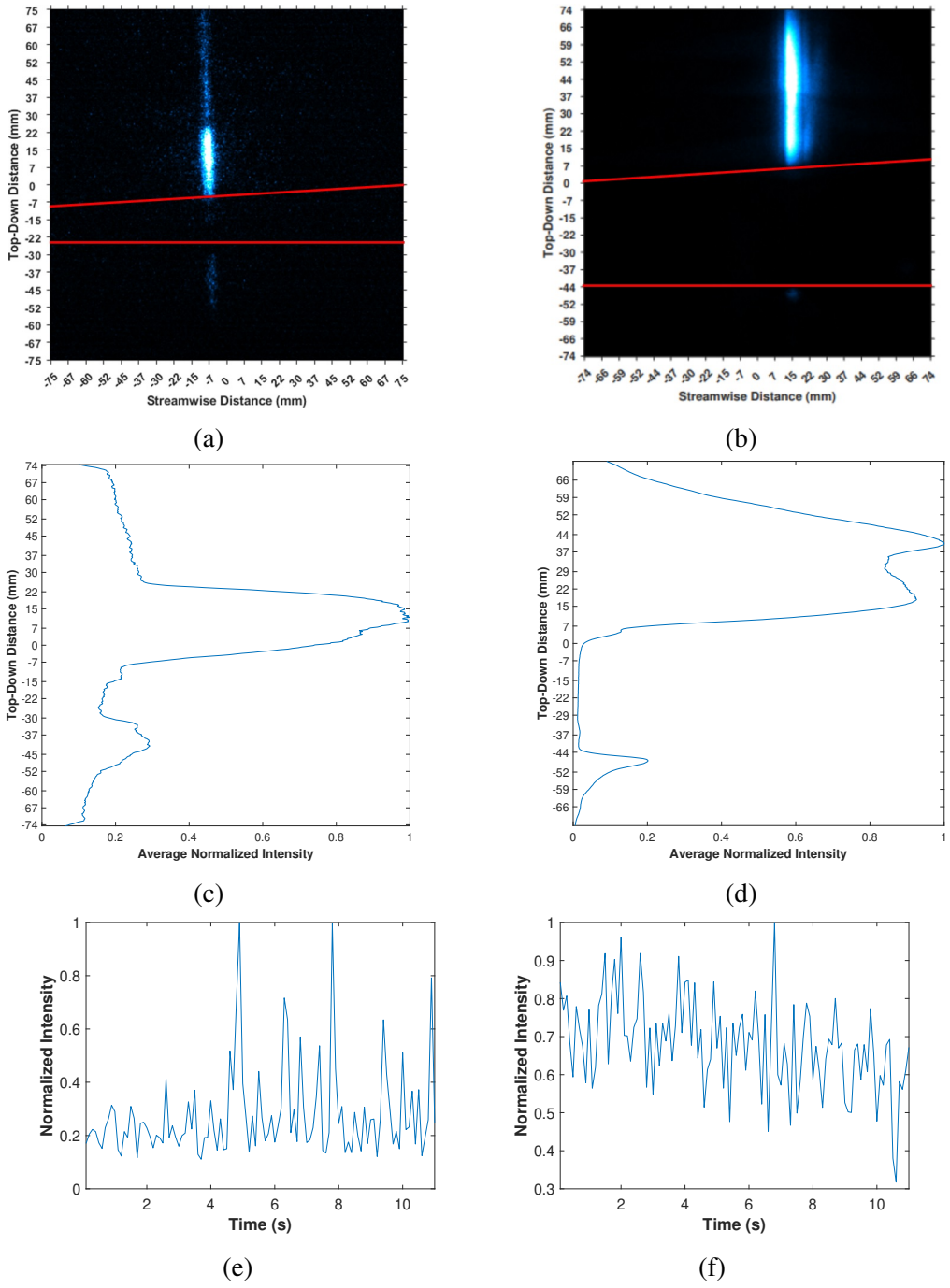

Figure 3.18: Figures a and b are the top-down distribution with the model at 1st and 3rd location, respectively. The model is outlined in red. The flow is moving from left to right and the laser beam is propagating from the top of the image to the bottom. Figures c and d are the normalized spatial intensity at the 1st and 3rd location, respectively. Figures e and f are the normalized temporal intensity during the ACE run at the 1st and 3rd location, respectively.

3.3.2 Spanwise Distribution

The spanwise NO distribution measurements were performed in a similar fashion as the top-down measurements. The beams were tuned to the same transition as described in section 3.3.1; however, they propagated in the spanwise direction. The beams propagated through an array of cylindrical lenses to produce a $\sim$2.5 cm wide $\sim$800 μm sheet. For the model-out experiment, the beam path was 13 cm from the test section floor. For the model-in experiment, the plasma was not operating and the trip insert was used. The chosen beam paths were dependent on the boundary layer height along the plate. It was of interest to visualize wake structures emanating from the trip insert. The sheeted beams were angled to match the angle of the plate (2.75°). For the 1st location, the beam path was 3 mm normal to the plate and 5 mm normal to the plate for the 3rd location. The cameras were oriented above the test section and visualized the 1st and 3rd locations of the test section. The cameras were not angled to account for the angle of the sheeted beam. It was assumed any aberrations due to the out-of-plane view would be negligible at the current field of view resolution. The cameras had a relative delay of 20 ns and operated at 10 Hz at the maximum intensifier gain. The model-in measurement had a gate width of 20 ns due to the low S/N within the boundary layer. The model-out experiment had a gate width of 10 ns. Figure 3.19 displays the experimental setup of the spanwise NO distribution campaign.

At the 1st and 3rd location without the model, the NO distribution was $\sim$50 mm centralized within the test section core. The images shown in Figures 3.20a and 3.20b are representative single-shot images. The reflection of the sheeted beam located on the left portion of the image for Figure 3.20a and right portion for Figure 3.20b. The same image analysis performed on the top-down distribution image sets was also performed on the spanwise distribution image sets. There appeared to be structures present in the freestream based on the sudden changes in fluorescence intensity seen in the blue trace shown in Figures 3.20c and 3.20d. The red trace located on the same plots represents the first derivative of the average normalized intensity and were more sensitive to subtle changes in the gas density. However, it may be due to the non-uniform mixing occurring upstream of the flow conditioners. A wake-like structure was observed at $\sim$-20 mm and $\sim$+20 mm

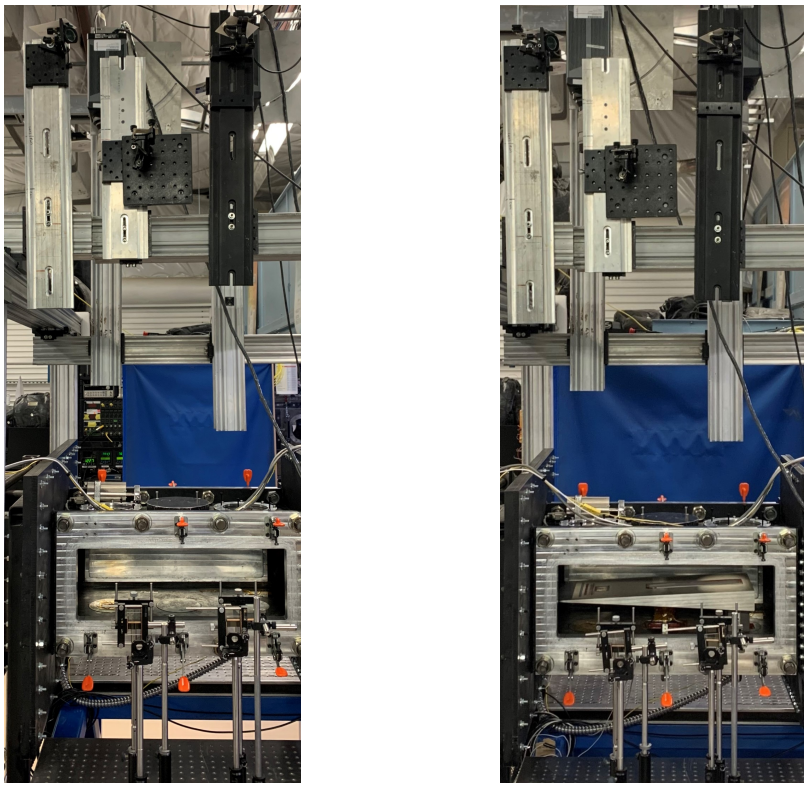

(a) (b)

Figure 3.19: Figure a and b are the model-out and model-in spanwise distribution campaign.

of the spanwise distance for both representative images. The structure at ∼-20 mm was attributed to the $^1/_{16}$" thermocouple tube extending from the ceiling to the midpoint of the settling region downstream of the flow conditioners. The structure at ∼+20 mm was attributed to a pitot probe spanning the same distance. A local intensity minimum was observed within the NO distribution for both images as shown in Figures 3.20c and 3.20d. The decrease in signal within the core was assumed to be from the same effects described previously. There was a 50% relative decrease in signal intensity from the start to the beginning of the run as shown in Figures 3.20e and 3.20f. The spanwise measurements were sensitive to this because the run duration was longer.

The spanwise distribution measurements with the model mounted within ACE provided a visual effect of the trips insert. The NO distribution maintained a ∼50 cm span across the plate at both locations as seen in the representative images in Figures 3.21a and 3.21b. The diamond

shaped trips were visible at the 1st location from the scattered NO fluorescence. The image analysis for the first location did not include the image counts resulting from the scattering off the trips due to a potential bias in the final plot. The wake structures produced from the trips are clearly visible 60 mm downstream of the trips inserts. The NO fluorescence signal appeared to decrease directly downstream of a geometric trip as seen in the blue trace of Figure 3.21c. The fluctuating structure in the blue trace had good agreement with the relative 6 mm trip spacing. The decrease in signal from the trip wake was similar to the observations seen for the wake structures emanating from seeders mounted downstream the flow conditioners. The image at the 3rd location contained extensive turbulent structures from 40 mm to 440 mm. At 450 mm, the turbulent structures appeared to be dampened which was an unexpected finding given the near fully developed turbulence 30 mm upstream. Near this location, an expansion fan interacts with the turbulent boundary layer. The two regions at the 3rd location were analyzed separately to avoid convoluting the profiles. It appeared there were potential wake features present in both regions based on the first derivative traces shown in Figures 3.22c and 3.22d. However, the wake features were subtle in the downstream region. More extensive measurements, *i.e.* thermometry and velocimetry, needs to be performed separately within these two regions to discern a potential change in flow behavior.

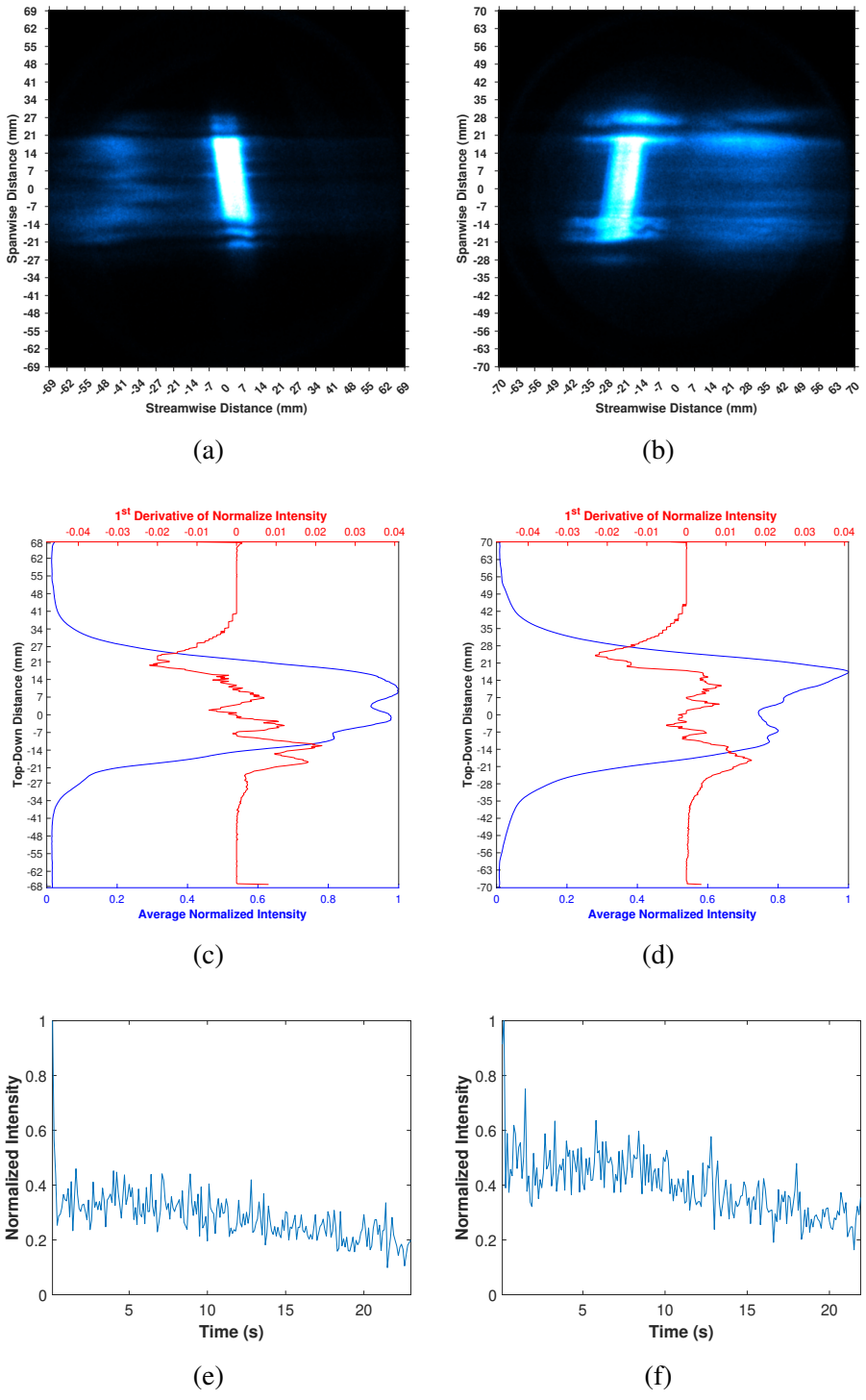

Figure 3.20: Figures a and b are the spanwise distribution with the model at 1st and 3rd location, respectively. The flow is moving from left to right and the laser beam is propagating from the top of the image to the bottom. Figures c and d are the normalized spatial intensity at the 1st and 3rd location, respectively. Figures e and f are the normalized temporal intensity during the ACE run at the 1st and 3rd location, respectively.

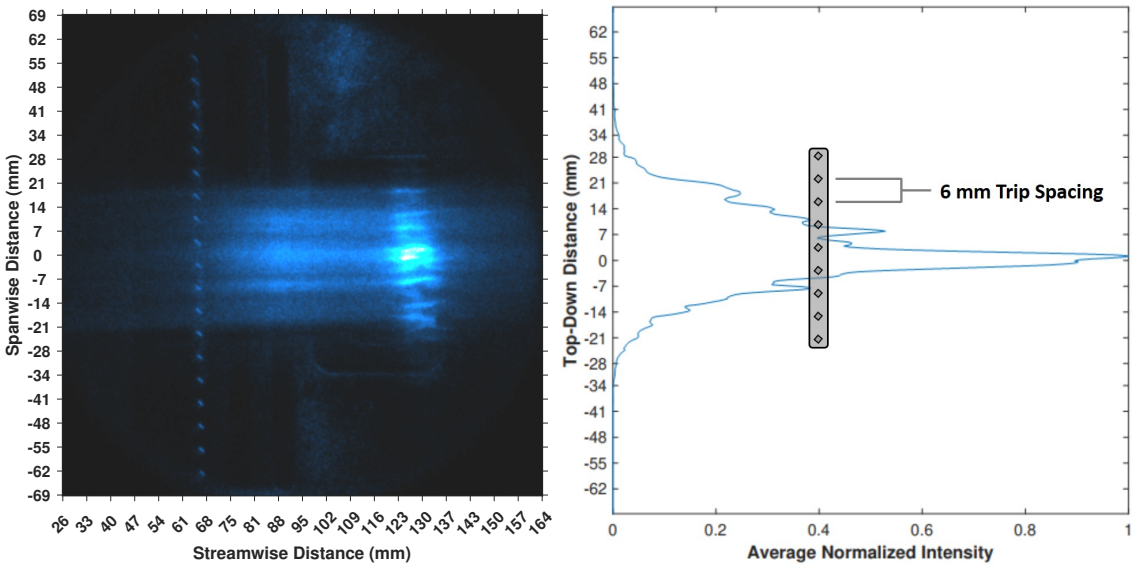

(a) (b)

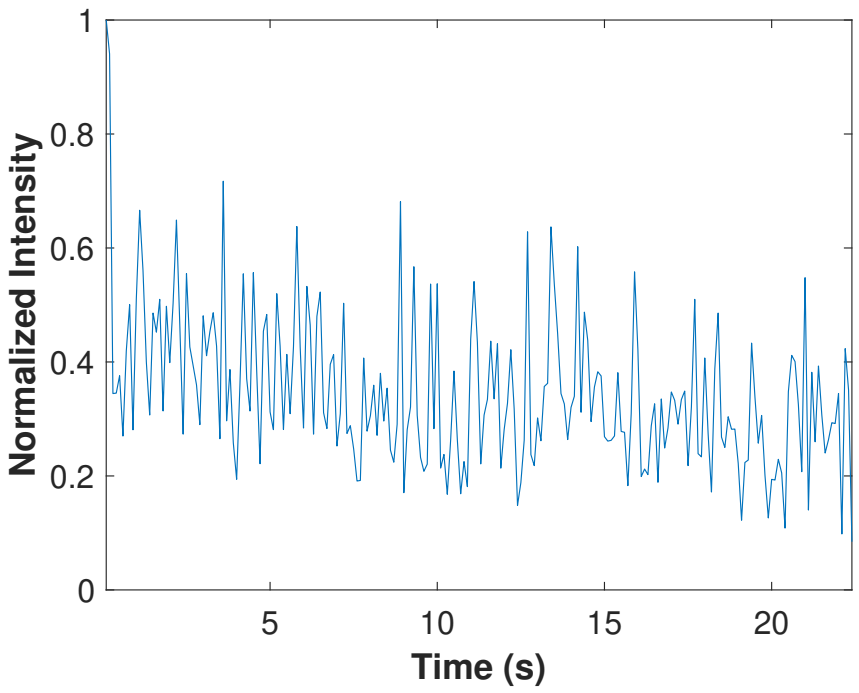

(c)

Figure 3.21: Spanwise NO distribution at the 1st with the model mounted within ACE. The flow is moving from left to right and the laser beam is propagating from the bottom to the top of the image. Figure a is the spatial distribution. Figure b is the normalized spatial intensity. Figure c is the normalized temporal intensity.

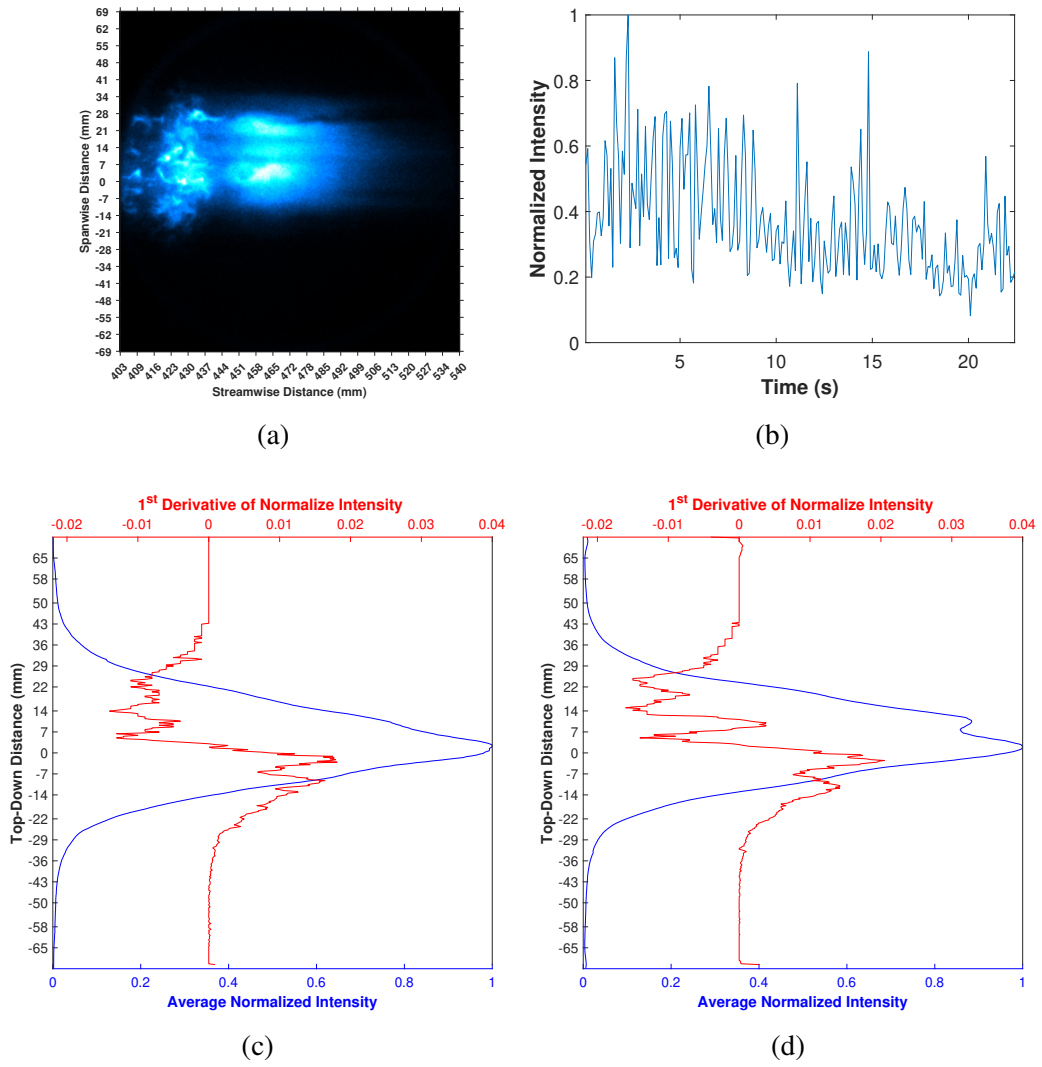

Figure 3.22: Spanwise NO distribution at the 3rd with the model mounted within ACE. The flow is moving from left to right and the laser beam is propagating from the bottom to the top of the image. Figure a is the spatial distribution. Figure b is the normalized temporal intensity. Figure c is the normalized spatial intensity from 403 mm to 440 mm. Figure d is the normalized spatial intensity from 448 mm to 485 mm.

4.1 Thermometry Analysis

The local rotational and vibrational temperatures were determined using the fluorescence ratio of two images acquired at two different vibronic transition states. Using a Boltzmann derived equation and a known temperature region an empirical constant, C_{12}, was determined. The same Boltzmann derived equation and the empirically determined C_{12} were used to determine the local temperature in the unknown regions of a collected image.

All processed images were background corrected and then FFT blurred in the same process described earlier for the image scaling. The image blurring was on the order of 4 to 5 pixels which correlated to a spatial blurring of $\sim$400 to $\sim$500 μm. The angular and x-y spatial displacement corrections from the grid card analysis were used to accurately overlap the two images in the lab frame. The resulting image ratio was then rotated to account for the relative beam propagation angle due to the optical access of the test section. Each column in the rotated image had its own respective C_{12} correction. The C_{12} was determined using a defined moving average region of interest, ROI, defined by the user. The user defined the ROI center according to the location of the known freestream temperature region. Figure 4.1 displays the analysis related to the C_{12} constant. The known freestream rotational temperature was acquired by the NAL DAQ which records all of the tunnel conditions during the run. The known freestream vibrational temperature was determined using a vibrational decay kinetic model which will be described in detail later. The user then defined the length and width of the rectangular ROI. The C_{12} constant was determined using equation,

$$\frac{S_1}{S_2} = C_{12} e^{(-\frac{\Delta E_{21}}{k_B T_{rot}})} \tag{4.1}$$

where the known S_1/S_2 ratio was the user defined ROI, ΔE_{21} was the energy difference calculated using the Dunham expansion, and T_{rot} was the known temperature. With the C_{12} established for each column, the local temperature for the unknown portions of the image were determined using

Equation 4.1. Upper and lower bounds of the resulting temperatures were defined to minimize the appearance of non-physical temperatures.

The analyzed images of an entire run were processed using a statistical treatment algorithm to reduce the number of spurious temperatures from the final temperature data set. The local average temperature was calculated using the batch of instantaneous temperature profiles. Temperature values outside of a 2σ statistical distribution were not accounted for in the final image data set. The statistically treated batch of temperature profiles was then treated once more with the same statistical algorithm. Following the two algorithm treatments, the resulting image profiles were then rotated until the plate surface was level with respect to the imaging plane. The entire field of view for these experiments was on the scale of $\sim$50 mm $\times$ $\sim$50 mm; however, the resulting temperature maps were smaller due to the individual sheeted beam widths and the total beam overlap. The analysis provided instantaneous temperature maps, an average temperature profile, local relative temperature fluctuations, the standard deviation of the local temperature, and the total number of accepted temperatures used following the statistical treatment.

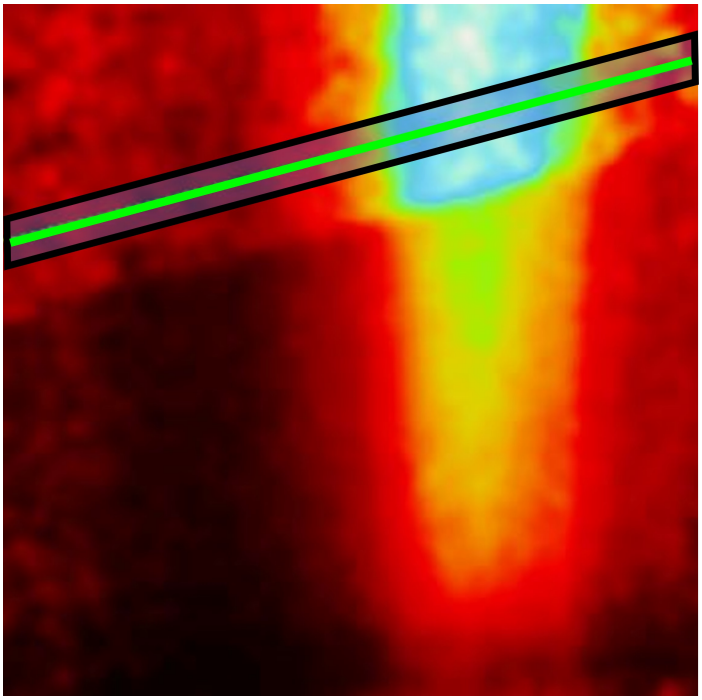

(a)

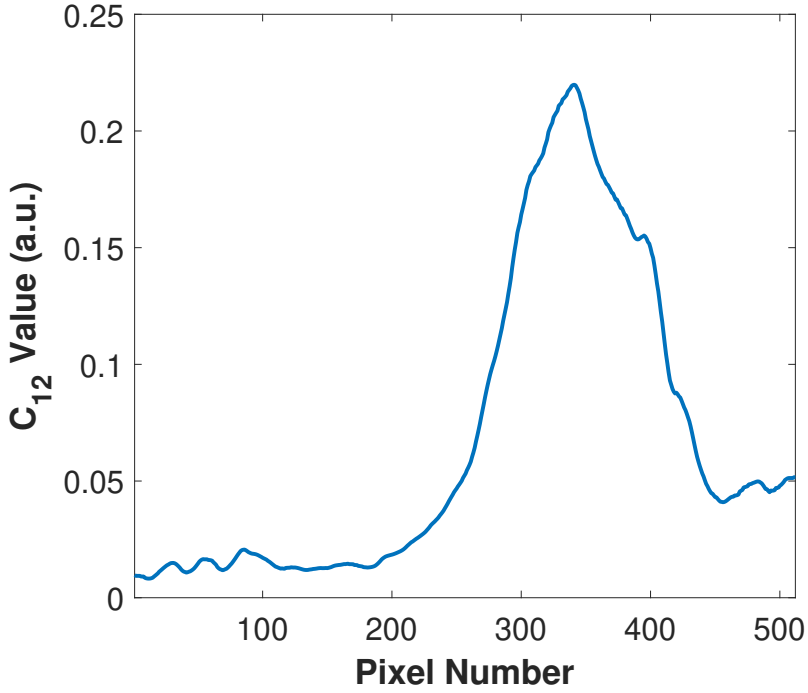

(b)

Figure 4.1: Figure a is an example ratio image with the user defined ROI (green line) where the surrounding black rectangle is the region averaged to improve the C_{12} validity. Figure b is the calculated C_{12} value for an entire 512×512 image.

4.2 Temperature Uncertainty Analysis

The first goal of the thermometry campaign was to obtain instantaneous temperature maps to quantify the potential change in fluctuations within a turbulent boundary layer. The second goal was to determine if the technique was sensitive enough to empirically measure any perturbations in the fluctuation profiles due to the introduction of thermal non-equilibrium via vibrationally excited N_2. Therefore, it was critical in quantifying the relative uncertainty for the thermometry experiments to compare the true turbulent temperature fluctuations. The total uncertainty of the measurement was a convolution of the laser irradiance fluctuations, spatial beam inhomogeneities, measured fluorescence intensities, and seeded NO gas densities. Toward the surface the number of uncertainty factors increased due to a decrease in the S/N ratio, NO fluorescence scatter from the mounted window insert, and plate vibrations during the run. The relative temperature uncertainty, ∂T, was quantified using equation,

$$\frac{\partial T}{T} = \frac{k_b T_{rot}}{\Delta E} \frac{\partial R_{12}}{R_{12}} \tag{4.2}$$

where the temperature uncertainty, $\frac{\partial T}{T}$, scales with the measured fluorescence ratio uncertainty $\frac{\partial R_{12}}{R_{12}}$. [91][92] The temperature uncertainty was minimized by maximizing the energy difference between the two probed rotational states. The shot-to-shot laser power fluctuations were $\sim$10% for each probe laser as shown in Figure 4.2. The following example of uncertainty analysis pertains to the L1 PLIF thermometry measurement where the fluctuations were assumed to be at a minimum given the relative stability of a laminar boundary layer. Recall during section 4.1 the calculated temperatures within the defined threshold values went through a statistical treatment bound to a 2σ distribution restriction. In Figure 4.3 it was observed that a majority (85%-95%) of the determined freestream temperatures were within the 2σ restrictive window. However, within the boundary layer it was apparent the number of accepted values began to decrease, especially at the region closest to the wall (<1mm). The raw relative ratio fluctuations and the laser power corrected ratio fluctuations related to the *J* 1.5 and *J* 8.5 states are visualized in Figure 4.4. Accounting for the

laser power fluctuations were useful in determining the potential sources of systemic uncertainty error. The laser power corrected ratio fluctuation map was used to quantify the spatially resolved relative temperature uncertainty. The uncertainty was expected to increase normal to the plate due to the temperature dependence in Equation 4.2. A map of the relative temperature fluctuations for the laser power corrected treatment is seen in Figure 4.4b. The relative temperature uncertainty in the freestream was on the order of 3% to 5% and peaked within the boundary layer at 25% to 30%. The observed temperature uncertainties were expected according to the work performed by Sanchez-Gonzalez within a pulsed hypersonic facility.[93][42] The observed temperature uncertainty within the freestream of the thermometry profiles approached the uncertainty limit for instantaneous measurements using the two-line NO PLIF technique.[94] The analysis was further expanded by calculating the relative temperature uncertainty of the resulting average temperature map as seen in Figure 4.5.

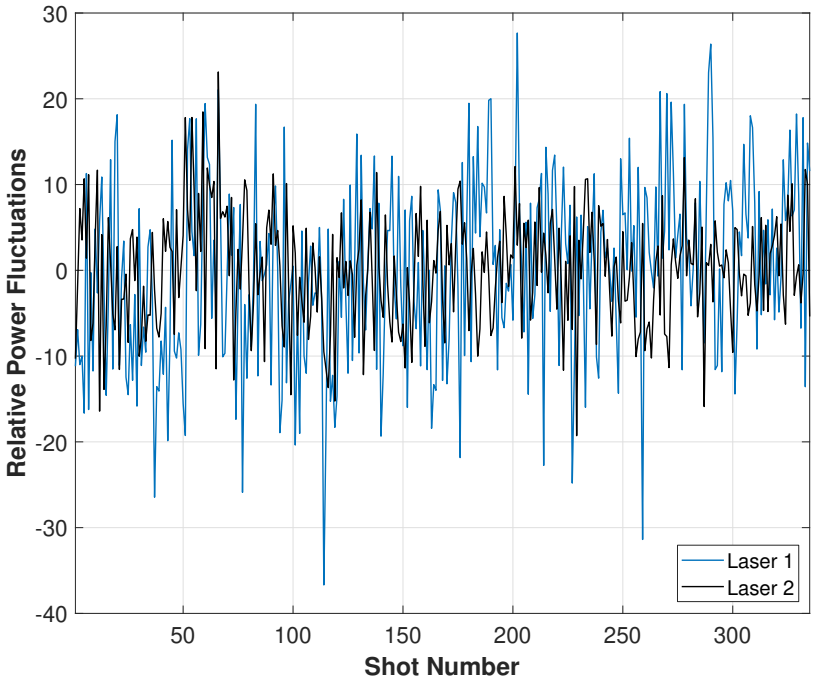

Figure 4.2: Laser power fluctuations about the mean for the two probe lasers. Laser 1 probed the J 1.5 $A^2\Sigma^+$ ($v' = 0$) $\leftarrow$ $X^2\Pi_{1/2}$ ($v'' = 0$) transition. Laser 2 probed the J 8.5 $A^2\Sigma^+$ ($v' = 0$) $\leftarrow$ $X^2\Pi_{1/2}$ ($v'' = 0$) transition.

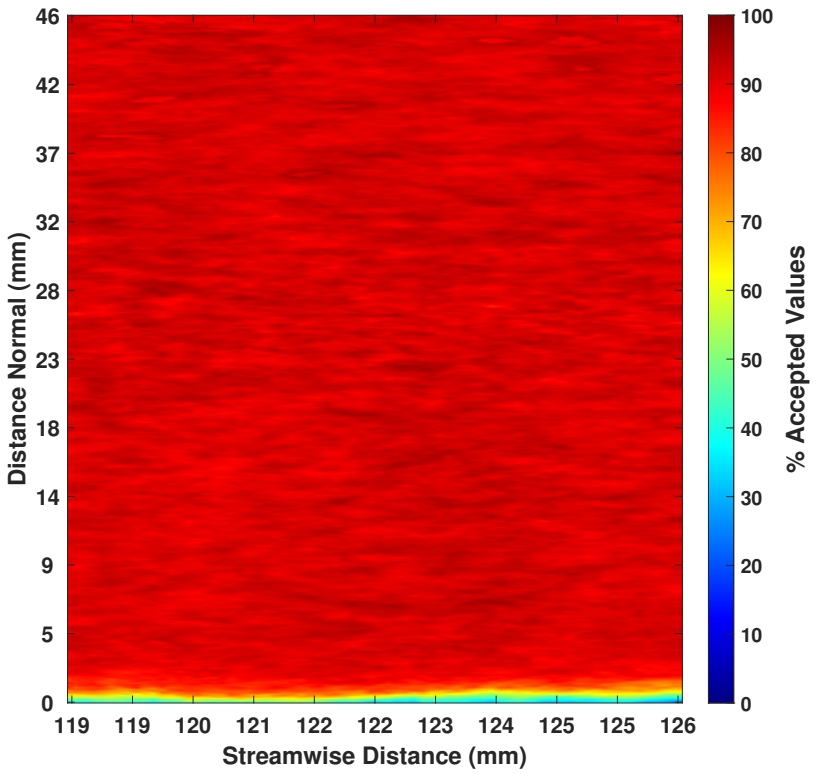

Figure 4.3: Spatially resolved L1 relative number of accepted temperature values map.

An average temperature map, Figure 4.6, was generated from the total set of instantaneous temperature maps. The average temperature map was horizontally averaged to provide a single 1-D dimensional temperature profile normal to the surface of the plate. The average temperature maps spanned $\sim$1 cm regions so the boundary layer growth was assumed to be negligible. The temperature uncertainty for the resulting curve was again determined using Equation 4.2 where the % R_{12} was calculated row by row. This method of analysis gave rise to smaller temperature uncertainty values because the resulting 1-D temperature profile was from the horizontal average of an averaged image. The temperature uncertainty within the freestream was 0.5% and increased to 9% for the L1 case as seen in Figure 4.7. The temperature uncertainty analysis using the ratios from the averaged temperature map were similar to the laminar boundary layer temperature uncertainties determined by Danehy *et al.*[95]

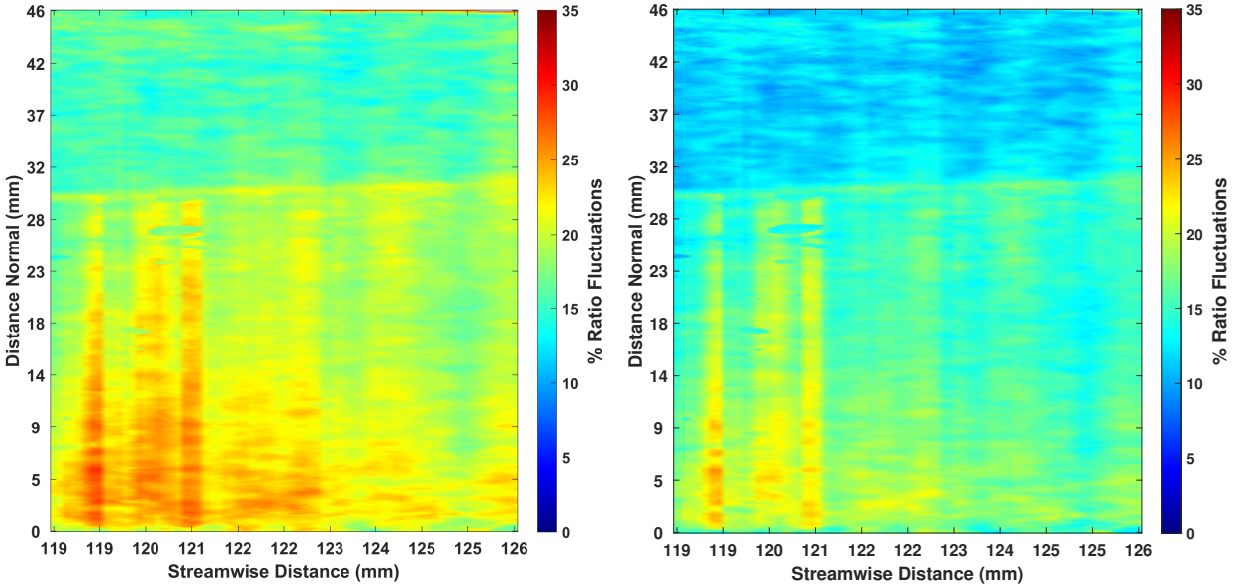

Figure 4.4: Spatially resolved L1 relative ratio fluctuation maps. Figure a is the raw relative ratio fluctuations and Figure b is the laser power corrected relative ratio fluctuations.

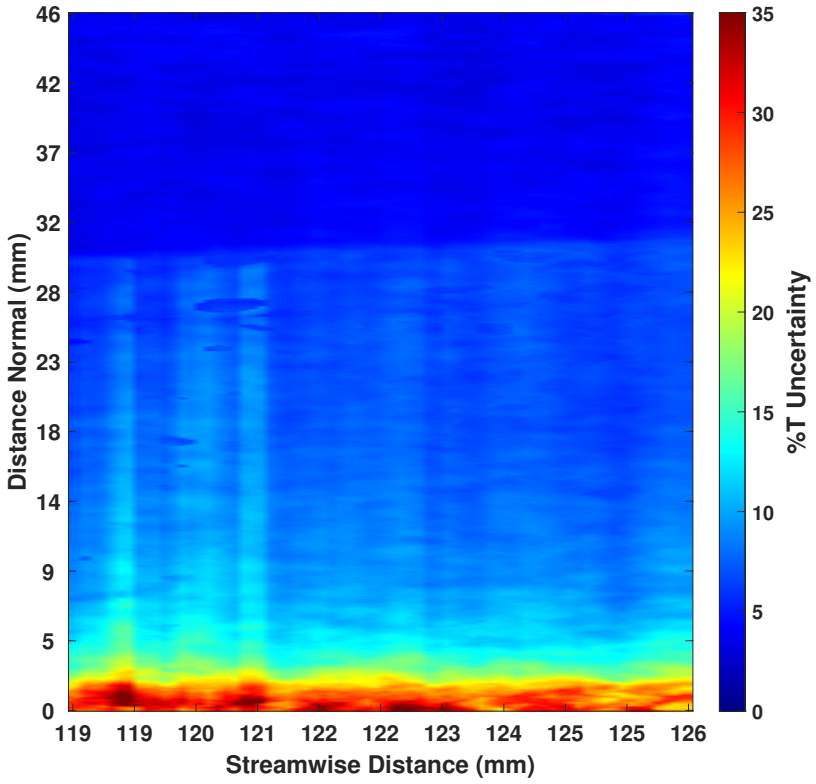

Figure 4.5: Spatially resolved L1 relative temperature uncertainty map.

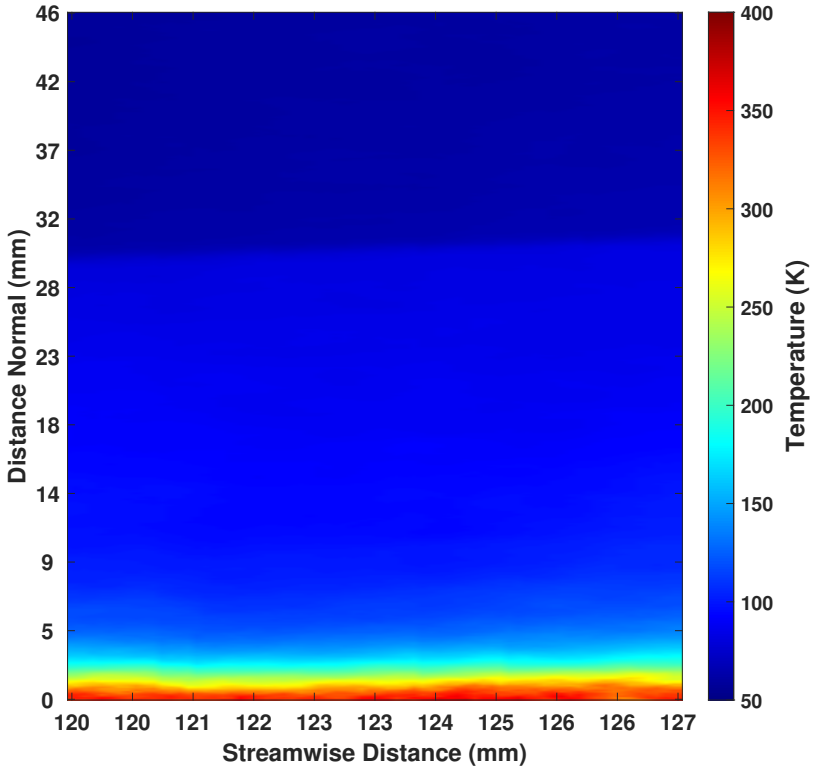

Figure 4.6: Spatially resolved L1 average temperature map.

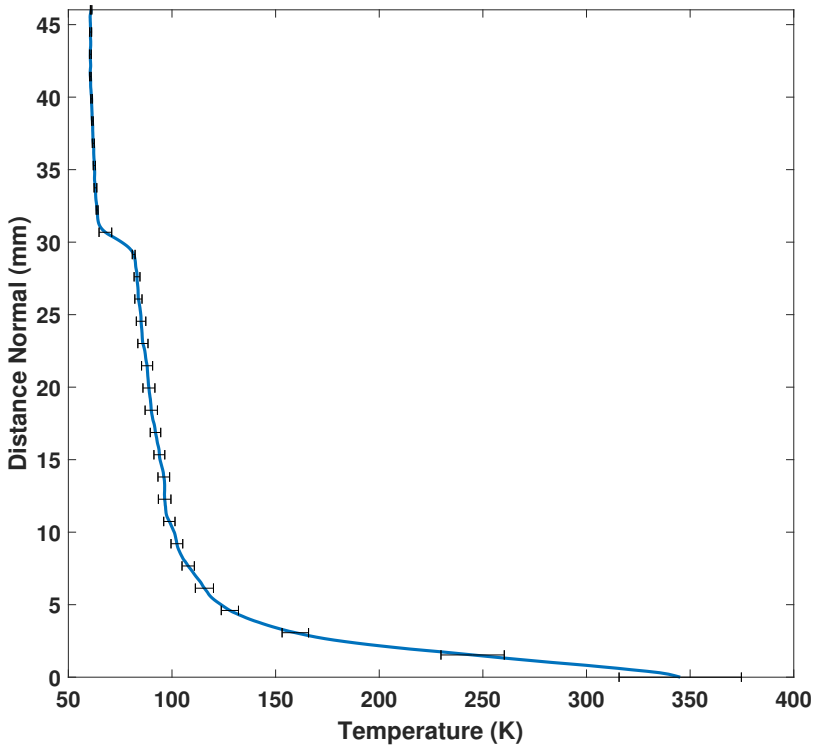

Figure 4.7: Horizontally averaged L1 temperature curve with absolute temperature uncertainty bars.

4.3 Freestream Two-Line PLIF Rotational Thermometry

Characterizing the freestream rotational temperature with PLIF thermometry provided baseline conditions for the ACE facility. The freestream temperature measurement was a metric used to quantify how much the observed temperature fluctuations were due to uncertainty error. The freestream temperature fluctuations were assumed to be 1% based on work by Semper.[46] The freestream was characterized at the 1st location without the model mounted within the test section. The tunnel conditions are shown in Table 4.1.

Mach Number	P_T (Torr)	P_∞ (Torr)	T_T (K)	T_∞ (K)	Re / m
5.8	1800	1.4	420 K	55	3 X 10^6

Table 4.1: Freestream thermometry tunnel conditions.

The sum frequency mixing laser systems were tuned to the *J* 1.5 and *J* 8.5 transitions of the Q_{21}/R_1 $A^2\Sigma^+$ ($v' = 0$) $\leftarrow$ $X^2\Pi_{1/2}$ ($v'' = 0$) branch. The *J* 1.5 transition was probed first followed by the *J* 8.5 transition 500 ns later. The beams propagated from the top-down within the ACE test section through a pair of cylindrical lens to produce a $\sim$1" 800 μm sheet. The sheet was focused 7 $^1/_{16}$" from the side of the test section to the spanwise center. The two beams had a $\sim$1" overlap region within the center of the test section. The laser power fluctuations were collected during the duration of the run. The dual ballast setup was pressurized to 180 PSIA with a 1% NO in N_2 gas mixture. A dual camera 10 Hz configuration was employed. The cameras were aligned on opposite sides of the test section and had a field of view of $\sim$50 mm within the test section center. The cameras were gated directly after the laser scatter and had a relative time delay of 485 ns. The gate width for both cameras was 3 ns.

The two fluorescent images related to the probed *J* states are shown in Figure 4.8. The *J* 1.5 image had a greater S/N ratio relative to the *J* 8.5 image due to the 8:1 population ratio at 60 K. The resulting temperature map, relative temperature fluctuation map, and relative temperature

uncertainty map are seen in Figure 4.9. The temperature fluctuations were determined using the equation

$$T' = T - \overline{T} \tag{4.3}$$

where T' is the temperature fluctuation, T is the instantaneous temperature, and $\overline{T}$ is the average temperature. The presented fluctuation map provides spatially resolved relative T'_{RMS} fluctuations. The freestream temperature was relatively uniform with no observable local hot regions within the measured 90 cm $\times$ 30 cm core region of the flow. The magnitude of the temperature fluctuations and relative temperature uncertainty increased along the borders of the two maps as seen in Figures 4.9b and 4.9c. The same horizontal averaging was performed as described in Section 4.2 to obtain a 1-D temperature curve. The freestream relative fluctuation map was also horizontally averaged to obtain a 1-D freestream fluctuation curve related to the core of the ACE test section. The observed freestream fluctuations were on the order of 2% to 8% within the core, however given the relative temperature uncertainty the results agreed well with previous freestream ACE measurements.[45][46]

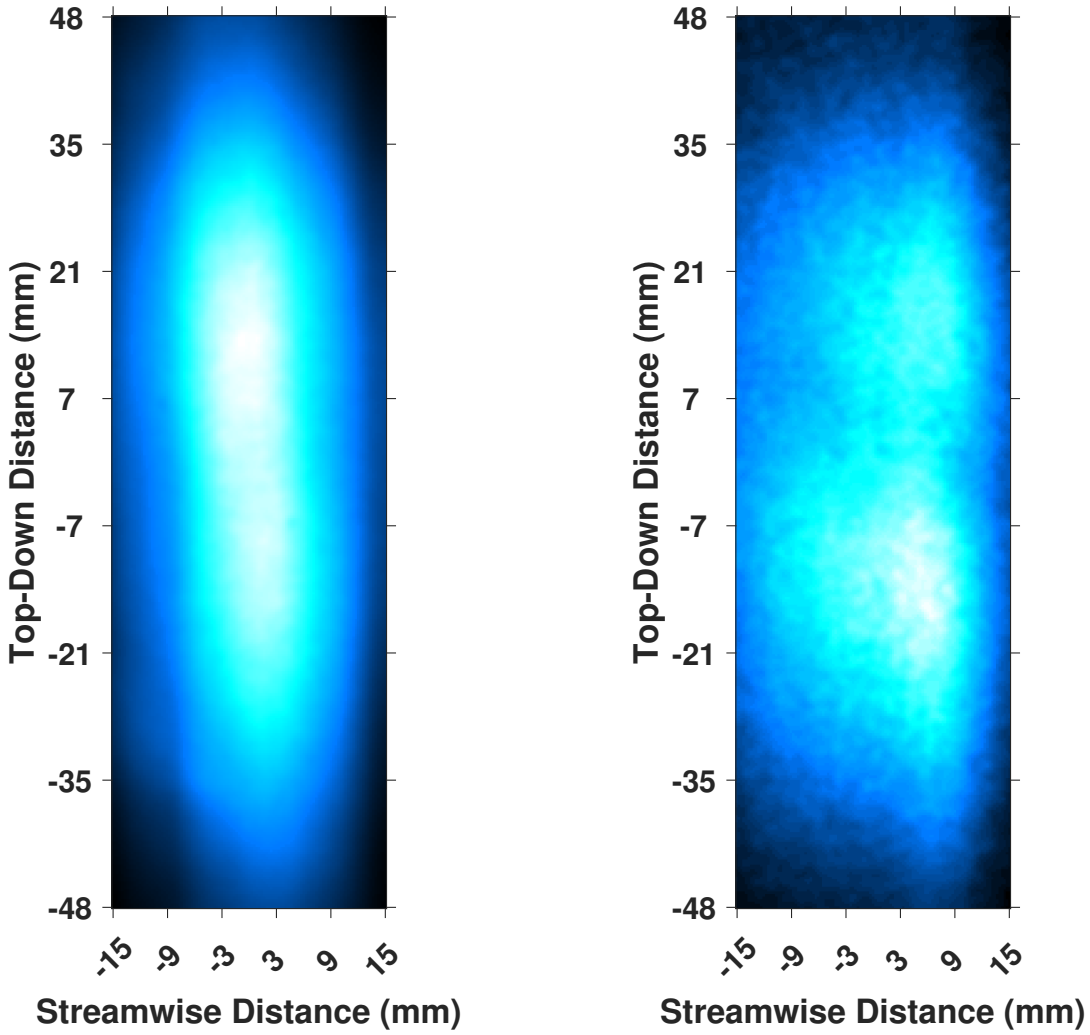

(a) (b)

Figure 4.8: Fluorescent image averages of the freestream flow. Figure a correlates to the J 1.5 $A^2\Sigma^+$ ($v' = 0$) $\leftarrow$ $X^2\Pi_{1/2}$ ($v'' = 0$) transition. Figure a correlates to the J 8.5 $A^2\Sigma^+$ ($v' = 0$) $\leftarrow$ $X^2\Pi_{1/2}$ ($v'' = 0$) transition.

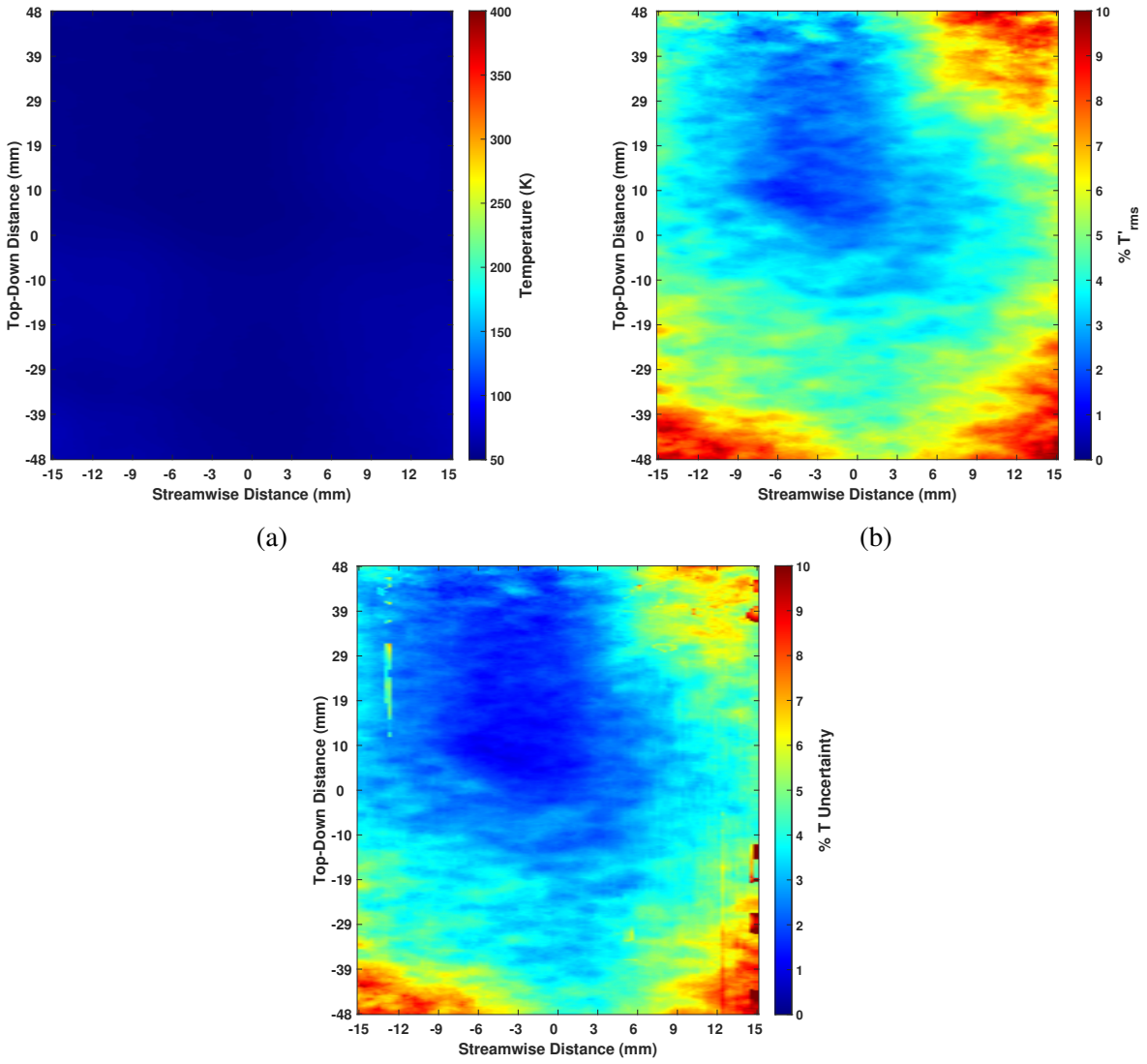

(a) (b) (c)

Figure 4.9: Freestream thermal maps. Figure a is the average temperature map. Figure b is the relative RMS temperature fluctuations. Figure c is the relative temperature uncertainty.

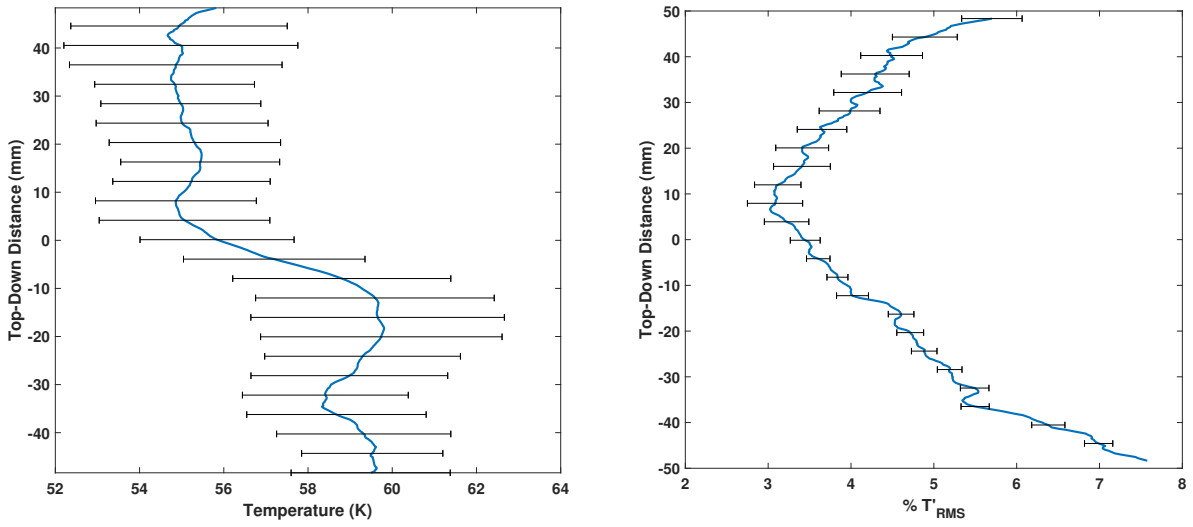

(a) (b)

Figure 4.10: Horizontally averaged freestream thermometry measurements. Figure a is the 1-D temperature curve. Figure b is the 1-D relative temperature fluctuation curve.

4.4 Two-line PLIF Rotational Thermometry of a Turbulent Boundary Layer

4.4.1 Thermometry Experimental Setup

Quantifying the rotational temperature profile normal to the surface was a metric used to probe the role of TNE within a turbulent boundary layer. Two-line PLIF rotational thermometry experiments were performed at the 1st and 3rd locations of the flat plate. The tunnel conditions for the campaign are shown in Table 4.2.

Mach Number	P_T (Torr)	P_∞ (Torr)	T_T (K)	T_∞ (K)	Re / m
5.8	3800	3.2	430 K	58	6 X 10^6

Table 4.2: Two-line PLIF rotational thermometry conditions.

The sum frequency mixing laser systems were tuned to the J 1.5 and 8.5 transitions of the Q_{21}/R_1 branch $A^2\Sigma^+$ ($v' = 0$) $\leftarrow$ $X^2\Pi_{1/2}$ ($v'' = 0$). The J 1.5 transition was probed first followed by the J 8.5 500 ns later. The beams propagated from the top-down direction within the ACE test section. The beams passed through the same array of cylindrical lenses to produce two $\sim$1.5 cm wide 800 μm sheets. The beams overlapped a region of $\sim$50 mm normal to the surface. A total of six runs were performed out at each location. The beams passed through the window insert of the plate at the 1st location which was $\sim$120 mm from the leading edge. The beams were aligned at the spanwise center of the plate, 108 mm from the side. For the turbulent trough measurements the beams were aligned 103 mm from the right side of the plate when looking from the leading edge. The beams passed through the second fused silica window of the plate at 405 mm downstream of the leading edge. The beams had the same spanwise positions for the 3rd location as the 1st location. The beam power for each laser shot was collected and correlated to the respective acquired image.

The dual ballast setup was pressurized to 180 PSIA with a 0.5% NO in N_2 mixture. A dual camera 10 Hz configuration was employed. The cameras were aligned on opposite sides of the test section and had a field of view of $\sim$50 mm normal to the plate. The cameras were gated directly

after the laser scatter and again had a relative time delay of 500 ns. The gate widths were varied from 10 to 40 ns. The plasma was powered on following the introduction of the NO/N_2 mixture and turned off after the NO/N_2 seeding was stopped. A separate program collected the plasma operating conditions during the ACE tunnel run. Figure 4.11 displays the two-line PLIF rotational thermometry setup.

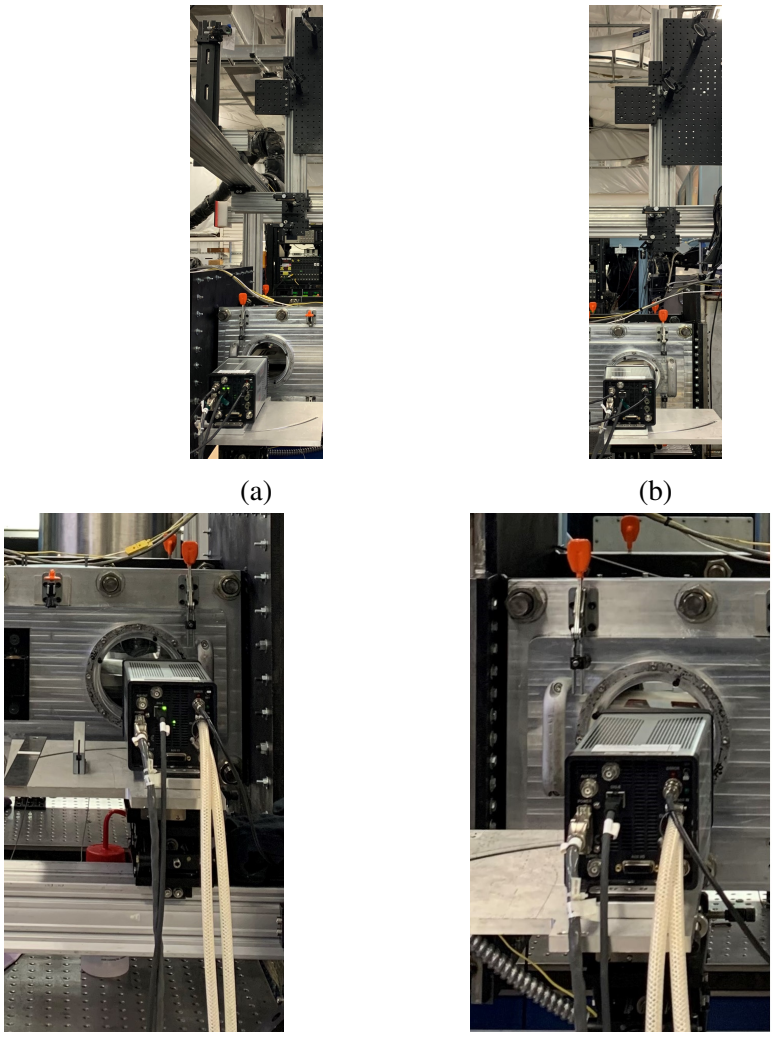

(a) (b)

(c) (d)

Figure 4.11: Experimental configuration for rotational thermometry campaign. Figures a and b are the 1st and 3rd location, respectively, for the ACE right side. Figures c and d are the 1st and 3rd location, respectively, for the ACE left side.

4.4.2 Quantifying Observed Thermal Perturbations

Initial PLIF thermometry measurements of the thermal boundary layer along the flat plate provided unexpected absolute temperatures near the surface. There appeared to be a thermal perturbation when seeding relatively high concentrations of NO in N_2 mixtures. A small set of experiments were performed to characterize the perturbation for the L1 experiment. The L1 experiment was performed to identify the source of the thermal perturbation without convoluting a potential trip or plasma effect. The temperature profile was measured for NO seeding concentrations of 1%, 5%, and 20% which correlated to local concentrations of 0.01%, 0.05%, and 0.20%. The measured wall temperature, Figure 4.12a, for the highest local NO concentration was $\sim$80 K when using Equation 4.1 and a freestream temperature of 58 K. This measured wall temperature was non-physical because the plate was mounted within the facility during preheat and the plate was known to experience some degree of thermal loading during tunnel operation. Additionally, embedded surface thermocouples measured a wall temperature of $\sim$360 K. The predicted cold wall temperature implied the local freestream temperature must be tens of Kelvin higher to obtain a reasonable wall temperature as seen in Figure 4.12b. When the wall temperature was fixed at 360 K, the predicted freestream thermal perturbation for the 0.20% NO experiment was on the order of 50 to 100 K. As the freestream approached the bow shock the temperature increased giving rise to a thermal perturbation gradient. The thermal gradient may be correlated to the density gradient observed in Section 3.3.1 where there was an observed decrease in the NO S/N ratio towards the seeded gas centerline. For the lowest NO concentration experiment, 0.01%, the observed freestream thermal perturbations were much smaller and were on the order of 10 to 15 K as shown in Figure 4.12d. There did not appear to be a thermal gradient above the bow shock. These experiments are summarized in Figure 4.13 where the freestream temperature increased with increasing NO concentration. The curves also suggests the local temperature uncertainty increased as well with increasing NO concentration.

To account for the thermal disconnect it was hypothesized the PLIF measurement perturbed the local flow on the timescale of the PLIF measurement *i.e.* 500 ns. Two potential perturbation

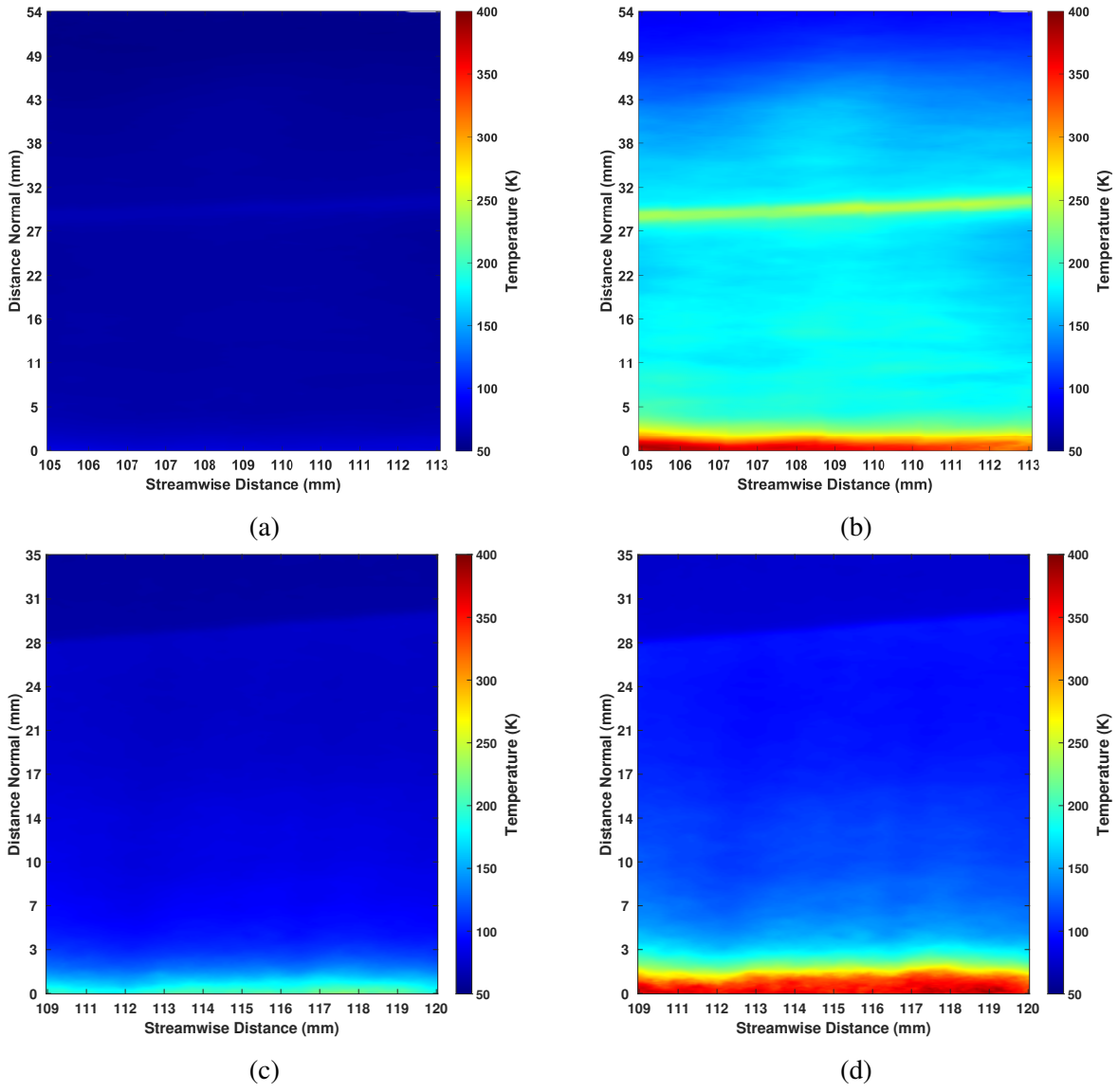

Figure 4.12: Observed freestream thermal perturbations as a function of the local NO concentration. Figures a and b have NO concentrations of 0.20% and Figures c and d have NO concentrations of 0.01%. The freestream was assumed to be 60 K for a and c. The wall was assumed to be 360 K for b and d.

sources stemmed from NO $A^2\Sigma^+$ state collisional quenching and photodissociation of the nascent N_xO_y species. Calculations were performed to characterize the local thermal perturbation resulting from NO $A^2\Sigma^+$ collisional relaxation. The two collisional quenching species were assumed to be O_2 and NO with O_2 accounting for a vast majority (>95%) of the collisional quenching. The following model assumed the laser sheet was 1 cm $\times$ 800 μm with an output of 8 mJ/pulse and

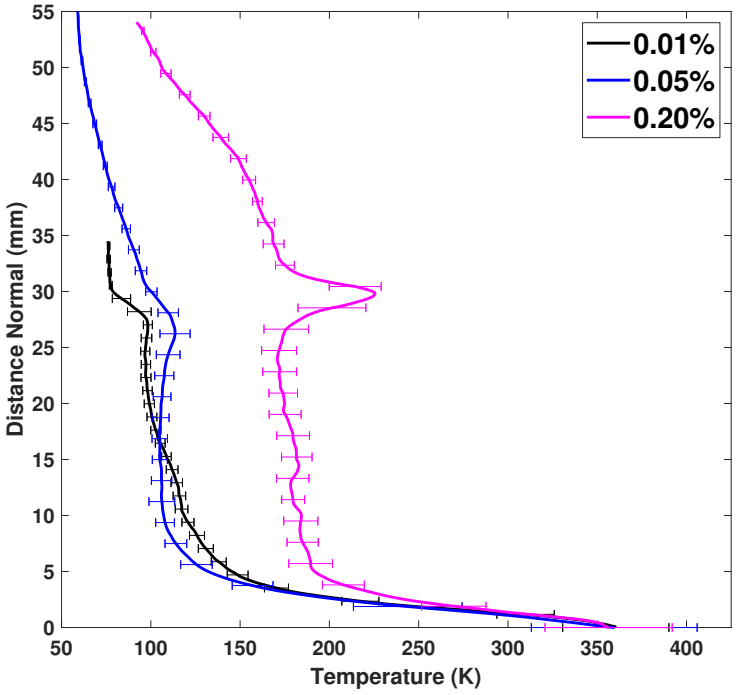

Figure 4.13: Temperature curves for three different local NO concentrations. The wall temperature was fixed at 360 K to compare the apparent freestream thermal perturbation.

constant freestream pressure of 3.3 Torr. The relative absorption was determined to be 2.2% using the absorption coefficient of 1.92×10^{-19} cm^2 molecule^{-1}. [96] The model calculates the thermal perturbation as a function of the local temperature due to the known thermal gradient normal to the plate. Equations 3.5 and 3.6 were used to calculate the temperature dependent quenching to fluorescence ratio. Figure 4.14a displays the ratio as a function of temperature for two different NO freestream concentrations. The quenching fraction was used to determine how much of the absorbed photon energy was partitioned to the translational, rotational, and vibrational modes of the bath gas species *i.e.* N_2, O_2, and NO. The equipartition equation for a diatomic species is written as

$$E_{tot} = \underbrace{\frac{3}{2}k_B T}_{trans.} + \underbrace{k_B T}_{rot.} + \underbrace{k_B T}_{vib.} \tag{4.4}$$

where E_{tot} is the total absorbed photon energy multiplied by the collisional quenching fraction.

On the time scale of the experiment it was assumed the vibrational energy does not contribute to the short-term instantaneous (<2 μs) thermal perturbation due to the V-T and V-V energy transfer rates.[97] For the upper limit case seen in Figure 4.14b the expected temperature rise within the ACE freestream was on the order of 7.5 K. For the lower limit case, Figure 4.14c, the maximum temperature perturbation was 0.04 K which was negligible. In either case the calculated thermal perturbations following collisional quenching does not account for the observed thermal perturbations on the order of 100 K.

As mentioned previously, the other perturbation source may be due to the presence of the N_xO_y species described in Section 3.3.1 where the concentrations were dependent on the seeded NO concentration. The heat of formation of all the N_xO_y species was relatively low and given their low freestream concentrations the subsequent thermal perturbations from the chemical reactions was assumed to be small. Instead, the probable cause of the measured thermal perturbations was due to the production of rotationally hot NO following various photochemical reactions. The photodissociation process of NO_2 has been studied extensively in the UV region. The wavelength region above 350 nm appears to follow statistical models and have a predicted rotational distribution of 850 K for the NO $X^2\Pi$ ($v'' = 0$) state and 1400 K NO $X^2\Pi$ ($v'' = 1$) state.[39] However, the resulting rotational distribution below 350 nm becomes dependent on the photodissociation energy and the measured NO $X^2\Pi$ vibronic bands. A study by Welge *et al.* characterized the photodissociation dynamics of NO_2 at 337 nm which stated the rotational distribution was highly non-statistical for the NO $A^2\Sigma^+ \leftarrow X^2\Pi$ (0-1) and (0-2) transitions. They measured a three temperature distribution of 65 K, 1600 K, and 295 K depending on the *J* state range.[98] Dyer *et.al* photodissociated NO_2 at 248.5 nm and probed the NO $A^2\Sigma^+ \leftarrow X^2\Pi$ (0-5) transition to observe a two temperature distribution of 130 K for $J<9$ and 750 K for the higher *J* states.[99] A study by Bernsetin *et al.* measured the rotational distribution following the photodissociation of NO_2 with a 226 nm beam. They stated the temperature of their molecular beam was 11 K, but measured a nascent rotational distribution of 200 K for the NO $A^2\Sigma^+ \leftarrow X^2\Pi$ (0-0), (1-1), and (2-2) transitions following NO_2 dissociation.[100] For the PLIF experiments in ACE, the nascent NO rotational distribution

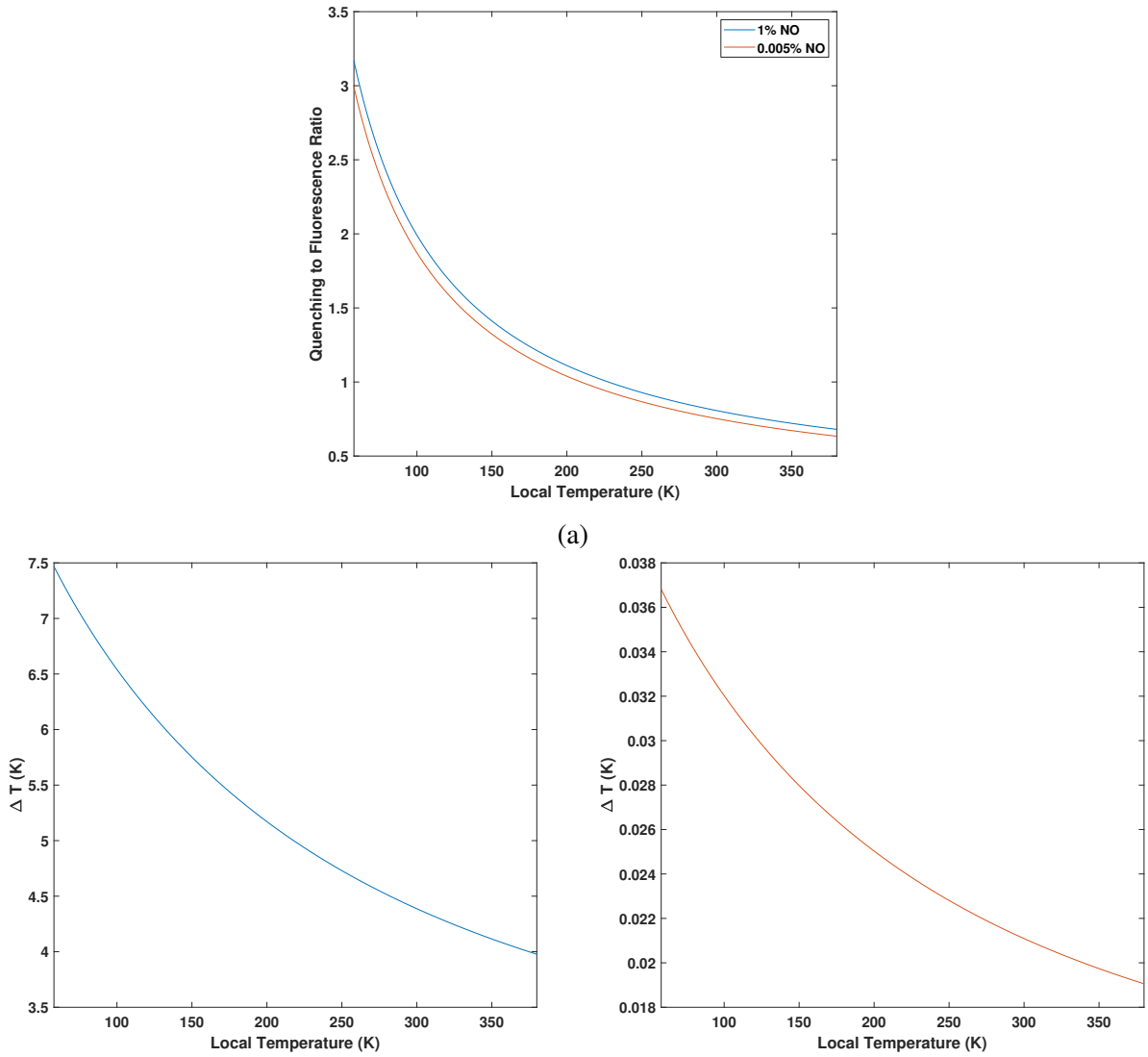

Figure 4.14: Thermal perturbation following the excitation of the $A^2\Sigma^+$ ($v' = 0$) $\leftarrow$ $X^2\Pi_{1/2}$ ($v'' = 0$) transition. Figure a displays the temperature dependence of the quenching to fluorescence ratio. Figures b and c are the predicted temperature rise for NO freestream concentrations of 1% and 0.005%, respectively.

following NO_2 photodissociation was unknown, however the literature suggests the presence of a non-negligible short-term rotational thermal perturbation. A set of experiments performed by Vallance *et al.* characterized the photodissociation dynamics for the NO_2 and N_2O_4 systems.[101]

Their NO_2 photodissociation scheme is shown in equation

$$NO_2 + h\nu\ (226\ \text{nm}) \rightarrow NO + O(^3P_J) \tag{4.5}$$

where the $O(^3P_J)$ species represents the oxygen atom spin-orbit fragments. The oxygen atom speed distribution was bimodal which was evident of competing exit channel dynamics. They observed a narrow NO $X^2\Pi$ ro-vibronic distribution from v′ = 4-6 with a peak at at v′ = 5 when performing the experiment with low concentrations of NO_2. The two-photon dissociation process was performed at higher pressure and is detailed in the equation

$$N_2O_4 + h\nu\ (226\ \text{nm}) \rightarrow NO_2' + NO_2'' \tag{4.6}$$

$$NO_2'' \rightarrow NO + O(^3P_J) \tag{4.7}$$

where the NO_2'' cofragment had an internal energy ratio of 11:2 relative to the NO_2' cofragment. The dissociation of the NO_2'' species produces a low-velocity O^3P_J component compared to the $O(^3P_J)$ species produced from a direct dissociation of NO_2. The subsequent available energy was then distributed among the electronically excited NO states or the NO $X^2\Pi$ (v = 1 , 2, 3) ro-vibrational modes. Therefore the nascent NO $X^2\Pi$ population may have varying internal energy distributions depending on the photodissociation energy and photochemical pathway.

The NO dimer has been shown to strongly absorb in the UV region with an absorption maximum at 205 nm.[102] The NO dimer photodissociation at 193 nm produces two distinct exit channels shown in equation[103]

$$(NO)_2 \rightarrow NO\ (A^2\Sigma^+) + NO\ (X^2\Pi), \tag{4.8}$$

$$(NO)_2 \rightarrow NO\ (B^2\Pi) + NO\ (X^2\Pi). \tag{4.9}$$

The nascent rotational distributions for the NO $A^2\Sigma^+$ state were rotationally excited and agreed fairly well with statistical models relating to the v′ = 0-2 rovibronic transitions.[104] The NO $B^2\Pi$

(0-8) band had a bimodal rotational distribution of 400 K and 1400 K for the low *J* and high *J* components, respectively.[105] Reisler *et al.* photodissociated the NO dimer at 221.7 nm and 213 nm to find the NO $A^2\Sigma^+$ state rotational distributions agreed well with predictive statistical models, but began to deviate at the higher photon energy.[106][107] Within the ACE environment there was suspected to be considerable collisional quenching for both of these electronically excited NO products; however, the thermal perturbations would be negligible due to the relatively low NO dimer concentration.

The final species to consider was the N_2O_3 species which was the predominant nascent N_xO_y specie following the introduction of a high NO concentration mixture. The photochemical literature related to N_2O_3 species is limited, however Bartz *et al.* studied the photodissociation using the excitation scheme

$$N_2O_3 + h\nu\ (355\ \mathrm{nm}) \rightarrow NO + NO_2. \tag{4.10}$$

They observed 90% of the available photon energy went into the translational energy of the NO cofragment.[90] However, as mentioned Vallance *et al.* observed a two-photon photodissociation process with the N_2O_4 species resulting in the production of a rotationally hot NO cofragment. There may be a similar process for the N_2O_3 species, however there are limited studies investigating the N_2O_3 photodissociation at 226 nm. The potential secondary photochemical process may be the cause of the thermal perturbations when performing the two-line PLIF rotational thermometry technique within ACE.

4.4.3 Thermal Characterization of Turbulent Boundary Layer

To minimize the potential for a thermal perturbation the turbulent PLIF thermometry experiments were performed with a local NO concentration of 0.005%. At this concentration there was no appreciable freestream thermal perturbation observed during the turbulent thermometry campaign. The campaign consisted of 12 experiments located at the 1st and 3rd locations and described using the notation in Table 2.1. The L1 thermometry measurement was critical in understanding

the baseline fluctuations with the perturbations introduced by the geometric trips and DC glow-discharge plasma. A representative average and instantaneous L1/LP1 flow visualization image is shown in Figure 4.15. The oblique shock was clearly defined at ∼30 mm normal to the surface by the large discontinuity in the fluorescence S/N ratio. There was a large rise in the S/N ratio observed across the shock due to an increase in the local number density. Using oblique shock relations the pressure was expected to increase 45% relative to the freestream which correlated to 4.8 Torr.[108] Numerous weak Mach waves were observed due to multiple forward/backward steps along the model due to the PEEK insert, laminar insert, two copper electrodes, and window insert. Due to the weakness of these Mach waves the expected pressure and temperature rise across these shocks was difficult to estimate. Near the surface there were no discernible flow structures; however, the relative S/N appeared to gradually decrease. Assuming the pressure increase was negligible across the Mach waves, the pressure remained constant. Due to a known temperature increase towards the surface, the number density *i.e.* the S/N ratio was expected to decrease. The lack of flow

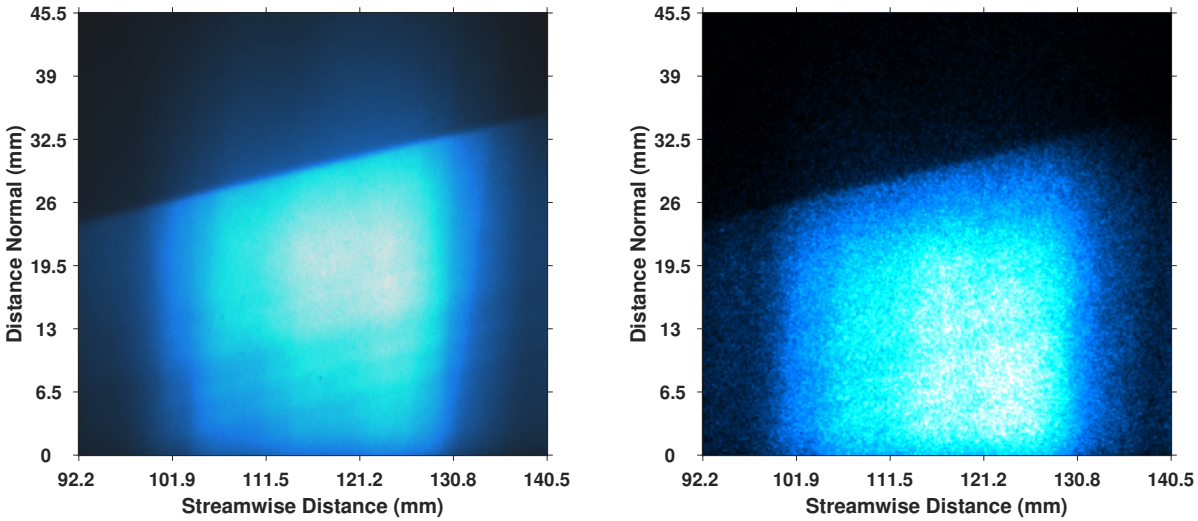

(a) (b)

Figure 4.15: Representative L1 fluorescent images. Figure a is an average fluorescent image and Figure b is an instantaneous fluorescent image.

structure was expected for the L1 laminar boundary layer. The fluctuations near the surface were

also assumed to be minimal due to the ordered behavior of a laminar boundary layer. Experiments performed by Leidy *et al.* observed laminar boundary layer fluctuations on a flat plate to be ∼66% smaller than the turbulent counter part.[48] The L1 temperature and relative %T fluctuation maps are shown in Figures 4.16a and 4.16b, respectively. The freestream temperature fluctuations above the oblique shock were measured to be 3% to 5% which agreed well with the ∼1.5% RMS pressure fluctuations measured by Semper *et al.*[46] Due to the relatively low S/N above the bow shock, the defined R_{12} region was beneath the bow shock. The known temperature for this region was adjusted until the calculated freestream temperature corresponded to a freestream temperature of 58 ± 2 K. The corresponding % T uncertainty map is shown in Figure 4.16b, where the uncertainty grows from 3.5% in the freestream to upwards of 30% at the wall. The ratio fluctuations near the wall were ∼20% where the low S/N ratio and fluorescence scatter off the wall accounted for the largest portion of the measured %T uncertainty. The L1 temperature map illustrated instantaneous temperature discontinuity across the oblique shock. Directly upstream of the oblique shock there was a small freestream temperature rise to 63 K. Using the oblique shock angle relations, the temperature change for an ideal gas at Mach 5.7 should be ∼12% of the freestream temperature.[108] However, the temperature increase across the shock was measured to be 83 K, a 30% increase in temperature. Downstream of the oblique shock, the temperature gradually increased normal to the surface reaching 170 K at ∼2.5 mm. The gradual temperature increase was attributed to the multiple weak shocks produced by the steps of the PEEK insert, laminar insert, two copper electrodes, and window insert. There was not a strong temperature discontinuity observed across the small Mach waves. At ∼4 mm above the surface there was a rapid temperature increase towards the surface due to the entropy and boundary layer. The entropy layer is a known fluid layer formed along blunt bodies such as the leading edge of the flat plate. The leading edge of the plate has a blunted curvature geometry to discourage flow detachment. Entropy layers are a result of the flow passing through an oblique shock formed at the blunted leading edge. The stronger the shock, the larger the change in entropy, so nearest the leading edge the flow experiences a near normal shock producing a large entropy change. As the curvature of the shock increases normal to the surface,

the entropy change decreases across the shock giving rise to an entropy gradient. Entropy layers were first characterized by Stetson *et al.* when comparing boundary layer transition points between blunt and sharp cone geometries.[109] Ferdov *el.al.* determined the growing entropy layer has the potential to introduce velocity and temperature gradients which can convolute with the boundary layer forming along the body.[110] They determined the entropy layer instabilities influenced the turbulent transition and was ultimately swallowed by the turbulent boundary layer. The thermal distinction between the entropy and boundary layer was difficult to discern within the presented measurements. Following the 2σ statistical treatment, >85% of the determined freestream temperature values were accepted, however up to $\sim$50% of the temperature values were discarded within 1 mm of the surface. The LP1 thermal profiles are shown in Figure 4.17 and were observed to be relatively similar to the L1 profiles. The LP1 temperature profile near the surface was nearly identical to the L1 temperature map with a surface temperature of 350 K. The LP1 freestream %T fluctuations were measured higher at 5% to 8%, but accounting for the %T uncertainty they agreed well with the L1 freestream results. The horizontally averaged temperature and fluctuation profiles for the L1 and LP1 experiments are shown in Figure 4.18. The near identical temperature profiles indicated a thermal perturbation was not introduced by the upstream plasma. Any thermal heating experienced from the plasma would be the most significant at this location due to its close proximity. The uncertainty for the LP1 measurement was higher and was attributed to the fluorescence scatter being higher relative to the L1 experiment. The %T fluctuations were nearly identical, however again due to the fluorescence scatter during the LP1 experiment the fluctuations were larger. In Figure 4.18b, the local minimum at 25 mm and 14 mm above the surface for the L1 and LP1 experiment, respectively, were attributed to the user defined R_{12} regions.

The thermometry measurements performed at location 1 with the trips insert provided noticeably different data sets with regards to the visible flow structures and subsequent thermal profiles. Representative average and instantaneous images for the TW1/TWP1 and TT1/TTP1 measurements are shown in Figure 4.19. The obvious difference between the laminar and turbulent fluorescent images was the additional two well-defined shock-like structures beneath the oblique bow

shock. The trip geometry produced a trip shock ∼20 mm normal to the surface which was directly beneath the bow shock. Below the trip shock was a shear layer that formed at ∼10 mm above the surface. The shear layer formation was due to the formation of a pair of counter-rotating vortices produced by the trip geometries.[111] These vortices transfer low velocity elements within the boundary layer into the freestream while also transferring high velocity elements into the slow-moving boundary layer. The weaker Mach waves from the small steps were less defined compared to the L1 experiment, but were still distinguishable in the image averages, Figures 4.19a and 4.19c. Due to the presence of these shocks there was expected to be thermal discontinuities across each of them. In Figure 4.19b there were visible wave-like features directly downstream of the geometric trips indicating the trip geometries were mechanically introducing turbulent wake structures. However, in Figure 4.19d, a TT1 fluorescent image, the wake structures appeared to be absent.

The thermometry analysis for the TW1 experiments shown in Figure 4.20 yielded an interesting temperature profile due to the additional shock structures. Directly downstream of the oblique shock the temperature increased to 83 K where it remained relatively constant until the trip shock. There was a ∼20% temperature increase across the trip shock located ∼20 mm normal to the surface where the local temperature peaked at 100 K. However, immediately downstream of the trip shock there was a gradual ∼20% temperature decrease toward the shear layer located ∼10 mm normal to the surface. The local temperature immediately upstream of the shear layer was 83 K. The decrease in pressure was attributed to an expansion occurring downstream of the trip shock. The same flow behavior was observed by O'Byrne *et al.* within their T4 free-piston shock tunnel facility.[95] Downstream of the shear layer the flow increased in temperature toward the surface reaching a temperature of 365 K. The freestream above and below the bow shock %T uncertainty was 5% to 9%. However, similar to the L1 and LP1 experiments the %T uncertainty increased rapidly within the boundary layer due to the increase in temperature near the surface. The relative temperature fluctuations down to 4.5 mm were measured to be 2% to 5%, however the fluctuations increased to ∼20% at the plate surface. The observed flow structures and measured flow behavior appeared nearly identical in the TWP1 experiment. The wall temperature was observed to be

nearly 380 K, but given the uncertainty the temperature was similar for the TW1 experiment. The horizontally averaged temperature and fluctuation profile for the TW1 and TWP1 experiments are shown in Figure 4.22. The entire temperature profile appeared nearly identical with both exhibiting a clear indication of the rapid temperature changes across the two relatively strong shock and shear layer structures. There was no definitive heating occurring near the surface due to the plasma, similar to the results observed in the L1 and LP1 experiments. The plasma also appeared to not have a measurable effect on the fluctuations within the tripped boundary layer.

The TT1 and TTP1 experiments both had similar temperature profiles relative to one another. There was a noticeable 12% temperature rise across the trip shock to $\sim$94 K. Immediately downstream of the trip shock, the temperature decreased by 12% back to 84 K. Comparing the TW1/TWP1 and TT1/TTP1 experiments, the flow behavior across the trip shock was similar; however, the temperature changes were more pronounced directly downstream of the trip geometry *i.e* the TW1/TWP1 experiments. The horizontally averaged temperature profiles are shown in Figure 4.25. The %T fluctuations for the TT1/TTP1 were 3% to 5% from the freestream down to $\sim$6 mm above the surface. Again the fluctuations increased to 20% to 23% at the plate surface. There was not a measurable difference in the temperature profile normal to the surface during plasma operation. The plasma appeared to not have a measurable effect on the boundary layer fluctuation profile. All of the measurements performed at the 1st location suggest the plasma does not affect the measured bulk flow temperature. However, due to the relative temperature uncertainty the two-line PLIF rotational thermometry technique may not be sensitive to subtle changes in the temperatures near the surface.

Due to the 12° angle of the oblique bow shock, it propagated above the available optical access of the ACE test section. Therefore, the measurements at the 3rd location were collected beneath the shock, so the known freestream temperature was based on the thermometry results from the 1st location analysis. The Mach waves and the two additional trip shock structures produced by the trip geometry were also not observed at the 3rd location measurement. Representative average and instantaneous images for the L3/LP3 locations are shown in Figure 4.26. The L3 fluorescent

images were different relative to the L1 fluorescent images for a variety of reasons. Due to the optical access at 405 mm the laser sheet propagation angle was much larger relative to the wall normal. Also, the edge of the laser sheet was cutoff by the ACE optical port prior to entering the test section. The cutoff laser edge can be seen striking the plate at ∼390 mm. Another observed flow feature was the shock spanning from 38 mm to 26 mm above the surface. The feature was attributed to the reflected expansion wave emanating from the backward facing step of the nozzle/test section interface. Beneath this shock structure the freestream temperature was set to be 82 K for the 3rd location thermometry analysis. The L3 thermal profiles are shown in Figure 4.27. The observed boundary layer height was on the order of ∼4.5 mm with a wall temperature of 350 K. The %T fluctuations were on the order of 3 to 5% throughout the freestream and increased rapidly to ∼17% at the surface. The boundary layer profile, temperature, and %T fluctuations were very similar to the observed profiles for the L1/LP1 experiments. As mentioned previously the boundary layer at the 3rd location may have swallowed the entropy layer formed at the leading edge. The LP3 thermal profiles are shown in Figure 4.28. The temperature profile was nearly identical with a thermal boundary layer height of ∼4.5 mm and a wall temperature of 355 K. The LP3 %T uncertainty profile was relatively higher compared to the L3 temperature uncertainty profile. However the %T fluctuation profile remained on the order of 3% to 5% throughout the freestream, however increased to 20% at the surface. The horizontally averaged temperature and %T fluctuation profiles are shown in Figure 4.29. The temperature curves were identical to one another, indicating the plasma did not thermally perturb the downstream laminar thermal boundary layer. The %T fluctuations were also unaffected when the plasma was operating.

The 3rd location measurements with the trip geometry insert provided remarkable resolution related to the large-scale turbulent structures that evolved along the length of the plate. Representative images for the TW3/TWP3 and TT3/TTP3 measurements are shown in Figure 4.30. The turbulent structures were on the order of 10 mm to 12 mm above the surface of the model as seen in Figure 4.30b and 4.30d. Additionally, in the image average the decrease in the S/N for both the wake and trough measurements was more pronounced due to the height of the turbulent boundary

layer. The thermal profiles for the TW3 experiment are shown in Figure 4.31. The instantaneous temperature map in Figure 4.31a illustrate the variable temperature profiles within the resolved structures. There was a small 2% decrease in the freestream temperature across the expansion wave shock from 84 K to 82 K. Based on the TW3 temperature profile the boundary layer was visibly thicker than the laminar case. The rotational thermal boundary layer was observed to be upwards of 9 mm with a wall temperature of 350 K. The temperature fluctuation map showed the freestream %T fluctuations on the order of 3% to 4%. The %T fluctuations began to increase at $\sim$12 mm above the surface and peaked at 33% at 5 mm above the surface. The %T fluctuations then decreased down to 24% at the wall. The local %T fluctuation maximum indicated there was shear stress interface between the the outer turbulent layer and laminar sub-layer. The same fluctuation profile was described by Lowson when describing the local pressure fluctuations within a separated turbulent boundary layer.[112] Kistler *et al.* measured the pressure fluctuation profile normal to the surface and also observed a local maximum in the pressure fluctuations directly above a flat plate surface.[113] The fluctuations near the wall approached the measured fluctuations for the laminar experiment performed at this location suggesting the flow near the wall behaved similarly. The relative number of accepted temperature values near the wall decreased for the TW3 experiments to 40%-50% which was attributed to the low S/N ratio near the surface. The thermal profiles for the TWP3 experiment are shown in Figure 4.32. The TWP3 temperature profile was observed to be very similar in terms of the rotational thermal boundary layer height and a 350 K wall temperature. The fluctuation profile was nearly identical where the maximum relative temperature fluctuation was 5 mm above the surface. A direct comparison of the temperature and relative temperature fluctuation profile is shown in Figure 4.33. The fluctuation profile remained consistent for the TW3/TWP3 experiments suggesting the nascent $N_{2,v=1}$ population did not affect the turbulent behavior along the length of the plate. As mentioned previously turbulent decay was observed downstream an RF plasma due to the production of $N_{2,v=1}$.[17] However, the RF plasma was capable of generating 3 to 6 times the power output and the flow contained trace amounts of water which coupled the $N_{2,v=1}$ energy to the surrounding bulk flow. The bulk flow temperature increased caus-

ing an increase in flow viscosity resulting in a turbulent dampening pathway. Recall the air is dry in ACE so the $N_{2,v=1}$ was assumed to be frozen in the flow due to the inefficient V-T and V-V energy transfer mechanisms. Vibrational relaxation at the wall was presumed to be the main vehicle coupling the vibrational energy to the bulk flow. Current literature suggests diatomic vibrational relaxation occurs on the sub-picosecond to tens of picoseconds timescale; however, these studies focus on interactions between a single diatomic molecule and a single crystal moiety.[114][115] Nonetheless, in the results discussed thus far there was no observable local boundary layer heating which suggests there was no change in the fluid viscosity. This implies there was not a thermally driven turbulent dampening mechanism which agrees well with the relative temperature fluctuations. Similar thermal profiles were observed for the TT3 and TTP3 experiments and they can be seen in Figures 4.34 and 4.35. Again the 2% decrease across the reflected expansion was observed for both cases. The rotational thermal boundary layer heights for both cases were observed to be $\sim$12 mm with TT3 and TTP3 having wall temperatures of 348 K and 355 K, respectively. The fluctuations were on the order of 3% to 5% which appeared to reach the limitation of the two-line PLIF rotational thermometry technique. Due to the similarity in the thermal profiles for the wake and trough cases it was assumed the turbulence was fully developed at the downstream location. However, the fluctuation profiles for both the TT3 and TTP3 experiments were 12 mm from the surface. The horizontally averaged temperature and %T fluctuation curves were observed to be nearly identical for both of the turbulent trough cases. This agreed with previous results that the plasma appeared to have no measurable effect on the turbulent flow along the length of the plate.

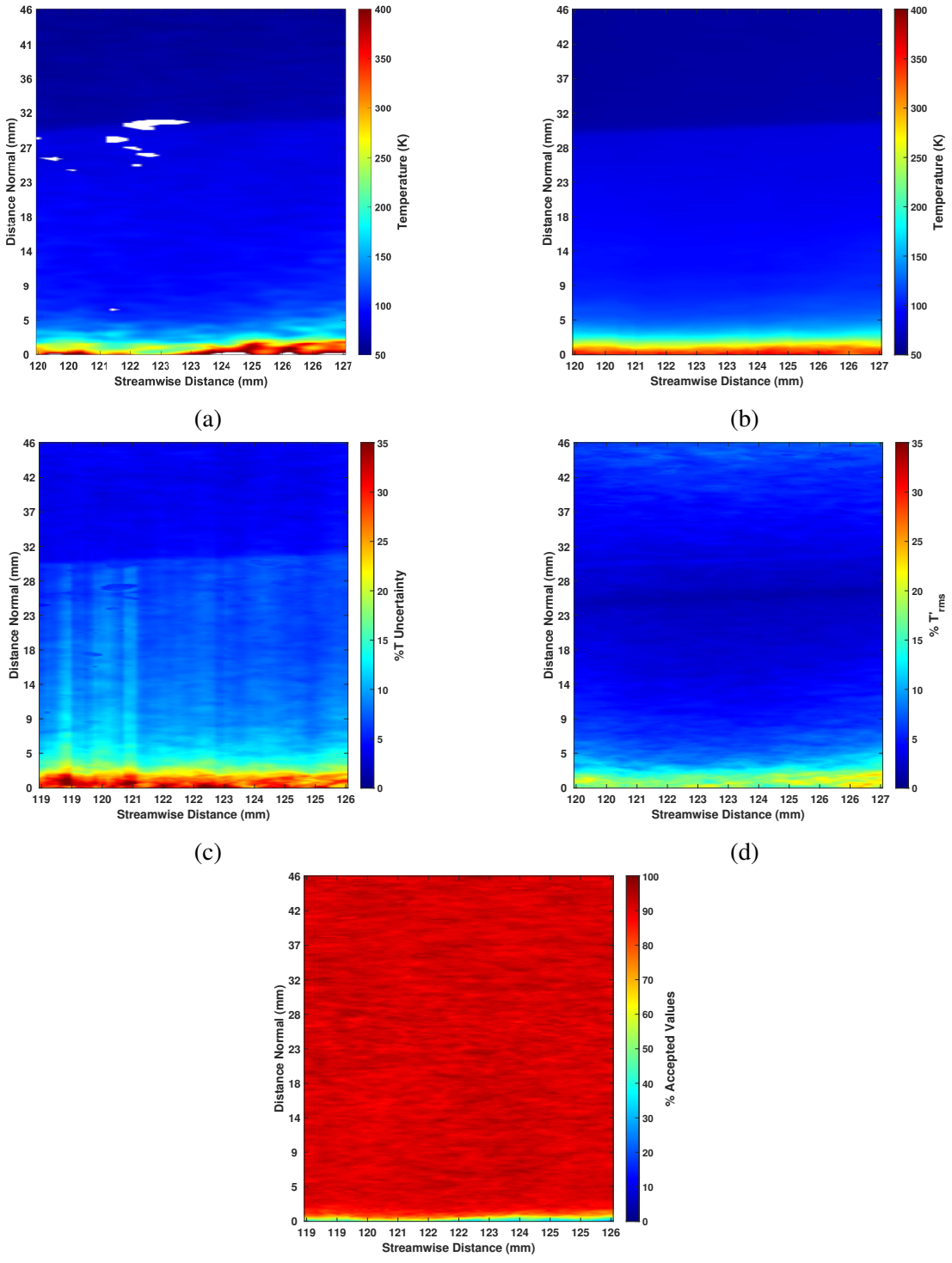

Figure 4.16: Rotational thermal L1 profiles. Figure a is a representative instantaneous temperature map. Figure b is the average temperature map. Figure c is the relative temperature uncertainty map. Figure d is the relative temperature fluctuation map. Figure e is the relative accepted number of values map.

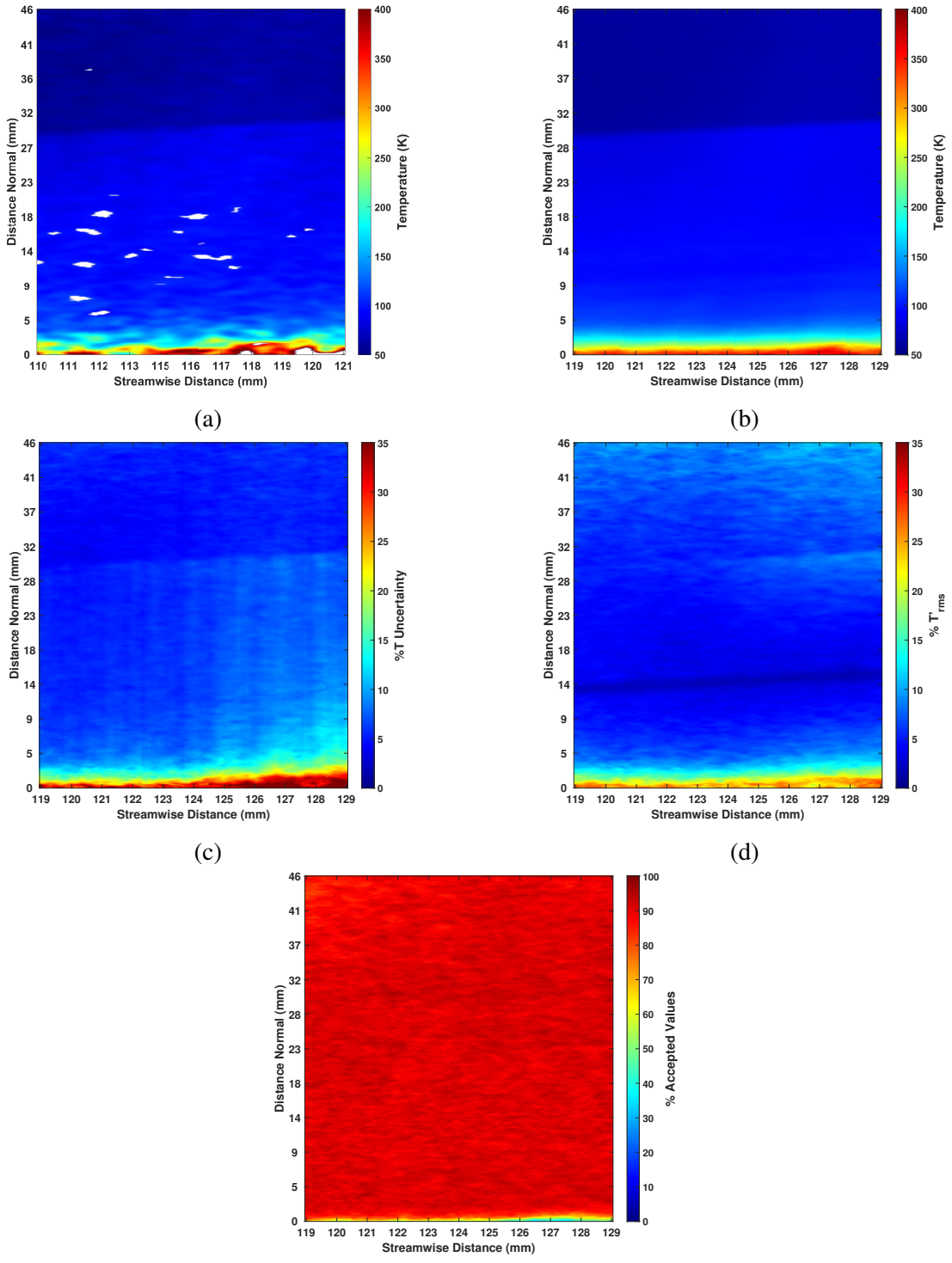

Figure 4.17: Rotational thermal LP1 profiles. Figure a is a representative instantaneous temperature map. Figure b is the average temperature map. Figure c is the relative temperature uncertainty map. Figure d is the relative temperature fluctuation map. Figure e is the relative accepted number of values map.

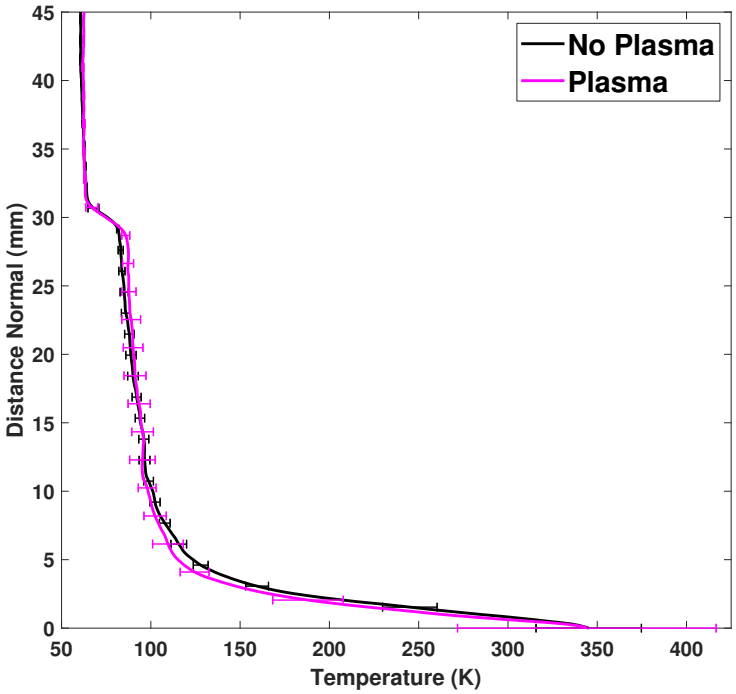

(a)

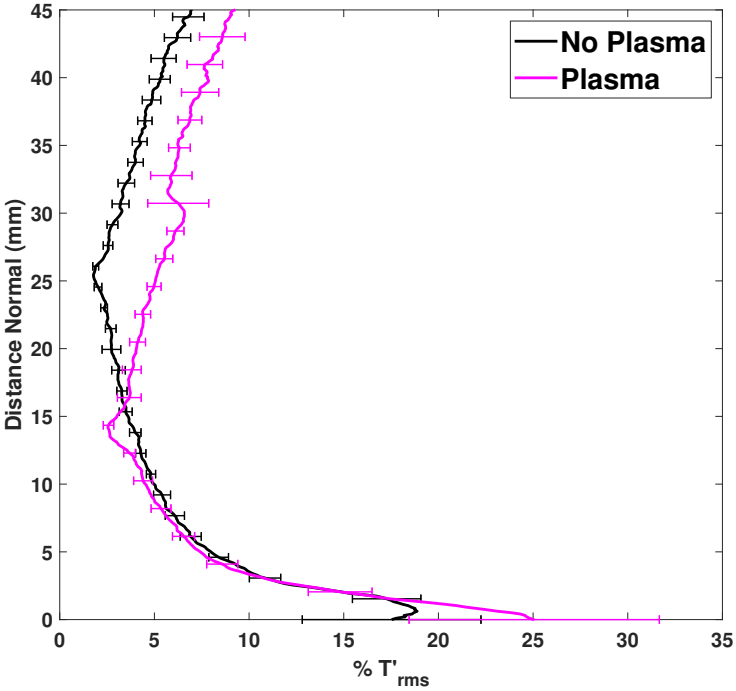

(b)

Figure 4.18: Overlayed rotational thermometry L1 and LP1 curves. Figure a is the 1-D temperature curve. Figure b is the 1-D fluctuation curve.

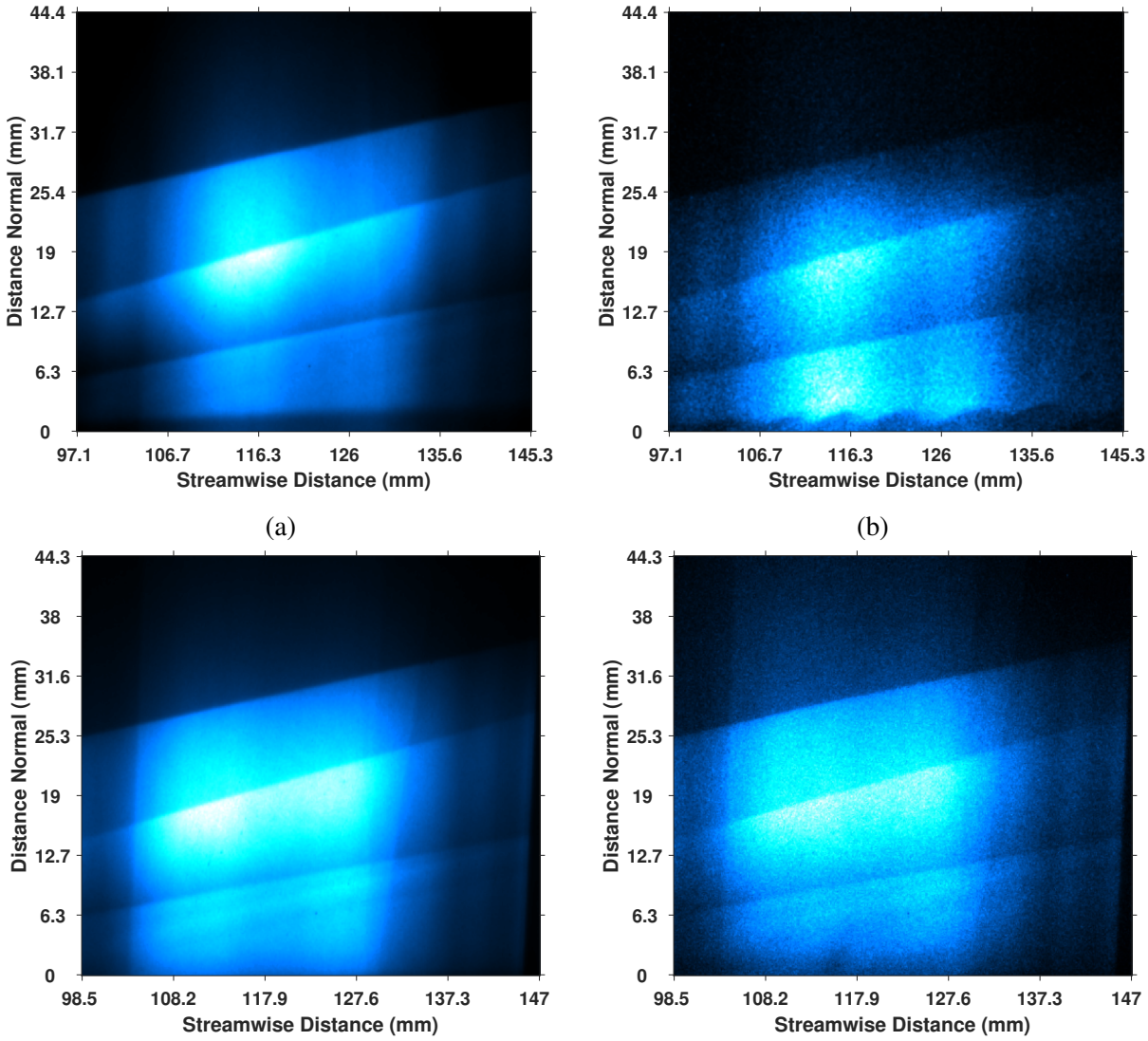

Figure 4.19: Representative fluorescent images for the TW1 and TT1 experiments. Figures a and b are the average an instantaneous images relating to the TW1 experiments. Figures c and d are average instantaneous images relating to the TT1 experiments.

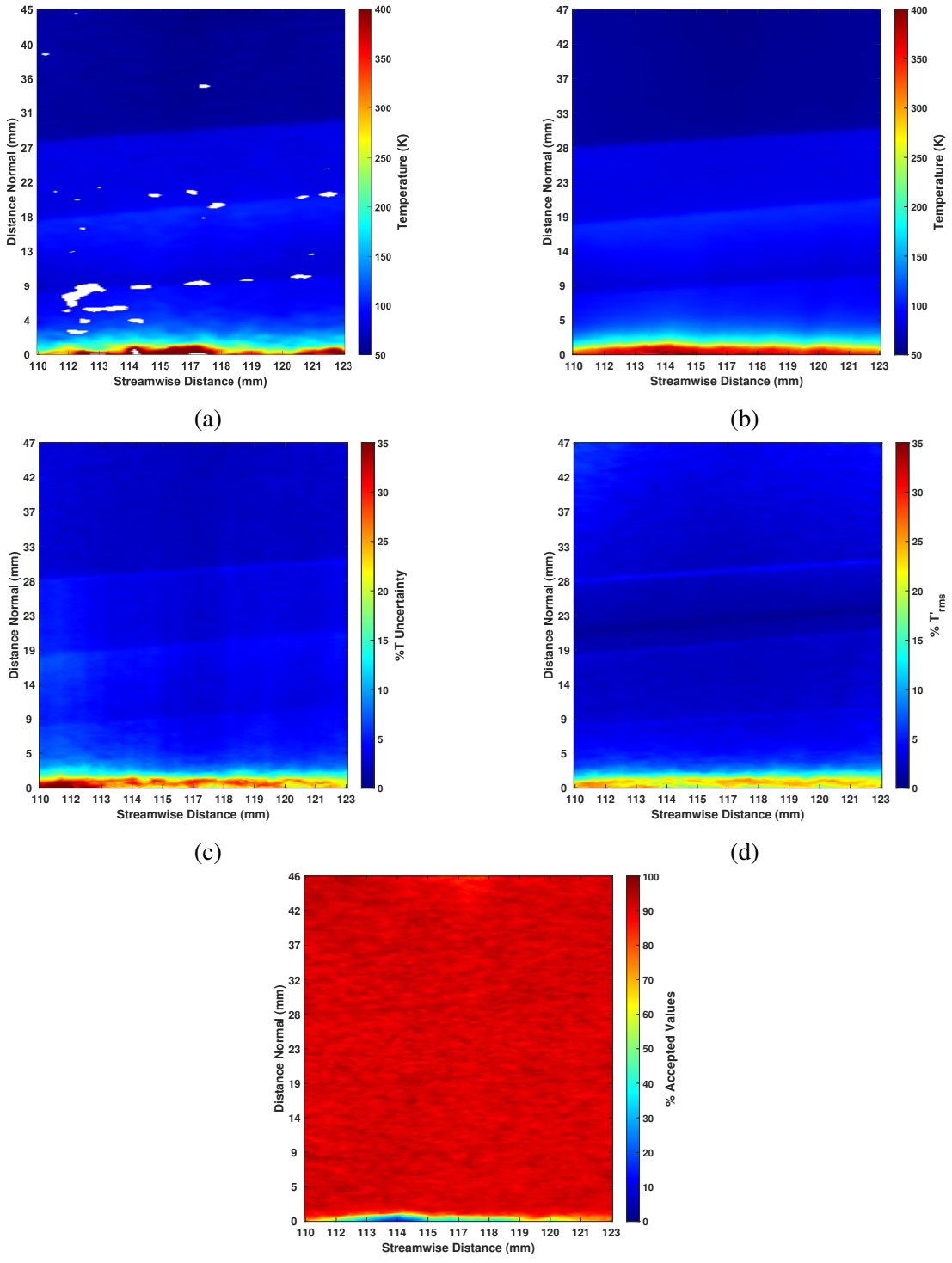

Figure 4.20: Rotational thermal TW1 profiles. Figure a is a representative instantaneous temperature map. Figure b is the average temperature map. Figure c is the relative temperature uncertainty map. Figure d is the relative temperature fluctuation map. Figure e is the relative accepted number of values map.

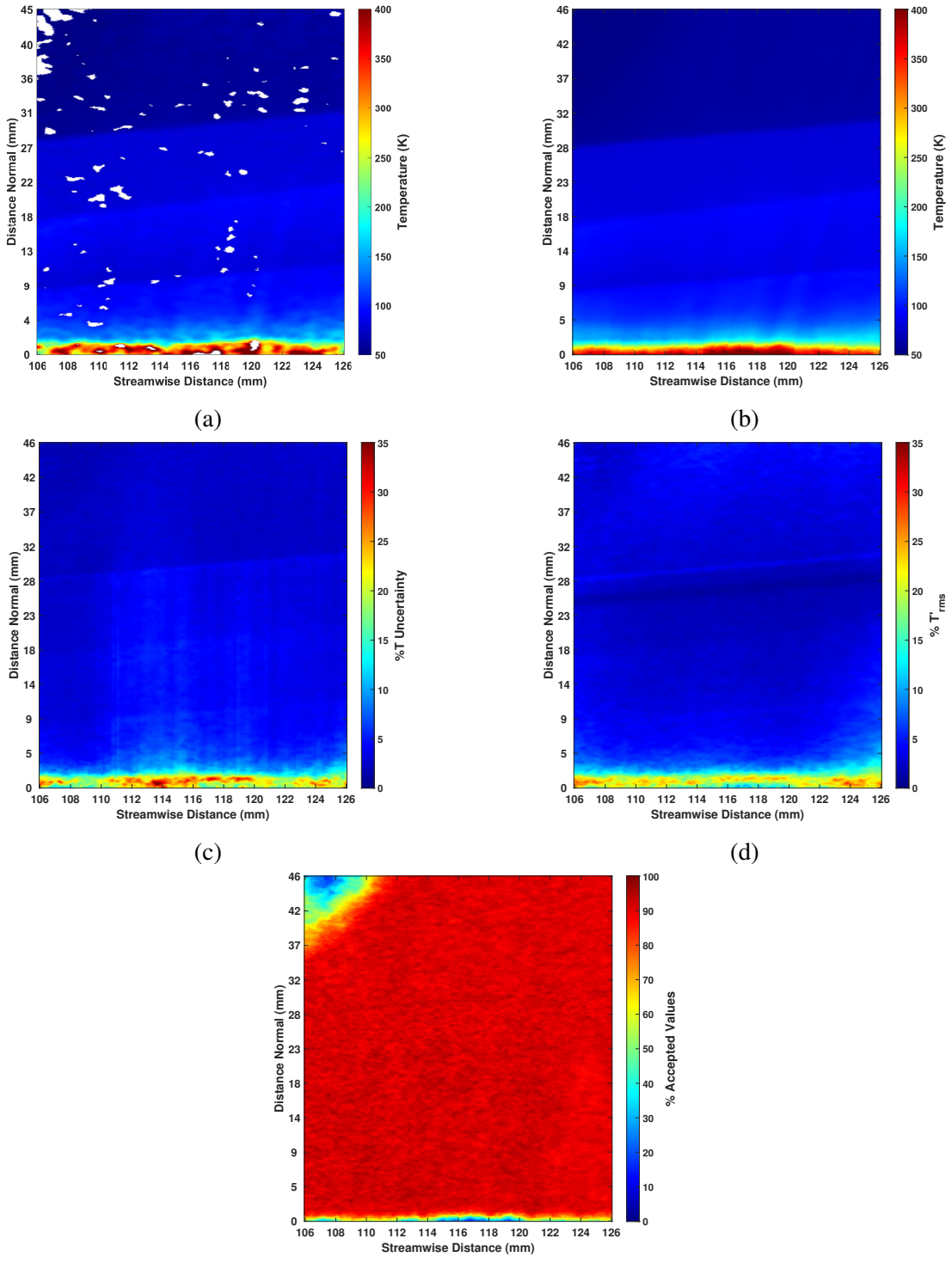

Figure 4.21: Rotational thermal TWP1 profiles. Figure a is a representative instantaneous temperature map. Figure b is the average temperature map. Figure c is the relative temperature uncertainty map. Figure d is the relative temperature fluctuation map. Figure e is the relative accepted number of values map.

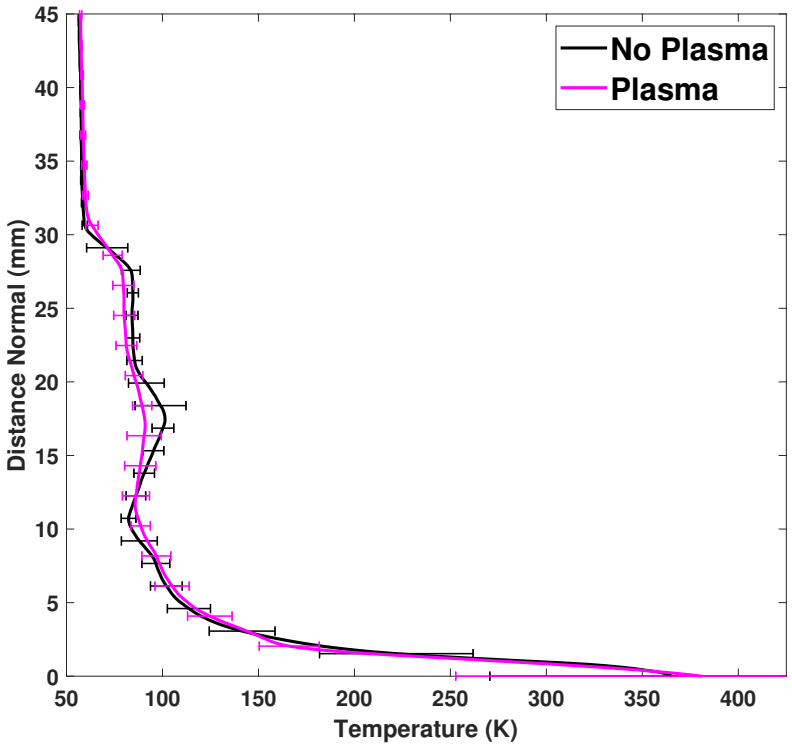

(a)

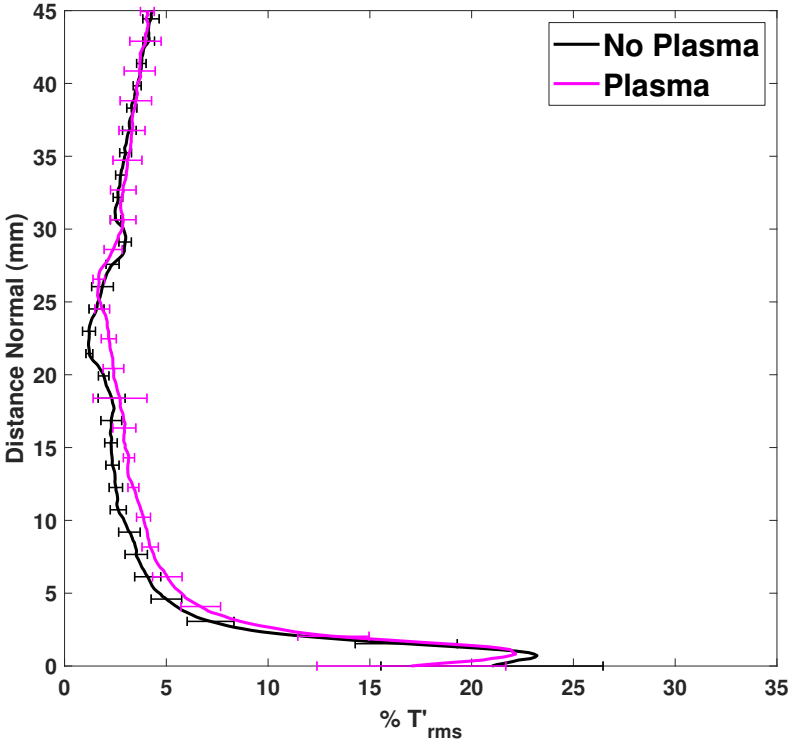

(b)

Figure 4.22: Overlayed rotational thermometry TW1 and TWP1 curves. Figure a is the 1-D temperature curve. Figure b is the 1-D fluctuation curve.

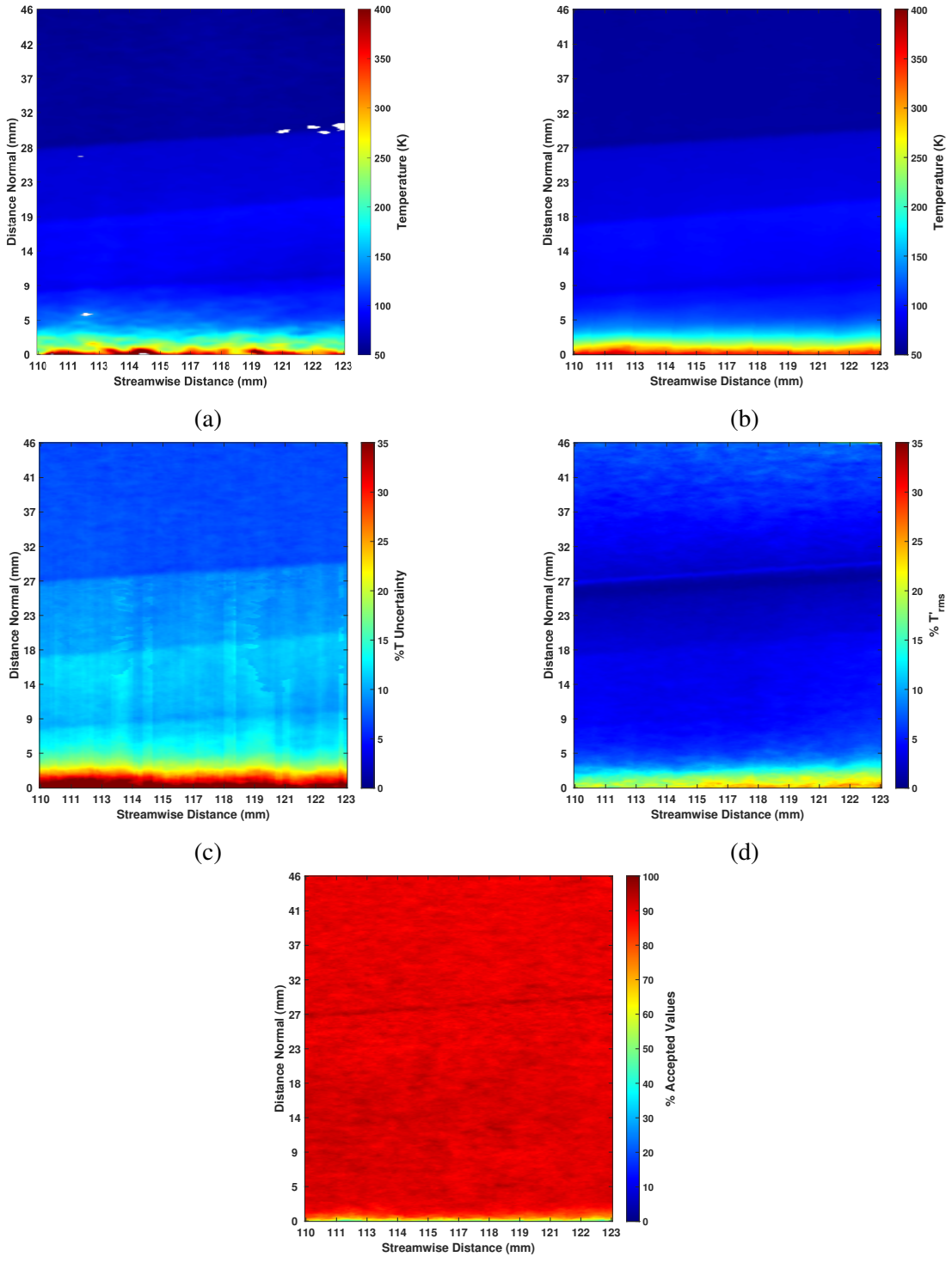

Figure 4.23: Rotational thermal TT1 profiles. Figure a is a representative instantaneous temperature map. Figure b is the average temperature map. Figure c is the relative temperature uncertainty map. Figure d is the relative temperature fluctuation map. Figure e is the relative accepted number of values map.

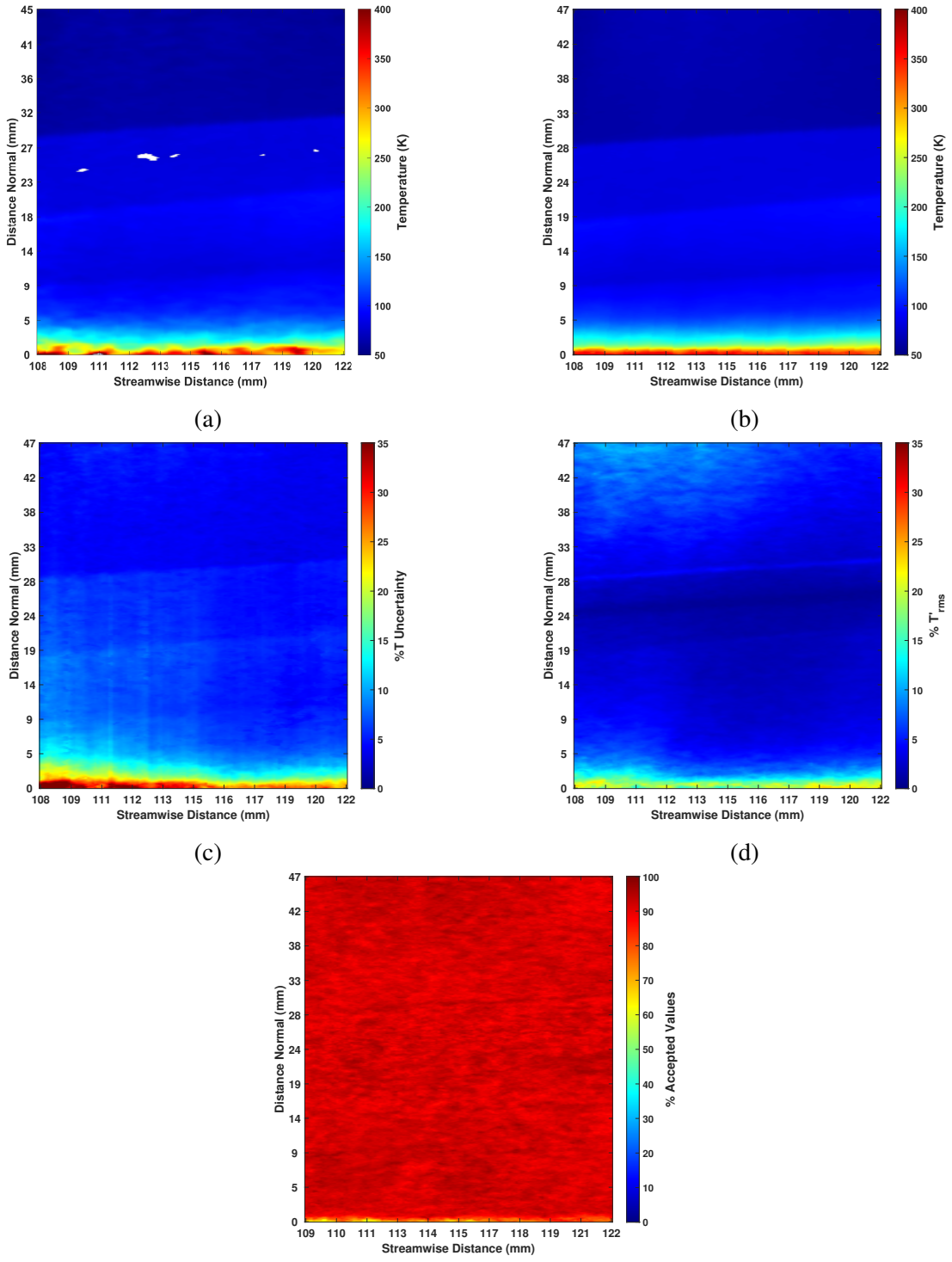

Figure 4.24: Rotational thermal TTP1 profiles. Figure a is a representative instantaneous temperature map. Figure b is the average temperature map. Figure c is the relative temperature uncertainty map. Figure d is the relative temperature fluctuation map. Figure e is the relative accepted number of values map.

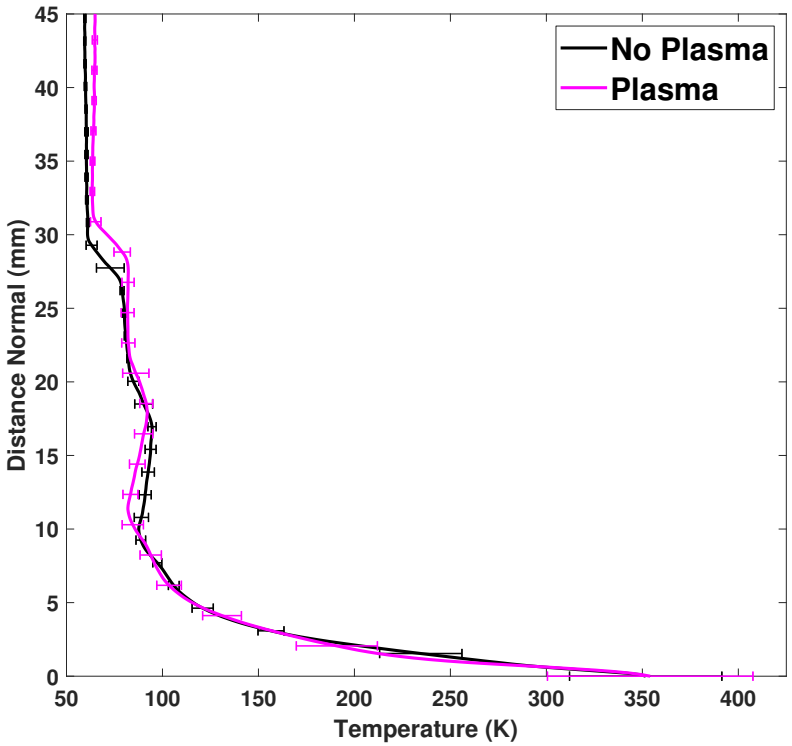

(a)

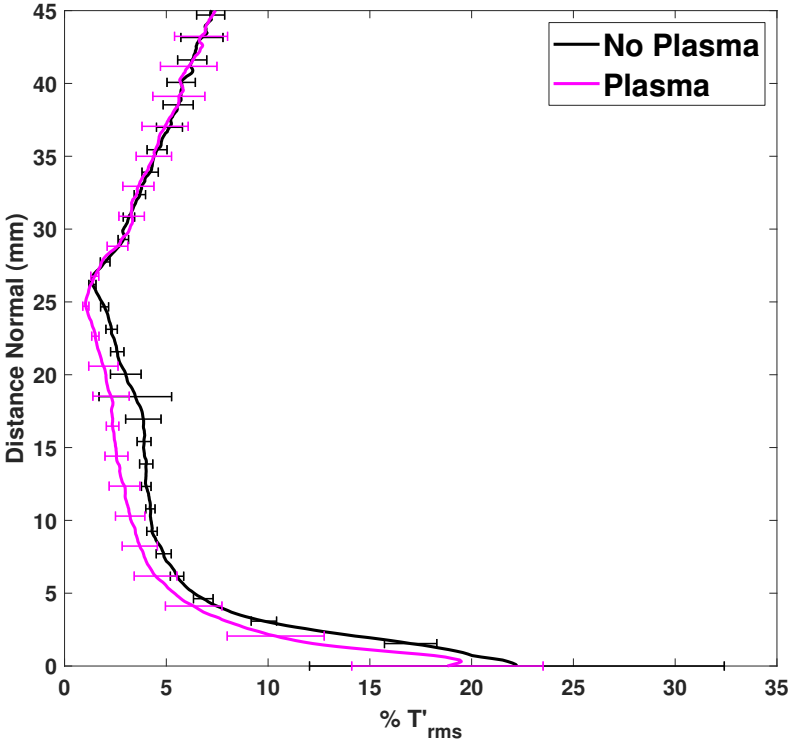

(b)

Figure 4.25: Overlayed rotational thermometry TT1 and TTP1 curves. Figure a is the 1-D temperature curve. Figure b is the 1-D fluctuation curve.

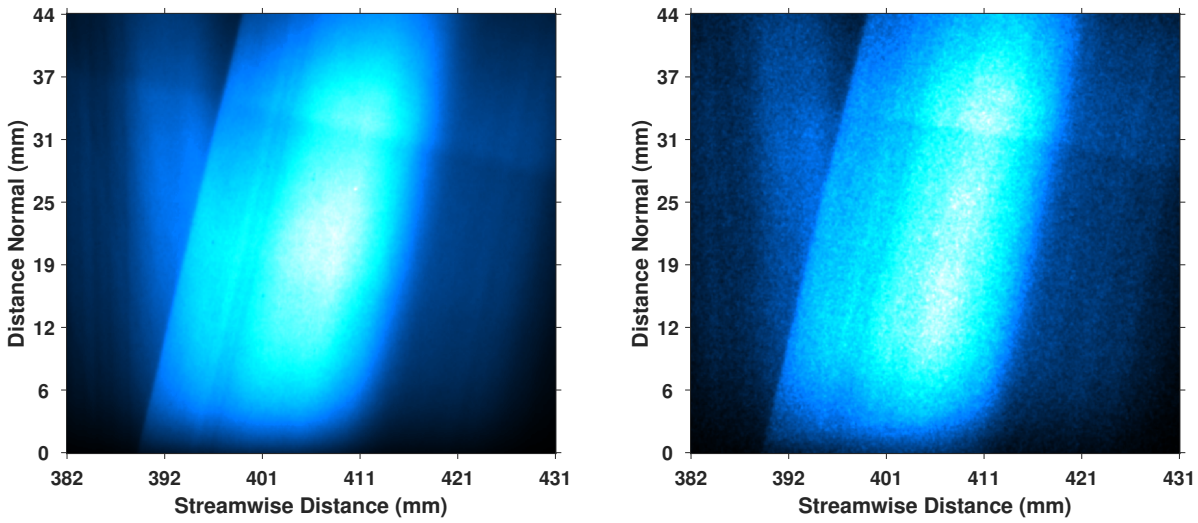

(a) (b)

Figure 4.26: Representative L3 fluorescent images. Figure a is an average fluorescent image and Figure b is an instantaneous temperature image.

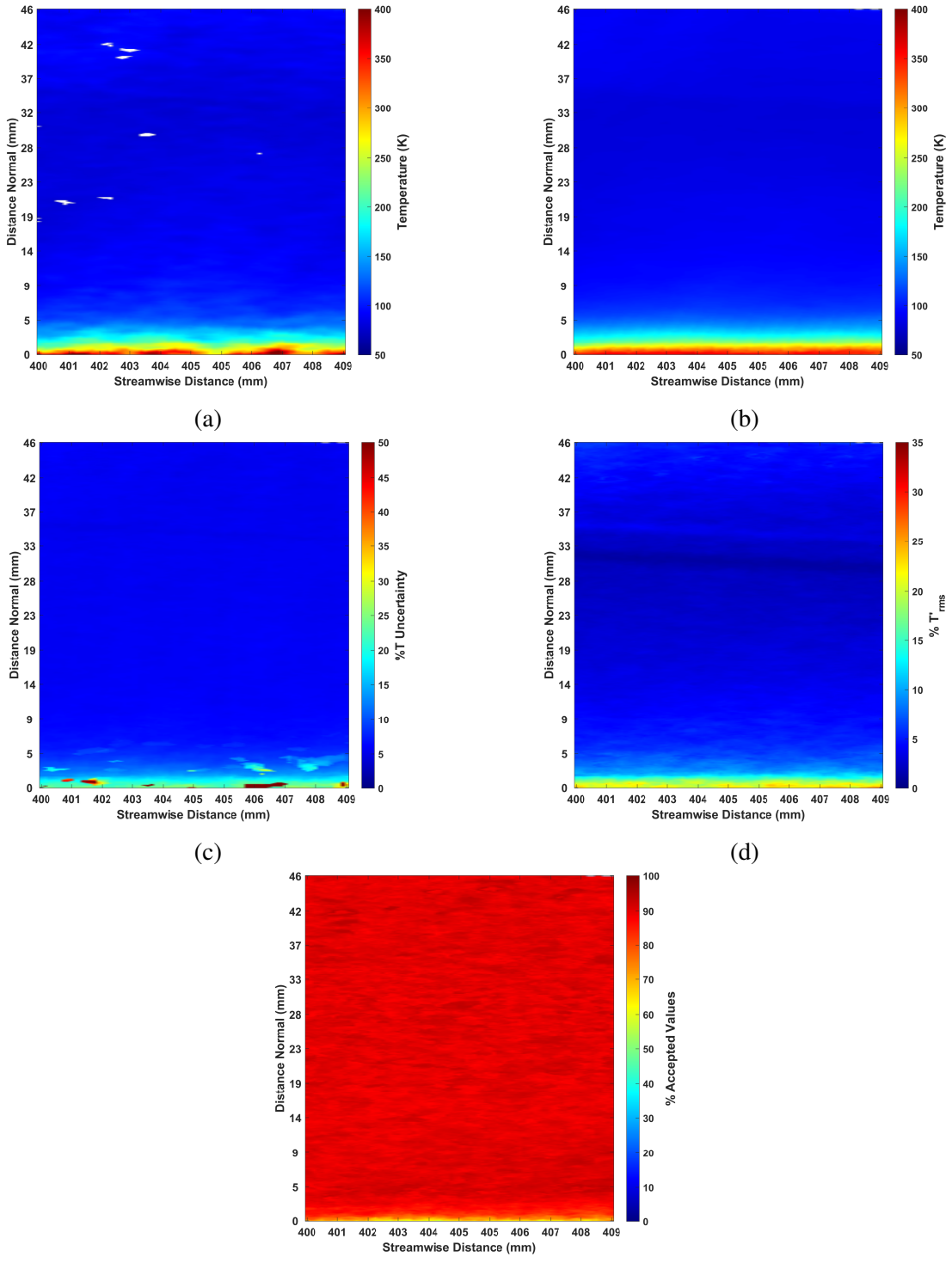

Figure 4.27: Rotational thermal L3 profiles. Figure a is a representative instantaneous temperature map. Figure b is the average temperature map. Figure c is the relative temperature uncertainty map. Figure d is the relative temperature fluctuation map. Figure e is the relative accepted number of values map.

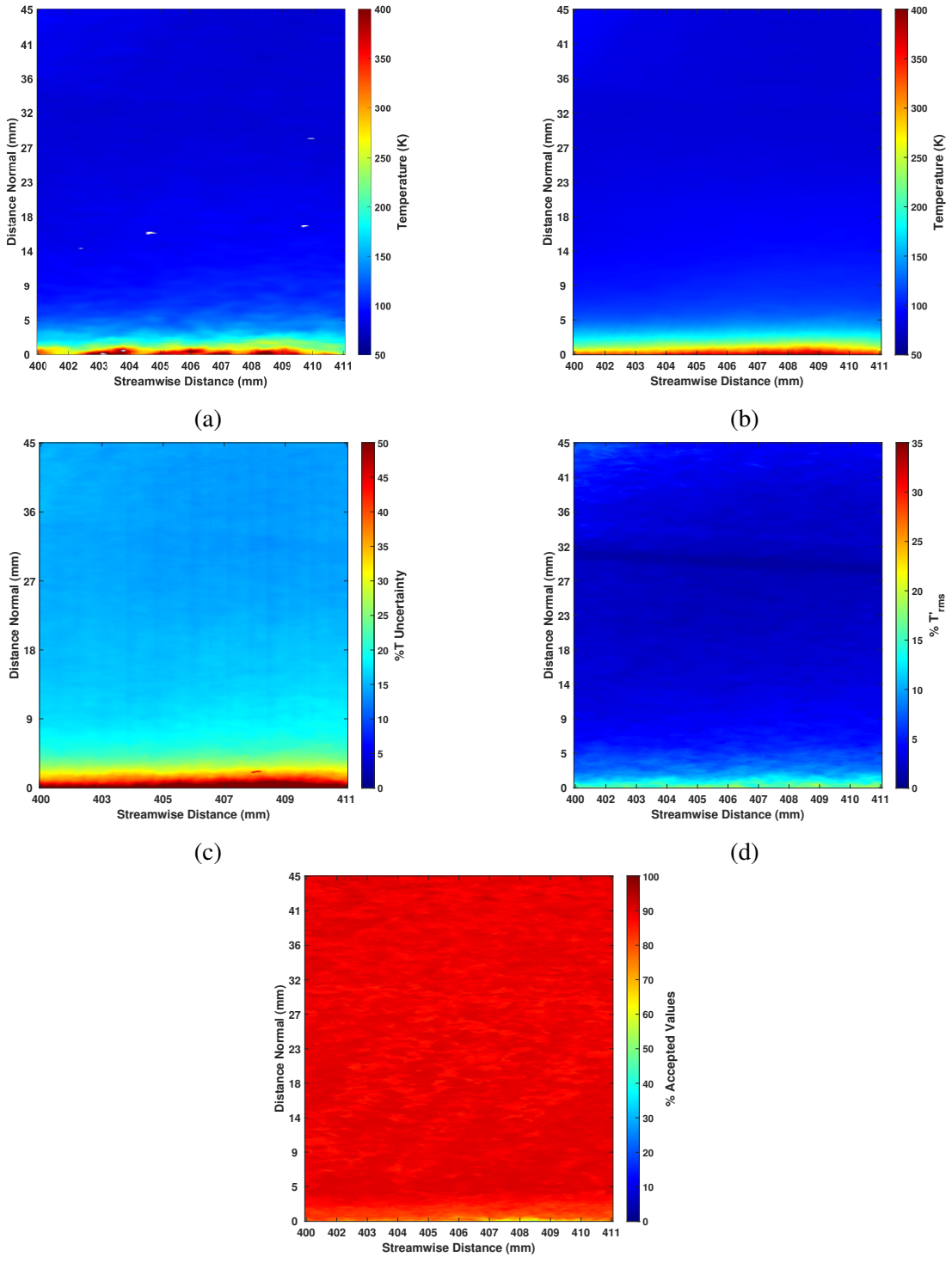

Figure 4.28: Rotational thermal LP3 profiles. Figure a is a representative instantaneous temperature map. Figure b is the average temperature map. Figure c is the relative temperature uncertainty map. Figure d is the relative temperature fluctuation map. Figure e is the relative accepted number of values map.

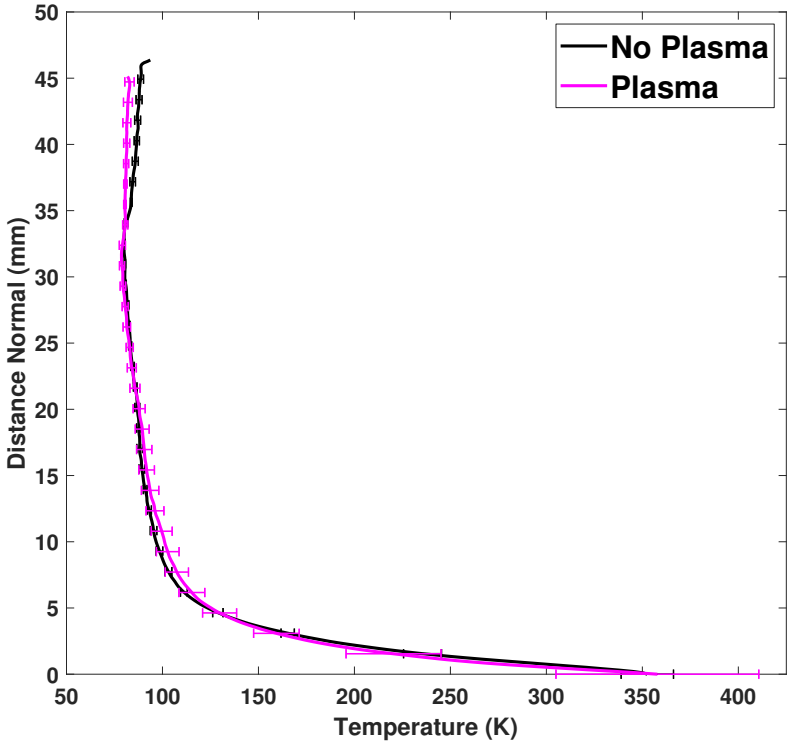

(a)

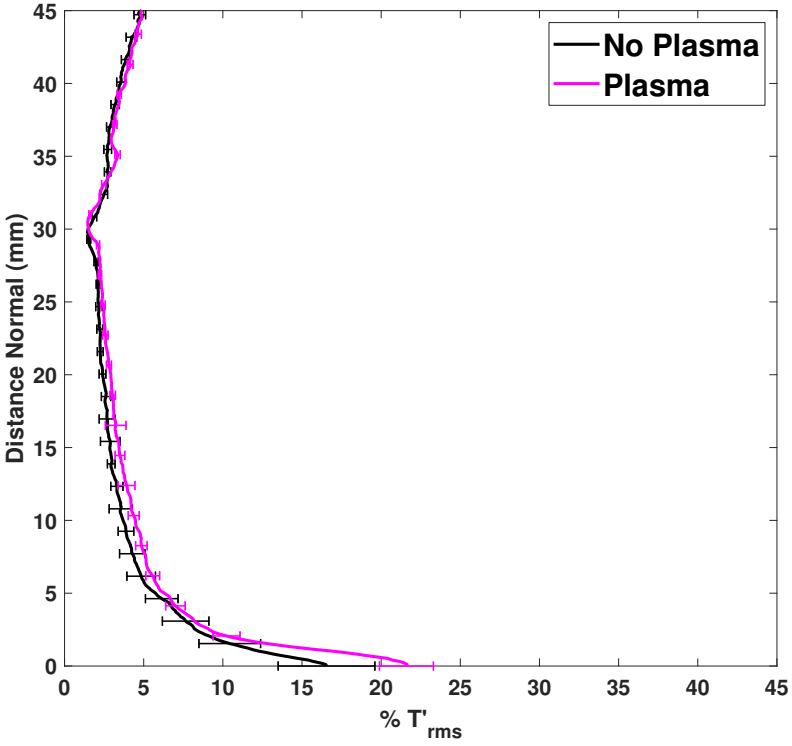

(b)

Figure 4.29: Overlayed rotational thermometry L3 and LP3 curves. Figure a is the 1-D temperature curve. Figure b is the 1-D fluctuation curve.

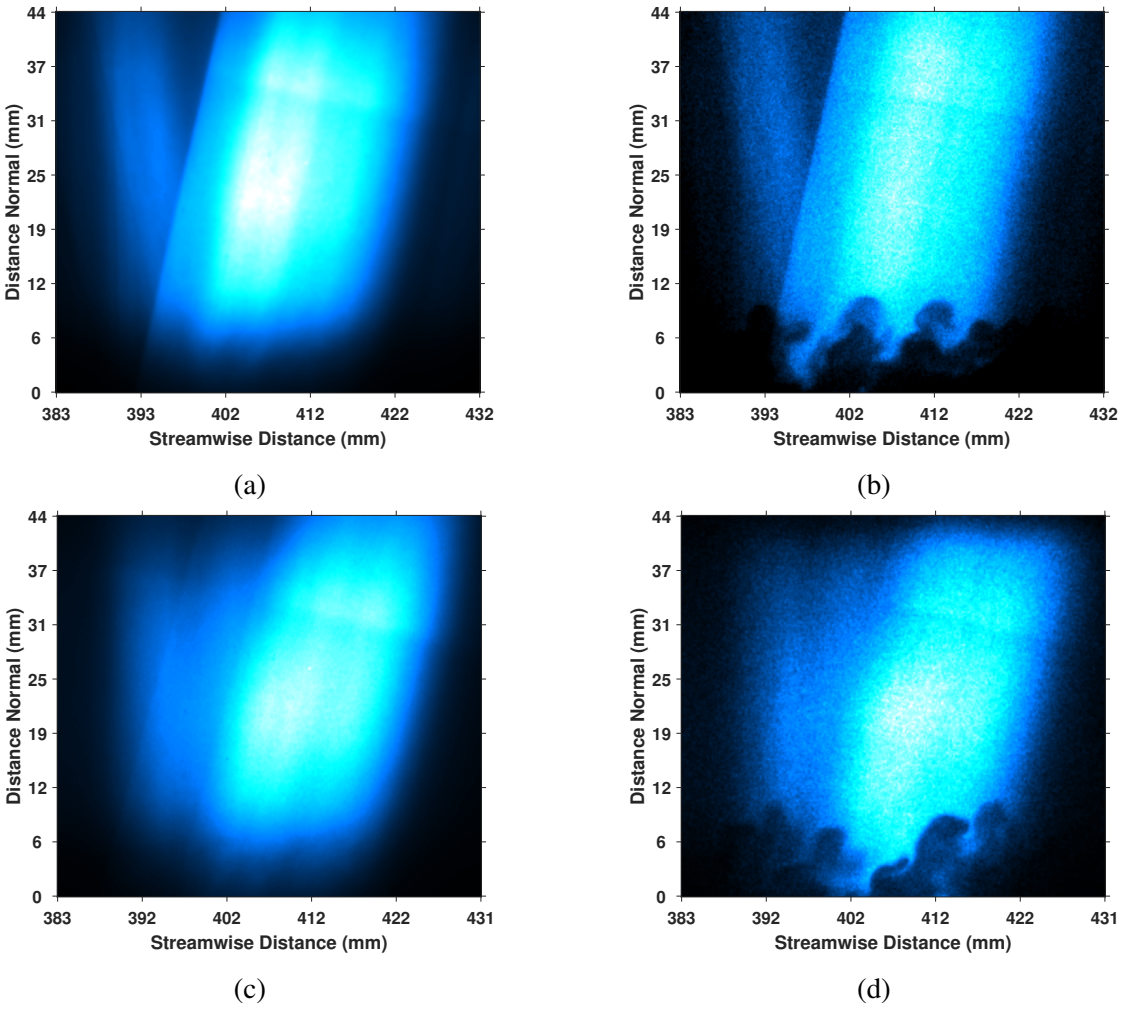

Figure 4.30: Representative fluorescent images for the TW3 and TT3 experiments. Figures a and b are the average an instantaneous images relating to the TW3 experiments. Figures c and d are average instantaneous images relating to the TT3 experiments.

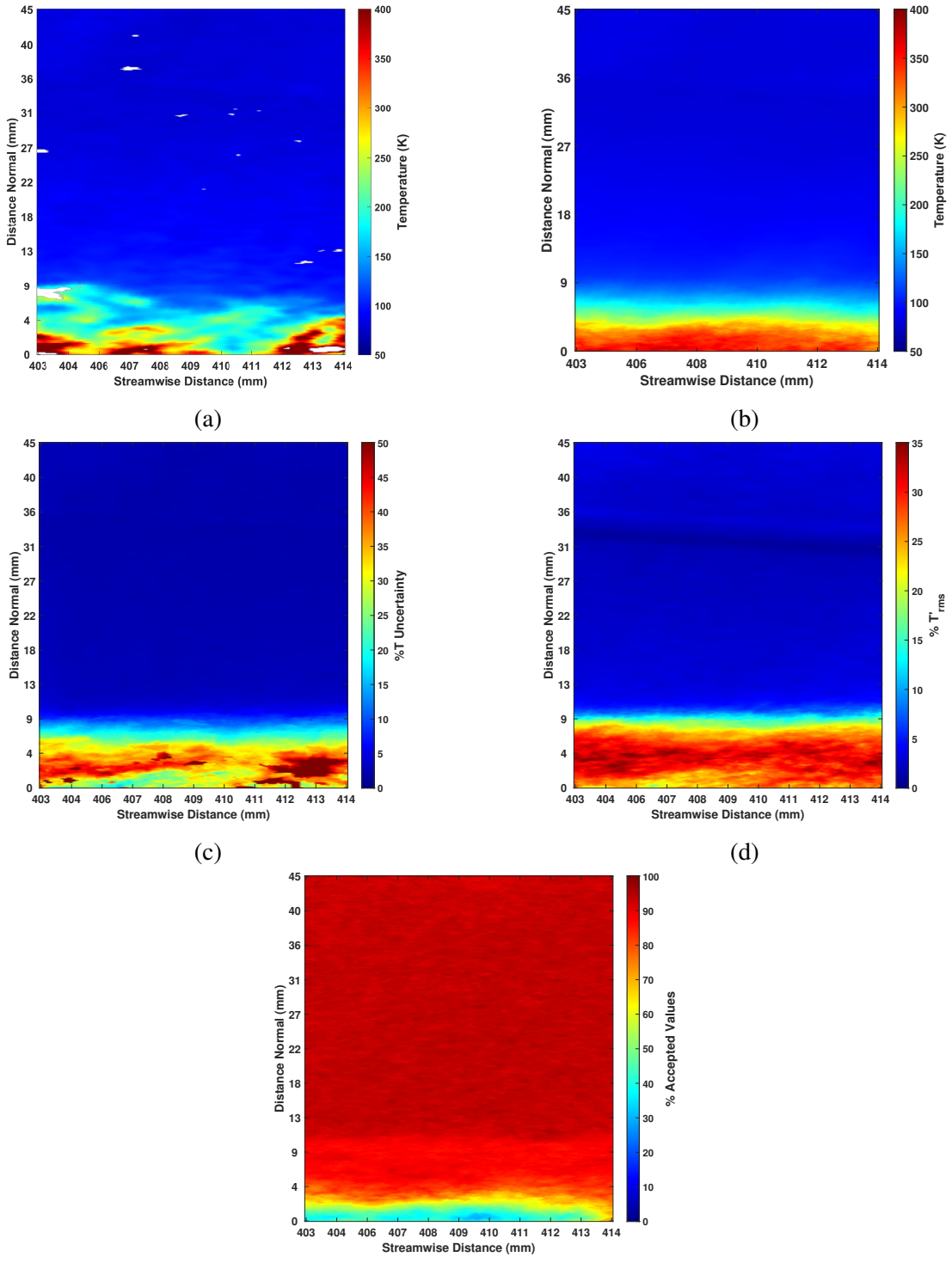

Figure 4.31: Rotational thermal TW3 profiles. Figure a is a representative instantaneous temperature map. Figure b is the average temperature map. Figure c is the relative temperature uncertainty map. Figure d is the relative temperature fluctuation map. Figure e is the relative accepted number of values map.

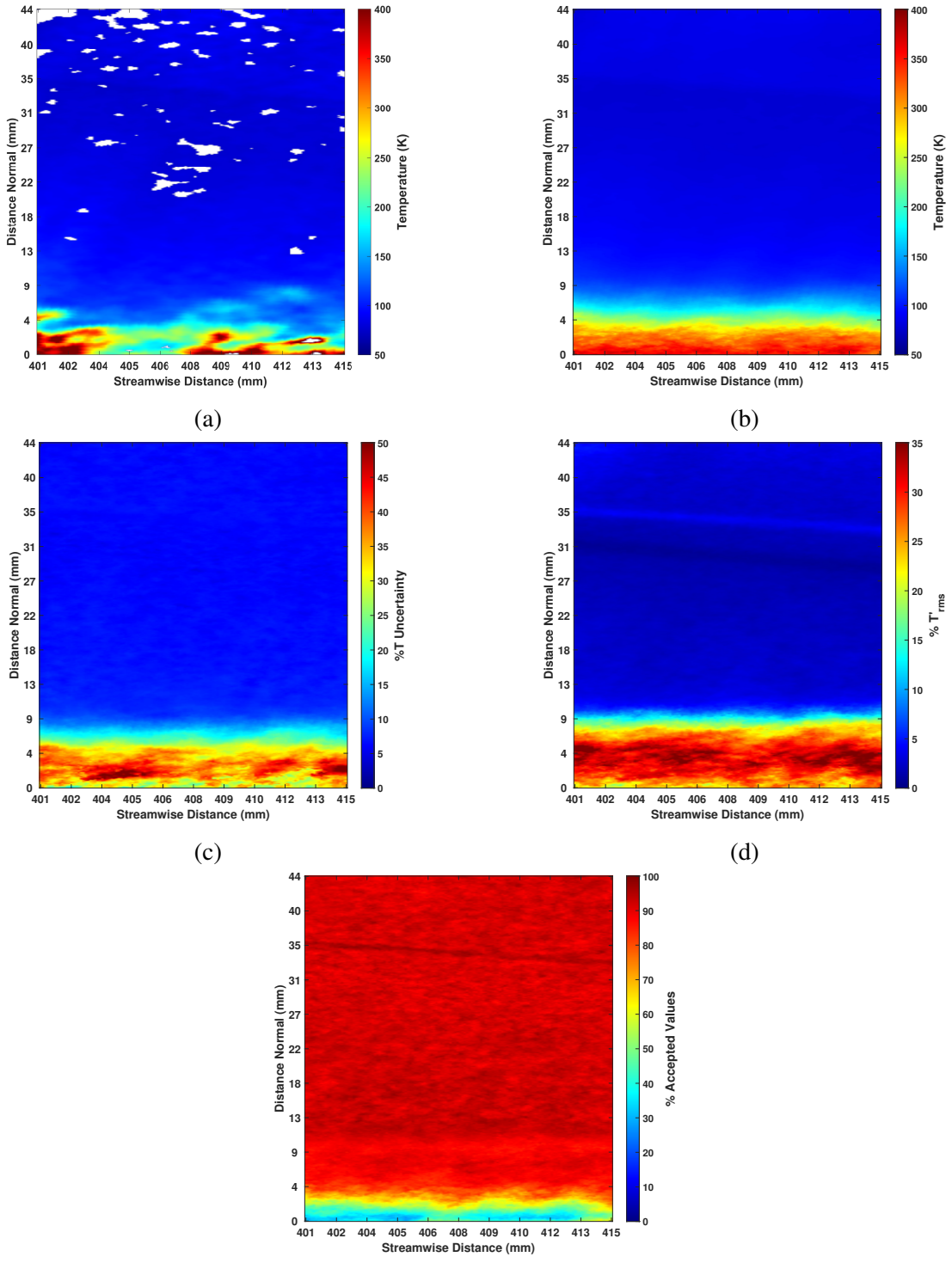

Figure 4.32: Rotational thermal TWP3 profiles. Figure a is a representative instantaneous temperature map. Figure b is the average temperature map. Figure c is the relative temperature uncertainty map. Figure d is the relative temperature fluctuation map. Figure e is the relative accepted number of values map.

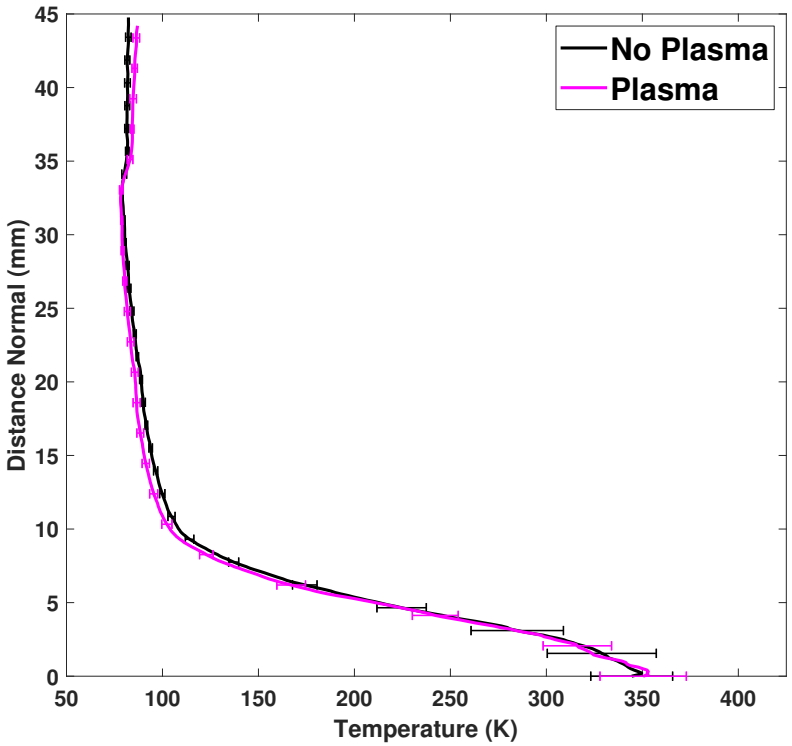

(a)

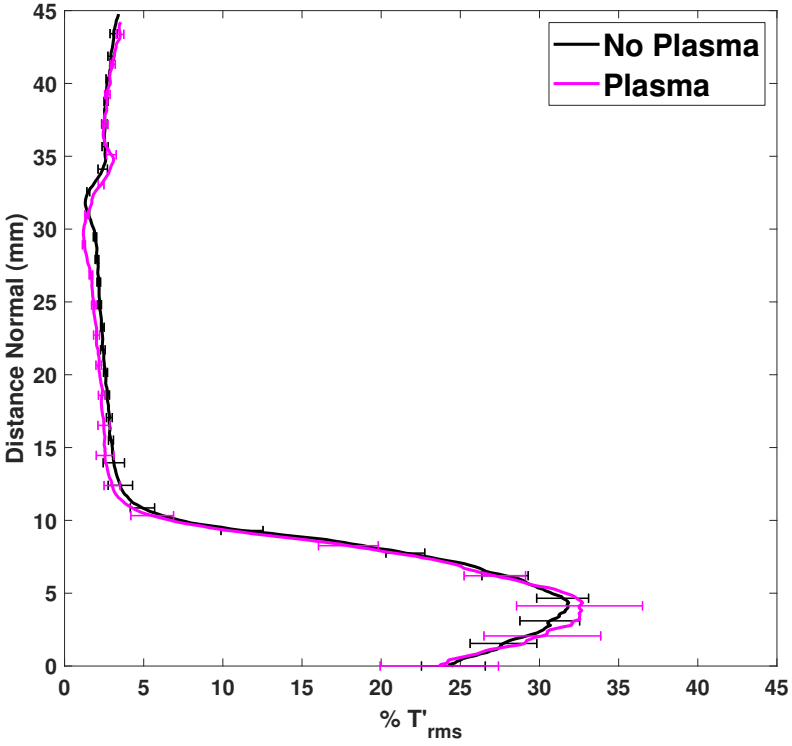

(b)

Figure 4.33: Overlayed rotational thermometry TW3 and TWP3 curves. Figure a is the 1-D temperature curve. Figure b is the 1-D fluctuation curve.

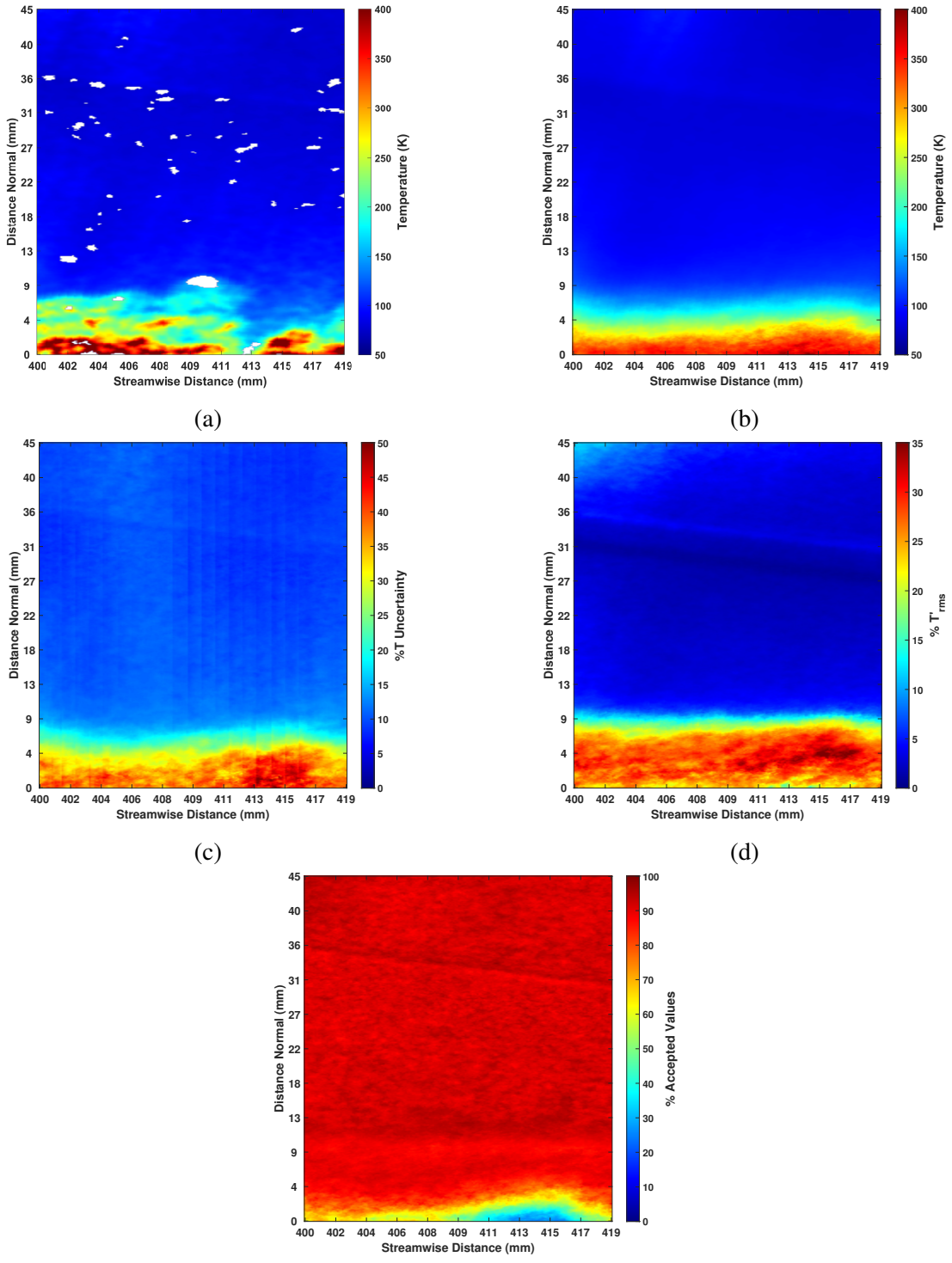

Figure 4.34: Rotational thermal TT3 profiles. Figure a is a representative instantaneous temperature map. Figure b is the average temperature map. Figure c is the relative temperature uncertainty map. Figure d is the relative temperature fluctuation map. Figure e is the relative accepted number of values map.

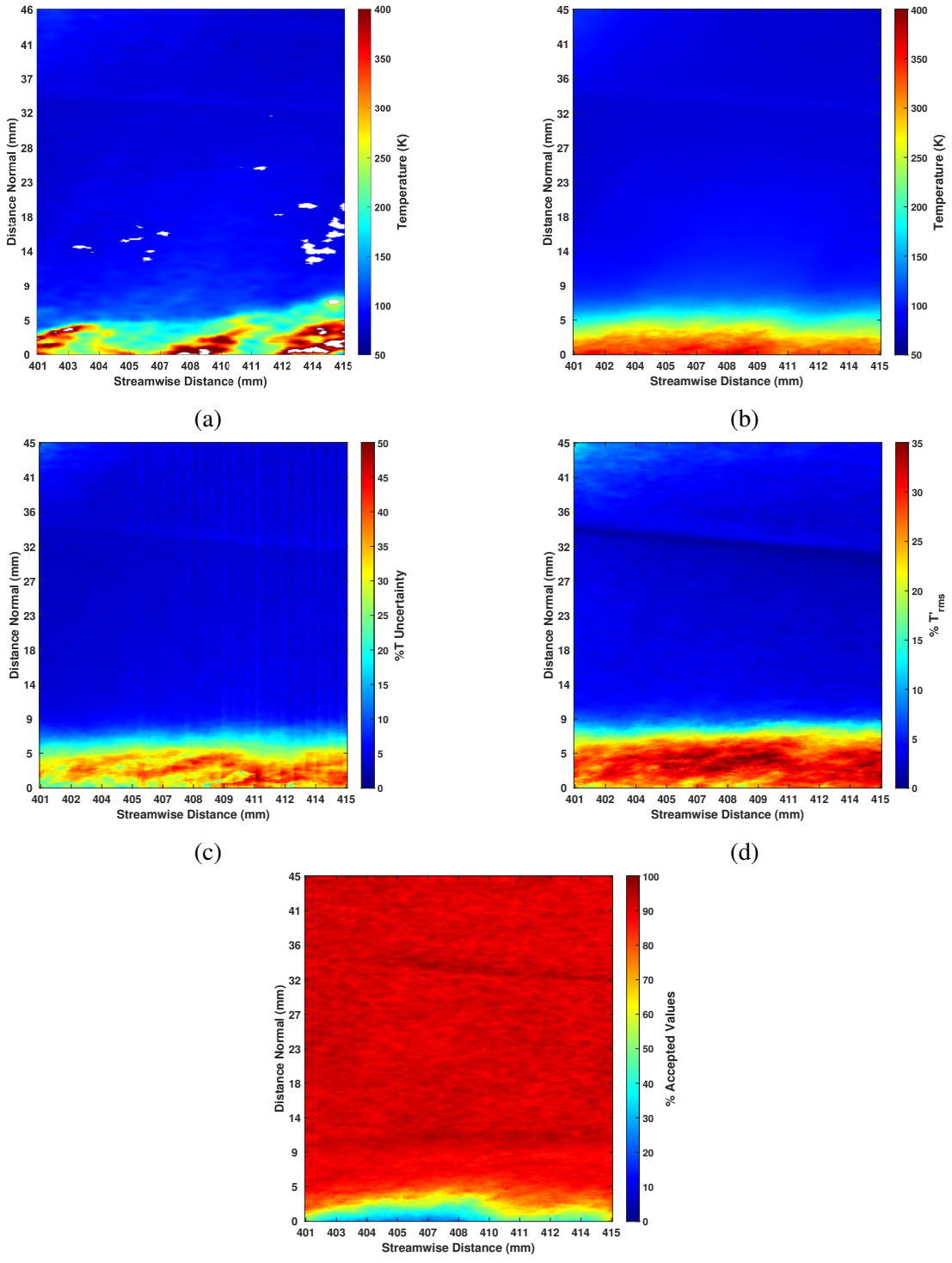

Figure 4.35: Rotational thermal TTP3 profiles. Figure a is a representative instantaneous temperature map. Figure b is the average temperature map. Figure c is the relative temperature uncertainty map. Figure d is the relative temperature fluctuation map. Figure e is the relative accepted number of values map.

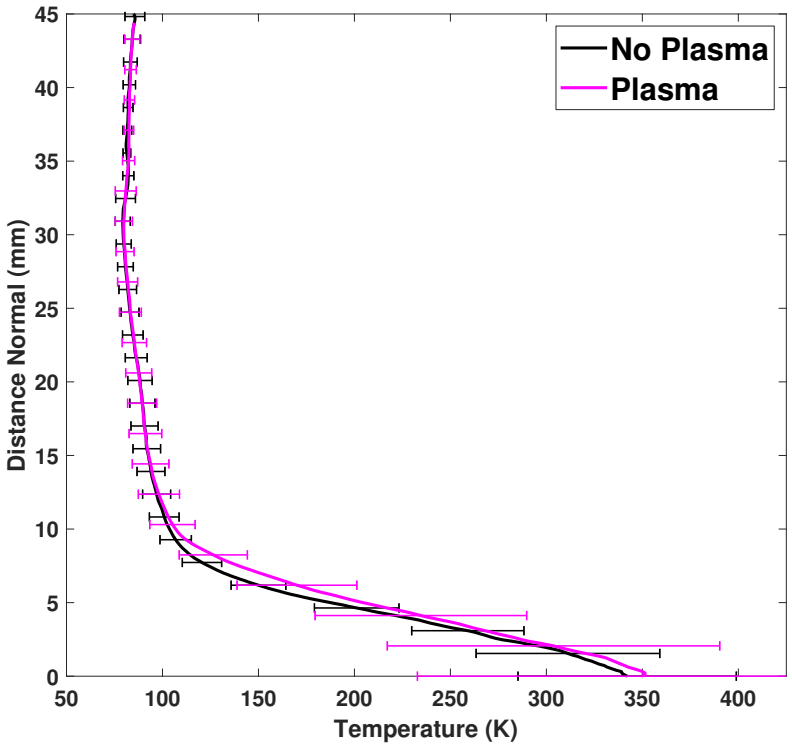

(a)

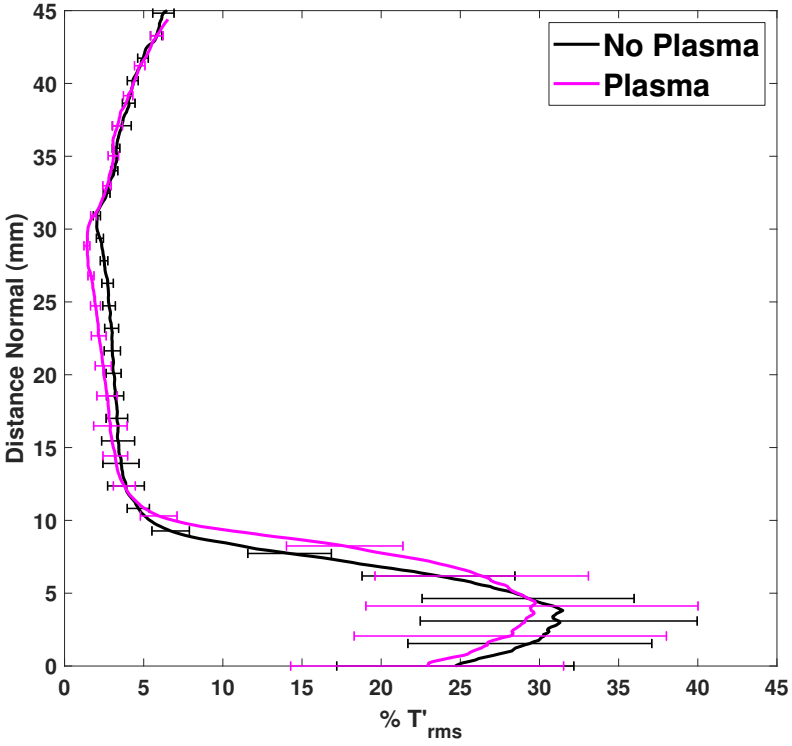

(b)

Figure 4.36: Overlayed rotational thermometry TT3 and TTP3 curves. Figure a is the 1-D temperature curve. Figure b is the 1-D fluctuation curve.

5. VIBRATIONAL THERMOMETRY

5.1 Freestream Vibrational Temperature Model

Measuring the absolute temperature of the flow using the PLIF thermometry technique was dependent on knowing the absolute temperature for a portion of the image. As the temperature and density of the flow decreased during the isentropic expansion process the translational and rotational modes thermalized with respect to one another.[116][117][118][119][120] The stagnation density, temperature, and ACE nozzle contuor yield a freestream flow with a translational/rotational temperature assumed to be $\sim$60 K. However, when considering the vibrational temperature during the isentropic expansion there has been evidence of TNE relative to the translational and rotational temperature.[121][122][123][124] In the following velocimetry chapter it became evident the ACE freestream contained some degree of TNE among the NO $X^2\Pi$ internal modes of the flow.

Danehy *et al.* have characterized the vibrational temperature for the T2 shock tunnel using PLIF thermometry by probing probed three different NO $A^2\Sigma^+ \leftarrow X^2\Pi$ vibrational transitions *i.e.* (0,0), (0,1), and the (0,2) bands. By plotting

$$ln\left(\frac{N_p}{EB_{J'J''}(2J''+1)exp(\frac{-F_{J''}}{k_BT_{rot}})}\right) \tag{5.1}$$

versus the vibrational energy, $G_{v''}$, the slope of the resulting straight line is equal to -1/(k_BT_{vib}). In Equation 5.1 N_p is the fluorescence signal, *E* is the laser pulse energy, $B_{J'J''}$ is the Einstein absorption coefficient, $F_{J''}$ is the rotational energy, and T_{rot} is the rotational temperature. Other experimental methods have measured the vibrational temperature within various flows such as CARS or optical emission spectroscopy (OES); however, these techniques provide integrated spatial averages and lack the capability of 2-D spatial resolution. [125][126][127][128][129] Another proposal was to assume the vibrational temperature was equal to the adiabatic wall temperature; however, there have been several studies suggesting a potential slip condition for the vibrational energy. This implied the wall vibrational energy transfer at the wall may be inefficient giving rise

T(K)	Pressure (Torr)	Local Speed of Sound (m/s)
430	3879	414.9

Table 5.1: Stagnation Conditions.

to an unknown vibrational temperature at the surface. [130][131][132]

A kinetic model was developed to provide a theoretical freestream vibrational temperature to perform analysis of the PLIF vibrational thermometry experiments. The model accounts for the V-T and V-V energy exchange among N_2, O_2, and NO as the flow isentropically expands through the ACE nozzle. The model used the flow conditions starting from the throat of a Mach 5.9 nozzle contour to the exit to account for the decreasing pressure, temperature, and velocity profiles along the flow centerline. The stagnation conditions are seen in Table 5.1 and it was assumed the flow was thermalized at the nozzle throat. The temperature, pressure, and velocity expansion profiles are shown in Figure 5.1. The list of vibrational energy exchange reactions considered for the model are seen in Table 5.2. The vibrational relaxation constants were calculated using the equation,

$$k_{V-T,\mathrm{v}=1} = \frac{k_B T}{pt(T)(1 - e^{-\frac{\theta_\mathrm{v}}{T}})} \tag{5.2}$$

where θ_v is the vibrational characteristic temperature *pt(T)* are temperature dependent constants defined by Candler *et al.*[133] The change in the relative NO $X^2\Pi$ (v = 1) fraction due to the V-T energy exchange reactions with the collisional partners, *i* is calculated in the equation,

$$Rate_{V-T,\mathrm{v}} = \sum_i \{[n_{\mathrm{NO,v}=1} n_i k_{V-T} - e^{\frac{-\Delta E}{k_B T}} n_{\mathrm{NO,v}=0} n_i k_{V-T,\mathrm{v}}]\} \tag{5.3}$$

where $n_{\mathrm{NO,v}}$ is the total NO number density (molecules/cm^{-3}), n_i is the total number density of the collisional partner, and ΔE is the energy difference of $NO_{v=0}$ and $NO_{v=1}$.[134][97] A similar equation was used to calculate the change in the relative NO $X^2\Pi$ (v = 1) fraction due to the V-V energy exchange reactions. The temperature dependent $k_{V-V,\mathrm{v}}$ reaction constants were also from

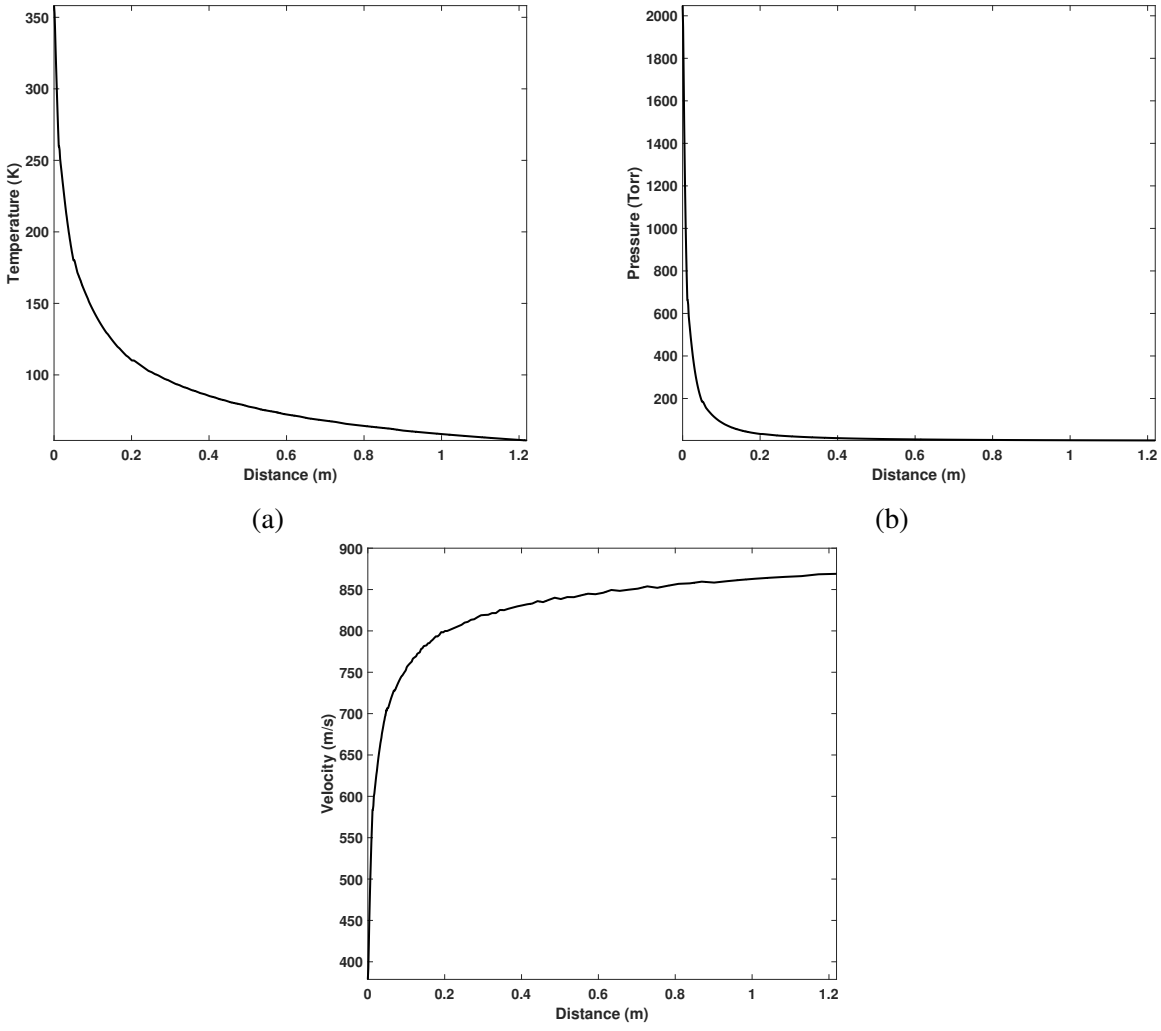

Figure 5.1: Mach 5.9 isentropic expansion profiles of the ACE nozzle. The temperature, pressure, and velocity profiles are shown in Figures a, b, and c, respectively.

Candler *et al.*[133] The calculation moved in a step-wise manner where a set of initial conditions *i.e.* the throat conditions were used to calculate the change in $NO_{v=1}$ number density over a defined time step. The time steps were equidistant to mitigate the rise of any non-physical species populations. The ratio of v = 1:v = 0 fraction for each species was calculated after each time step to determine the vibrational temperature using the Boltzmann equation,

$$\frac{N_{\mathrm{v=1}}}{N_{\mathrm{v=0}}} = e^{-\frac{\Delta E_{vib}}{k_B T}} \tag{5.4}$$

where E_{vib} is the vibrational energy difference between $NO_{v=1}$ and $NO_{v=0}$. This process was propagated along the centerline to produce a species dependent vibrational temperature profile. Figure 5.2 depicts the thermal dependence of the energy exchange reactions shown in Table 5.2. The energy exchange processes for all of the modeled reactions immediately become orders of magnitude less efficient as the temperature decreases. The NO V-T and NO-O_2 V-V energy exchange processes were the most efficient relaxation pathways for the three modeled diatomic systems. The predicted vibrational temperature profiles are shown in Figure 5.3. The O_2 curves were intentionally offset by 3 K for clarity. The solid curves in the plot are the decay profiles resulting from the V-T and V-V pathways as shown in Table 5.2. The dashed curves are the decay profiles without V-T relaxation among the diatomic species. In both cases the N_2 and O_2 curves remained vibrationally frozen at the 358 K throat temperature. The NO vibrational temperature rapidly decreases by 36% and became vibrationally frozen at 230 K. The NO vibrational temperature decay curve was very similar to the temperature curve of the ACE nozzle in Figure 5.1a which implied the relaxation pathways shut down as the temperature rapidly decreased. This rapid NO vibrational decay behavior was also observed in a V-T and V-V kinetic model developed by Andrea Hsu.[135] The dashed curves are intentionally shown to highlight the contribution of the V-T relaxation, specifically the effect of the NO V-T relaxation pathway. Without the V-T relaxation mechanisms the NO vibrational temperature decreased by 10% and becomes frozen at 322 K. The N_2 and O_2 dashed curves were identical relative to the solid curves. The following section will describe in

detail the results of the two-line PLIF vibrational thermometry campaign where a majority of the presented analysis was performed using the predicted freestream vibrational temperature of 230 K. However, the analysis was repeated at an NO freestream vibrational temperature of 358 K to provide an upper limit case for the measured vibrational temperature profiles. Using the above kinetic model, the throat temperature would have to be 516 K to yield a freestream NO vibrational temperature of 358 K.

Vibrational Translational (V-T) Energy Exchange Reactions
$N_{2_{v=1}}+N_2 \underset{k_{-1}}{\overset{k_1}{\longleftrightarrow}} N_2+N_2$
$N_{2_{v=1}}+O_2 \underset{k_{-2}}{\overset{k_2}{\longleftrightarrow}} N_2+O_2$
$N_{2_{v=1}}+NO \underset{k_{-3}}{\overset{k_3}{\longleftrightarrow}} N_2+NO$
$O_{2_{v=1}}+N_2 \underset{k_{-4}}{\overset{k_4}{\longleftrightarrow}} O_2+N_2$
$O_{2_{v=1}}+O_2 \underset{k_{-5}}{\overset{k_5}{\longleftrightarrow}} O_2+O_2$
$O_{2_{v=1}}+NO \underset{k_{-6}}{\overset{k_6}{\longleftrightarrow}} O_2+NO$
$NO_{v=1}+N_2 \underset{k_{-7}}{\overset{k_7}{\longleftrightarrow}} NO+N_2$
$NO_{v=1}+O_2 \underset{k_{-8}}{\overset{k_8}{\longleftrightarrow}} NO+O_2$
$NO_{v=1}+NO \underset{k_{-9}}{\overset{k_9}{\longleftrightarrow}} NO+NO$
Vibrational Vibrational (V-V) Energy Exchange Reactions
$N_{2_{v=1}}+O_2 \underset{k_{-10}}{\overset{k_{10}}{\longleftrightarrow}} N_2+O_{2_{v=1}}$
$N_{2_{v=1}}+NO \underset{k_{-11}}{\overset{k_{11}}{\longleftrightarrow}} N_2+NO_{v=1}$
$NO_{v=1}+O_2 \underset{k_{-12}}{\overset{k_{12}}{\longleftrightarrow}} NO+O_{2_{v=1}}$

Table 5.2: Vibrational relaxation equations.

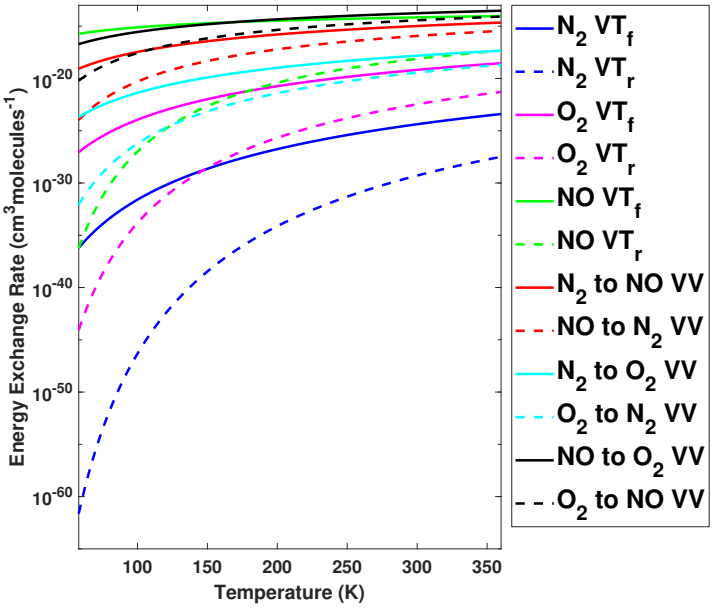

(a)

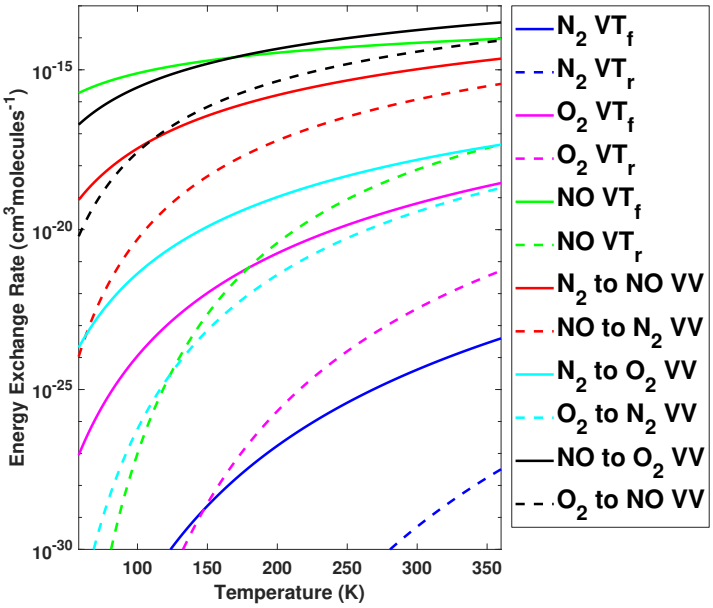

(b)

Figure 5.2: Energy exchange rates as a function of temperature. The subscripts f and r refer to the forward and reverse reaction, respectively. Figure b is zoomed in for clarity.

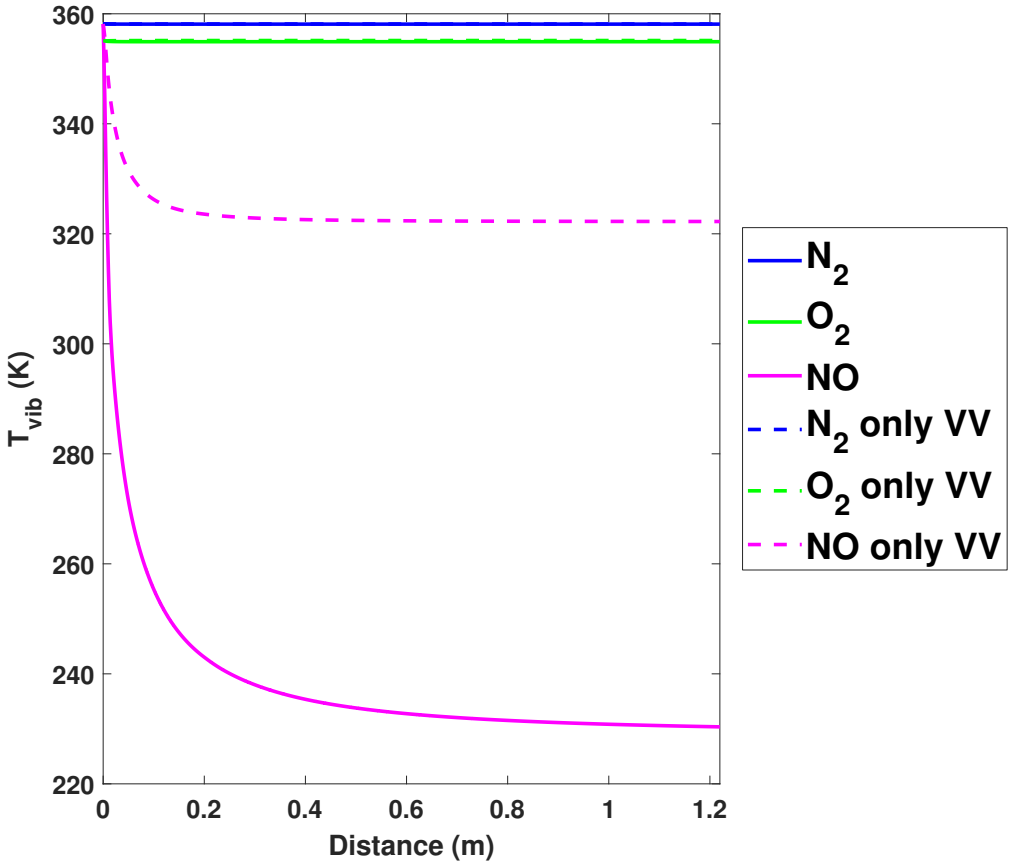

Figure 5.3: Vibrational temperature of N_2, O_2, and NO during isentropic expansion. The solid curves include V-T and V-V energy exchange reactions. The dashed lines include only V-V energy exchange reactions.

5.2 Two-Line PLIF Vibrational Thermometry

During the invisible ink NO LIF velocimetry campaigns, a background signal profile was observed when the NO $A^2\Sigma^+ \leftarrow X^2\Pi$ (v=1) transition was probed. As discussed above, during the isentropic expansion vibrational TNE among the diatomic species produced a two-temperature distribution between the translation/rotational modes and the vibrational modes. The translational and rotational modes were assumed to thermalize on the order of 10 collisions which occurred on the time scale of the isentropic expansion.[117] However, vibrational relaxation was much slower due to the inefficiency of vibrational energy transfer where thermalization can take up to $\sim 1 \times 10^4$ collisions. Additionally, when performing the velocimetry measurements with the plasma on, a nascent NO $X^2\Pi$ (v=1) population was observed. The production of the vibrationally excited NO population was assumed to occur through two possible mechanisms shown in equations

$$\mathrm{NO}\ (\mathrm{v}=0) + e^- \rightarrow \mathrm{NO}^- \rightarrow \mathrm{NO}\ (\mathrm{v}=1) + e^- \tag{5.5}$$

$$\mathrm{NO}\ X^2\Pi + e^- \rightarrow \mathrm{NO}\ A^2\Sigma^+ + e^-. \tag{5.6}$$

Equation 5.5 details the inelastic scattering process where the NO^- anion species is short-lived. Based on a review performed by Song *et al.* the NO vibrational excitation cross section spectrum had resonant features related to the intrinsic NO vibrational energy.[136] The reported resonant absorption energy range for Equation 5.5 was 0.5 to 2 eV with an absorption cross section of $\sim$2-5 $\times\ 10^{-16}$ cm^2. The second mechanism, Equation 5.6, relies on the electron-impact excitation to excite the $A^2\Sigma^+$ (v′ = 0) $\leftarrow X^2\Pi$ (v″ = 0) transition. Following the electronic transition, a nascent NO $X^2\Pi$ (v = 1) population was produced through fluorescence and collisional quenching relaxation pathways. The absorption energy maximum for electronic excitation is 1.9 eV with an electronic absorption cross-section of 1.1×10^{-17} cm^2.[136] Based on experiments performed by Casey Broslawski it was assumed the DC glow-discharge plasma used for the presented experiments had a free electron energy range of 1 to 2 eV. Therefore, it was assumed the predominant mechanism for NO $X^2\Pi$ (v = 1) production was inelastic electron scattering detailed in Equation 5.5.

The combination of the ACE freestream TNE coupled with the NO vibrational TNE produced from the plasma motivated the following vibrational thermometry campaign. Direct measurements related to the vibrational decay within a turbulent boundary layer profile are non-existent which provided further motivation for the following campaign. The experiment was performed similarly as the two-line PLIF rotational thermometry campaign. The vibrational temperature profile was characterized at all three locations along the plate for the laminar and turbulent wake cases. Based on the results of the two-line PLIF rotational thermometry campaign, turbulent trough experiments were not performed. The ACE tunnel conditions were the same as presented in Table 4.2.

The sum frequency mixing laser systems were tuned to the *J* 4.5 of the Q_{21}/R_1 branch $A^2\Sigma^+$ ($v' = 0$) $\leftarrow$ $X^2\Pi_{1/2}$ ($v'' = 0$) transition and *J* 4.5 transition of the Q_{21}/R_1 branch $A^2\Sigma^+$ ($v' = 1$) $\leftarrow$ $X^2\Pi_{1/2}$ ($v'' = 1$) transition. The $NO_{v=1}$ transition was probed first because it was assumed the relaxation of the NO $A^2\Sigma^+$ ($v'' = 1$) state to the NO $X^2\Pi$ ($v' = 0$) state would have a negligible perturbation on the ground state NO $X^2\Pi$ (v = 0) population. The $NO_{v=0}$ population was probed 500 ns later with the second beam. Both beams propagated from the top-down direction of the ACE test section. The beams were overlapped up to 30 mm above the surface and were focused 108 mm from the right side of the flat plate. The beams probed 120 mm, 260 mm, and 405 mm downstream of the leading edge. The beams propagated through the same set of cylindrical arrays to achieve a 2 cm wide 800 μm sheet. The beam power for each laser shot was collected and correlated to the respective acquired image.

The dual ballast system was pressurized to 180 PSIA with a 15% NO in N_2 mixture. A dual camera 10 Hz configuration was employed. The cameras were aligned on opposite sides of the test section and had a field of view of $\sim$30 mm normal to the plate. The cameras were gated directly after the laser scatter and had a relative time delay of 500 ns. The gate width for the camera collecting the $NO_{v=1}$ fluorescence was set to 125 ns and the gate width for the $NO_{v=0}$ fluorescence was 3 ns. The plasma was powered on following the introduction of the N_2/NO gas mixture and turned off after the N_2/NO seeding was stopped. A separate program collected the plasma power during the ACE tunnel run. The experimental setup for two-line PLIF vibrational

thermometry is shown in Figure 5.4.

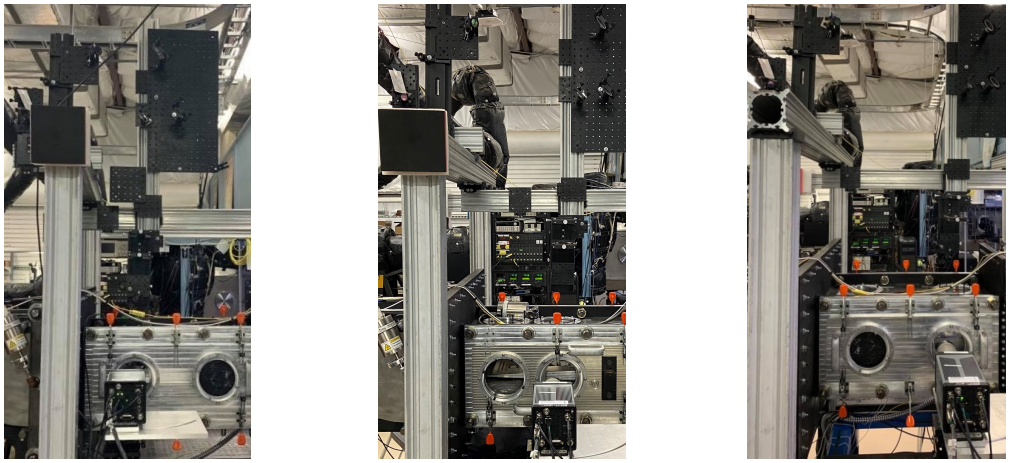

(a) (b) (c)

Figure 5.4: Vibrational thermometry campaign. Figures a, b, and c were the experimental configuration for the 1st, 2nd, and 3rd locations, respectively.

The initial probe laser was intentionally chosen to excite the $A^2\Sigma^+$ ($v' = 1$) $\leftarrow$ $X^2\Pi_{1/2}$ ($v'' = 1$) transition. Under the current experimental conditions the relaxation of the NO $A^2\Sigma^+$ ($v' = 1$) state would yield a NO $X^2\Pi$ ($v = 0$) population 10^{-8} times smaller relative to the freestream NO $X^2\Pi$ ($v = 0$) population. All experiments were performed with $\sim$50 μm resolution and collected an area of $\sim$25 mm $\times$ 10 mm normal to the surface. The 1st location fluorescence experiments were performed beneath the leading edge bow shock because the flow behavior above the bow shock was well characterized as shown in Section 4.4.3. The L1 and LP1 experiments were useful in understanding the initial conditions immediately downstream of the plasma. Representative fluorescent images following the $A^2\Sigma^+$ ($v' = 1$) $\leftarrow$ $X^2\Pi_{1/2}$ ($v'' = 1$) transition for the L1 and LP1 experiments are presented in Figure 5.5. The fluorescent images for the $A^2\Sigma^+$ ($v' = 0$) $\leftarrow$ $X^2\Pi_{1/2}$ ($v'' = 0$) are not shown for brevity; however, the profile was similar to the fluorescent images shown in Section 4.4.3. In both experiments the freestream NO $X^2\Pi$ ($v = 1$) population was clearly observed with a gradual decrease in the S/N ratio towards the surface. The L1 experiment had a S/N ratio near the dark count regime of the collected images. This was attributed to the relatively low NO

$X^2\Pi$ (v = 1) population coupled with the low density profile directly above the surface. The nascent NO $X^2\Pi$ (v = 1) population near the surface was immediately evident when comparing the L1 and LP1 fluorescent images. At the 1st location the NO $X^2\Pi$ (v = 1) population was observed to be $\sim$2 mm normal to the surface. Similar to the rotational thermometry results the vibrational temperature profiles related to L1 and LP1 experiments are shown in Figures 5.6 and 5.7, respectively. As seen in Figure 5.6b the vibrational temperature gradually decreased toward the surface with a local minimum of $\sim$210 K 2 mm above the surface; however, it recovered to a wall temperature of 220 K. The observed temperature decrease was unexpected when considering the limiting cases of a vibrational no-slip versus slip at the surface. In the no-slip case the vibrational temperature would thermalize to the 360 K wall temperature as seen in the rotational thermometry results. In a full slip case the vibrational energy transfer would be highly inefficient near the surface and the vibrational temperature would be frozen from the freestream to the surface. The L1 fluctuation map illustrated a peak in the vibrational temperature fluctuations of 4% at 5 mm normal to the surface. Nearly 85% to 95% of all the vibrational temperature values were accepted following the 2σ statistical treatment. This was the case for all of the laminar experiments. There was not an observed decrease in the accepted temperature values towards the surface unlike the trend observed in the rotational thermometry results. The LP1 temperature map exhibited a clear increase in the vibrational temperature directly above the plate surface. There was a rapid temperature rise 2.5 mm normal to the surface with a peak vibrational temperature of 275 K at $\sim$0.5 mm. Using the measured LP1 temperature profile, the height of the cathode layer directly upstream was assumed to be on the order of 2.5 to 3 mm. The LP1 temperature uncertainty map, Figure 5.7c, further supports this because there was a rapid decrease in the relative temperature uncertainty below 2 mm due to the increased S/N ratio. The temperature fluctuations in Figure 5.7d showed a similar profile as the L1 fluctuations because there was a local maximum at 5 mm normal to the surface. However, there appeared to be a second local fluctuation maximum of 4% located $\sim$2 mm above the surface.

The L2 and LP2 experiments yielded similar results observed in the 1st location laminar ex-

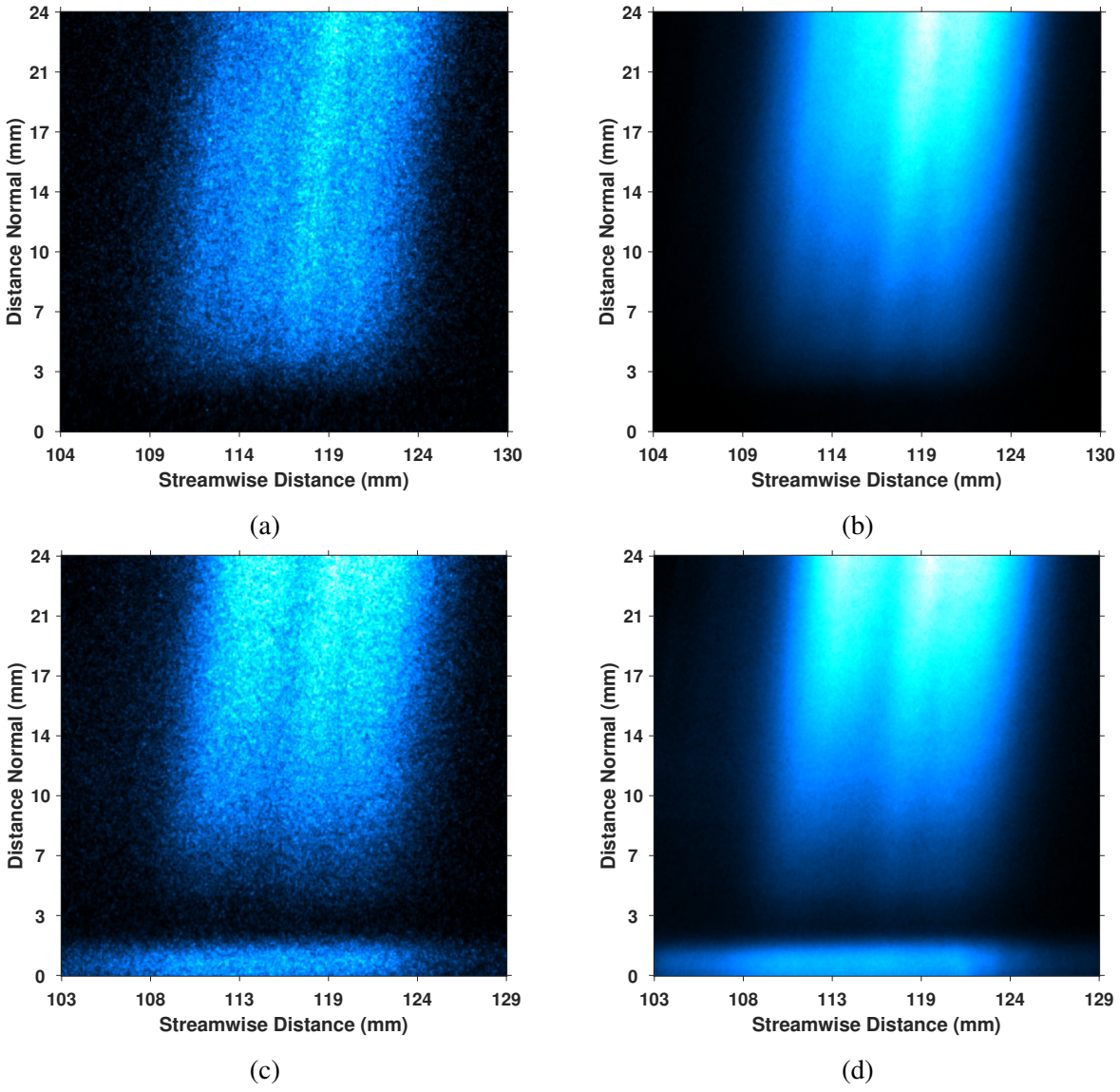

Figure 5.5: Representative L1 and LP1 images. Figures a and c are instantaneous images relating to L1 and LP1, respectively. Figures b and d are average images relating to L1 and LP1, respectively.

periments with subtle differences. Representative fluorescent images of the 2nd location laminar experiments are shown in Figures 5.8 and 5.9. The NO TNE observed in the LP1 case was observed in the LP2 experiment; however, the NO $X^2\Pi$ (v = 1) population broadened to 3 mm. The broadening origin of the NO TNE layer will be discussed in detail later. The L2 fluorescent images was similar to the L1 fluorescent images in terms of the NO $X^2\Pi$ (v = 1) S/N ratio decreasing

towards the surface. The thermal profiles for the L2 and LP2 experiments are shown in Figures 5.9 and 5.10. The L2 vibrational temperature again decreased towards the surface with a minimum vibrational temperature of ∼215 K. There was a noticeable temperature decrease below 4 mm with a local minimum of ∼215 K 2 mm above the surface. The L2 freestream vibrational temperature fluctuations were on the order of 1% to 2% and gradually increased toward the peak temperature fluctuation of 4% maximum 5 mm above the surface. The fluctuations below 5 mm were were on the order of 3% to 4% which was larger than the L1 case. The LP2 temperature peaked at ∼260 K 2 mm above the surface. The relative temperature uncertainty map, Figure 5.10c, provides a clear depiction of the location of the NO $X^2\Pi$ (v = 1) population based on the rapid decrease in the uncertainty below 4.5 mm. The freestream LP2 temperature fluctuations were 0.5% to 2.5% and increased to 4% at 5 mm. Below the 5 mm point the fluctuations decreased sharply to ∼2.5% near the wall.

The 3rd location measurements were very similar to the flow behaviors observed at the 1st and 2nd locations. Representative fluorescent images are shown in Figure 5.11 for the L3 and LP3 experiments. The same trend of a decreasing NO $X^2\Pi$ (v = 1) population towards the surface was observed again at the 3rd location. The LP3 NO $X^2\Pi$ (v = 1) population broadened to 4 mm which was consistent with the thermal boundary layer height observed for the rotational thermometry profiles. It was hypothesized the NO $X^2\Pi$ (v = 1) population may become entrained within the laminar boundary layer forming along the plate. The thermal profiles for the L3 and LP3 measurements are shown in Figures 5.12 and 5.13. The L3 vibrational temperature also decreased towards the surface with a local minimum temperature of ∼215 K 2 mm above the surface. The freestream temperature fluctuations were 1% to 2% with a peak of 4.5% at 6 mm, but the fluctuations appeared to decrease towards the surface as seen in the L1 and L2 experiments. The LP3 vibrational thermal boundary layer spanned ∼4.5 mm above the surface with a peak temperature of ∼250 K 2.5 mm above the surface. The LP3 relative temperature uncertainty map had a rapid decrease in the uncertainty below 5 mm. The freestream temperature fluctuations again were on the order of 2% with an increase to 4% at 6 mm and again rapidly decreased to ∼2.5% at the surface. The

curves in Figure 5.14 help in understanding the large scale NO vibrational temperature behavior along the plate.

Horizontally averaged temperature profiles with vibrational freestream temperatures of 230 K and 358 K are shown in Figures 5.14a and 5.14b, respectively. The two different freestream temperature plots show near identical trends, but with differing absolute temperatures. As mentioned earlier the L1 temperature profile did not agree with the two limiting cases of vibrational no-slip and slip. The L1 freestream vibrational temperature had a $\sim$5% temperature decrease from $\sim$17 mm to 5 mm and another $\sim$5% from 5 mm to 2.5 mm. The rapid decrease near the surface was unexpected, but at the wall the temperature appeared to recover to within 5% of the freestream temperature. The L2 and L3 profiles also had temperature decreases of 3% to 7% from 17 mm to 5 mm where the L1, L2, and L3 uncertainty bars overlap one another in the region. It should be noted the presented error bars resulted from the horizontal averaging of an average temperature map, so the error bars may be broader. The L2 temperature below 5 mm did appear to have an additional 5% temperature decrease from 5 mm to 2.5 mm and recover at the wall similar to the L1 temperature profile. The L3 temperature below 5 mm did not decrease further unlike the L1 and L2. The origin of the temperature decrease from 17 mm to 5 mm may be due to spatial non-uniformities in the vibrational temperature produced by the ACE nozzle. Spatial non-uniformities within a hypersonic flow is not uncommon and has been a focus of several studies.[124][130][137][138] Semper performed a freestream pitot survey of the ACE core at Mach 6 and observed a 0.5% decrease in the Mach number from the core toward the top and bottom of the ACE test section.[46] The leading edge of the flat plate was mounted 91 mm from the test section floor, so the presented vibrational temperature measurement may be a representation of a vibrationally frozen thermal gradient. A freestream vibrational temperature experiment was not conducted to support this hypothesis. The second possibility of the observed vibrational temperature decrease may be due to the V-T and V-V energy exchange processes. Due to the temperature dependence of these V-T and V-V rates they may turn back on closer to the surface. Based on the rotational thermometry results in Section 4.4.3 there was a gradual increase in the temperature outside the boundary layer followed by a

rapid temperature increase below 5 mm. Figure 5.15 illustrate the V-T and V-V rate dependence normal to the surface. The plots are zoomed in to focus on the more efficient energy exchange reactions *i.e.* as NO V-T and NO-O_2 V-V. As the temperature increased directly above the surface, the energy exchange rates increased by orders of magnitude which may account for the relatively large decrease in the vibrational temperature between 2.5 mm to 5 mm. Below 2.5 mm there was an observed temperature recovery which would indicate there was vibrational energy exchange at the surface causing a local temperature increase.

The laminar experiments with the plasma on *i.e.* LP1, LP2, and LP3 the freestream temperature profiles exhibit the same decrease as seen in the plasma off cases. However, the vibrational temperature profiles near the surface illustrate the NO vibrational thermal perturbation introduced by the plasma. The LP1 vibrational temperature had a rapid rise at 3 mm and peaked at 275 K for the 230 K freestream case and 485 K for the 358 K freestream case. The LP2 temperature profile broadened to $\sim$4 mm and had a peak temperature of 260 K or 435 K depending on the freestream temperature. Comparing the LP1 and LP2 temperatures the NO $X^2\Pi$ (v = 1) population appeared to be following the growth of the laminar boundary layer. The LP3 profile broadened further to $\sim$5 mm and its maximum temperature decreased to 250 K for the 230 K freestream case. The NO $X^2\Pi$ (v = 1) population introduced near the leading edge appeared to diffuse through the laminar boundary layer as it moved along the length of the plate. Using Fick's law of diffusion,

$$x = \sqrt{2Dt} \tag{5.7}$$

$$\text{where } D = \frac{2}{3}\sqrt{\frac{k_B^3}{\pi^3 m}}\frac{T^{\frac{3}{2}}}{Pd^2} \tag{5.8}$$

and the rotational thermometry profiles, predictive diffusion profiles were generated. For Equation 5.7, x is the diffused distance, D is the diffusion coefficient, and t is the elapsed time. In Equation 5.8, m is the molecular mass, T is the temperature, P is the pressure, and d is the molecular diameter. Figure 5.16 displays the estimated diffusion distances using the L3 and LP3 rotational thermometry profiles. Two elapsed times are shown to illustrate the range of diffusion along the

plate. The predicted diffusion through the boundary layer from the 1st location to the 3^{rd} location was on the order of 1 to 2 mm which agreed with the observed vibrational thermal boundary layer broadening. The horizontally averaged fluctuation profiles shown in Figures 5.14 and 5.15 both exhibited a gradual increase in the fluctuations toward the surface. For the L1, LP1, L2, and LP2 the fluctuations peaked at 3.5% to 4% 5 mm normal to the surface. Based on the rotational thermometry results the temperature rapidly increased at this point which was attributed to a convolution of the entropy and laminar boundary layer. Therefore, the interface between the freestream and these two layers may be responsible for the observed rise in the temperature fluctuations. The L1, L2, and LP2 fluctuations then decreased below 5 mm to $\sim$2.5% to 3%. The LP1 fluctuation profile had a local fluctuation maximum at 2 mm which was near the edge of the nascent NO $X^2\Pi$ (v = 1) population. The L3 and LP3 fluctuation profiles exhibited the same gradual fluctuation increase; however, the peak was at $\sim$6.5 mm. The L3 fluctuations rapidly decreased near the surface; however, another local fluctuation maximum appeared at 3 mm. The origin of the second LP3 maximum was not immediately known.

A vibrational thermometry campaign was also performed to understand how the turbulent mixing process affected the nascent NO $X^2\Pi$ (v = 1) population. The TW1 and TWP1 freestream NO $X^2\Pi$ (v = 1) profile was very similar to the previous results presented for the laminar cases. Representative fluorescent images are shown for TW1 and TWP1 in Figure 5.17. The shear layer at $\sim$11 mm was visible for both the TW1 and TWP1 experiments; however, the trip shock at $\sim$20 mm was less pronounced and difficult to visualize. The instantaneous fluorescent images in Figures 5.17a and 5.17c both exhibited a wavy interface at 4 mm between the freestream and the boundary layer. Below the interface was a rapid S/N decrease for the TW1 experiment which was consistent with the L1 results. The TWP1 fluorescent image displayed a defined NO $X^2\Pi$ (v = 1) population spanning 1.5 mm above the surface. There was an additional faint wave-like structure spanning from 1.5 mm to 4 mm as seen in Figure 5.17. The resulting TW1 and TWP1 thermal profiles are shown in Figures 5.18 and 5.19. In the TW1 temperature map, Figure 5.18b, the trip shock and shear layer were distinguishable at $\sim$22 mm and $\sim$13 mm, respectively, above the surface. Across the

TW1 trip shock there was a slight decrease in the vibrational temperature; however, it appeared to recover prior to the shear layer. Below the shear layer there was a gradual temperature decrease to 217 K at 4.5 mm. At 4.5 mm the temperature rapidly decreased to 210 K with a slight temperature recovery at the surface. The same behavior was seen for the L1, L2, and L3 experiments. This was again attributed to a possible increase in the V-T and V-V energy exchange processes due to the temperature increase within the boundary layer. The TW1 fluctuation profile was consistent with the L1 profile where the fluctuations gradually increased toward the surface and peaking at 4% 5 mm above the surface. Again the relative number of accepted TW1 temperature values was 85% to 95% for the entire map which was consistent for the presented turbulent vibrational thermometry maps. The TWP1 also displayed a slight temperature decrease across the trip shock and shear layer. The temperature further decreased below the shear layer to $\sim$210 K; however, given the uncertainty in Figure 5.19, the behavior was similar to the TW1 uncertainty profile. There was a rapid temperature increase beginning at 4 mm and peaking at $\sim$270 K at 0.5 mm above the surface. The vibrational thermal boundary was broadened relative to the LP1 thermal boundary layer which may be indicative of some initial mixing due to the trip geometries. The fluctuation profile shared some similarities with the other 1st location measurements, but contained additional structures. Below the trip shock and shear layer there were increases in the temperature fluctuations leading again to a local fluctuation maximum of 4% from 5 mm to 7 mm above the surface. There were two additional local fluctuation maximums located at $\sim$4 mm and $\sim$2 mm. The 4 mm fluctuation maximum was in the same location of the additional structure observed in the fluorescent images. This may be due to nascent wake structures introduced by the upstream trip geometries.

The TW2 and TWP2 measurements provided insight to the turbulent flow behavior at the 2nd location. The representative images shown in Figure 5.20 displayed intricate turbulent structures spanning 10 mm normal to the surface. One of the more interesting observations was seen in Figure 5.20d where the nascent NO $X^2\Pi$ (v = 1) population was difficult to distinguish. Unlike the LP2 and LP3 where the NO $X^2\Pi$ (v = 1) population was identifiable, the TWP2 image suggests the NO $X^2\Pi$ (v = 1) population experienced significant mixing. When comparing Figures 5.20b and

5.20d there was still evidence of a higher NO $X^2\Pi$ (v = 1) population near the surface. The TW2 temperature profile showed a gradual 5% temperature decrease from the freestream to the surface with no discernible local temperature minimum near the surface. Recall the L1, L2, and TW1 all had local temperature minimums below 5 mm; however, the TWP2 temperature was somewhat thermally consistent from the freestream to the surface. This may be due to the observed turbulent mixing seen at location 2 where warmer freestream elements mix with the colder elements closer to the surface. The TW2 fluctuation profile clearly illustrated the extent of the turbulent mixing behavior. There was a rise in the fluctuations to $\sim$4% at 9 mm and that remained constant all the way to the surface. The TWP2 thermal boundary layer was thicker at $\sim$8 mm and the maximum temperature of 255 K was observed at the surface. The turbulent mixing produced a more diffuse NO $X^2\Pi$ (v = 1) population relative to the the other profiles discussed thus far. The fluctuation profile was similar to the TW2 profile where the fluctuations began to rise to $\sim$4% at 9 mm. However, directly above the surface, <0.5 mm, the temperature fluctuations increased rapidly to $\sim$9% suggesting highly turbulent transitional behavior at this location. The following TW3 and TWP3 measurements provided information related to the vibrational energy transported through a fully turbulent boundary layer. The fluorescent images in Figure 5.23 provided excellent images of the turbulent structures spanning nearly 14 mm above the surface. Similar to the TWP2 results, the NO $X^2\Pi$ (v = 1) population was diffuse near the surface due to the turbulent mixing along the length of the plate. The TW3 temperature map exhibited a nearly uniform temperature of 230 K from the freestream to the plate surface. Due to turbulent mixing, the vibrational temperature profile appeared to thermalize along the length of the plate. The turbulent mixing appeared to extend to 12 mm above the surface based on the TW3 fluctuation map, Figure 5.24d. The TWP3 temperature map exhibited a vibrational thermal boundary layer of $\sim$10 mm with a peak temperature of 240 K 2.5 mm above the surface. Based on the diffuse NO $X^2\Pi$ (v = 1) population near the surface, it was postulated that the bulk of the temperature decrease was due to turbulent mixing and not V-T/V-V energy transfer. This was consistent with the rotational thermometry results because the absolute rotational temperature was unaffected by the plasma being on or off. If there was significant rota-

tional heating observed in the boundary layer then the V-T and V-V energy transfer mechanisms would have a greater impact along the plate. Similar to the horizontally averaged temperature and fluctuation plots for the laminar experiments, Figure 5.26 was generated to visualize the large-scale flow behavior. The TW1 temperature curve appeared nearly identical to the L1 temperature curve where there was a rapid decrease in the vibrational temperature at 4 mm. The TW1, ,TW2 and TW3 temperature curves appeared to reach a wall temperature of 225 K. Additionally, the TW2 and TW3 temperatures directly above the surface appeared to recover from the TW1 temperature decrease. The TWP1, TWP2, and TWP3 temperature curves show a clear thermal perturbation from the plasma. The TWP1 temperature curve peaks at 250 K at 0.5 mm above the surface and approaches a wall temperature of 270 K. There was an additional feature beginning at 3 mm where there appeared to be a convolution between two different thermal curves. The additional structure was attributed to the NO $X^2\Pi$ (v = 1) population seen in Figure 5.17c which may be due to turbulent mixing caused by the upstream trip geometries. Downstream the TWP2 temperature curve there was an immediate decrease in the peak vibrational temperature, but an overall broadening of the vibrational thermal boundary layer to 10 mm. The boundary layer reached a peak temperature of 255 K at the wall. The decrease in the observed temperature curve was attributed to large scale turbulent mixing. The final temperature curve, TWP3, appeared to have a thermal boundary layer of $\sim$12 mm and had a maximum temperature of 245 K $\sim$2.5 mm from the surface. The TWP3 wall temperature was 235 K which followed the trend of decreasing temperature along the plate for the plasma on experiments. Based on the turbulent behavior the vibrational temperature within the boundary layer appeared to be approaching equilibrium with the freestream temperature. The TW1, TW2, and TW3 fluctuation plots all showed a gradual increase in fluctuations toward the surface. Below 5 mm the fluctuations began to grow along the plate and peaked at 4% to 5% near the surface for the TW3 experiment. The peak at the surface was unexpected because the fluid closest to the surface for a turbulent boundary should have laminar behavior. The disconnect between theory and the empirical results may be due to the relatively low S/N at the surface which gave rise to large uncertainty bars. When comparing the TW1 and TW3 fluctuation curves, it was

apparent the fluctuating layer was broadening due to the growth of the turbulent boundary layer. The TWP1, TWP2, and TWP3 fluctuation curves had unexpected behavior near the surface. The TWP1 curve had multiple fluctuation maximums which were observed in the relative fluctuation map discussed earlier. The peak fluctuation at 4% 5 mm above the surface was attributed to the interface between the freestream and convoluted entropy and turbulent boundary layers. Recall the second fluctuation maximum at 4 mm was attributed to the additional wake structure observed in the TWP1 fluorescent image. The origin of the third fluctuation maximum was unknown, but may be due to a shear layer interface developing from the trip geometries. The TWP2 fluctuation curve gradually increased and had a local fluctuation maximum of 3.5% at 8 mm above the surface. There was a rapid increase in the fluctuations at the surface in which the fluctuations increased to 8% in which the origin of it was unknown. The final fluctuation curve, TWP3, had a similar fluctuation curve as TWP2 where the fluctuations had a local maximum of 3.5% 8 mm above the surface. However, the fluctuations only increased slightly toward the surface to 3%. Again this was unexpected given because the flow near the surface of a fully turbulent boundary layer is the laminar sub-layer. The final plots in Figure 5.27 are a representation of the temperature dependent energy exchange processes. However, the bulk of the energy transport was attributed to the turbulent mixing occurring along the length of the plate.

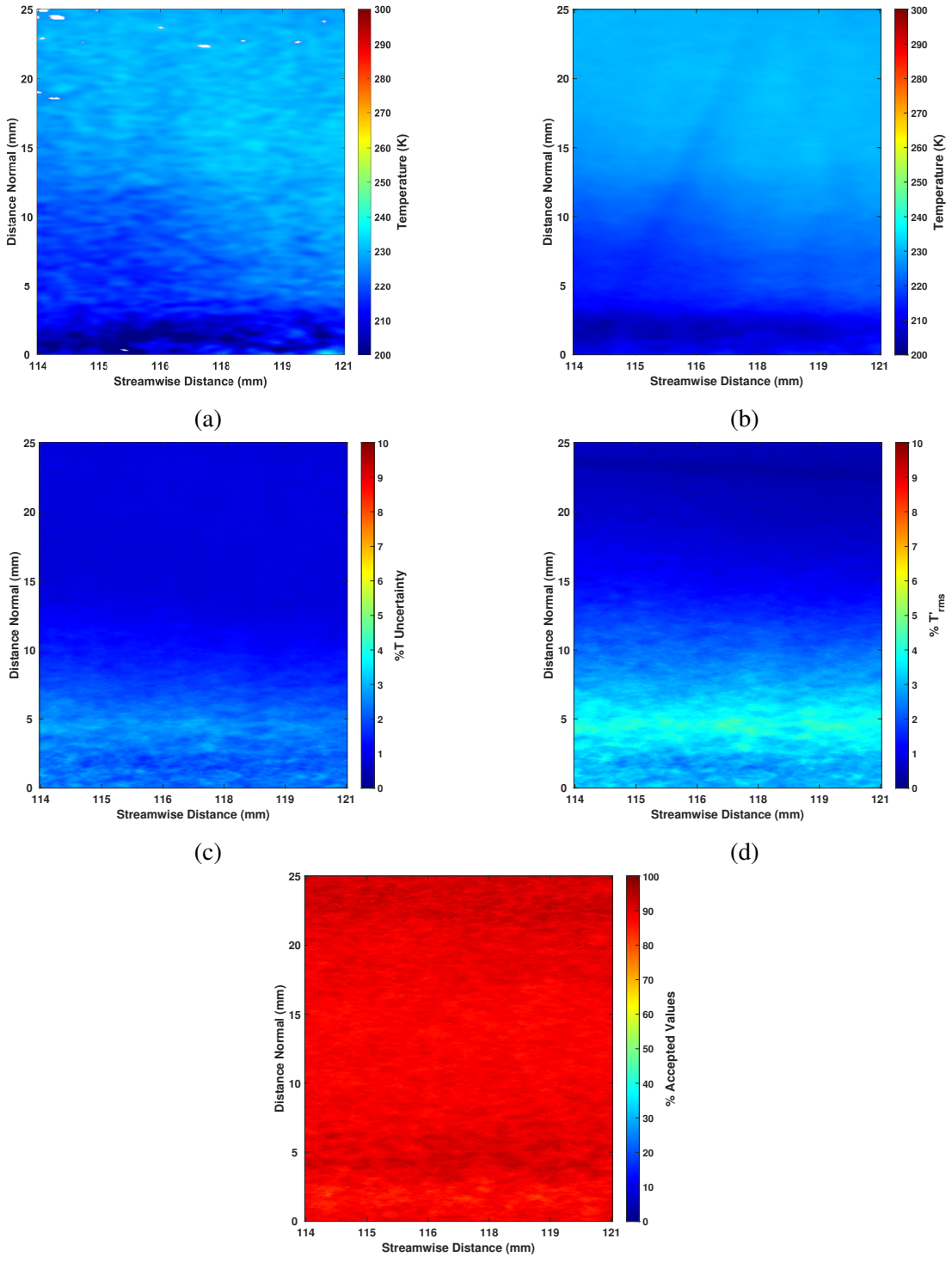

Figure 5.6: Vibrational thermal L1 profiles. Figure a is a representative instantaneous temperature map. Figure b is the average temperature map. Figure c is the relative temperature uncertainty map. Figure d is the relative temperature fluctuation map. Figure e is the relative accepted number of values map.

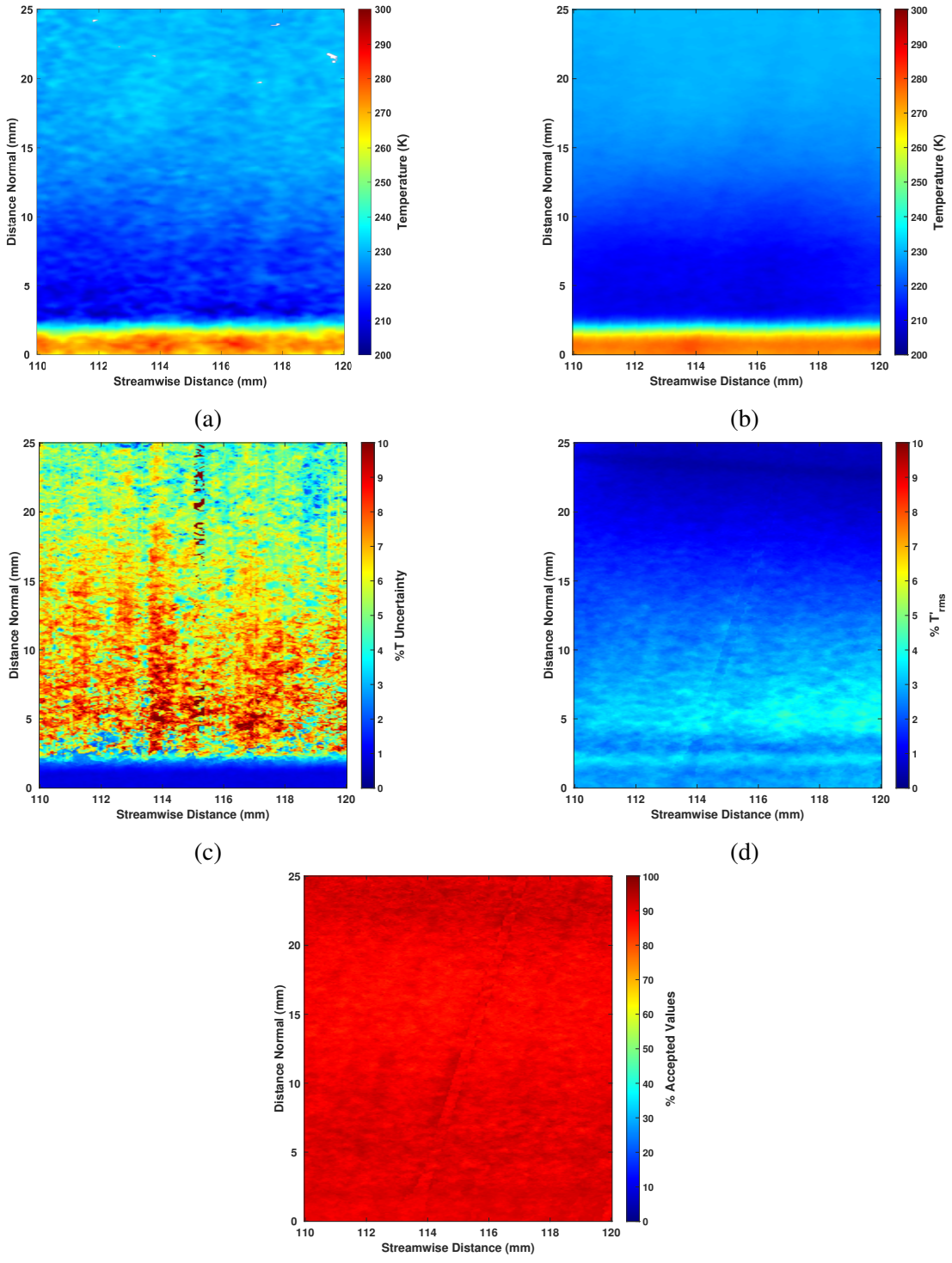

Figure 5.7: Vibrational thermal LP1 profiles. Figure a is a representative instantaneous temperature map. Figure b is the average temperature map. Figure c is the relative temperature uncertainty map. Figure d is the relative temperature fluctuation map. Figure e is the relative accepted number of values map.

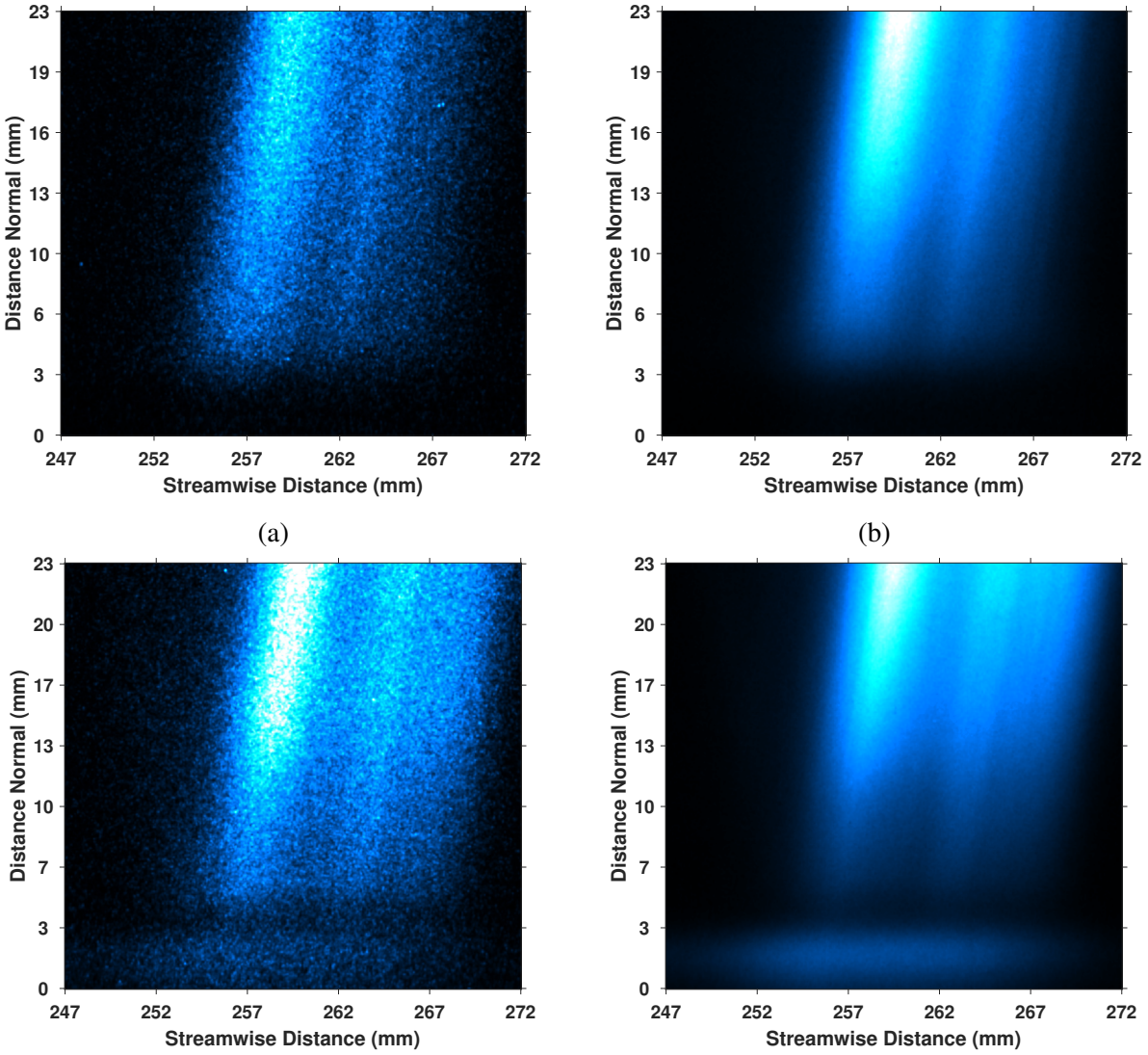

Figure 5.8: Representative L2 and LP2 images. Figures a and c are instantaneous images relating to L2 and LP2, respectively. Figures b and d are average images relating to L2 and LP2, respectively.

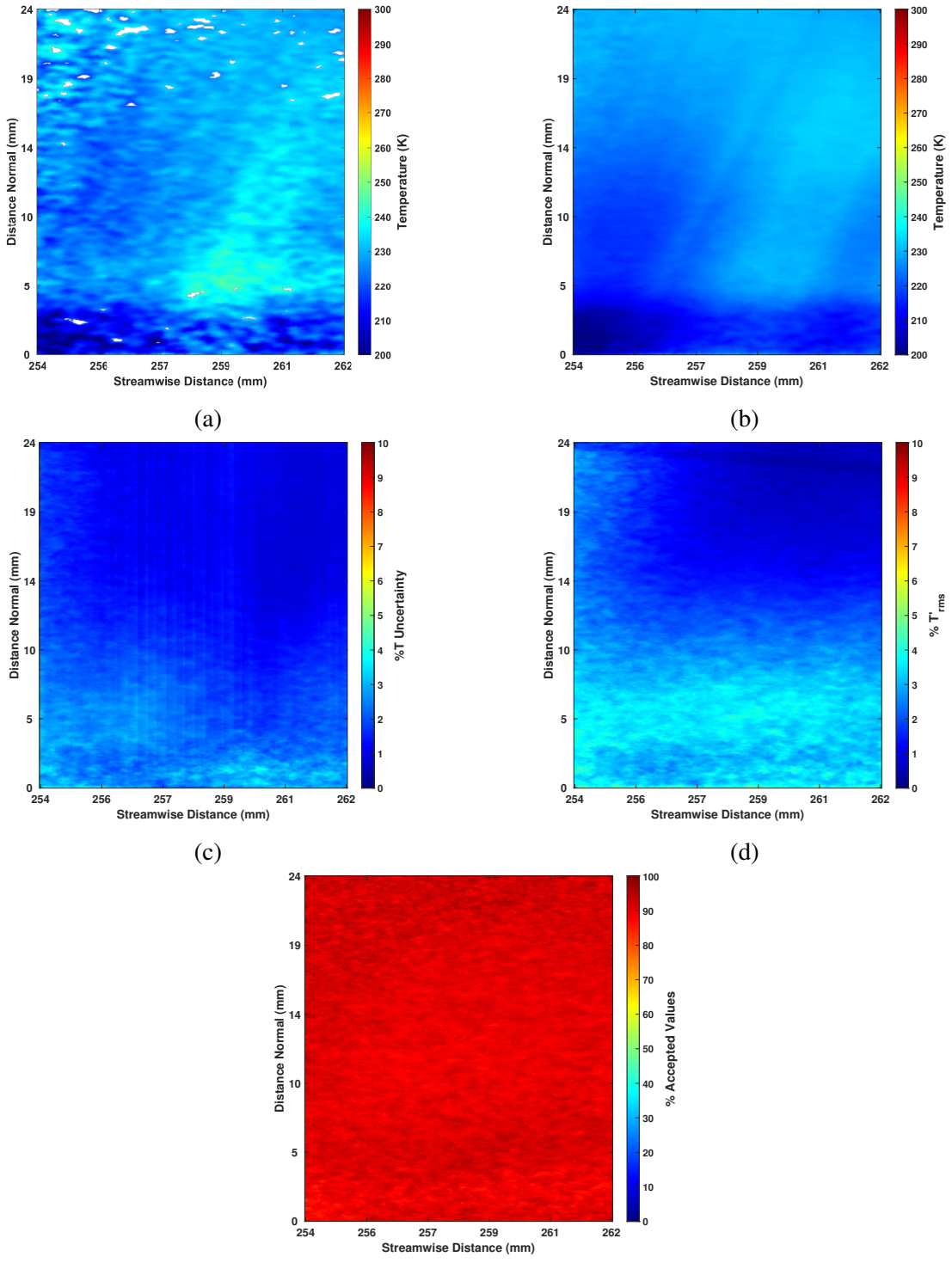

Figure 5.9: Vibrational thermal L2 profiles. Figure a is a representative instantaneous temperature map. Figure b is the average temperature map. Figure c is the relative temperature uncertainty map. Figure d is the relative temperature fluctuation map. Figure e is the relative accepted number of values map.

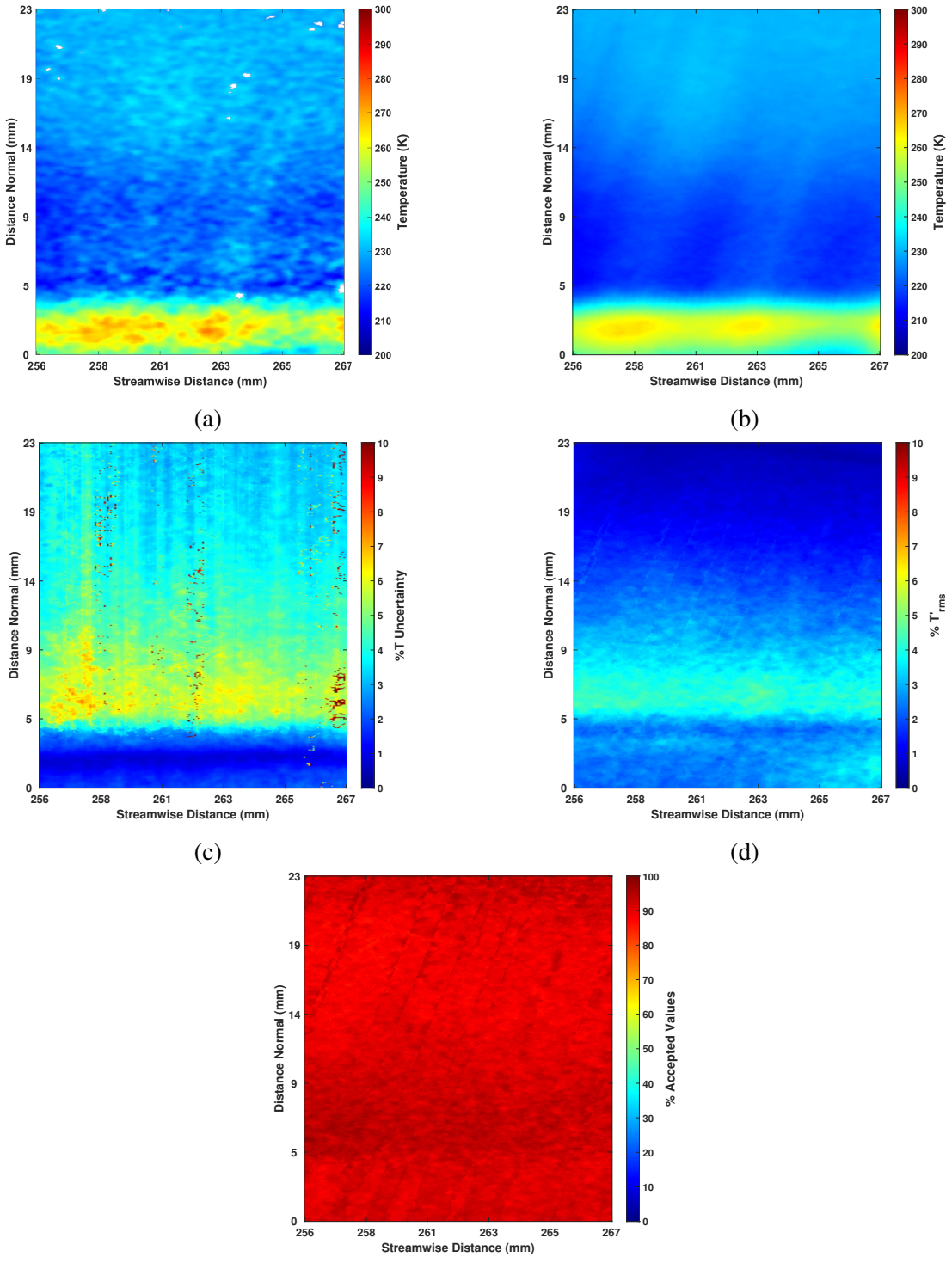

Figure 5.10: Vibrational thermal LP2 profiles. Figure a is a representative instantaneous temperature map. Figure b is the average temperature map. Figure c is the relative temperature uncertainty map. Figure d is the relative temperature fluctuation map. Figure e is the relative accepted number of values map.

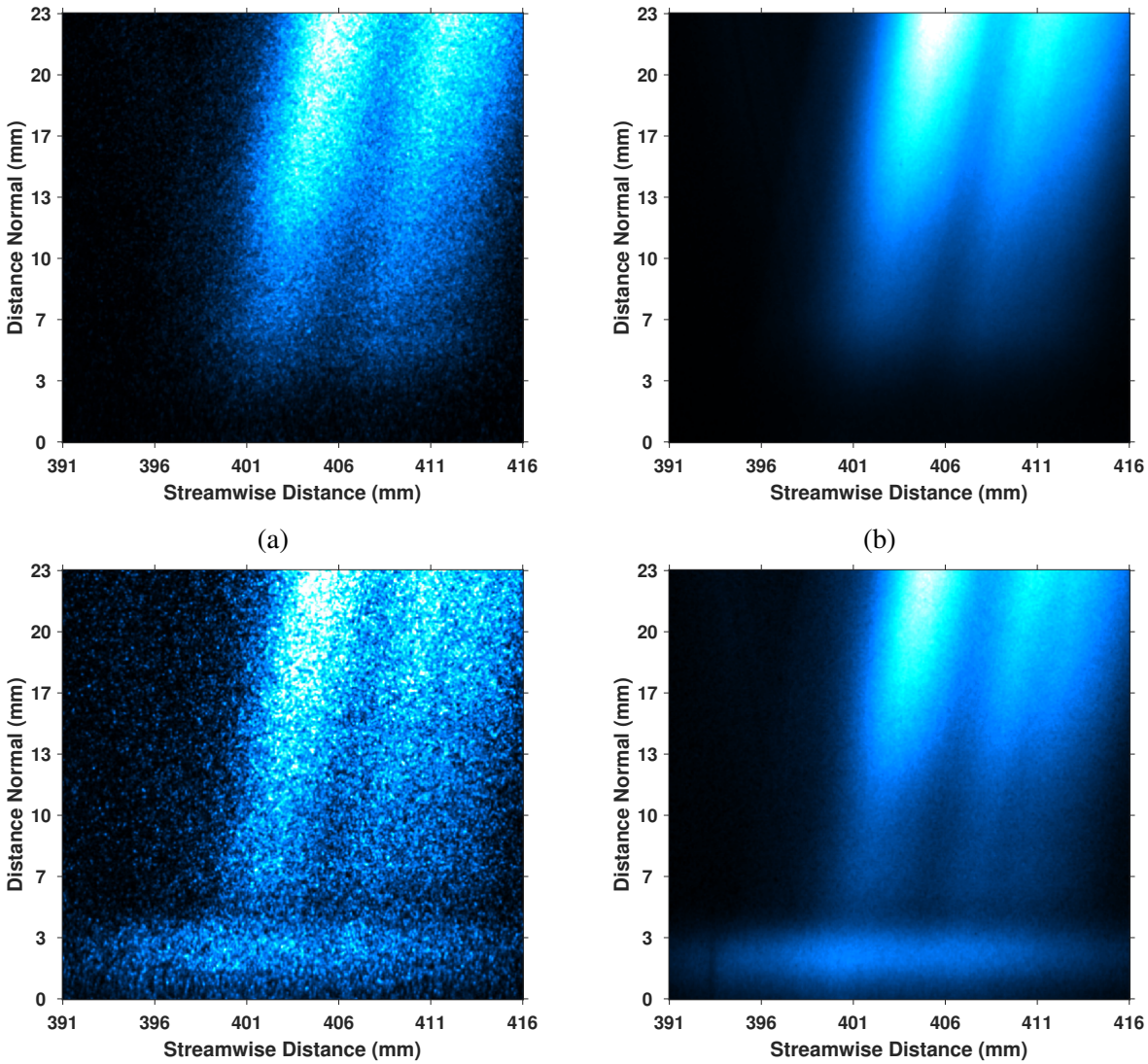

Figure 5.11: Representative L3 and LP3 images. Figure a and c are instantaneous images relating to L3 and LP3, respectively. Figure b and d are average images relating to L3 and LP3, respectively.

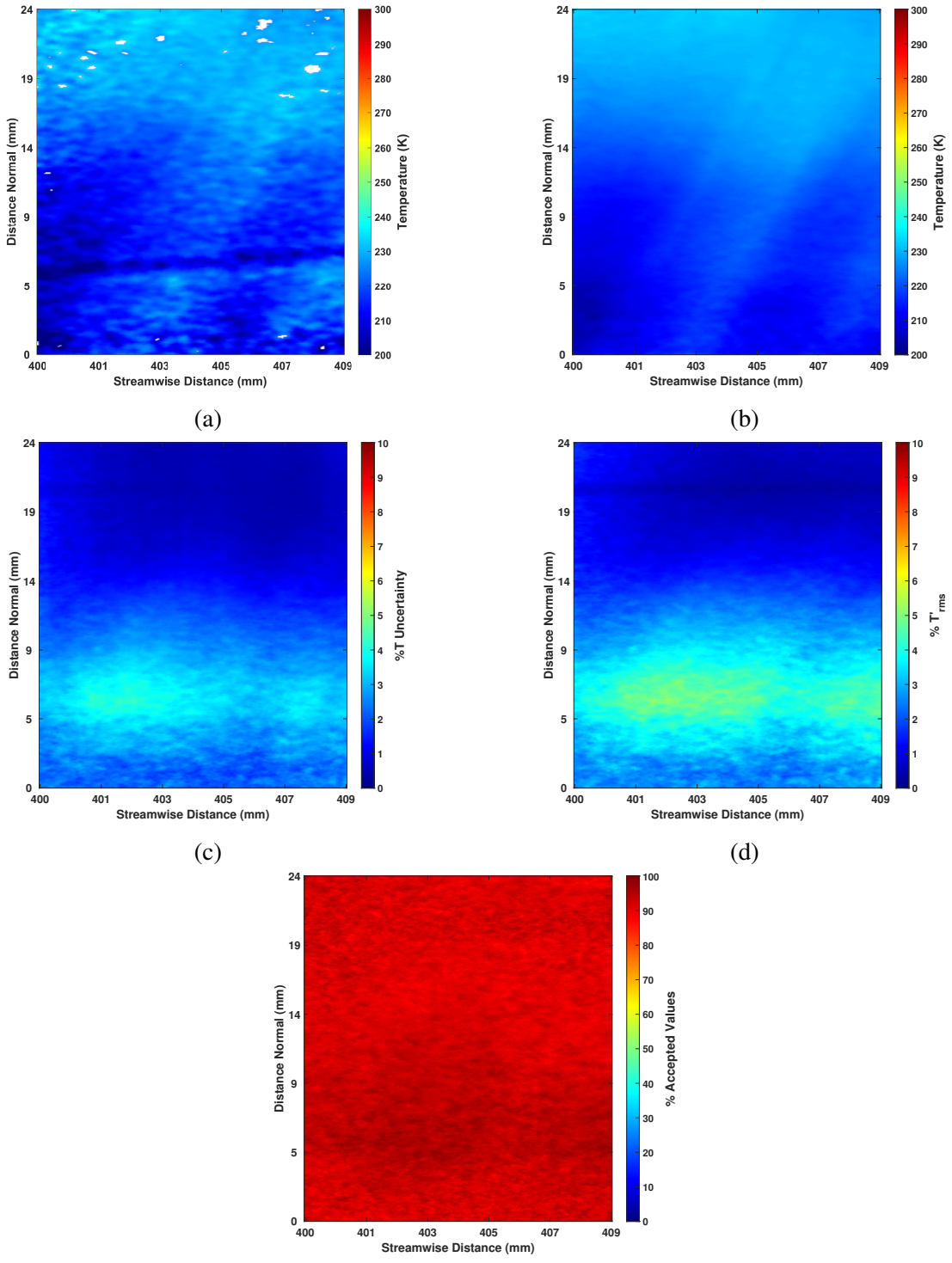

Figure 5.12: Vibrational thermal L3 profiles. Figure a is a representative instantaneous temperature map. Figure b is the average temperature map. Figure c is the relative temperature uncertainty map. Figure d is the relative temperature fluctuation map. Figure e is the relative accepted number of values map.

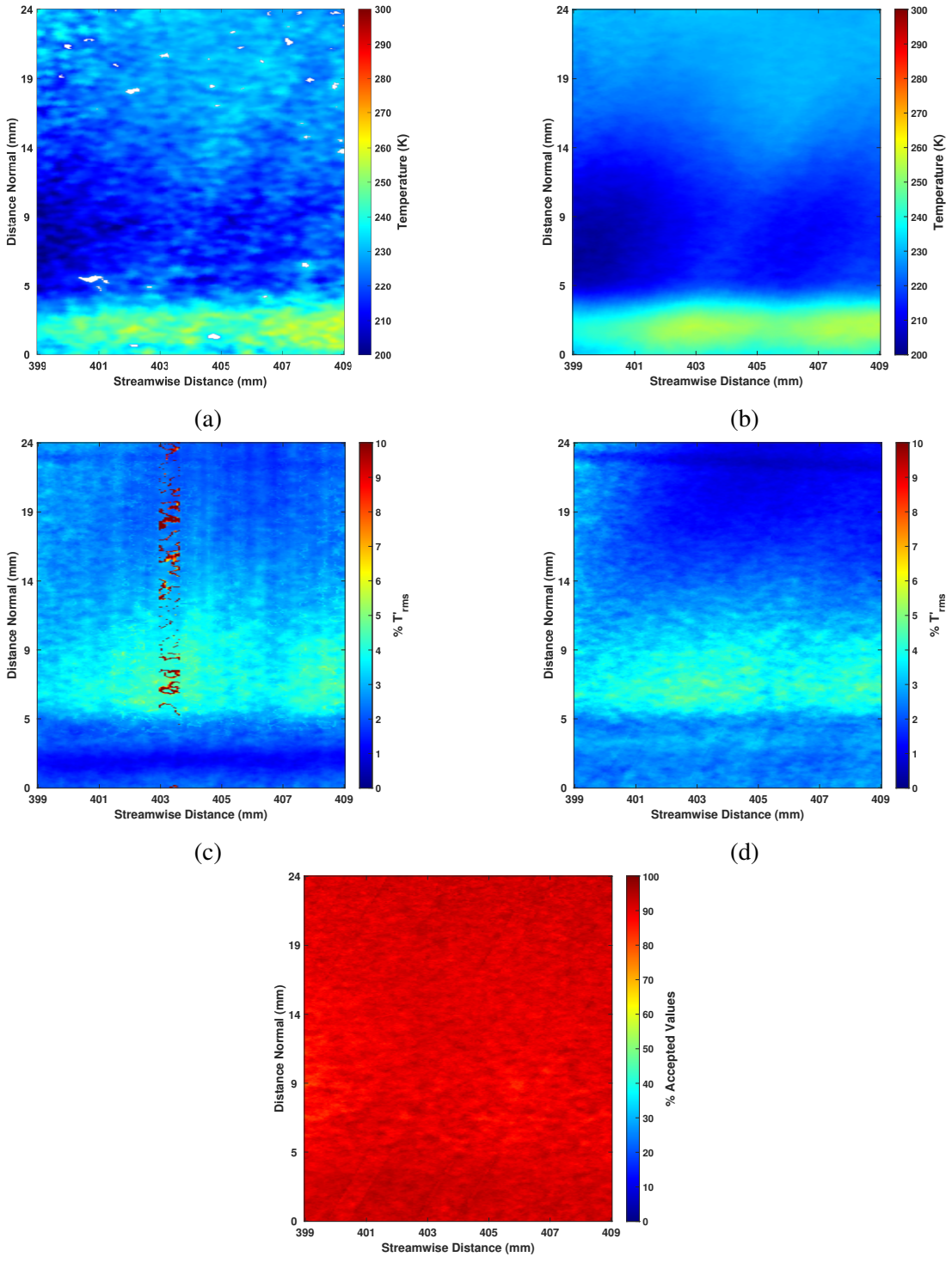

Figure 5.13: Vibrational thermal LP3 profiles. Figure a is a representative instantaneous temperature map. Figure b is the average temperature map. Figure c is the relative temperature uncertainty map. Figure d is the relative temperature fluctuation map. Figure e is the relative accepted number of values map.

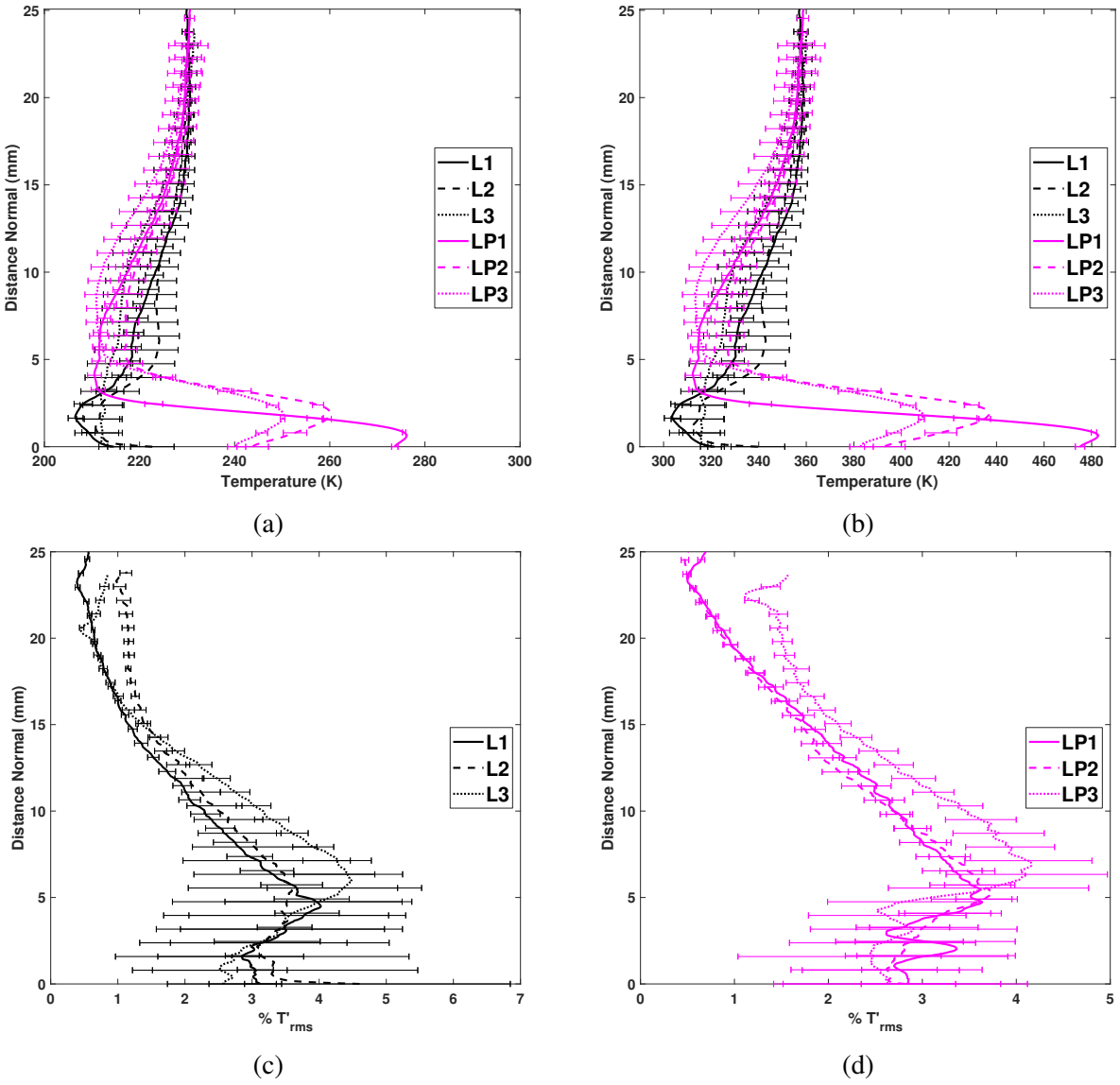

Figure 5.14: Overlayed vibrational thermometry laminar curves. Figure a is the 1-D temperature curve with a freestream of 230 K. Figure b is the 1-D temperature curve with a freestream temperature of 358 K. Figure c is the 1-D fluctuation curve corresponding to the 230 K freestream plasma off laminar experiments. Figure d is the 1-D fluctuation curve corresponding to the 230 K freestream plasma on laminar experiments.

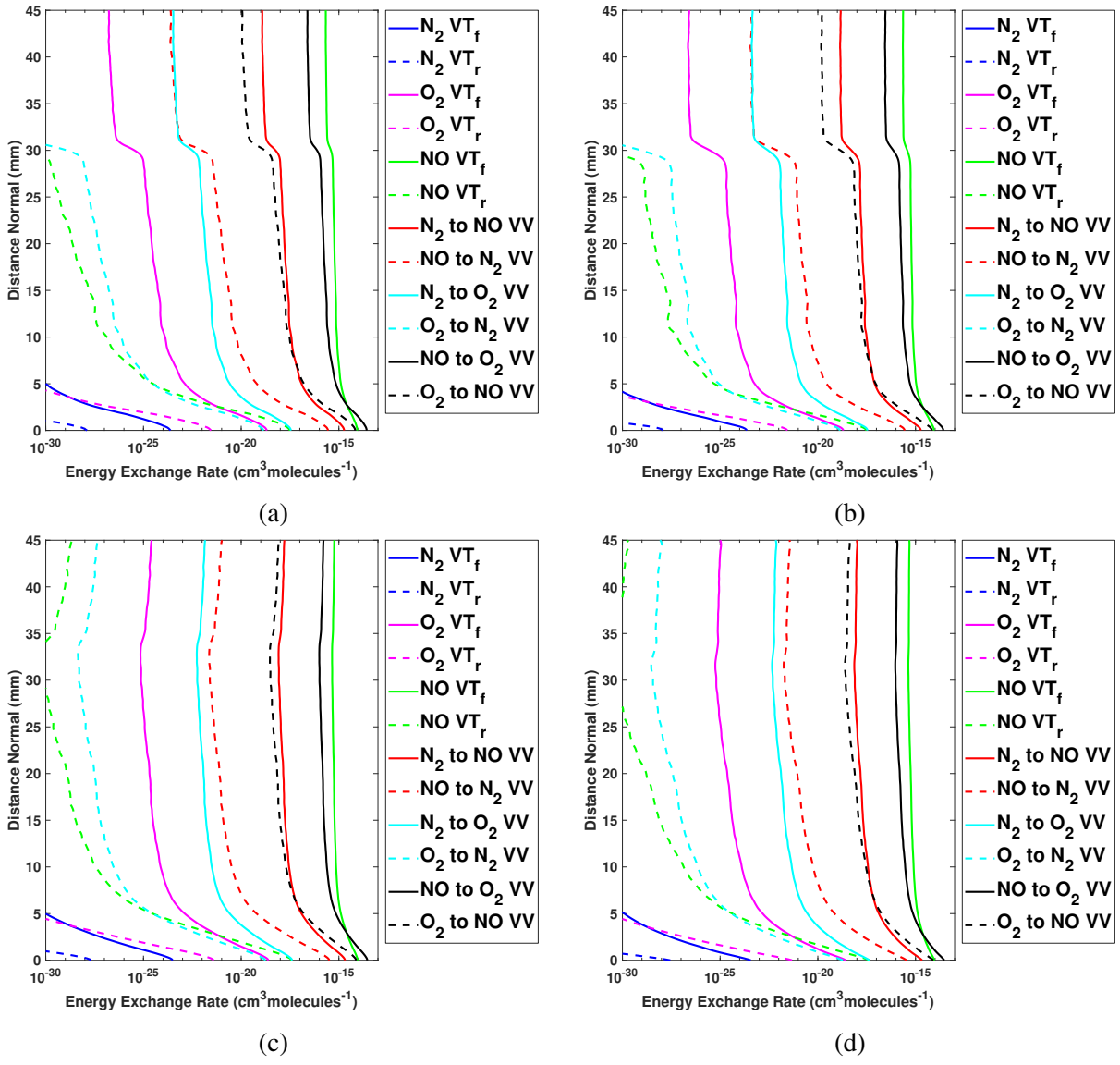

Figure 5.15: Temperature dependent energy exchange rates normal to surface using the 1-D laminar temperature curves. Figures a, b, c, and d correspond to the L1, LP1, L3, and LP3 temperature curves, respectively. All of the curves are zoomed in for clarity.

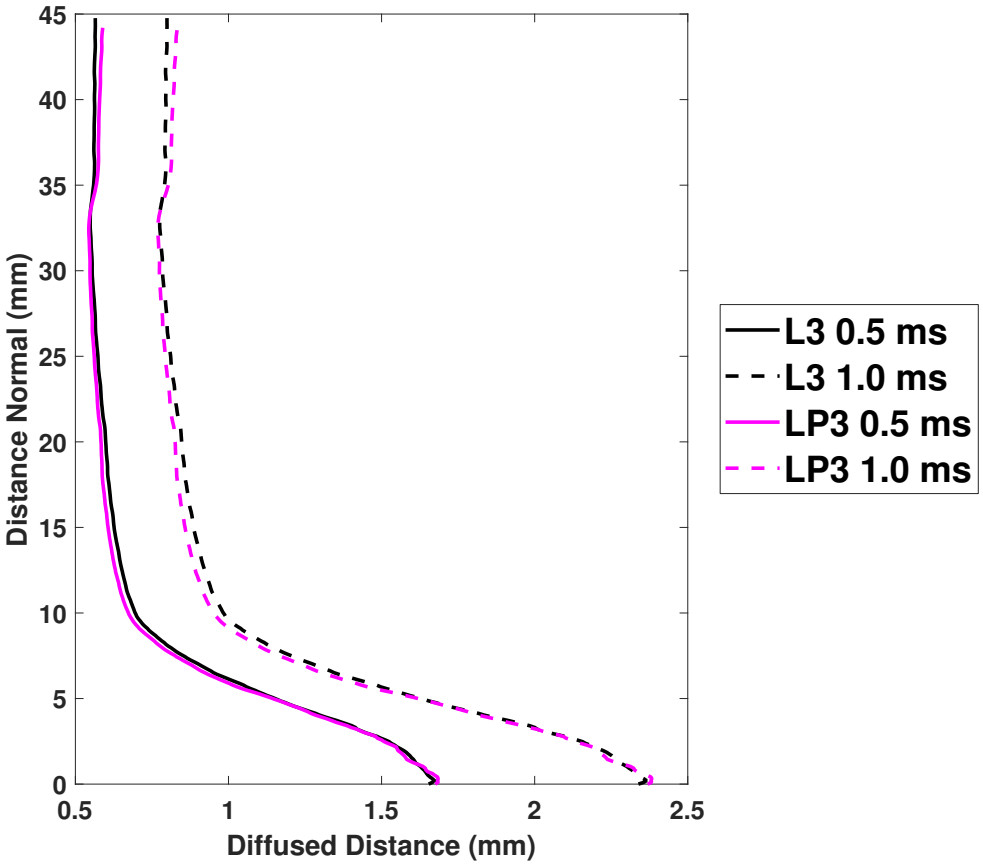

Figure 5.16: Predicted diffusion distance using Fick's Law of Diffusion. The L3 and LP3 temperature curves were used to determine the temperature dependent diffusion coefficient.

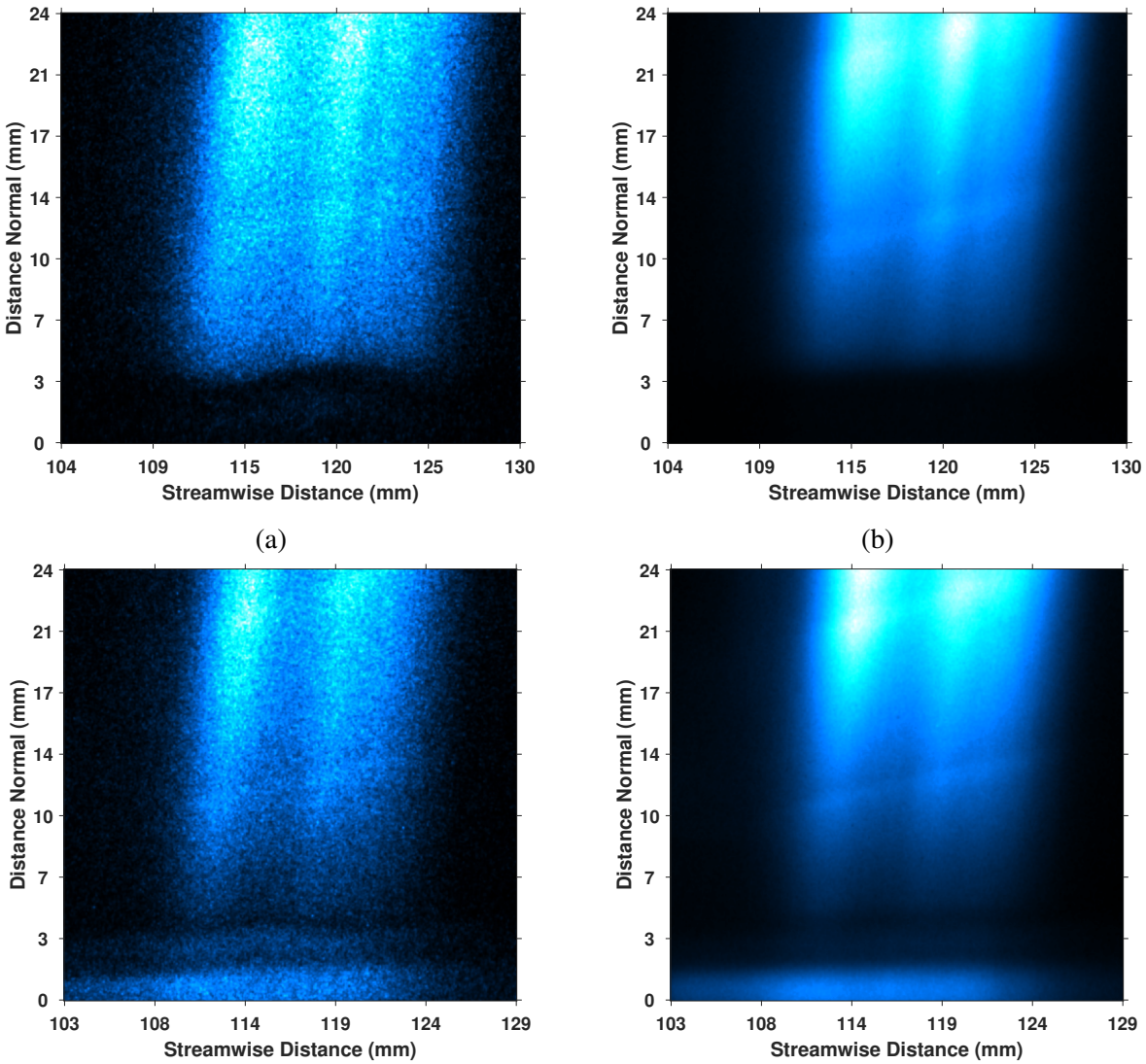

Figure 5.17: Representative TW1 and TWP1 images. Figures a and c are instantaneous images relating to TW1 and TWP1, respectively. Figures b and d are average images relating to TW1 and TWP1, respectively.

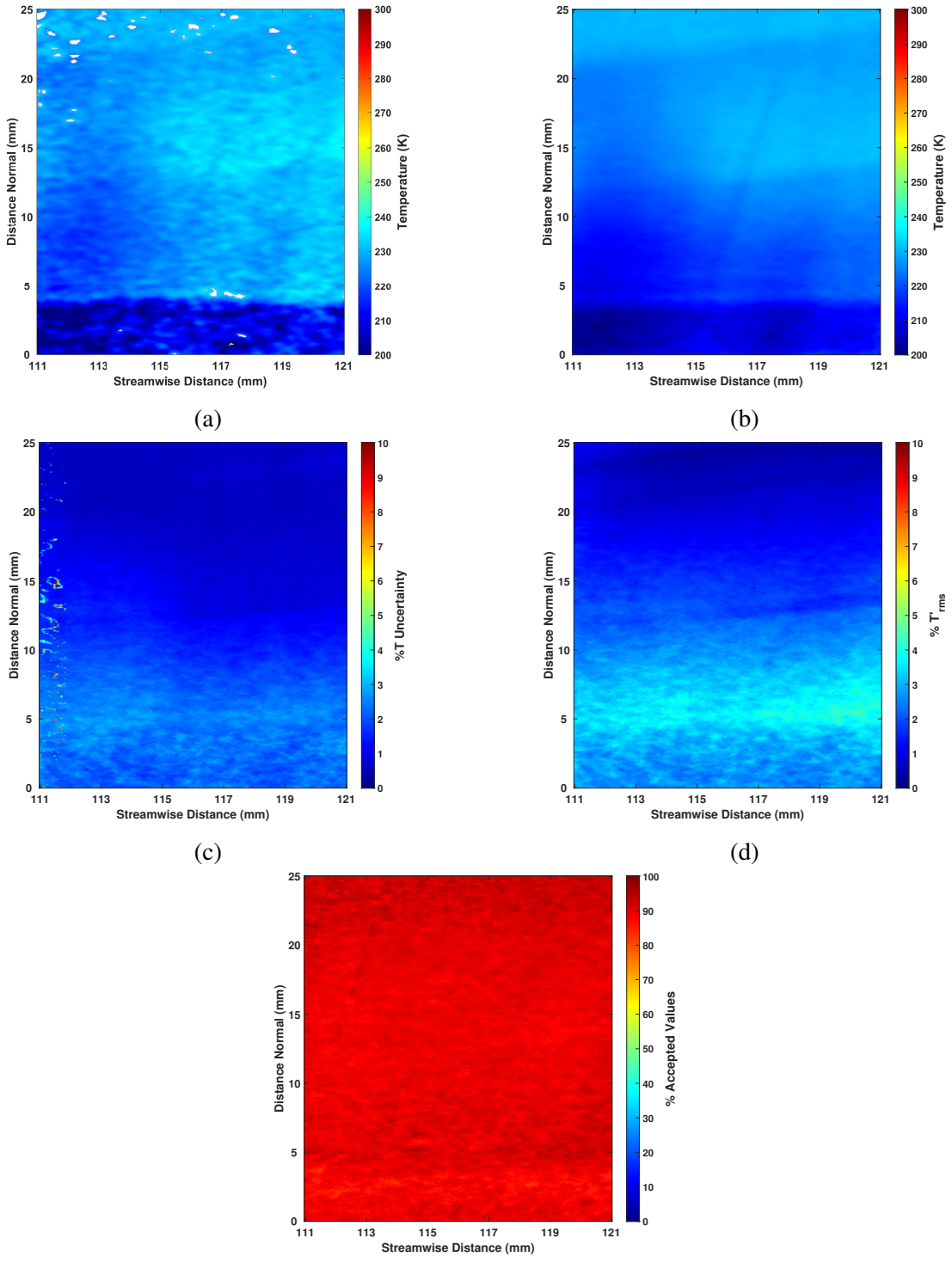

Figure 5.18: Vibrational thermal TW1 profiles. Figure a is a representative instantaneous temperature map. Figure b is the average temperature map. Figure c is the relative temperature uncertainty map. Figure d is the relative temperature fluctuation map. Figure e is the relative accepted number of values map.

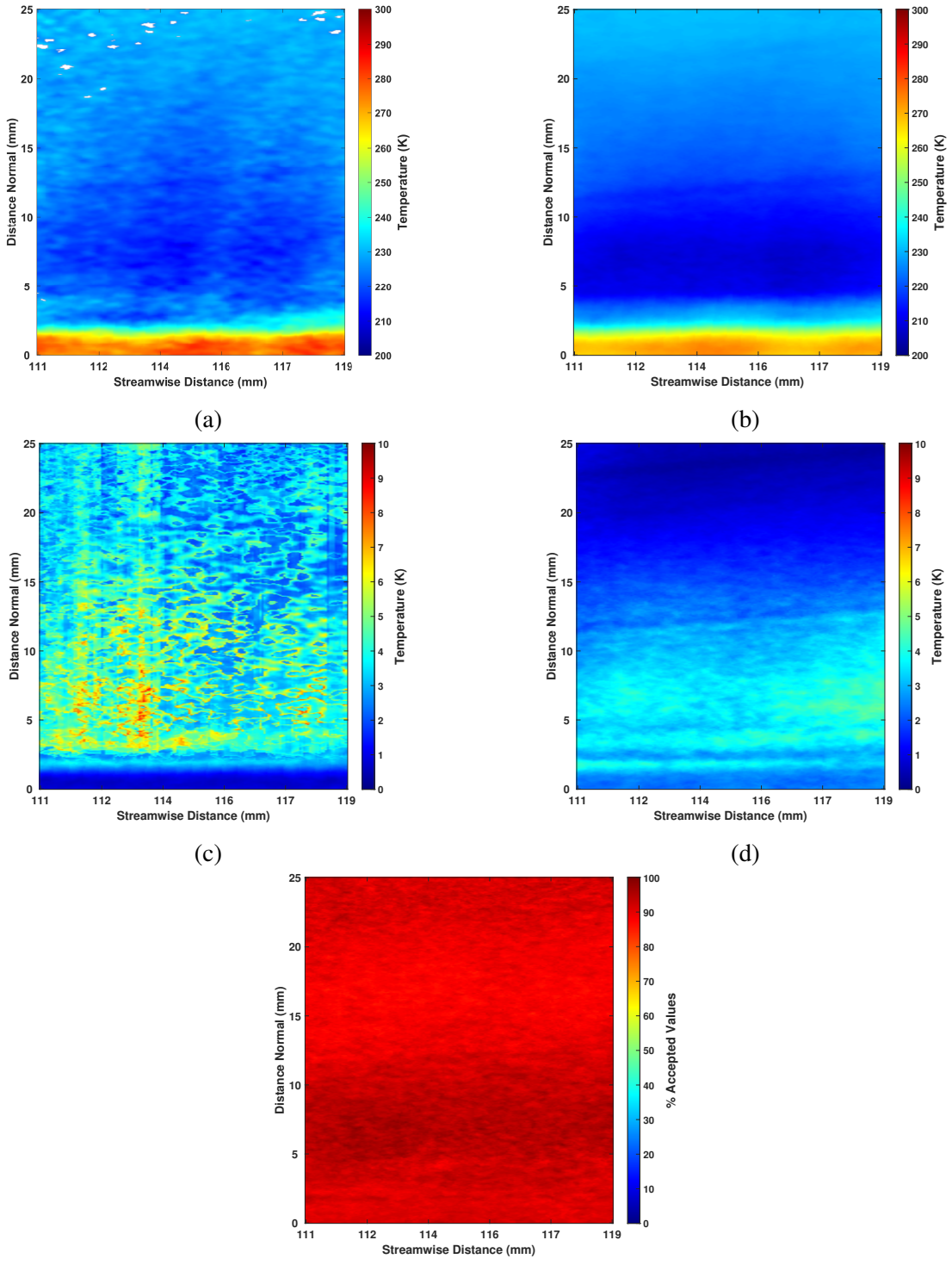

Figure 5.19: Vibrational thermal TWP1 profiles. Figure a is a representative instantaneous temperature map. Figure b is the average temperature map. Figure c is the relative temperature uncertainty map. Figure d is the relative temperature fluctuation map. Figure e is the relative accepted number of values map.

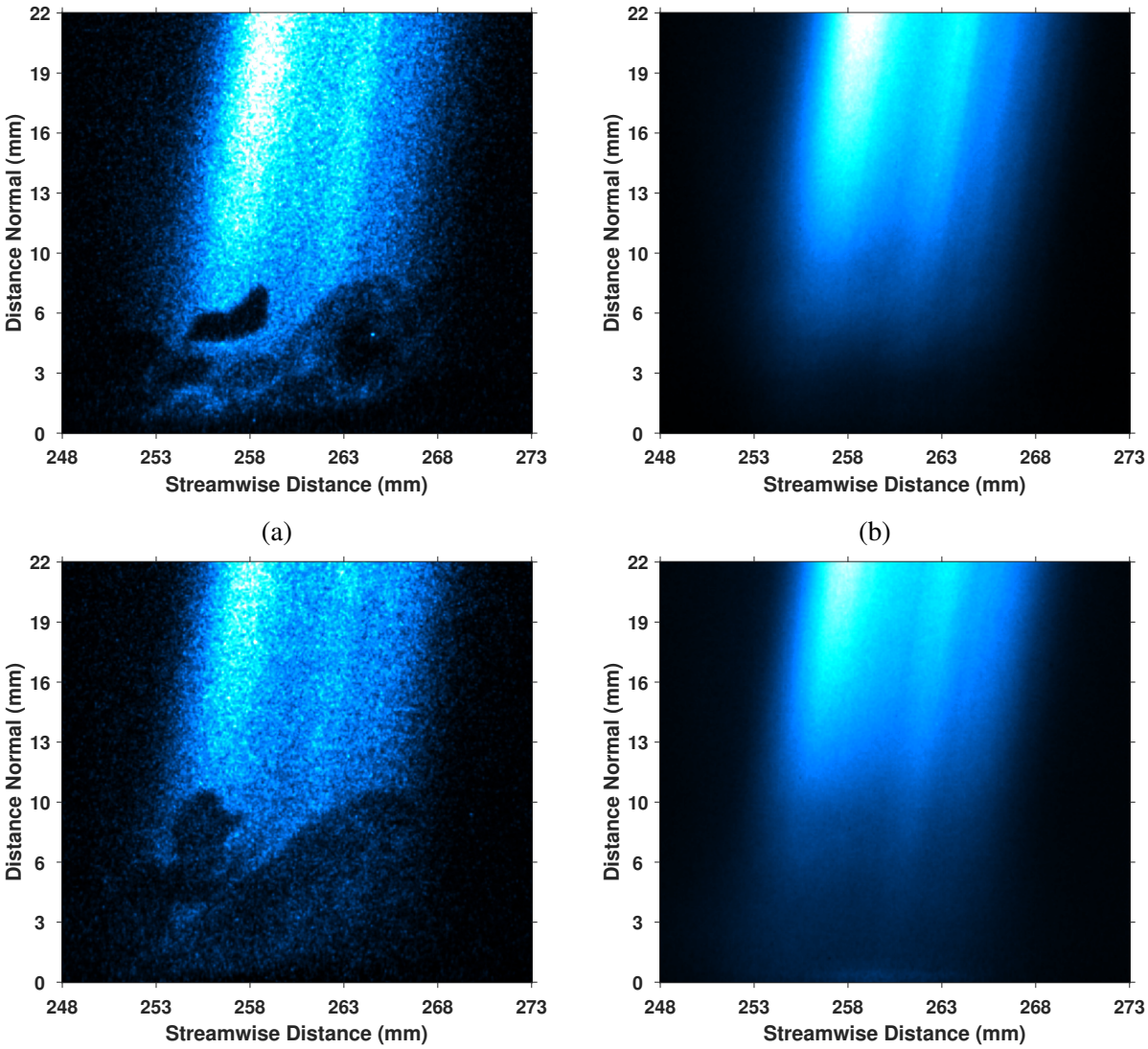

Figure 5.20: Representative TW2 and TWP2 images. Figures a and c are instantaneous images relating to TW2 and TWP2, respectively. Figures b and d are average images relating to TW2 and TWP2, respectively.

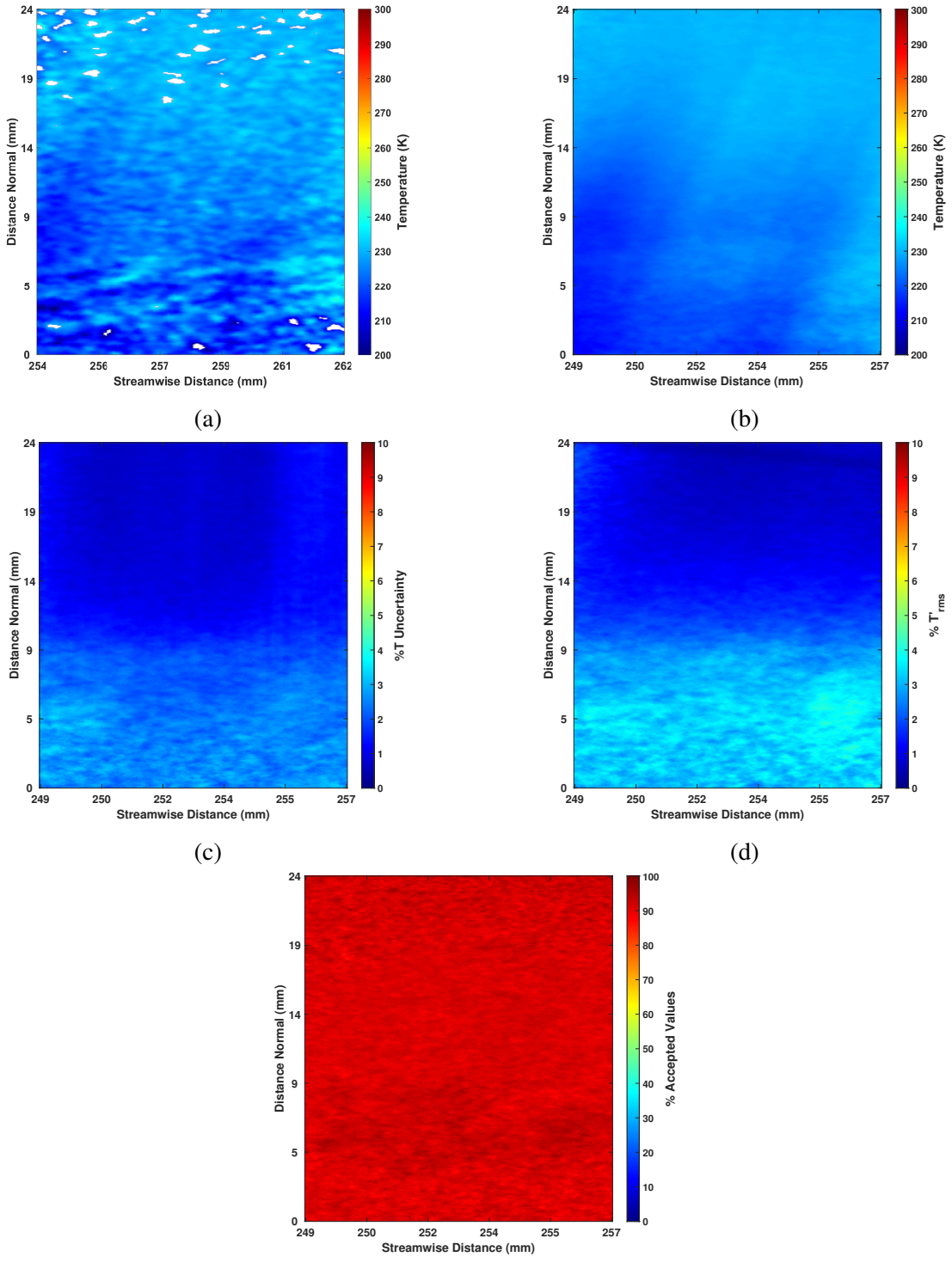

Figure 5.21: Vibrational thermal TW2 profiles. Figure a is a representative instantaneous temperature map. Figure b is the average temperature map. Figure c is the relative temperature uncertainty map. Figure d is the relative temperature fluctuation map. Figure e is the relative accepted number of values map.

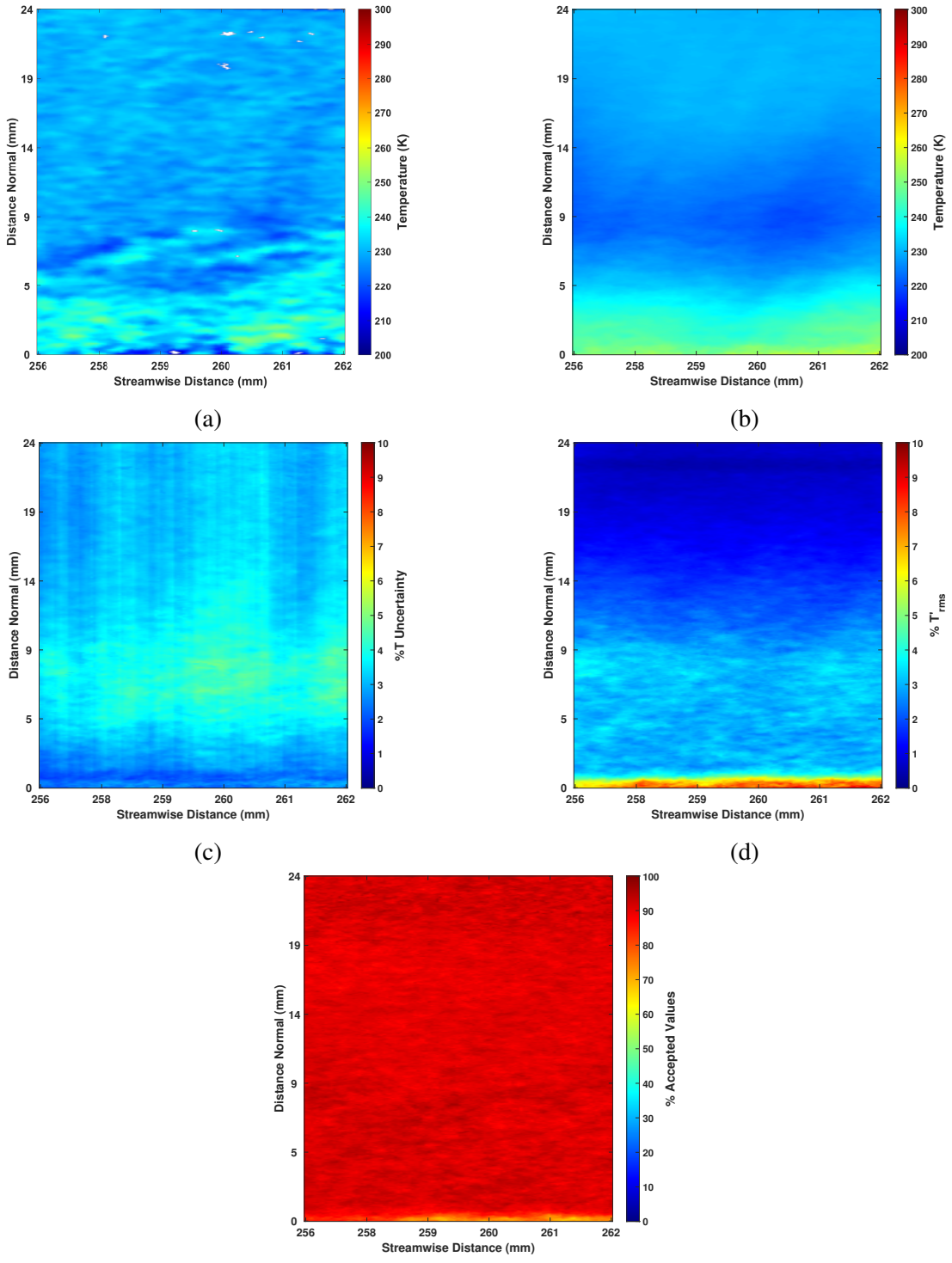

Figure 5.22: Vibrational thermal TWP1 profiles. Figure a is a representative instantaneous temperature map. Figure b is the average temperature map. Figure c is the relative temperature uncertainty map. Figure d is the relative temperature fluctuation map. Figure e is the relative accepted number of values map.

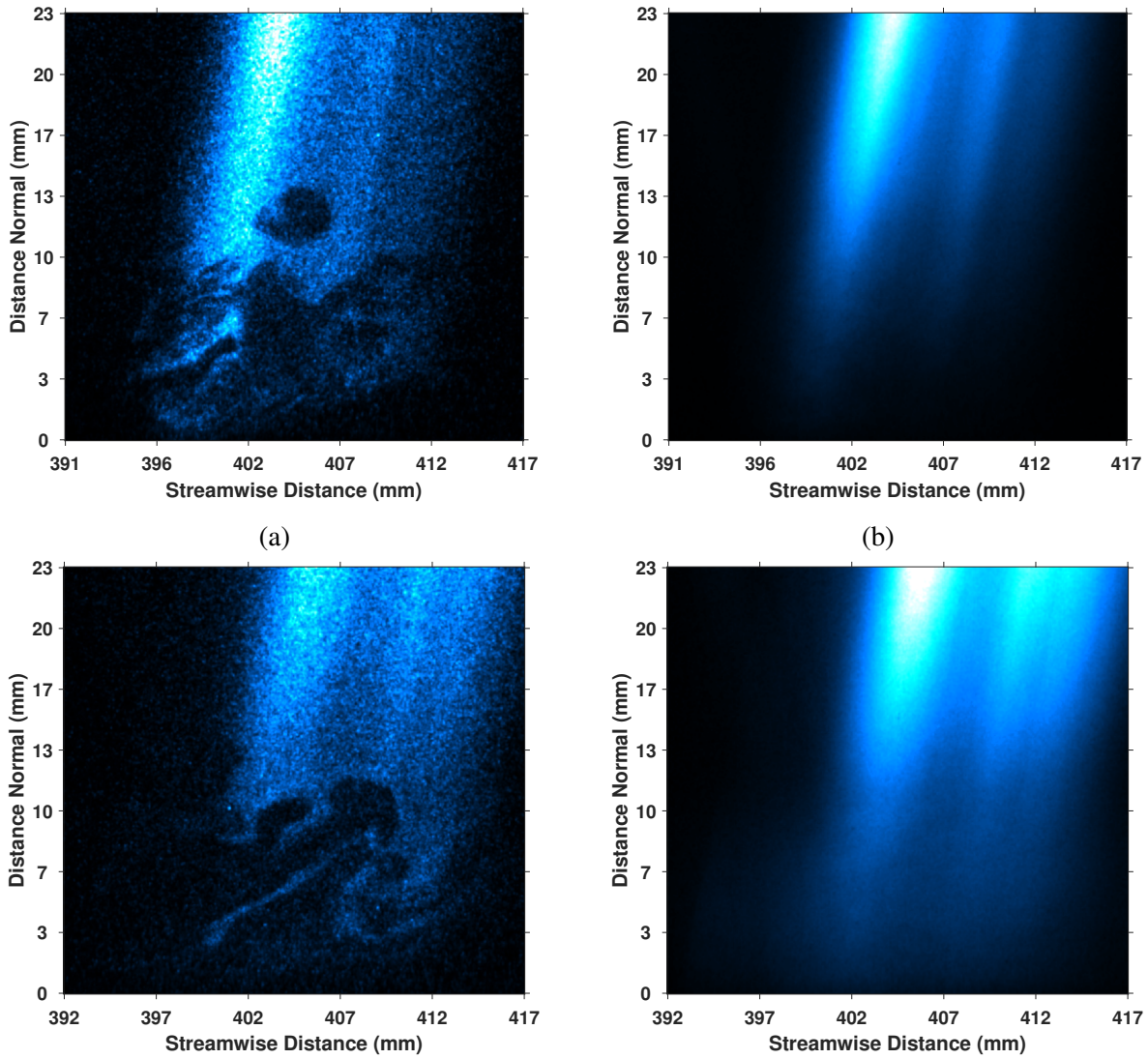

Figure 5.23: Representative TW3 and TWP3 images. Figures a and c are instantaneous images relating to TW3 and TWP3, respectively. Figures b and d are average images relating to TW3 and TWP3, respectively.

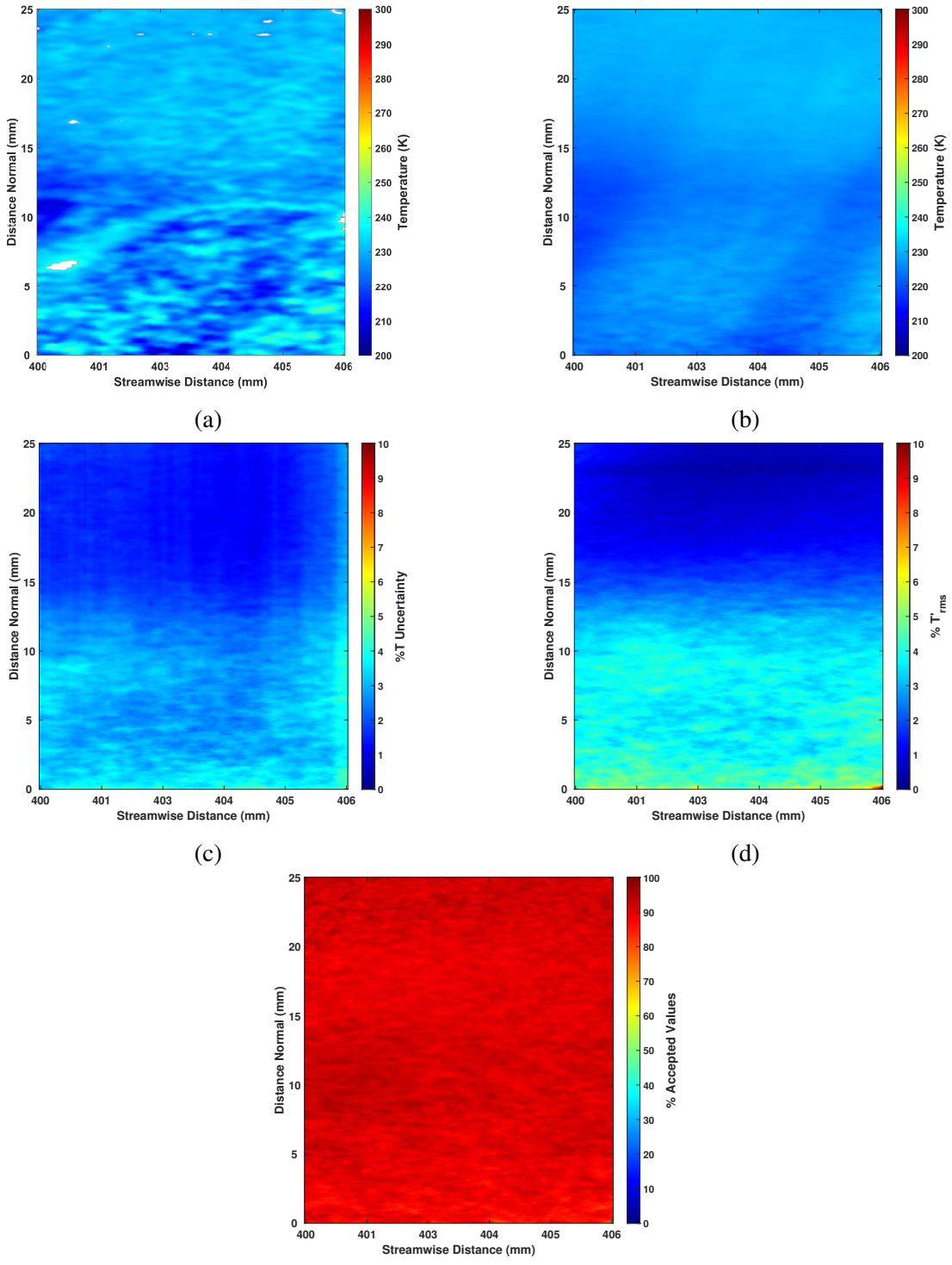

Figure 5.24: Vibrational thermal TW3 profiles. Figure a is a representative instantaneous temperature map. Figure b is the average temperature map. Figure c is the relative temperature uncertainty map. Figure d is the relative temperature fluctuation map. Figure e is the relative accepted number of values map.

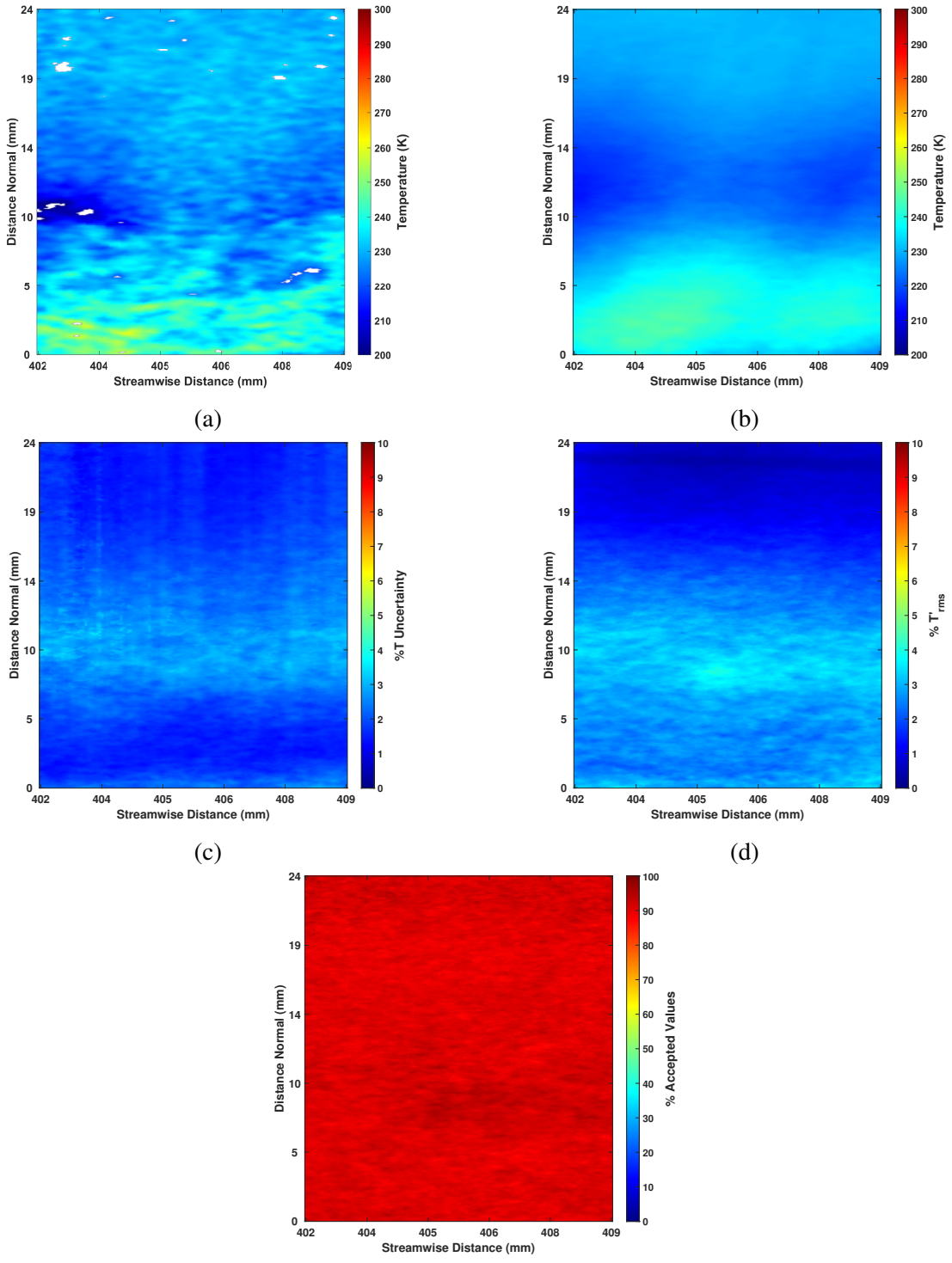

Figure 5.25: Vibrational thermal TWP3 profiles. Figure a is a representative instantaneous temperature map. Figure b is the average temperature map. Figure c is the relative temperature uncertainty map. Figure d is the relative temperature fluctuation map. Figure e is the relative accepted number of values map.

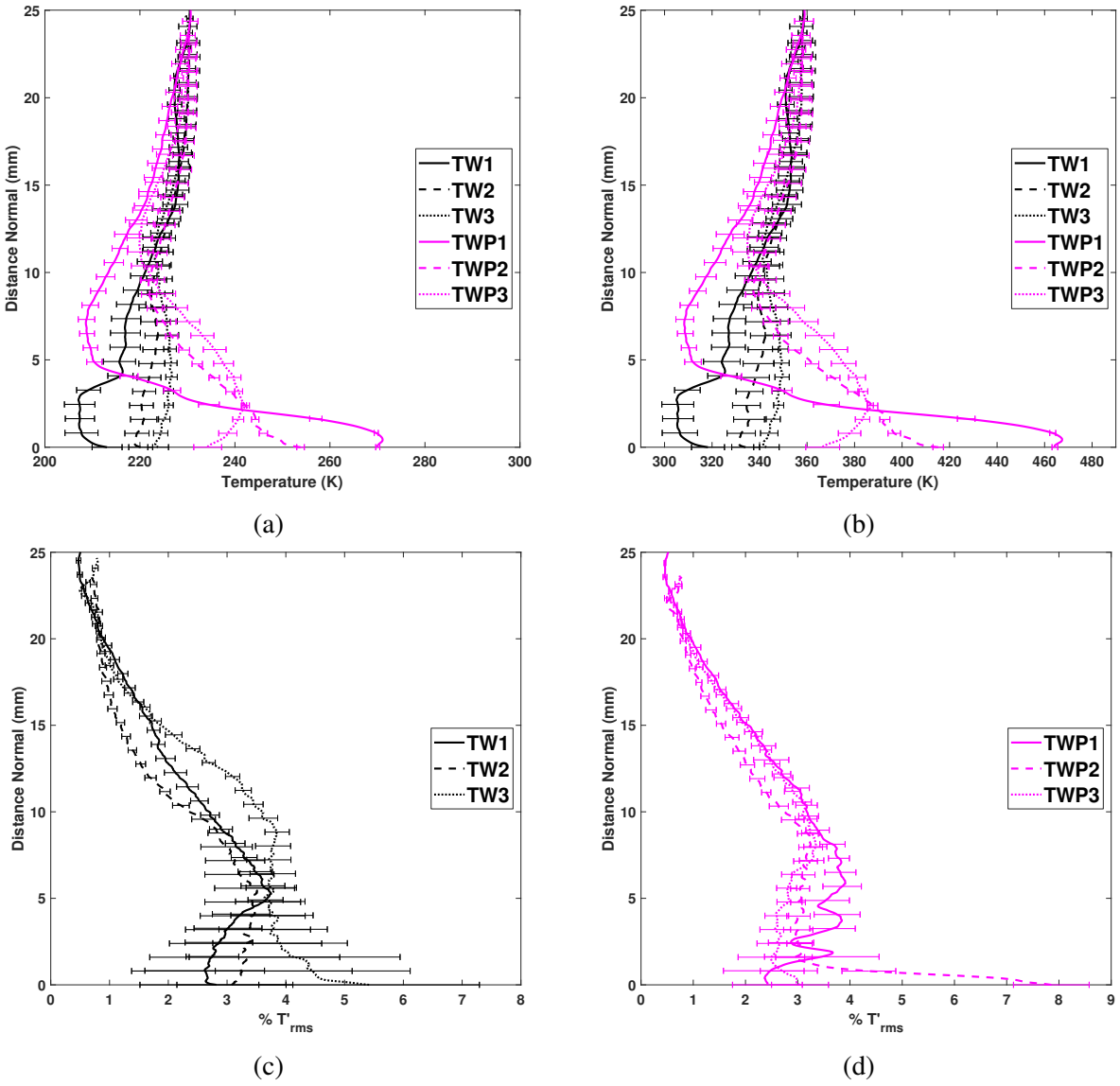

Figure 5.26: Overlayed vibrational thermometry turbulent curves. Figure a is the 1-D temperature curve with a freestream of 230 K. Figure b is the 1-D temperature curve with a freestream of 358 K. Figure c is the 1-D fluctuation curve corresponding to the 230 K freestream plasma off laminar experiments. Figure d is the 1-D fluctuation curve corresponding to the 230 K freestream plasma on laminar experiments.

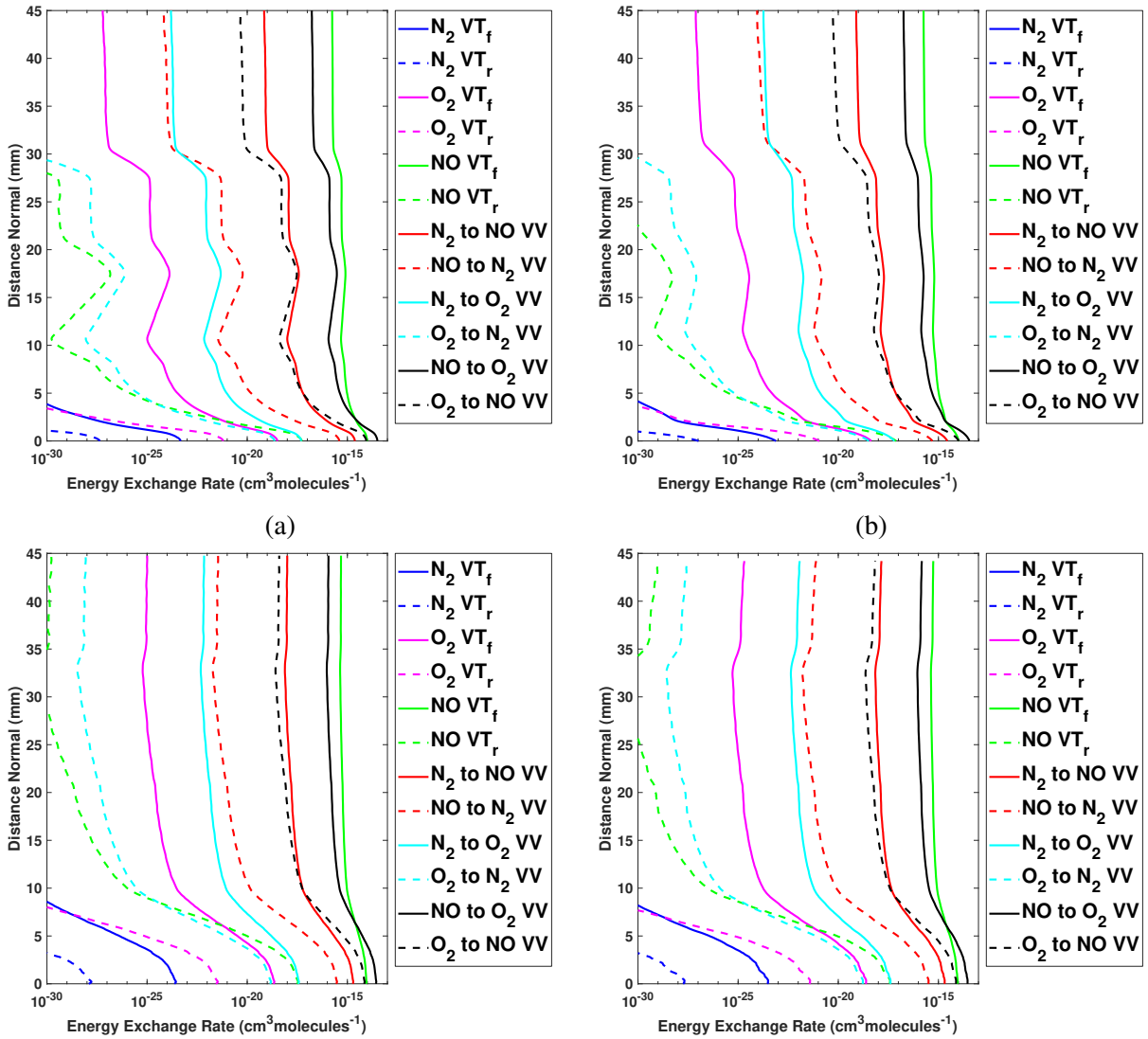

Figure 5.27: Temperature dependent energy exchange rates normal to surface using the 1-D turbulent temperature curves. Figures a, b, c, and d correspond to the TW1, TWP1, TW3, and TWP3 temperature curves, respectively. All of the curves are zoomed in for clarity.

6. VELOCIMETRY

6.1 Velocimetry Analysis

Velocimetry analysis was performed in the same manner for all of the following velocity measurements. The velocity profiles were highly dependent on the accuracy of the image scaling analysis. The ACE tunnel conditions were the same as presented in Table 4.2. All processed images were background corrected and FFT blurred in the same process as described for the image scaling. The angular and xy spatial displacement corrections from the grid card analysis were used to accurately overlap the two images. The image was rotated until the surface of the plate was parallel relative to the bottom of the image.

In an effort to reduce the computational time, interrogation windows were defined by the users. The edge detection algorithm described earlier was applied to the truncated interrogation windows. The centers of the write and read lines were defined by the algorithm and subsequently used to solved for the displacement in terms of pixels. However, in certain image sets there was significant blurring present in certain write line images due to overlapping surface reflections. This made it difficult for the algorithm to distinguish between the edges of the write line and reflected line. In these cases the write line edges were detected up to the blurred portion of the write line. The resulting centers of the write lines were used to generate a linear curve fit to produce a linear regression equation. The linear fit was used to find the unidentifiable write line centers. The read images did not suffer from the blurring effects and their centers were strictly found using the edge finding algorithm.

A pixel displacement threshold was applied to the image set according to the set time delay settings to reduce the possibility of non-physical spatial displacements. The pixel displacements were converted to a real spatial displacement using the grid card image scaling. The time delays used to find the velocity were determined using the approach of Danehy *et al.*[139] During the gate width the total fluorescent signal observed was undergoing an exponential down decay. The

excited state population fraction,

$$\frac{[\mathrm{NO}^*]_t}{[\mathrm{NO}]_0} = EXP(-k_{tot}t) \tag{6.1}$$

$$where\ k_{tot} = k_f + k_{q,\mathrm{NO}}[\mathrm{NO}] + k_{q,\mathrm{O_2}}[\mathrm{O_2}] \tag{6.2}$$

was dependent on the total fluorescent decay constant, k_{tot}. The $k_{q,X}$ constant for NO and O_2 are temperature dependent collisional quenching constants. The pressure was assumed to remain constant for the measured flow so the species number density changes as a function of temperature. Due to the boundary layer temperature profile, the fluorescence lifetime,

$$\tau = \frac{1}{k_{tot}} \tag{6.3}$$

varied normal to the surface. Therefore the resulting image was a function of the gate width and the τ. The temporal signature of the image was assumed to be when 50% of the total fluorescent signal was collected within the set gate width. The time delay used for the velocimetry images was found using the equation

$$t_{tot} = t_{camera} - t_{gate\ 1} + t_{gate\ 2} \tag{6.4}$$

where t_{camera} was the user defined time delay and t_{gate} variables were determined using the temporal corrections described above. These temporal corrections had a greater impact on images collected with a large gate width and high velocities. Figure 6.1 provides a visual of the fluorescence decay and gate width relation.

The resulting instantaneous velocity profiles were processed using the same statistical treatment process described earlier for the thermometry analysis. The analysis provided an average velocity profile, local % velocity fluctuations, the local velocity *rms*, and the total number of velocity points used following the statistical treatment.

The velocity uncertainty was a convolution of the scaling dimension error, time delay jitter,

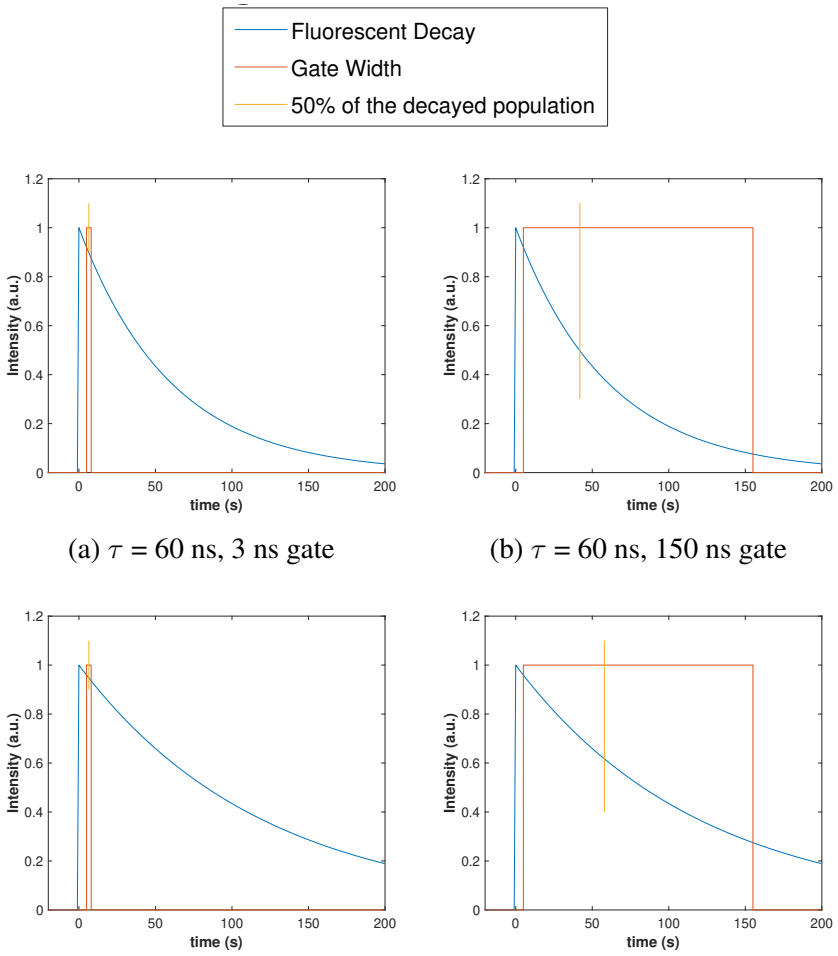

(a) τ = 60 ns, 3 ns gate

(b) τ = 60 ns, 150 ns gate

(c) τ = 120 ns, 3 ns gate

(d) τ = 120 ns, 150 ns gate

Figure 6.1: Velocimetry temporal corrections.

and the measured pixel displacement error. The uncertainty of these three sources were propagated using the equation,

$$\frac{\sigma_{u_\infty}}{\bar{u}} = \sqrt{(\frac{\sigma_d}{d})^2 + (\frac{\sigma_t}{t})^2 + (\frac{\sigma_x}{x})^2} \tag{6.5}$$

where *d* is the scaling dimension, *t* is the time delay, and *x* was the edge algorithm determined pixel displacement. The grid card analysis described earlier provided an uncertainty quantity associated with each image scaling dimension *i.e.* σ_d. The intrinsic jitter of the PI-MAX 4 camera was 35 ps.

6.2 Freestream Velocity Measurements

In building towards the invisible ink VENOM technique, an initial step was to characterize the freestream velocity and the corresponding fluctuations. Previous freestream measurements within the ACE tunnel determined the fluctuations to be on the order of 1%.[46] Characterizing the freestream velocity using MTV was important in demonstrating the accuracy and reproducibility of the technique in the ACE facility. All freestream velocity measurements were performed without a model so the maximum Reynolds number did not reach 6×10^6 / m. The ACE tunnel conditions for the freestream velocimetry are shown in Table 6.1.

Mach Number	P_t (Torr)	P_∞ (Torr)	T_t (K)	T_∞ (K)	Re / m
5.9	3100	2.5	420 K	56	5.0×10^6

Table 6.1: Freestream velocimetry tunnel conditions.

Initial MTV experiments characterized the spanwise freestream velocity. The frequency doubled laser system was used as the write beam and was tuned to the P_{21}/Q_1 bandhead $A^2\Sigma^+$ ($v' = 0$) $\leftarrow$ $X^2\Pi$ ($v'' = 0$) $X_{3/2}$ transition. The write beam was focused down to a single line using a 30 mm 2" spherical lens. The write beam was 4 $^1/_2$" from the test floor. A sum frequency mixing laser system was used as the read beam and was tuned to the P_{21}/Q_1 bandhead $A^2\Sigma^+$ ($v' = 1$) $\leftarrow$ $X^2\Pi$ ($v'' = 1$) $X_{1/2}$ transition. Both beams were tuned to transitions optimized for a $\sim$60 K freestream flow. The read beam propagated through a pair of cylindrcial lens to form a $\sim$3 cm wide 800 μm laser sheet. The write and read beams overlapped one another within the test section core. A single camera was mounted above the test section and operated in DIF mode. The two images were delayed 5 μs and the two images were gated after the laser scatter. The gate width following the write beam was set to 3 ns and the read beam gate width was gated at 50 ns. A single ballast was pressurized to 120 PSIA with a mixture of 5% NO in N_2. The mixture was pulsed into the ACE facility upstream of the flow conditioners at 2.5 Hz.

Representative spanwise fluorescent images are shown in Figure 6.2. The write and read lines had an excellent S/N ratio for both of the instantaneous and average images. Under the current resolution and delay time the line displaced $\sim$2 mm. The instantaneous write line image displayed subtle differences in the NO seeding profile; however, this effect was averaged out in Figure 6.3b. There were no large scale fluctuations observed in the read line which suggests the ACE core flow was relatively quiet. The NO $X^2\Pi$ (v = 1) freestream population can be seen in the upstream portion of the read images. The spanwise freestream velocimetry analysis is shown in Figure 6.3. Figure 6.3a details the average position of the write line. The write line was assumed to be straight because the collected image was collected instantaneously following the $A^2\Sigma^+$ (v′ = 0) $\leftarrow$ $X^2\Pi_{3/2}$ (v″ = 0) transition. However, the write line may be moving in the lab frame due to vibrations of the laser optics and the ICCD camera. The write line had a spatial fluctuation of 30 μm which correlated to $\sim$2 pixels under the current resolution conditions. The spanwise freestream velocity was constant within the test section core. The average freestream velocity for the entire run was determined to be 869.8 $\pm$ 7.7 m/s which agreed well with calculated NALDAQ velocity of 860 $\pm$ 8.6 m/s. The velocity fluctuations were determined using the following equation,

$$U' = U - \bar{U} \tag{6.6}$$

where U' is the velocity fluctuation, U is the instantaneous velocity, and $\bar{U}$ is the average velocity. The spanwise freestream fluctuations, U'_∞, were determined to be 0.5% to 0.8% which was in agreement with previous pitot probe measurements performed in the ACE facility.[46] Figure 6.3d plots U′ versus the write line position fluctuations. A correlation between the two values would suggest the measured fluctuations were an artifact from the velocimetry analysis. However, the plot displayed a random distribution which suggests the measured U′ were intrinsic to the freestream flow. This was verified by analyzing a simulated image data set using the edge finding algorithm. The uncertainty limit for the edge algorithm was determined to be $\sim$0.05 pixels. Therefore it was assumed the U′ uncertainty limit was reached based on the known intrinsic freestream fluctuations.

An additional plot, Figure 6.4, was made to visualize the temporal dependence of the determined freestream velocity. Recall the ACE facility was preheated prior to the run with a hot pebble bed reservoir. During the run the air continually passes through the heated element and causes the temperature of the ACE infrastructure to increase. The resulting freestream velocity increases during the run. The MTV results showed a 1.2% rise in the freestream velocity and this was also reflected in the calculated NALDAQ velocity profile. The MTV determined velocities were $\sim$1.5% higher; however, given the uncertainty of the two velocimetry techniques the freestream velocities agreed well with one another.

Following the characterization of the spanwise freestream velocity the top-down velocity was measured. The frequency doubled laser system was used as the write beam and was tuned to the P_{21}/Q_1 bandhead $A^2\Sigma^+$ ($v' = 0$) $\leftarrow$ $X^2\Pi_{1/2}$ ($v'' = 0$) transition. The write excitation wavelength was changed because the NO ground state population in the $X_{1/2}$ ground state was greater than the $X^2\Pi_{3/2}$ ground state at 60 K as shown in Figure 6.5. The write beam propagated through a pair of cylindrical lens to produce a $\sim$2 cm 800 μm sheet. The write laser sheet then propagated through a microcylindrical lens array to produce multiple write lines. The write beams propagated through the center of the test section, 7 $\frac{1}{16}$" from the side. A sum frequency mixing laser system was used as the read beam and was tuned to the P_{21}/Q_1 bandhead $A^2\Sigma^+$ ($v' = 1$) $\leftarrow$ $X^2\Pi_{1/2}$ ($v'' = 1$) transition. Both beams were tuned to rotational transitions optimized for a $\sim$60 K freestream flow. The read beam propagated through a pair of cylindrcial lens to form a $\sim$3 cm wide 800 μm laser sheet. A single camera was mounted on the side of the test section and operated in DIF mode. The two images were delayed 5 μs and the two images were gated after the laser scatter. The write beam gate width was 5 ns and the read beam gate width was 50 ns. A single ballast was pressurized to 120 PSIA with a mixture of 10% NO in N_2. The mixture was pulsed into the ACE facility upstream of the flow conditioners at 2.5 Hz.

Representative top-down fluorescent images are shown in Figure 6.2. The S/N ratio for the write lines was excellent for both instantaneous and average image. The read image however, had a more complex profile due to the appearance of additional lines compared to the write images.

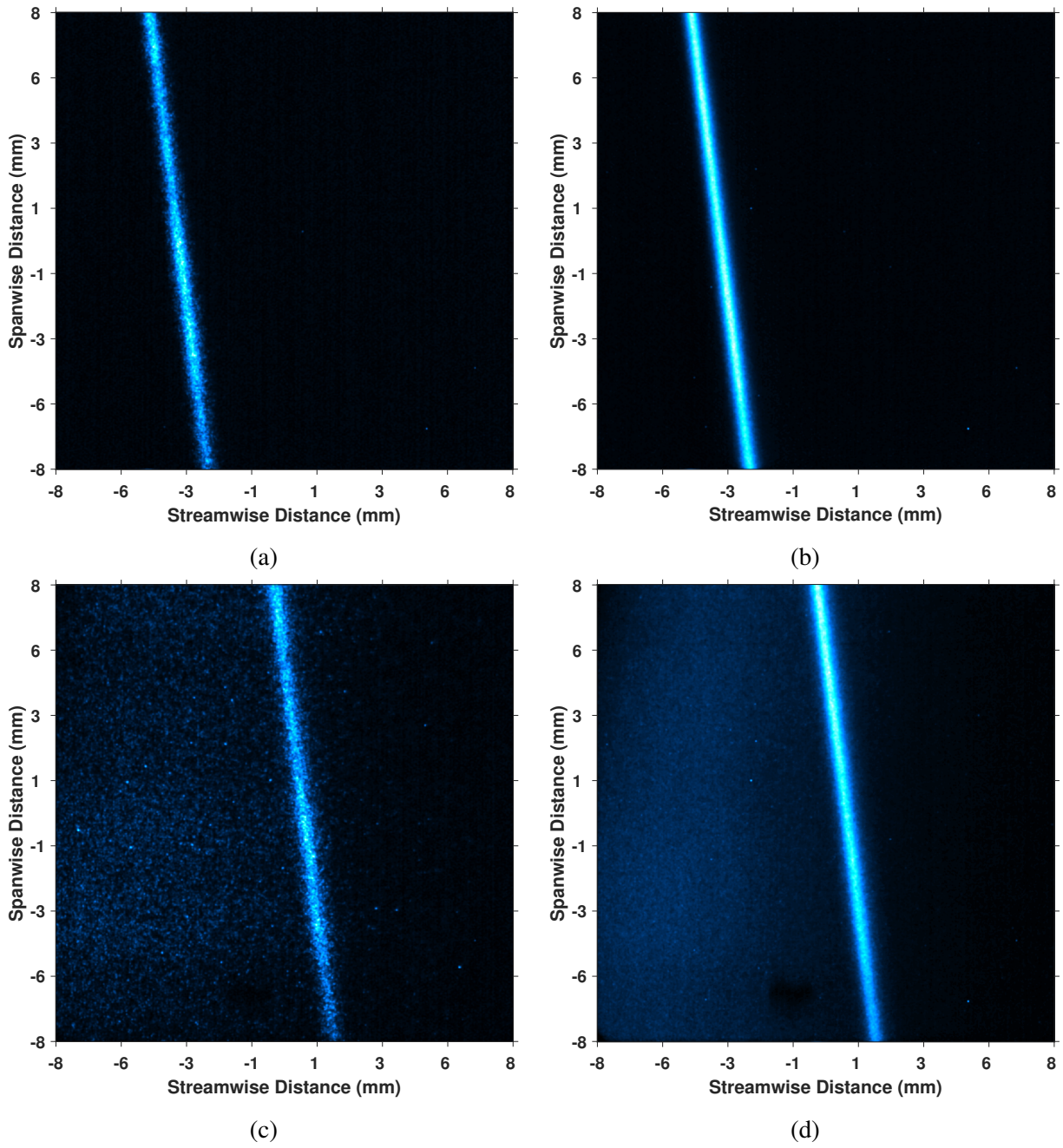

Figure 6.2: Representative spanwise fluorescent images where the flow is from left to right. Figures a and b are the instantaneous and average images, respectively, for the write line. Figures c and d are the instantaneous and average images, respectively, for the read line.

The image pair was captured using the DIF mode which was more sensitive to saturation effects. The inter-line transfer function was not able to clear the write image entirely from ICCD array prior to the read image collection. As a result the write lines appeared within the read image.

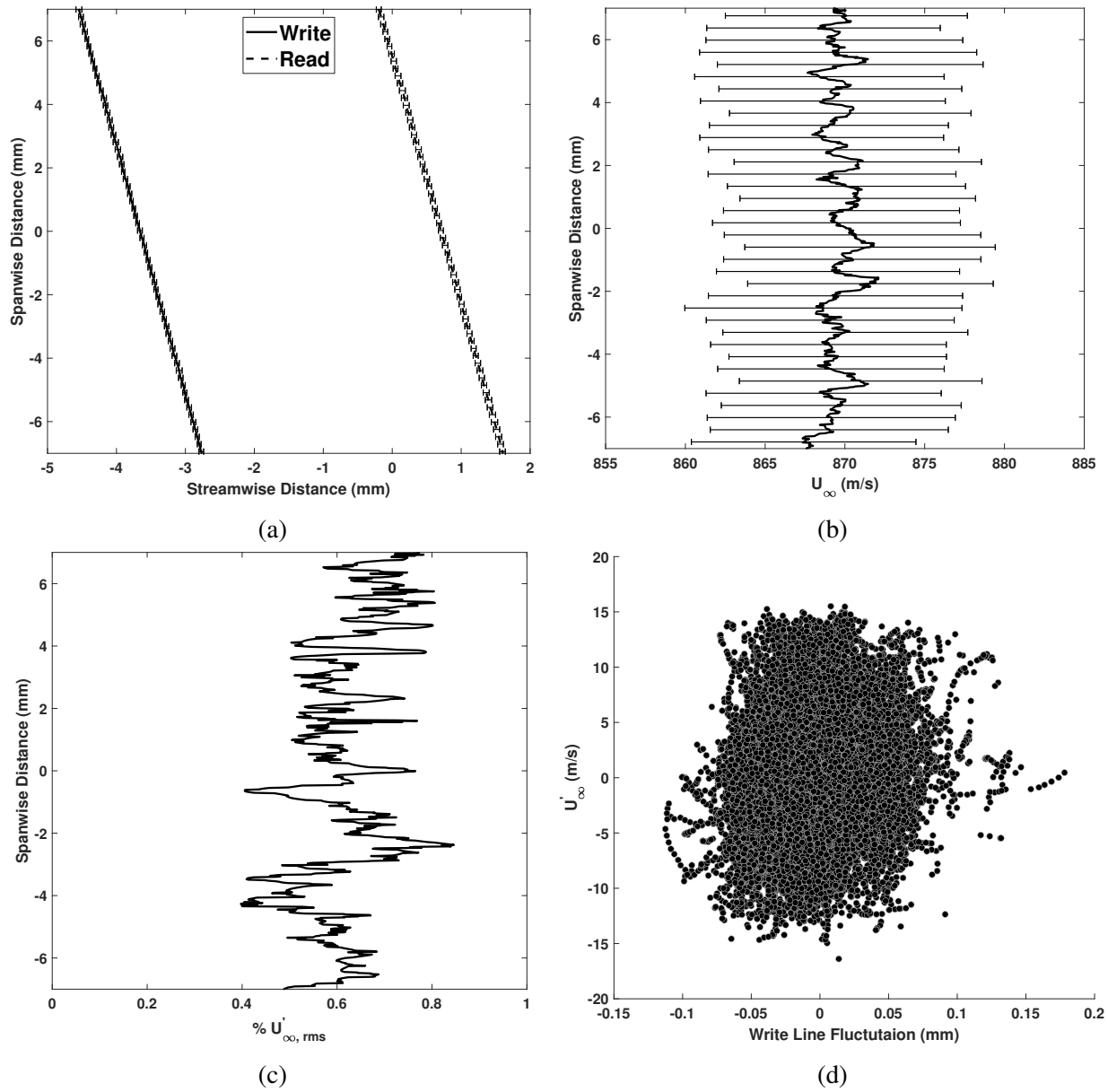

Figure 6.3: Spanwise velocimetry analysis.

The write lines at a streamwise distance of -9 mm, -2 mm, and 5 mm were analyzed and will be referred to as line 1, line 2, and line 3. The top-down velocimetry analysis plots are shown in Figure 6.7. The top-down velocity was determined to be 822.5 $\pm$ 9.0 m/s which was $\sim$5% slower than the measured spanwise velocity. All of the analyzed lines agree well with another as shown in Figure 6.7a. The velocity fluctuations varied from 0.5% to 0.95% which was in agreement with

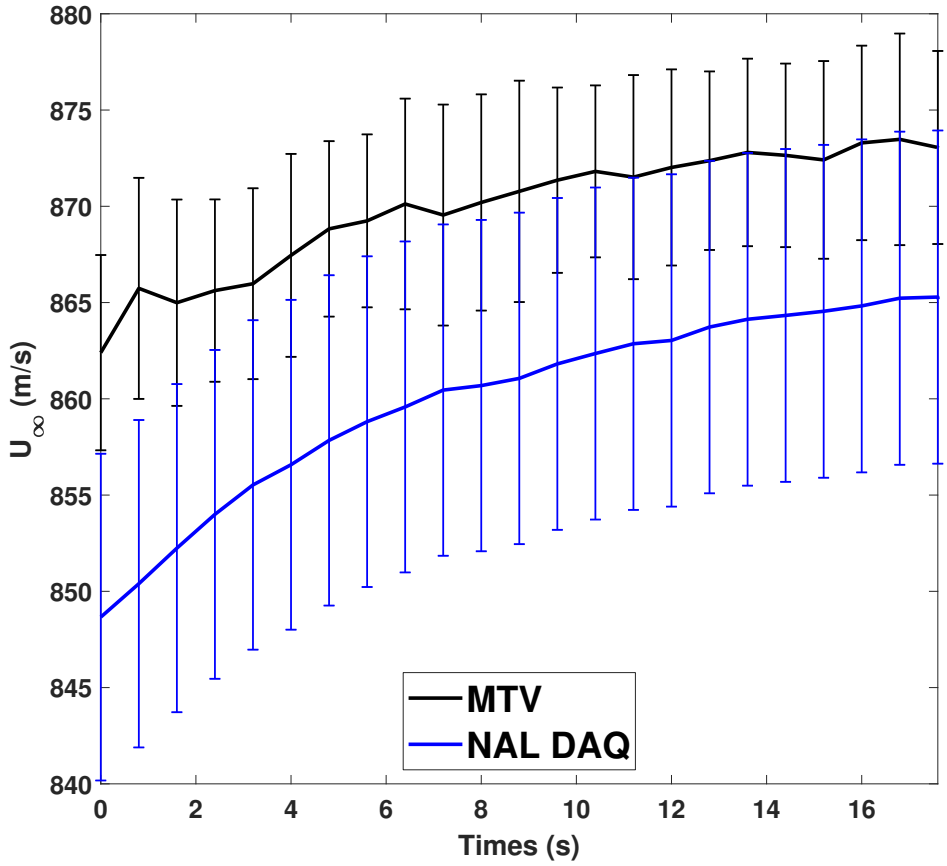

Figure 6.4: Comparison of determined temporal velocity profiles. The blue curve was the velocity profile determined using the isentropic relations and the run conditions collected by the NAL DAQ. The black curve was the velocity profile measured directly using MTV.

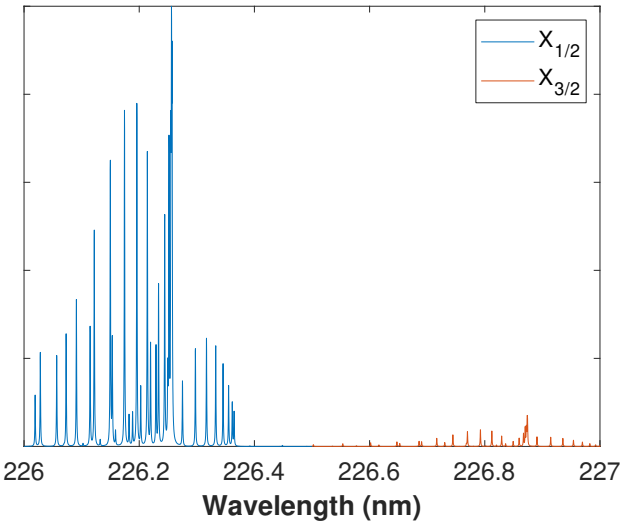

Figure 6.5: NO Absorbance Spectrum at 60 K.

the observed spanwise velocity fluctuations. The write and read lines are shown in 6.7c, but the small-scale uncertainty error bars are difficult to visualize. The line 1 spatial fluctuations were $\sim$30 μm which correlates to $\sim$1.3 pixels for the current resolution conditions. The spatial functions for lines 2 and 3 were on the same scale as line 1. Figure 6.7d did not show a correlation between the write line fluctuations and the velocity fluctuations which suggest the observed fluctuations were intrinsic to the freestream. The temporal freestream velocity plot shows the MTV determined velocity to be slower than the velocity calculated by the NAL DAQ. There was a slight increase in the MTV velocity during the run, but not as pronounced as the velocity increase observed with the spanwise measurements.

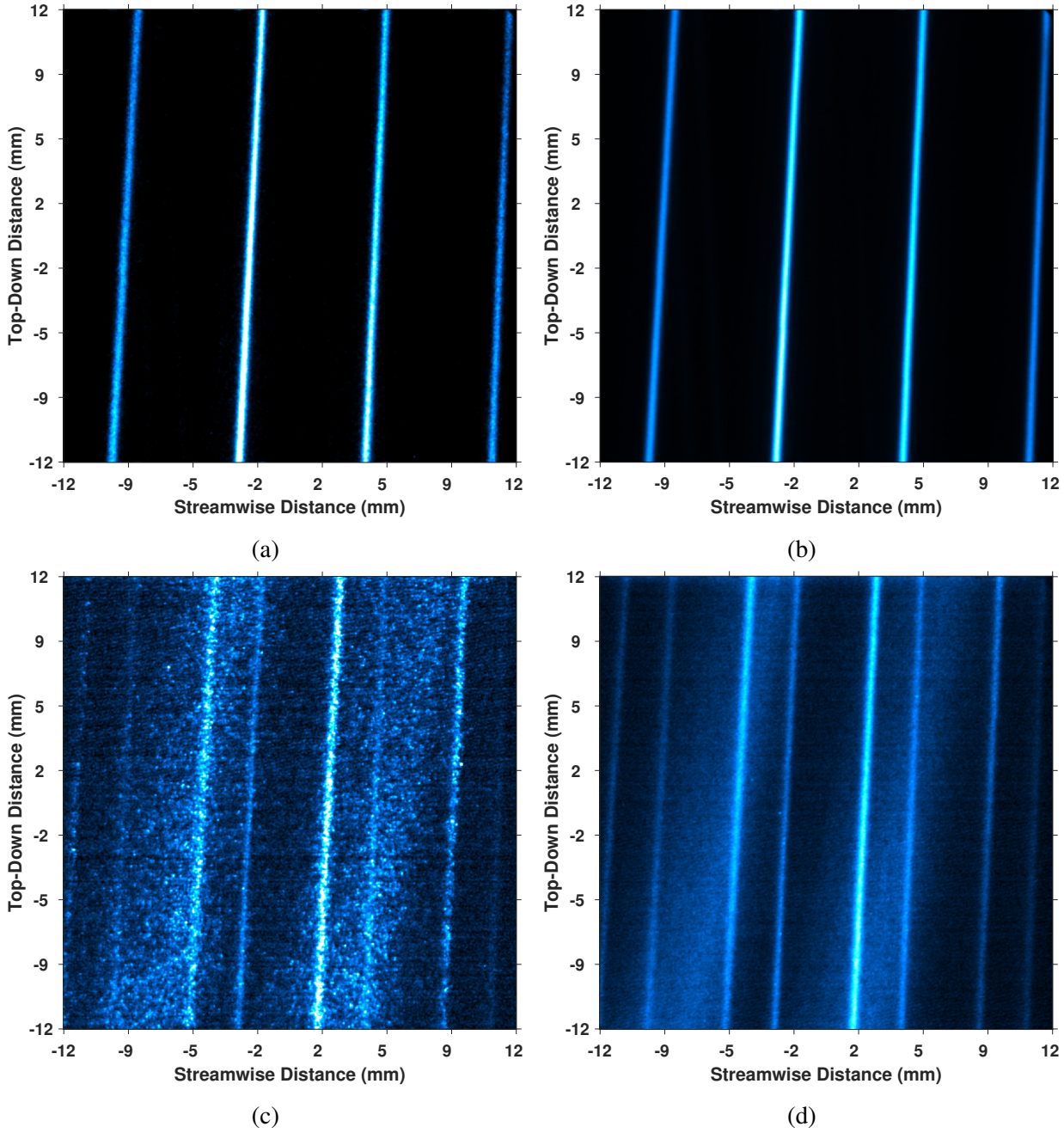

Figure 6.6: Representative top-down fluorescent images where the flow is from left to right. Figures a and b are the instantaneous and average images, respectively, for the write line. Figures c and d are the instantaneous and average images, respectively, for the read line.

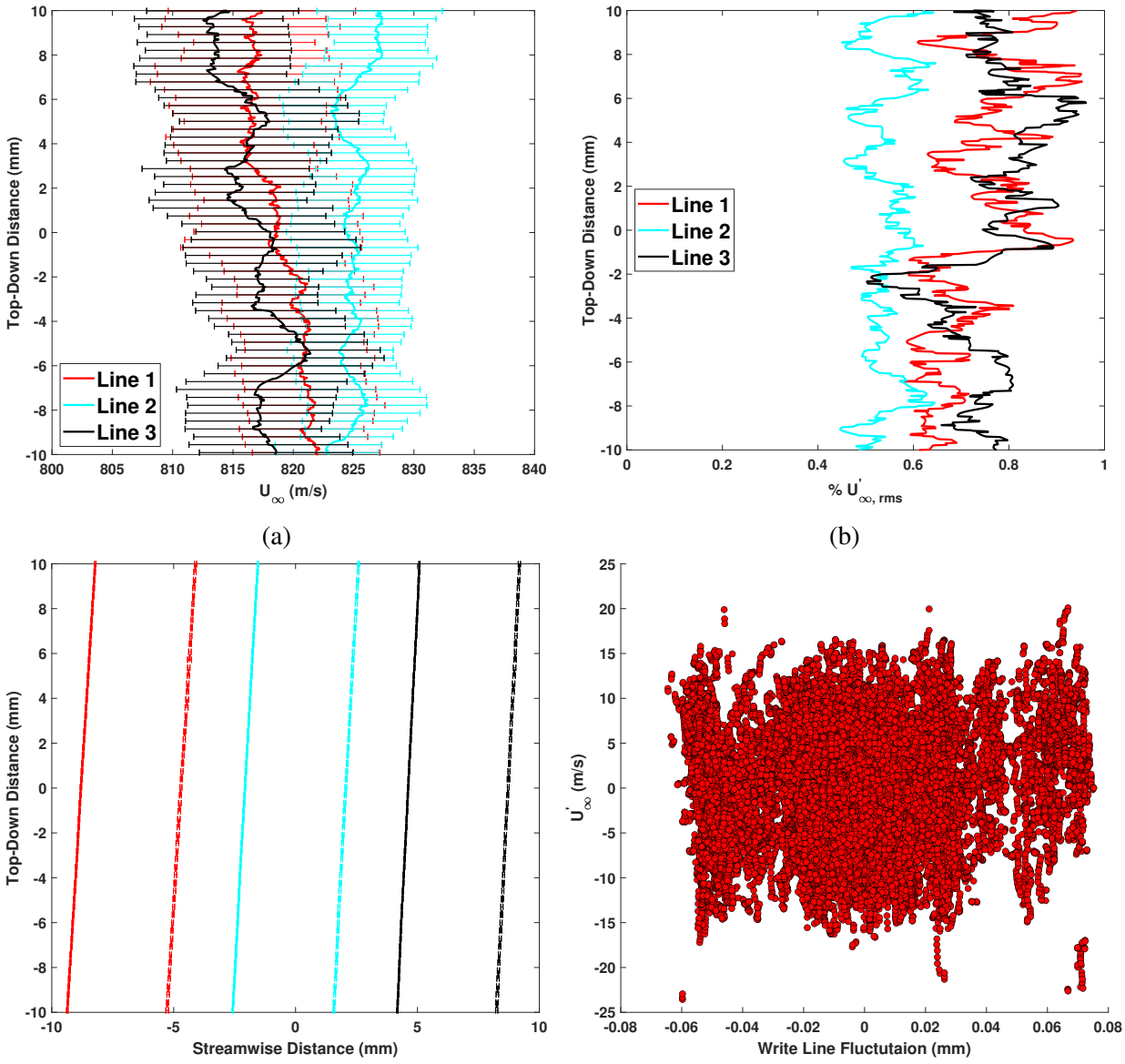

Figure 6.7: Top-down velocimetry analysis.

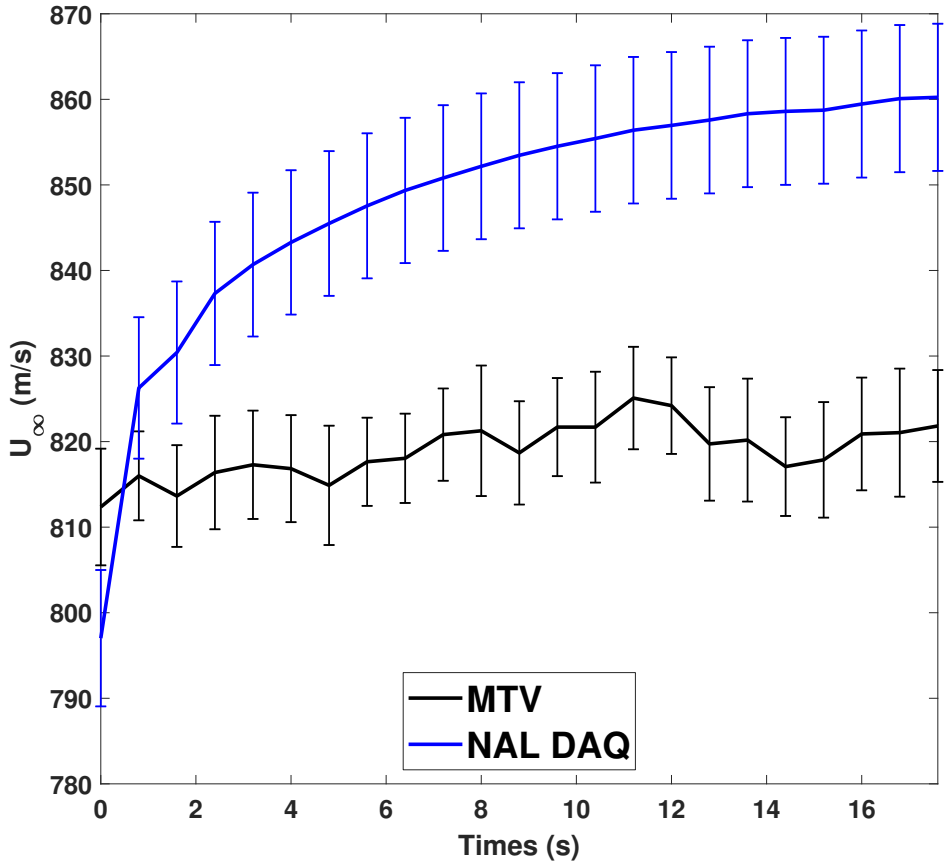

Figure 6.8: Comparison of determined temporal velocity profiles. The blue curve was the velocity profile determined using the isentropic relations and the run conditions collected by the NAL DAQ. The black curve was the velocity profile measured directly using MTV.

6.3 Modeling and Optimization of Boundary Layer Signal

Performing NO LIF experiments within the ACE tunnel was challenging due to the observed S/N profile normal to the surface. A gradual decrease in the NO LIF signal near the surface was observed in the rotational thermometry experiments. As mentioned previously, the pressure remained constant so an increase near wall temperature produced a decrease in the local number density. The vibrational thermometry images following the $A^2\Sigma^+$ (v′ = 1) ← $X^2\Pi_{1/2}$ (v″ = 1) transition had a smaller S/N relative to the NO $A^2\Sigma^+$ (v = 0) population. A relatively small nascent NO (v″ = 1) population was produced following the NO $A^2\Sigma^+$ (v′ = 0) state relaxation. The resulting NO $X^2\Pi$ (v″ = 1) population was dependent on the competing relaxation pathways of fluorescence and collisional quenching. The two relaxation pathways were different in their respective ground state vibrational distributions. These observations motivated the development of a model to predict the S/N profile normal to the surface.

The initial *J* state NO $X^2\Pi$ (v″=0) populations were calculated normal to the surface using the Boltzmann equation,

$$\frac{N_i}{N_{tot}} = \frac{g_i \, e^{-\frac{E_i}{k_B T}}}{g_j \sum_j e^{-\frac{E_j}{k_b T}}} \tag{6.7}$$

where g_i is the degeneracy, E_i is the Dunham expansion vibronic energy, k_B is the Boltzmann constant, and T is local temperature. The empirical temperature profile from the rotational thermometry campaign was used as the local temperature values. To determine a theoretical S/N profile normal to the surface, the population fraction of a select *J* NO $X^2\Pi$ (v″ = 0) state was multiplied by the local NO number density of the flow. The subsequent NO $X^2\Pi$ (v″ = 1) population following the relaxation of the NO $A^2\Sigma^+$ (v′ = 0) state was dependent on the *J* state population probed with the write laser.

The NO $X^2\Pi$ (v = 1) fraction was determined by considering the following relaxation due to spontaneous emission and collisional quenching as shown in Equations 3.2 and 3.3. Collisional quenching due to N_2 was assumed to be negligible. The total decay rate was determined using the

equation

$$k_{tot} = k_f + k_q(T)\left(\sum_i k_{q,i}(T)X_i\right)M \tag{6.8}$$

where k_f is the intrinsic fluorescence rate constant with a value of 5.19 $\times$ 10^6 s^{-1} and k_q rate constants.[65] The empirical temperature profile mentioned earlier was used in a set of inverse power-law equations to calculate the collisional quenching cross-sections for NO-NO and NO-O_2 collisions.[44][62] The collisional quenching cross-sections were used in the Equation 3.6 to determine the temperature dependent collisional quenching rate constant. As mentioned previously, the fluorescence and collisional quenching relaxation pathways produced different NO $X^2\Pi$ ($v'' = 0$) distributions of 0.28 and 0.10, respectively.[70][69]. The composition of the air in ACE produced a convolution of the two limiting cases. Therefore, the fluorescence and quenching fractions determined using equation 6.8 were multiplied by the NO $X^2\Pi$ ($v'' = 0$) population distributions to determine the resulting NO ($v' = 1$) fraction. The resulting fraction was multiplied by the excited NO $A^2\Sigma^+$ ($v' = 1$) population to determine a theoretical NO $X^2\Pi$ ($v'' = 1$) population. To determine a theoretical NO $X^2\Pi$ ($v'' = 1$) S/N profile normal to the surface, Equation 6.7 was employed to determine the population of a select *J* NO $X^2\Pi$ ($v'' = 1$) state. The results of the model were compared to a representative L3 MTV image pair presented in Figure 6.9. The write lines in Figures 6.9a and 6.9b are marked with the red rectangles. The additional lines were reflections from the window insert surface. The focal point for the write beam was above the image viewing area so the beams diverged toward the surface. The relative S/N decreased near the surface for both the write and read images. The total integrated signal of the write and read line was was plotted against the distance normal to generate the solid dark blue curves shown in 6.10 The gradual increase in the write beam S/N curve was attributed to the beam divergence. The sharp decrease was due to the decrease in the local density near the surface. The simulated write beam curve modeled the S/N trend well; however, the location of the decrease in the S/N ratio was predicted to be closer to the surface. The discrepancy was attributed to the nonuniform seeded NO gas density. The simulated

read curve predicted a local maximum above the surface. The local maximum was a function of the probed write and read *J* state combination because of their respective temperature dependent distribution. The instantaneous and average read curves both had local maximums at $\sim$10 mm where the simulated local maximum was at 4 mm above the surface.

The model allowed for an optimization of the MTV signal within the boundary layer and predicted a write/read combination of *J* 8.5 would yield the highest S/N ratio. An experiment was designed and performed to validate the model prediction. A small cubic cell was positioned within the ACE facility to mimick the environment for the velocimetry campaign. A N_2/NO mixture was introduced into the small static cell under slow flow conditions. The pressure was varied at a fixed temperature (293K) to change the NO number density. The probed write and read *J* state transitions were varied to observe the effects of the excitation combination. Table 6.2 details the 4 distinct write and read laser combinations used for the following cube experiments. The *J* 7.5 state was chosen based on the rotational distribution for the given static cell temperature. The cubic cell

	Write *J* 0.5	Write *J* 7.5
Read *J* 1.5	Case 1	Case 2
Read *J* 7.5	Case 3	Case 4

Table 6.2: Static cubic cell excitation combinations.

was was vacuumed down to reduce any effects of oxygen quenching. A slow flow of 1% NO in N_2 mixture was introduced continuously to maintain a constant pressure ranging from 1.0 Torr to 15 Torr. The write beam was tuned to *J* 0.5 or *J* 7.5 of the P_{21}/Q_1 $A^2\Sigma^+$ ($v' = 0$) $\leftarrow$ $X^2\Pi_{1/2}$ ($v'' = 0$) branch. The write beam propagated through a pair of cylindrical lens to produce a $\sim$2 cm 800 μm sheet. The laser sheet then propagated through a microcylindrical lens array to produce multiple write lines. The beams propagated straight through the cubic cell. A read beam was tuned to *J* 1.5 or *J* 7.5 of the P_{21}/Q_1 $A^2\Sigma^+$ ($v' = 1$) $\leftarrow$ $X^2\Pi_{1/2}$ ($v'' = 1$) branch. The read beam propagated through a cylindrical lens to produce a $\sim$1 cm 800 μm sheet. The sheeted read laser overlapped the write

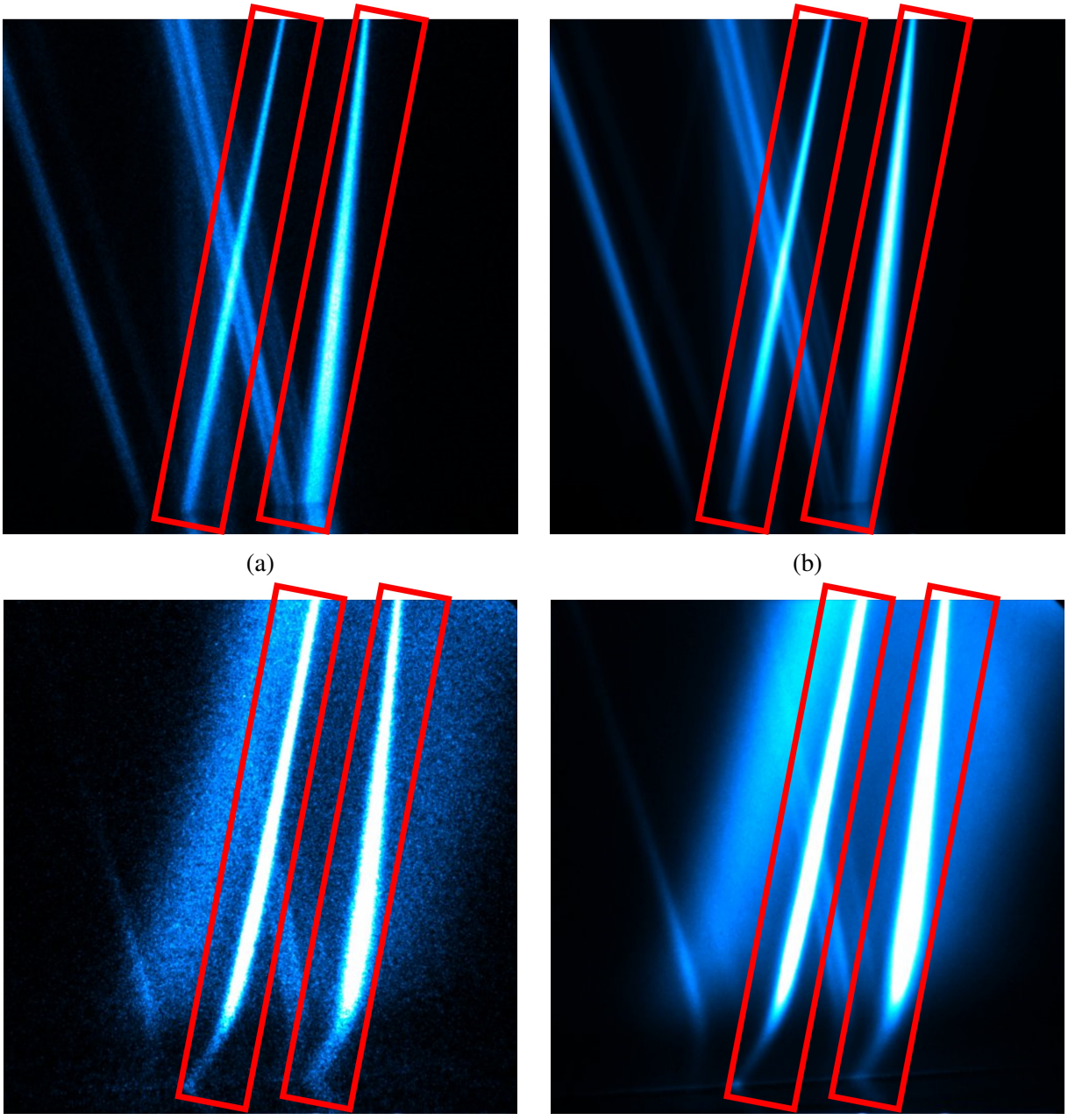

Figure 6.9: Representative MTV fluorescent images where the flow is from left to right. Figures a and b are the instantaneous and average images, respectively, for the write beam. Figures c and d are the instantaneous and average images, respectively, for the read beam.

lines within the cube center. A single camera operated in DIF mode and collected the write and read fluorescent profiles. The cameras had a delay of 2 μs and were gated directly after the laser scatter. The write gate width was set to 3 ns and the read gate width was to 50 ns. The cubic cell

experimental setup is shown in Figure 6.11.

Representative fluorescent images for the probed write transitions and the read transition combinations are shown in 6.12. Comparing Figures 6.12a and 6.12b, the write J 7.5 image had a better S/N fluorescent image. The case 4, Figure 6.12f, image was predicted be the optimal J state combination and this was seen by comparing it to the other image cases. The total integrated signal for the two probed write J states was quantified and normalized relative to one another. The normalized signal intensity was plotted versus the NO number density and the curves are shown in Figure 6.13a. As expected the relative fluorescent signal was greater for the J 7.5 state. The analysis was repeated for the 4 presented cases and shown in Figure 6.13b. The case 1 curve had the smallest observed signal intensity for all of the NO number densities which was expected. Cases 2 and 3 appeared nearly identical to one another given the offset in the write and read J state combinations. The case 4 curve had the largest observed signal intensity which validated the model described previously.

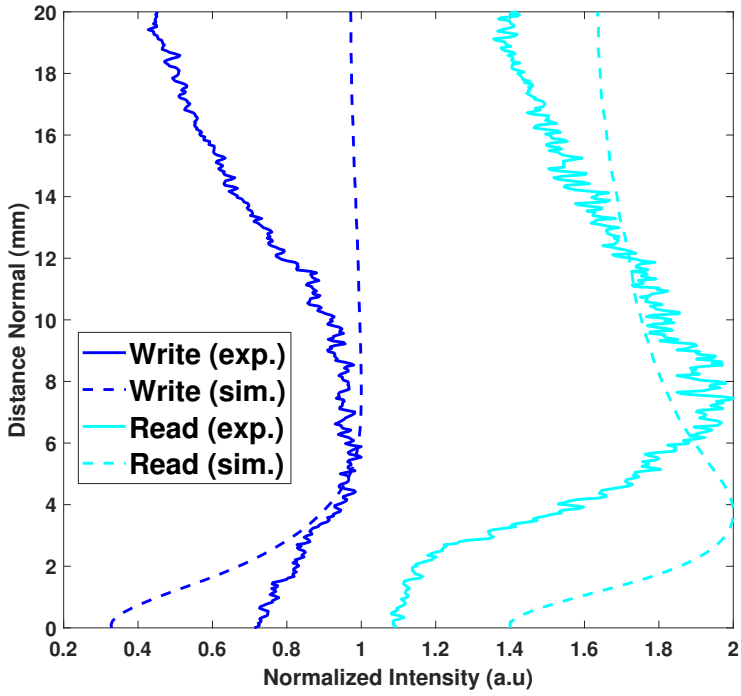

(a)

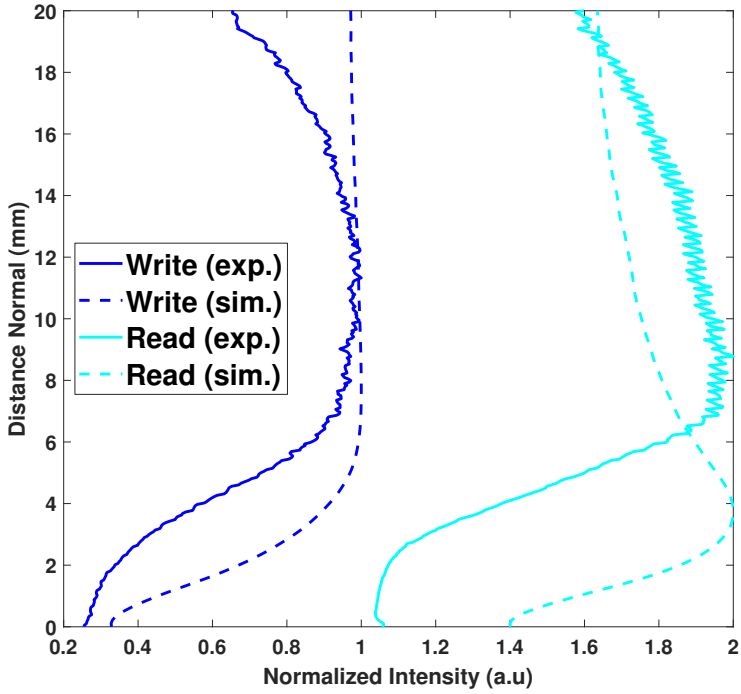

(b)

Figure 6.10: Representative MTV fluorescent images where the flow is from left to right. Figures a and b are the instantaneous and average images, respectively, for the write beam. Figures c and d are the instantaneous and average images, respectively, for the read beam.

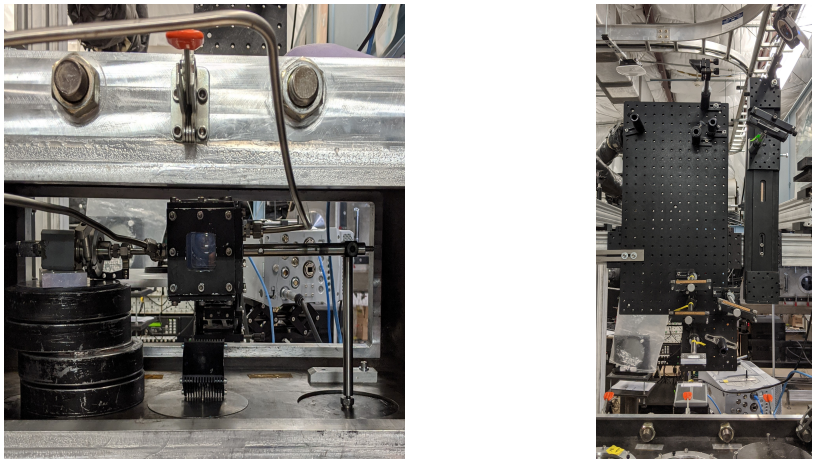

(a) Cube setup within ACE (b) Optical Setup

Figure 6.11: Optimization of NO laser excitation scheme.

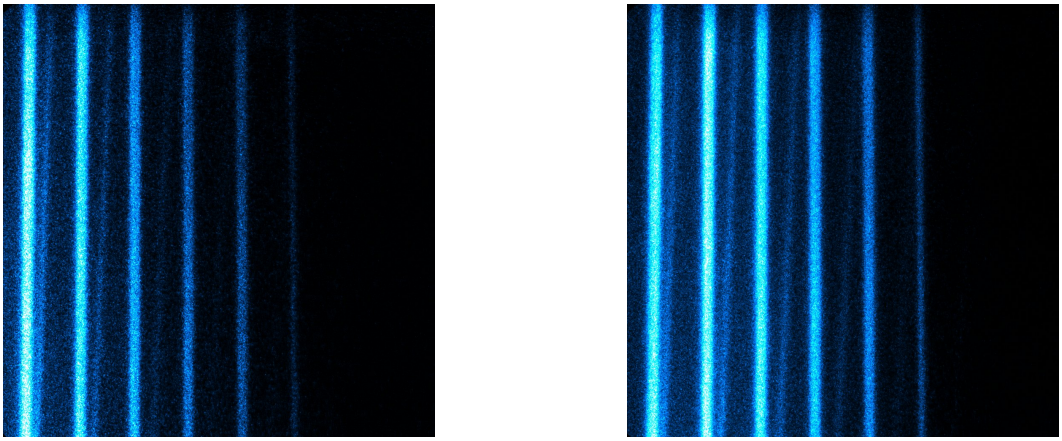

(a)

(b)

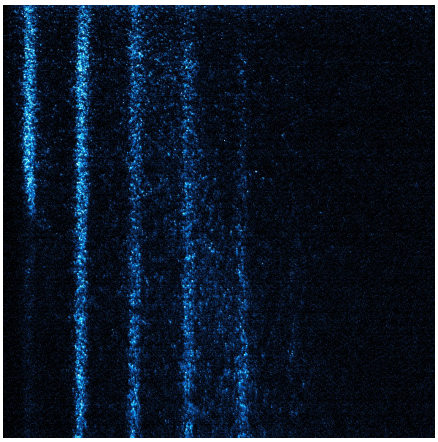

(c)

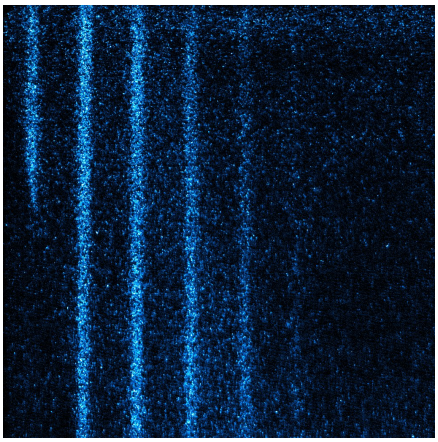

(d)

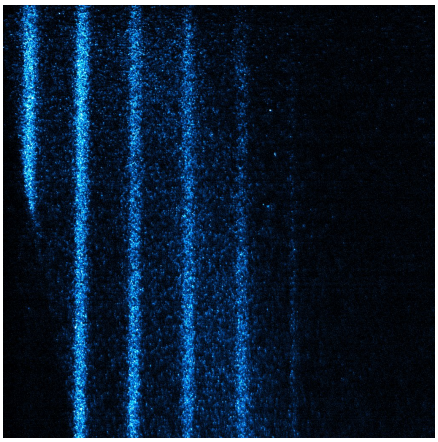

(e)

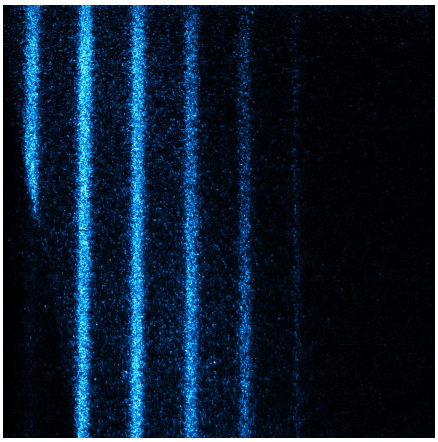

(f)

Figure 6.12: Representative instantaneous images of NO fluorescence following the excitation of select $A^2\Sigma^+ \leftarrow X^2\Pi$ ro-vibronic transitions. Figures a and b displays the write fluorescence following the excitation of the P_{21}/Q_1 J 0.5 and J 7.5 transitions, respectively. Figures c, d, e, and f displays the read fluorescence. Figures c and e wrote with J 0.5 and figures d and f wrote with J 7.5. Figures c and d read with J 1.5 and figures e and f read with J 7.5.

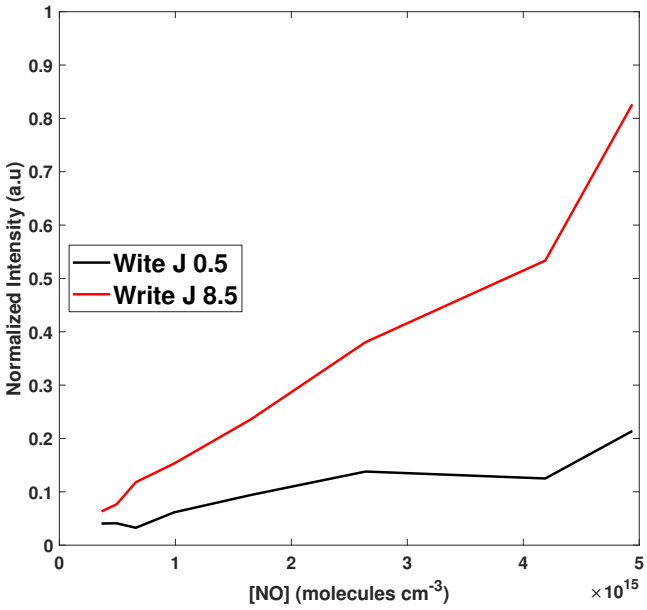

(a)

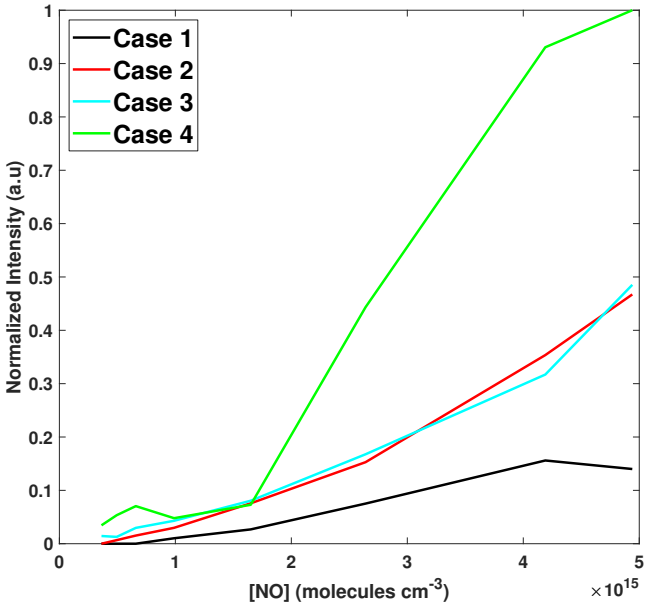

(b)

Figure 6.13: Relative S/N as a function of probed $A^2\Sigma^+ \leftarrow X^2\Pi$ ro-vibronic transitions. Figure a details the relative write fluorescence as a function of select J state and NO number density. Figure b details the relative read fluorescence as a function of select J state combinations and NO number density.

6.4 Streamwise MTV Campaign on a Flat Plate

A 12 run campaign was performed to characterize the role of the TNE within a laminar and turbulent boundary layer behavior. The velocity profile normal to the surface of the plate was characterized for the 1st and 3rd locations. Turbulent velocity profiles were collected downstream of a wake and trough to identify and quantify any potential downstream effects within the boundary layer. The velocity profile normal to the surface and the corresponding velocity fluctuations were the metrics used to compare plasma off and plasma off cases. The ACE tunnel conditions are the same as presented in Table 4.2.

A total of 3 sum frequency laser systems were used for the streamwise velocimetry campaign. Two beams were used as the write lasers and the third beam was the read laser. All beams propagated from the top-down direction of the ACE test section. The write beams were tuned to the J 8.5 of the P_{21}/Q_1 $A^2\Sigma^+$ ($v' = 0$) $\leftarrow$ $X^2\Pi_{1/2}\Pi_{1/2}$ ($v'' = 0$) transition. The read beam was tuned to the J 8.5 of the P_{21}/Q_1 $A^2\Sigma^+$ ($v' = 1$) $\leftarrow$ $X^2\Pi_{1/2}$ ($v'' = 1$) transition. The two write beams were focused down to a line using a f = 30 mm 2" spherical lens. Two separate write beams were used to increase the number of velocity measurements. The beam waist was near the edge of the field of view of the camera. For the wake experiments the beams propagated through the center of the plate at 108 mm from the side of the plate. For the trough experiment the beams propagated through the window inserts at 103 mm from the right side of the plate. A fast response photodiode (Thorlabs Type DET10A) was used to optimize the time settings on the digital delay generator to ensure the beams arrived inside the test section simultaneously. The read beam was sheeted using a pair of cylindrical lens to produce a $\sim$1 cm wide 800 μm sheet. The write laser and read laser had a 2 μs delay between them. The beam power for each laser shot was collected and correlated to the respective acquired image.

A dual camera setup was employed to increase the data acquisition rate to 10 Hz. The cameras had a delay of 2 μs and were gated after the laser scatter. The gate width following the write was beam was varied from 3 ns to 15 ns. The gate width for the read beam was varied from 125 ns to 150 ns. A dual ballast setup was pressurized to 180 PSIA with a 75% mixture of NO

in N_2. The N_2/NO mixture was continuously seeded throughout the duration of the ACE tunnel run. The plasma was powered on following the introduction of the N_2/NO mixture and turned off after the N_2/NO seeding was stopped. A separate program collected the plasma power during the ACE tunnel run. Figure 6.14 displays the experiment configuration for the streamwise velocimetry campaign.

The lasers were intentionally angled relative to the wall normal to ensure the reflected beam did not propagate in the reverse direction. This helps reduce the error in the edge finding algorithm. Representative L1 and LP1 write and read images are shown in Figure 6.15. The S/N decreased below 2.5 mm which suggested the presence of the thermal laminar boundary layer due to the local number density decrease. The L1 incident beams were located at $\sim$109 mm and $\sim$116 mm and will be referred to as Line 1 and 2, respectively. The other two observed laser lines were reflections from the top and bottom surface on the window insert. In the freestream the lines displaced $\sim$2 mm. Uncertainty error bars for the write lines are plotted in Figure 6.16a, but they appear small due to the relative spatial scale. The write lines fluctuated 0.25 to 0.40 pixels which scaled to 10 μm to 20 μm. However, given the known error of the algorithm, the true L1 fluctuations were 0.20 to 0.35 pixels. The origin of the fluctuations were attributed to the ACE facility vibrating during the course of the un. The surrounding table experiences small vibrations causing the optics and camera to vibrate.

The L1 velocity and relative fluctuation curves are overlayed for the two line pairs in Figure 6.16b. The velocity curve is below the bow shock and had a resulting L1 freestream velocity of 845 $\pm$ 13 m/s. The velocity curve exhibited a gradual decrease in the velocity to 835 m/s at 10 mm above the surface followed by a much higher rate of deceleration below this point. The L1 thermal profile presented in Section 4.4.3 had the same trend where there was notable temperature decrease beneath 10 mm. At 2.5 mm the velocity decreased to 650 m/s and this was attributed to the series of weak Mach waves produced by the various steps along the plate. Below 2.5 mm the velocity rapidly decreased due to the laminar boundary layer. Under the no-slip condition the velocity at the wall should be 0 m/s; however, due to the low S/N at the wall the measured velocity

was 70 m/s $\pm$30 m/s. The freestream velocity fluctuations were 1.3% and increased to 3% at 2.5 mm above the surface. Below 2.5 mm the relative fluctuations increased rapidly to 30% to 40%. This was assumed to be the height of the velocity boundary layer based on the current sensitivity of MTV technique within the ACE facility. The correlated fluctuation plots in Figures 6.16c and 6.16d show a distinct relationship between U$'$ and the distance from the wall. The large scale velocity fluctuations occurred exclusively within the boundary layer and were not correlated to the determined write line position fluctuations. The LP1 write and read lines behavior were similar to the L1 image pair. The nascent NO $X^2\Pi$ (v = 1) population described in detail in Section 5.2 was observed in the LP1 read image. The LP1 velocimetry profiles are shown in Figure 6.17. The dark region near the 2^{nd} read line was an artifact from the image pre-processing. The LP1 velocity curve had a freestream velocity of 845 m/s and also displayed a gradual decrease towards 10 mm. There was an 5% to 8% difference between the measured velocity from 9 mm to 2.5 mm. Within the boundary layer the velocity profiles converged to a wall velocity of 70 m/s. The fluctuation curves were identical to one another down to 1.5 mm where they diverged from one another. The MTV lines had very different fluctuation profiles near the surface. The line 1 fluctuation curve was similar to the curves observed for the L1 experiment; however, line 2 suggested there may be a dampening of the observed fluctuation. Given the uncertainty of the measurement at the surface, it appeared the TNE did not have a measurable effect on the velocity profile normal to the surface. Finally, the LP1 fluctuation correlation plots did not show a dependence between the determined write line position and the velocity fluctuations.

Following the laminar measurements, the trip insert was inserted to characterize the upstream turbulent velocity conditions. Representative TW1 and TT1 images are shown in Figure 6.18. The TWP1 and TTP1 images were similar and are not shown for brevity. The nascent NO $X^2\Pi$ (v = 1) population was visible in the upstream trip insert images. Recall there were additional structures present when the trip insert was present *i.e.* the trip shock and the shear layer. The trip shock was not observed; however, the S/N discontinuity across the shear layer region was faintly visible at 14 mm. The TW1 and TWP1 velocimetry profiles are shown in Figures 6.19 and 6.20. The

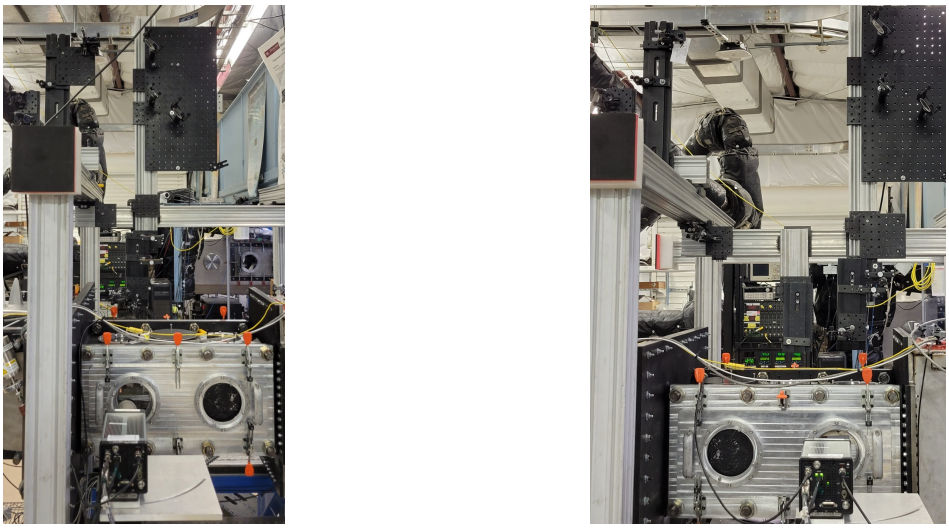

(a) (b)

Figure 6.14: Streamwise velocimetry campaign. Figures a and b were the experimental setup for the 1st and 3rd locations, respectively.

TW1 velocity curves both increase 3% from 20 mm to 14 mm which was consistent with the TW1 temperature results. The flow beneath the trip shock was assumed to undergoes an expansion based on the temperature decrease observed in this region of TW1 temperature curve. From 14 mm to 3 mm the temperature gradually decreased by 17% which was consistent with the temperature increase observed in the TW1 temperature curve. Due to the low S/N near the surface, the wall velocity was 100 m/s $\pm$ 50 m/s and 139 m/s $\pm$ 39 m/s for lines 1 and 2, respectively. The freestream fluctuations from 20 mm to 6 mm increased to 2% to 3% which was attributed to the additional flow structures introduced by the trip geometries. The velocity boundary layer height was 3 mm due to the rapid increase in the fluctuations. The thicker boundary layer may be due to the wakes introduced by the trip geometries. The observed boundary layer fluctuation magnitude was the same as what was observed for the laminar cases. Line 2 of the TW1 measurement appeared to have a slight correlation between the velocity fluctuations and the measured write line position. The TWP1 velocity curve only had a single analyzable line and it was similar to the TW1 velocity curve. There was also a slight 2% velocity increase from 20 mm to 15 mm and again a gradual velocity decrease below this point. There was a small feature at 3.5 mm in which the flow decelerated which

may be a indicative of a weak shock produced by the plate. Plasma induced pressure perturbations have been characterized downstream of a shallow cavity plasma discharge by Leonov *et al.* using fast-response PCB pressure transducers.[140] However, their plasma configurations were higher power and operated in the RF regime. The MTV technique may be sensitive to a small velocity perturbation; however, given the uncertainty error bars it may be an empirical artifact. The TWP1 fluctuations increased at 3.5 mm which maybe due to the weak plasma induced perturbation. The TWP1 boundary layer height was defined to be 3 mm with a wall velocity of 35 m/s $\pm$ 23 m/s. The lower wall velocity yielded a larger relative fluctuation profile compared to the TW1 curve.

The TT1 and TTP1 velocimetry results were very similar to the TW1 and TWP1 results. The TT1 and TTP1 velocimetry profiles are shown in Figures 6.21 and 6.22. There was not a TT1 velocity increase from 20 mm to 14 mm; however, there was a 5% to 6% increase in velocity present in TTP1 curves. Overall the trip insert velocity curves provided evidence of a small expansion beneath the trip shock which was stated in Section 4.4.3. The TT1 and TTP1 velocity curves also illustrated a gradual velocity decrease below 14 mm *i.e* due to the presence of the observed shear layer. Both of the trough velocity profiles had a rapid velocity decrease below 3 mm which agreed with the prior velocity boundary layer heights. Both of the TT1 and TTP1 fluctuation curves had sharp fluctuation increases from 2 to 3 mm above the surface and varied in the overall magnitude. The TT1 and TTP1 had wall velocities $\sim$100 m/s; however, TTP1 line 2 velocity was 200 m/s due to errors in measuring the velocity near the surface. A plasma induced perturbation was not resolved in the TTP1 velocity curve nor the fluctuation curve. The plasma did not have a discernible effect directly downstream when comparing the TT1 and TTP1 velocity and fluctuation curves.

The downstream laminar velocimetry measurements will be discussed first. Representative L3 and LP3 write and read images are shown in Figure 6.23. Similar to the upstream laminar measurements the L3 and LP3 S/N decreased rapidly below $\sim$4 mm suggesting the presence of the thermal laminar boundary layer. The average L3 and LP3 freestream velocity was 835 m/s which was consistent with the freestream velocity measurements upstream. The L3 and LP3 velocity gradually decreased to $\sim$700 m/s at 4 mm where it rapidly decreased beyond this point. The L3

and LP3 freestream fluctuations were both measured to be $\sim$1% which was consistent with the upstream measurements. The velocity fluctuations increased below 4 mm which suggested this was the laminar velocity boundary layer height. The relative velocity fluctuations were fairly large near the surface for both the L3 and LP3 measurements. The LP3 fluctuation correlation plots show a strong correlation between the measured velocity and the write line fluctuation. This appeared to be more pronounced in the freestream velocities fluctuations. The correlation was attributed to the write line moving in space relative to the ACE facility and this was determined to not affect the resulting velocities.

The turbulent MTV images provided a clear difference between the laminar and turbulent boundary layer behavior. Representative TW3 and TT3 write and read images are shown in Figure 6.26. The TWP3 and TTP3 images are not shown for brevity, but they had similar behavior. The turbulent boundary layer read images display a distinct turbulent profile compared to the laminar images. The turbulent read lines appeared to have a greater displacement closer to the wall relative to the laminar read lines. This was intuitive because the average velocity near the surface is larger for a turbulent boundary layer relative to the laminar case. The resulting TW3 velocimetry profiles reflected this behavior as shown in Figures 6.26b. In contrast to the laminar velocity curve, the TW3 velocity began to exhibit a steady decrease beginning at 14 mm. The velocity approached $\sim$500 m/s at $\sim$1.5 mm above the surface, where the laminar velocity at this location was $\sim$325 m/s. Below 1 mm the TW3 velocity decreased to a wall velocity of an average $\sim$75 m/s. The freestream fluctuations were $\sim$1% and began to increase to 11% gradually from 12 mm to 1.5 mm. Based on the fluctuation curve the turbulent velocity boundary layer height was 12 mm. Below 1.5 mm the fluctuations increased to above 50%. The fluctuations were assumed to decrease immediately above the surface due to the laminar sub-layer; however, the low S/N ratio made it difficult to resolve. The TWP3 velocimetry profiles were similar to the TW3 results as shown in Figure 6.27. The TWP3 velocity curve had a gradual decrease in velocity down to 1.5 mm above the surface where again the flow rapidly decelerated. At the 1.5 mm point the velocity was $\sim$550 m/s which was within the error compared to the TW3 velocity at this height. The corresponding

fluctuation curve also exhibited an increase fluctuations below 12 mm where it increased to 12% at 1.5 mm above the surface. The relative fluctuations rapidly increased above %50 below 1.5 mm and appeared to have a peak in the turbulent fluctuations for both MTV lines. However, given the uncertainty of the technique at this location it may be an artifact. The measured TW3 and TWP3 turbulence at the downstream location was consistent with the rotational thermometry results in terms of the nascent TNE having no effect on the turbulent behavior. The empirical velocity metric *i.e.* the velocity fluctuations appeared the same for both the plasma on and plasma off cases. This was the expected result based on the similarity between the TW3 and TWP3 rotational thermometry fluctuation curves. The fluctuation correlation curves for the TW3 and TWP3 did not exhibit a correlation between the write line location and velocity fluctuations. The TT3 and TTP3 curves will be discussed briefly due to their similarity to the turbulent wake results. Both of the trough image sets had only a single analyzable line. The TT3 an TTP3 velocity began increasing steadily at 13 mm and 11 mm normal to the surface, respectively. The velocities at 1.5 mm for the TT3 and TTP3 cases were both 600 m/s which agreed well with the turbulent wake experiments. The fluctuation profiles further supported the previous observation of a $\sim$12 mm turbulent velocity boundary layer height. Lastly, the nascent TNE did not have a measurable effect on the turbulent behavior which has been consistent with all of the presented thermometry and velocimetry results.

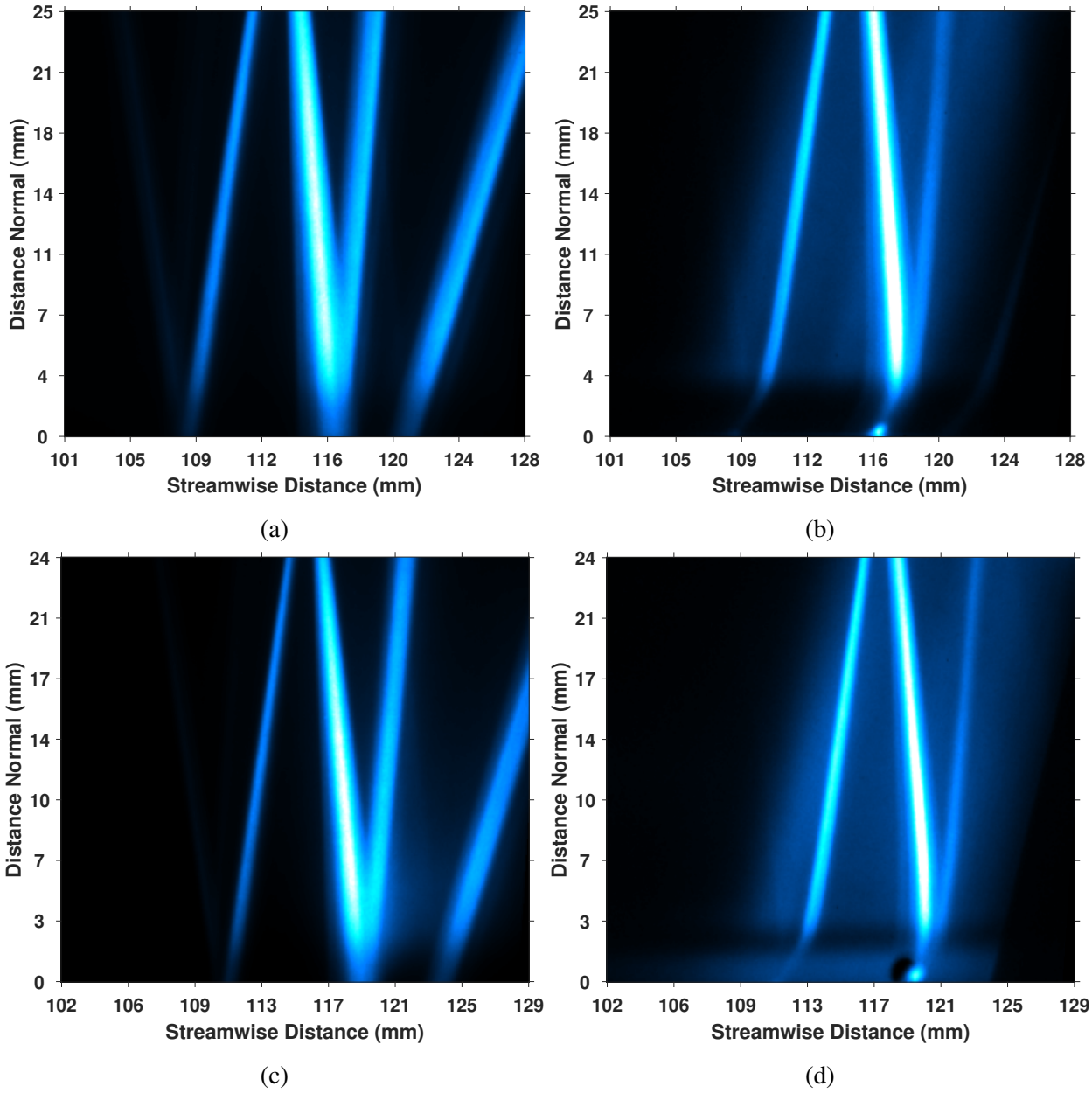

Figure 6.15: Representative fluorescent L1 and LP1 flat plate MTV images. Figures a and b are the L1 write and read image, respectively. Figures c and d are the LP1 write and read image, respectively.

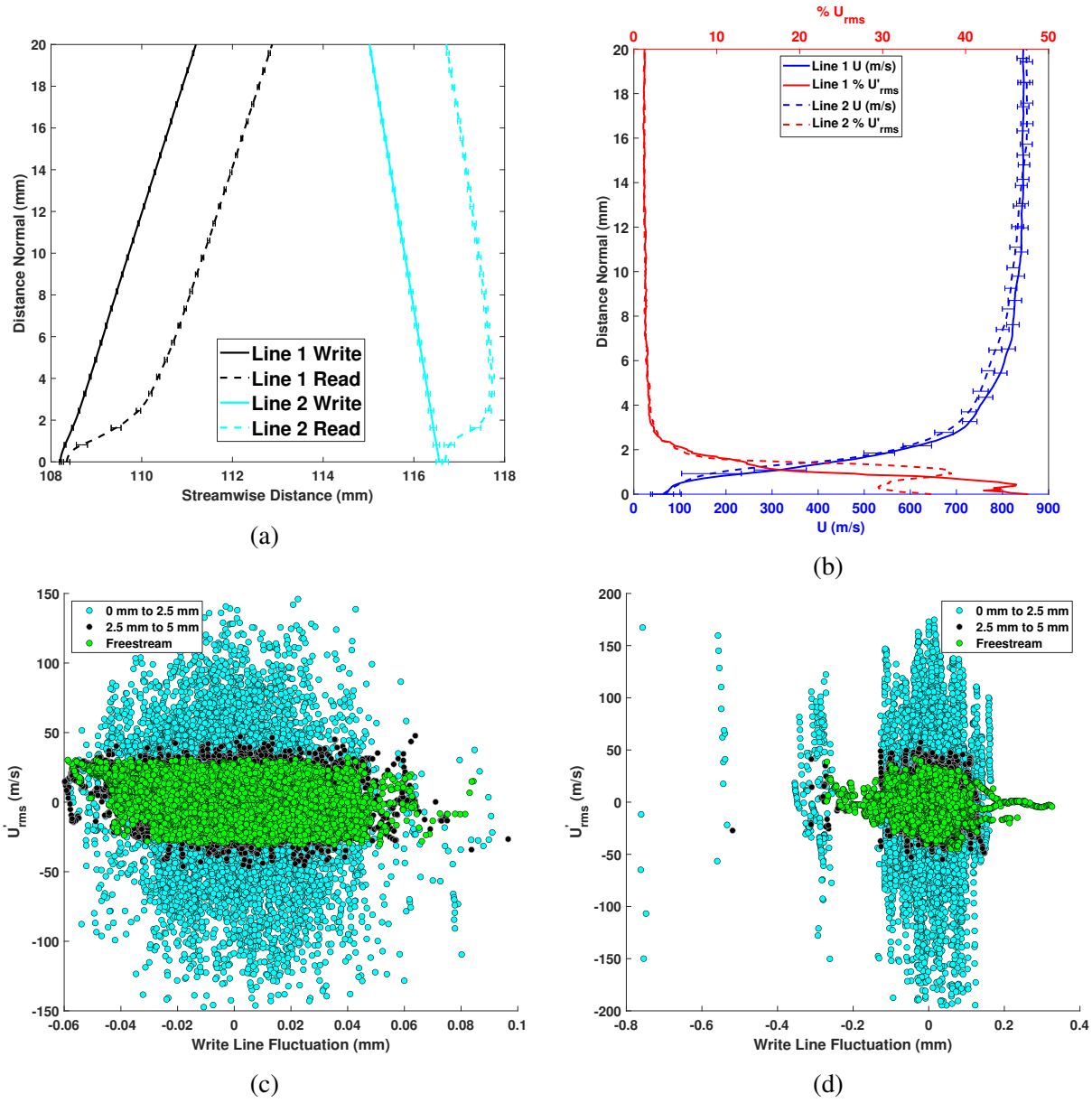

Figure 6.16: Streamwise L1 velocimetry profiles. Figure a are the write and read line positions. Figure b displays the velocity normal to the surface and the corresponding fluctuations. Figure c and d are the fluctuation correlation plots related to line 1 and 2, respectively.

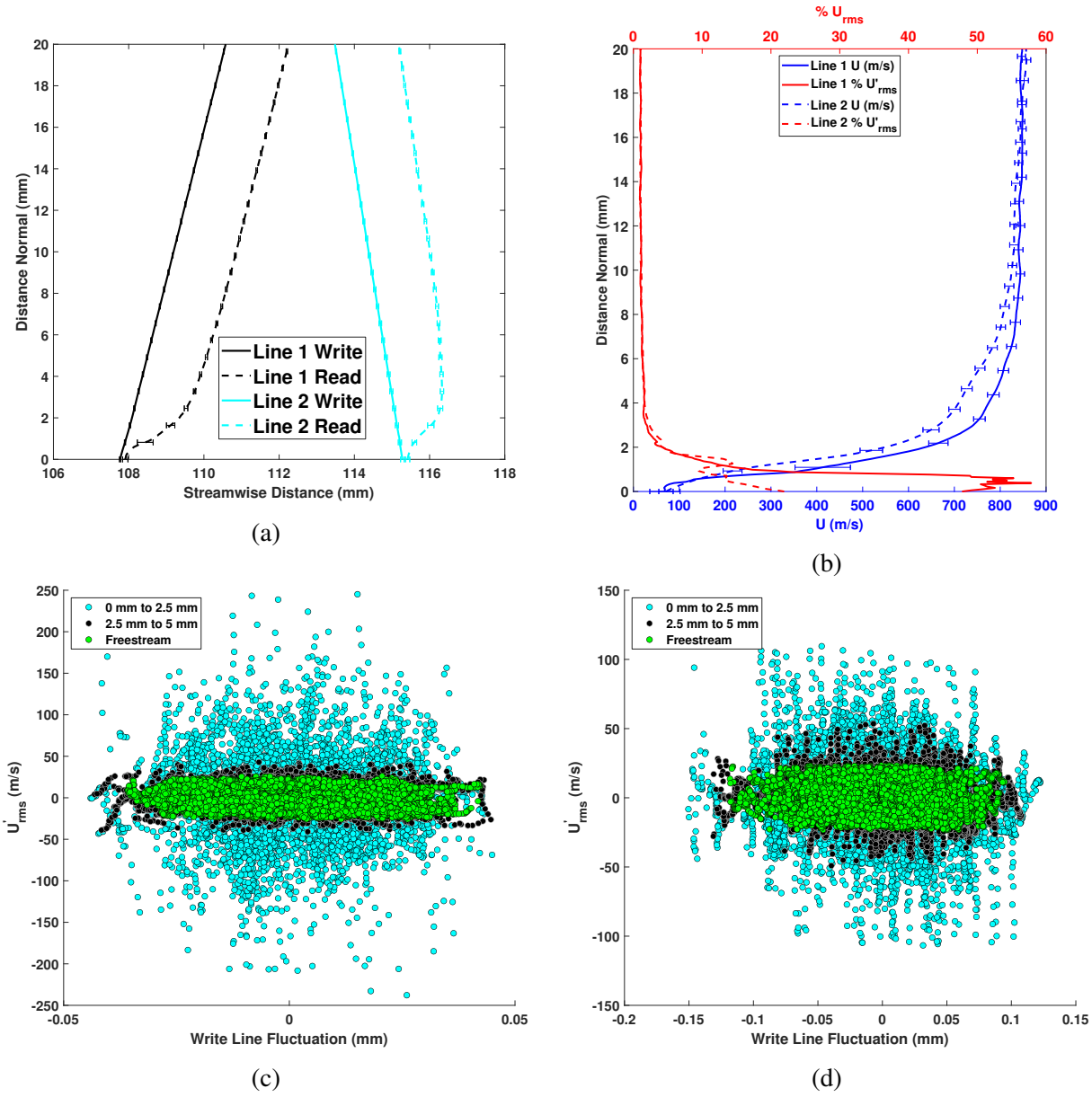

Figure 6.17: Streamwise LP1 velocimetry profiles. Figure a displays the write and read line positions. Figure b displays the velocity normal to the surface and the corresponding fluctuations. Figure c and d are the fluctuation correlation plots related to line 1 and 2, respectively.

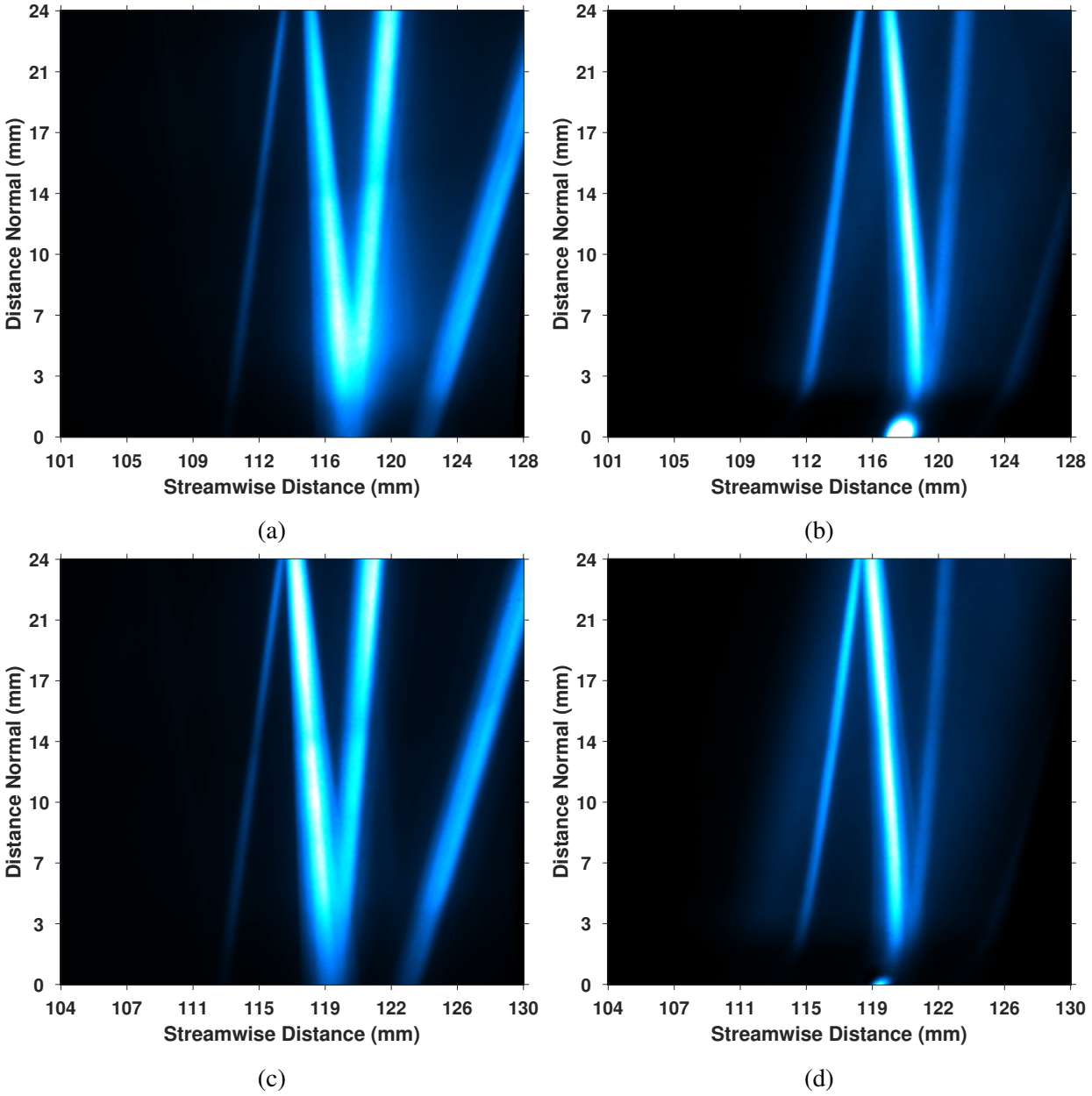

Figure 6.18: Representative fluorescent TW1 and TT1 flat plate MTV images. Figures a and b are the TW1 write and read image, respectively. Figures c and d are the TT1 write and read image, respectively.

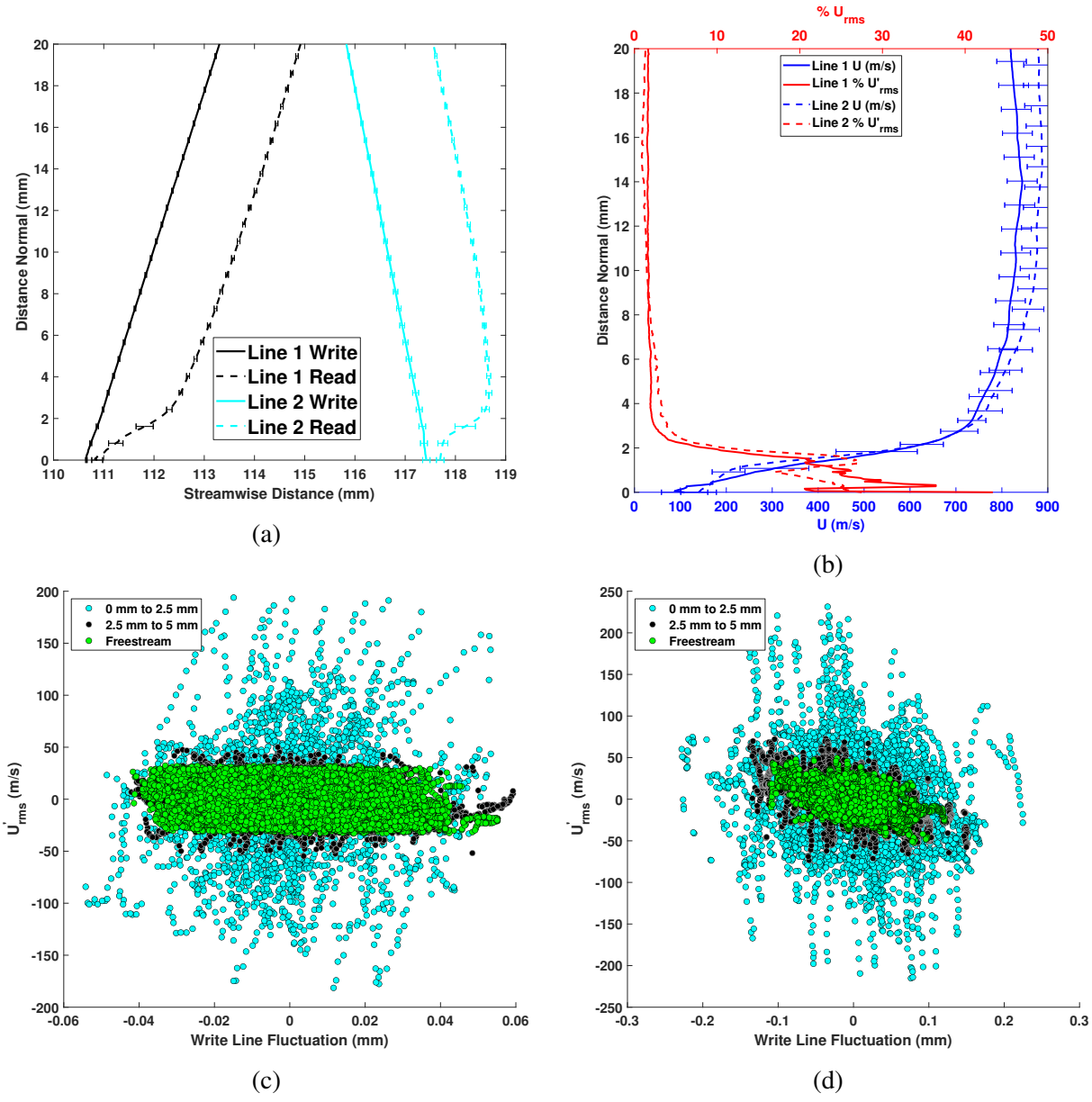

Figure 6.19: Streamwise TW1 velocimetry profiles. Figure a illustrates the determined write and read line positions. Figure b displays the velocity normal to the surface and the corresponding fluctuations. Figure c and d are the fluctuation correlation plots related to line 1 and 2, respectively.

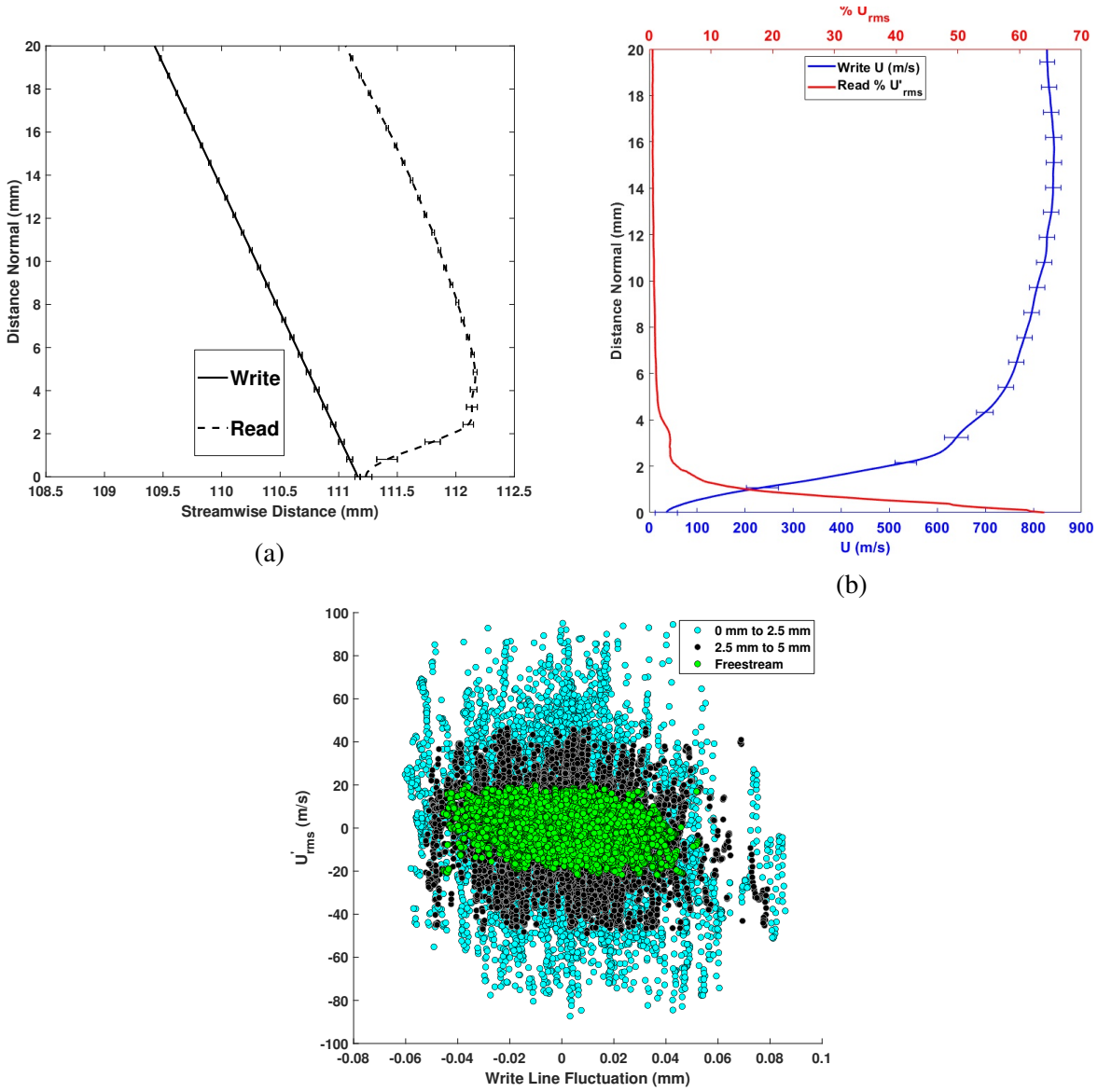

Figure 6.20: Streamwise TWP1 velocimetry profiles. Figure a is the write and read line position. Figure b displays the velocity normal to the surface and the corresponding fluctuations. Figure c is the fluctuation correlation plot related to line 1.

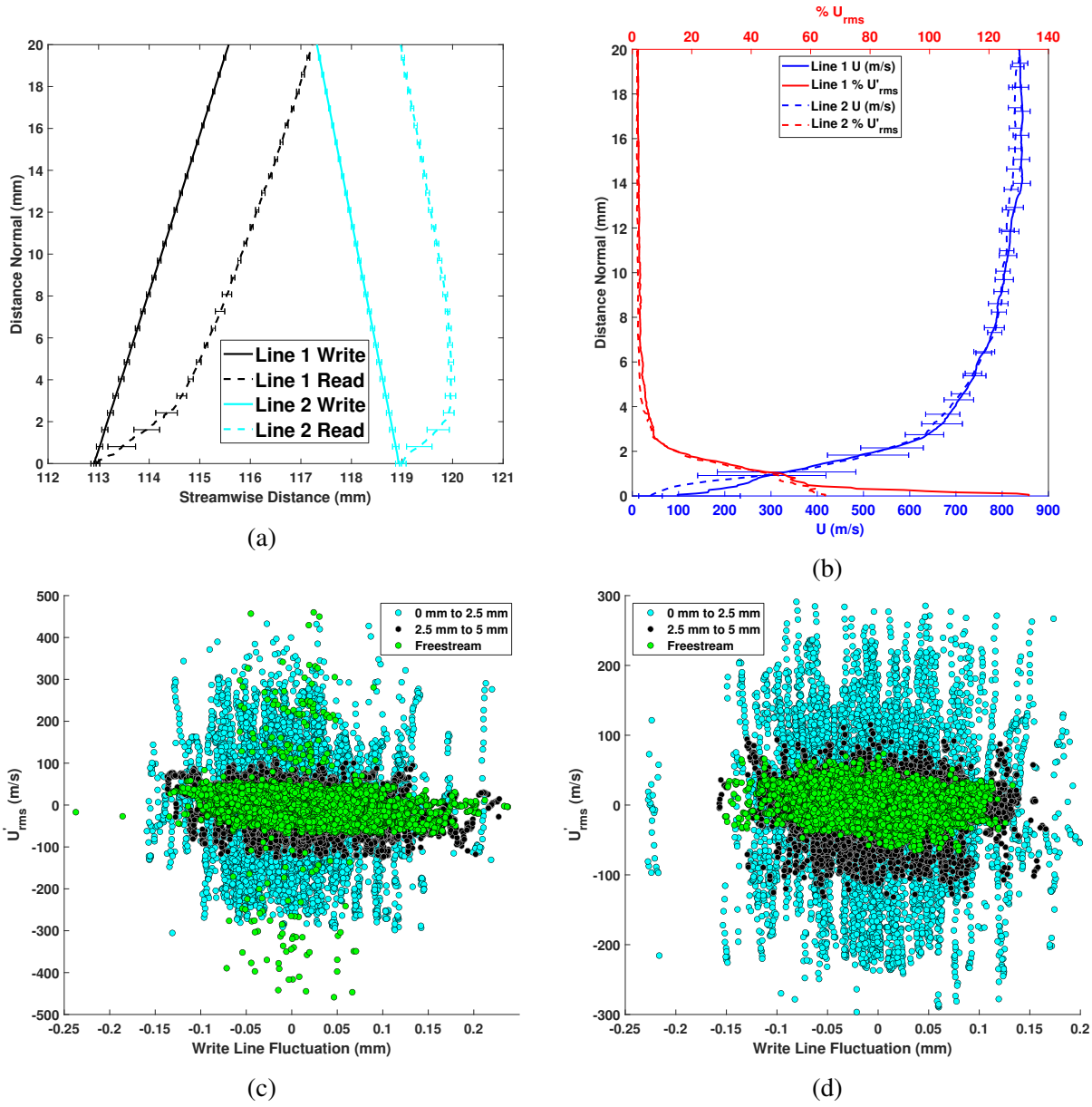

Figure 6.21: Streamwise TT1 velocimetry profiles. Figure a displays the write and read line positions. Figure b displays the velocity normal to the surface and the corresponding fluctuations. Figure c and d are the fluctuation correlation plots related to line 1 and 2, respectively.

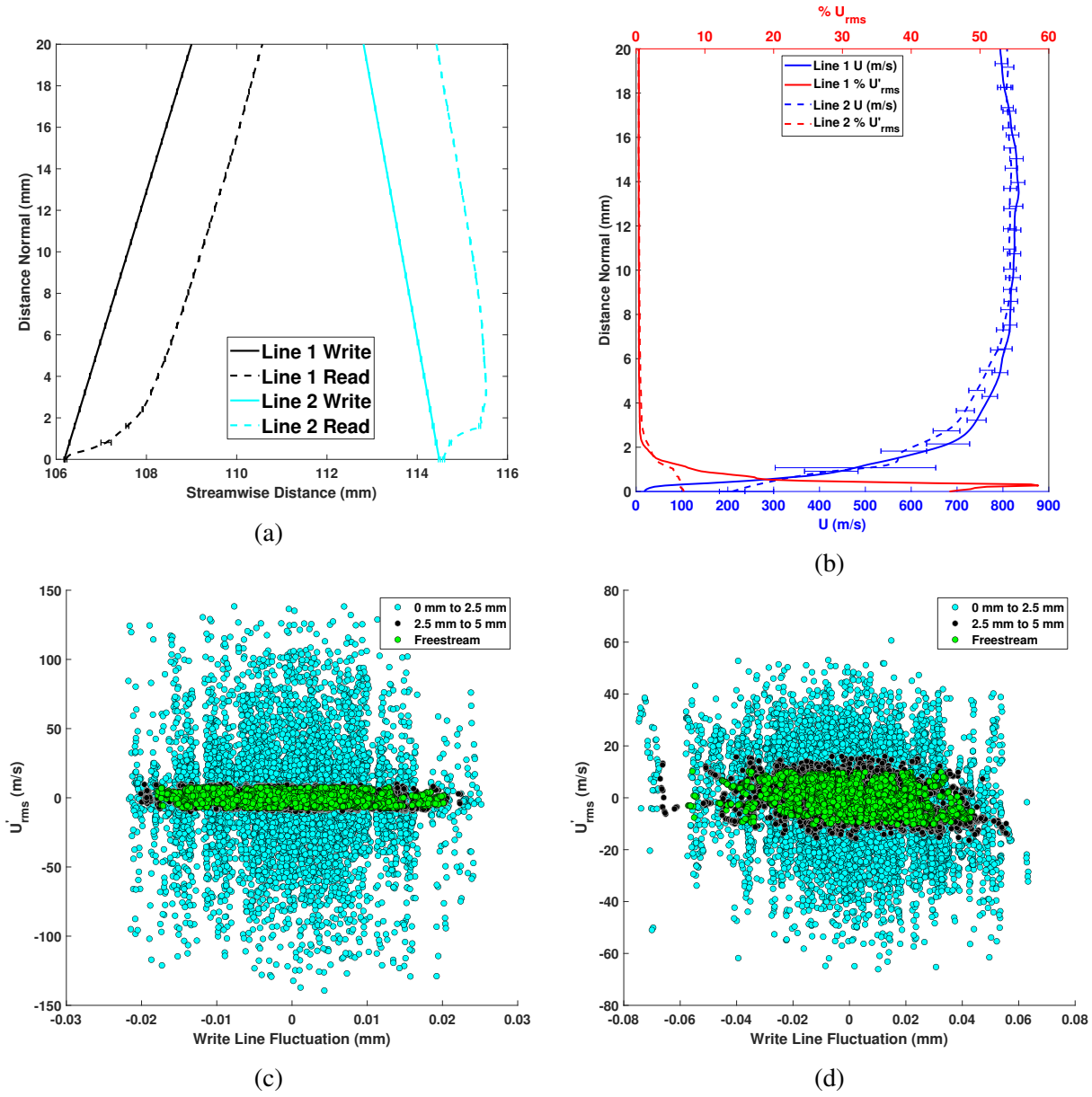

Figure 6.22: Streamwise TTP1 velocimetry profiles. Figure a displays the write and read line positions. Figure b displays the velocity normal to the surface and the corresponding fluctuations. Figure c and d are the fluctuation correlation plots related to line 1 and 2, respectively.

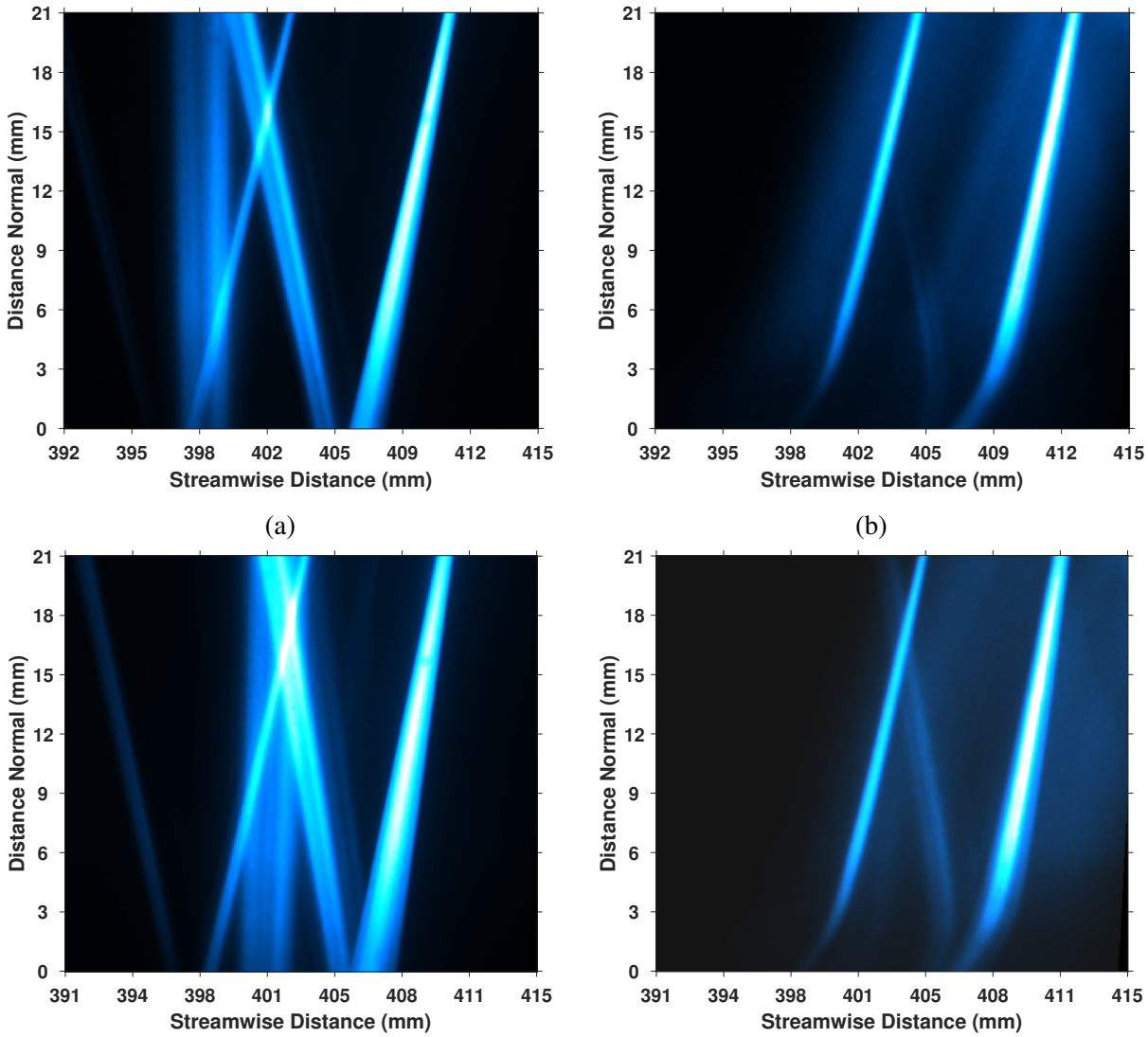

(a) (b)

(c) (d)

Figure 6.23: Representative fluorescent L3 and LP3 flat plate MTV images. Figures a and b are the L3 write and read image, respectively. Figures c and d are the LP3 write and read images, respectively.

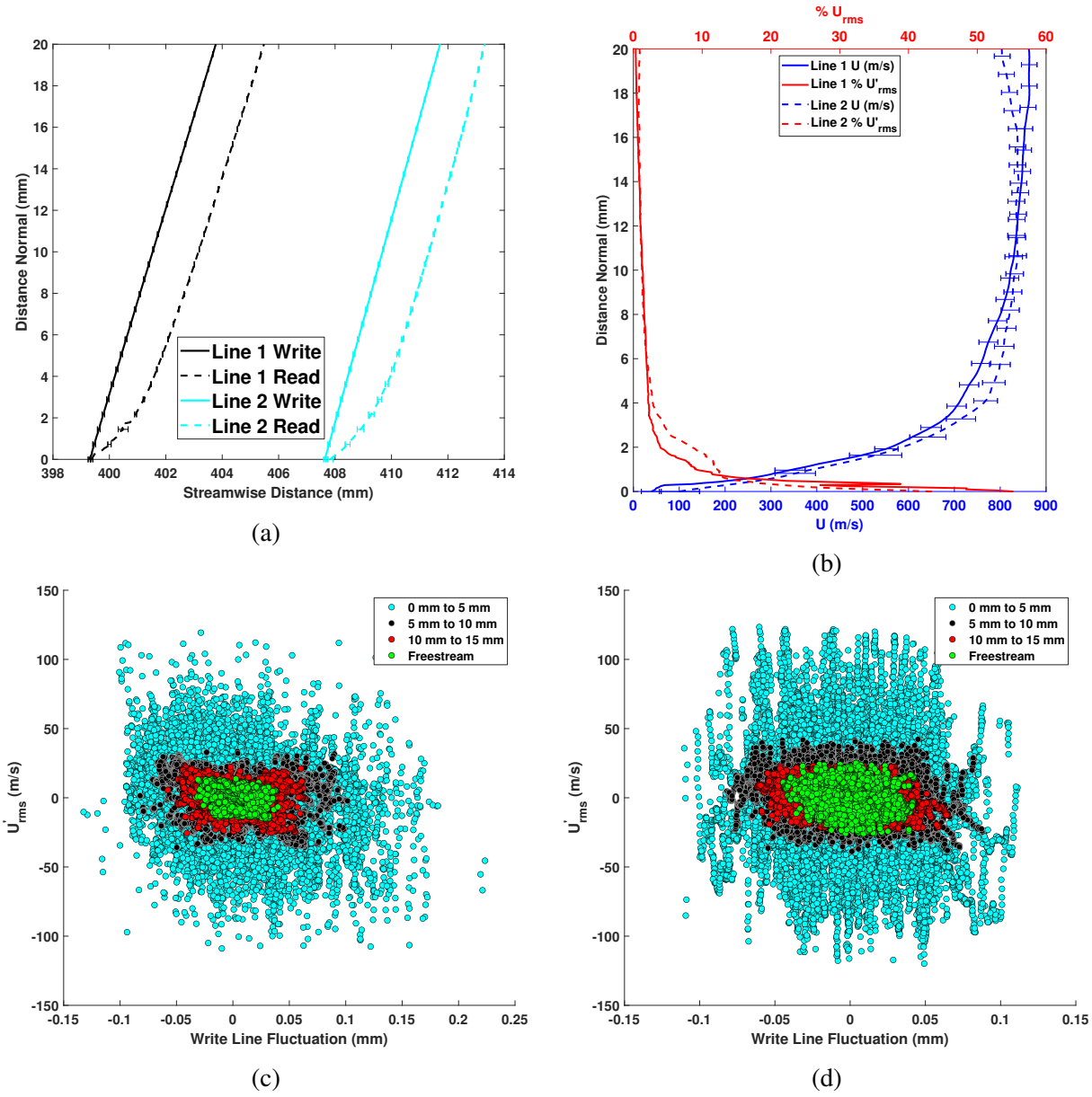

Figure 6.24: Streamwise L3 velocimetry profiles. Figure a displays the write and read line positions. Figure b displays the velocity normal to the surface and the corresponding fluctuations. Figure c and d are the fluctuation correlation plots related to line 1 and 2, respectively.

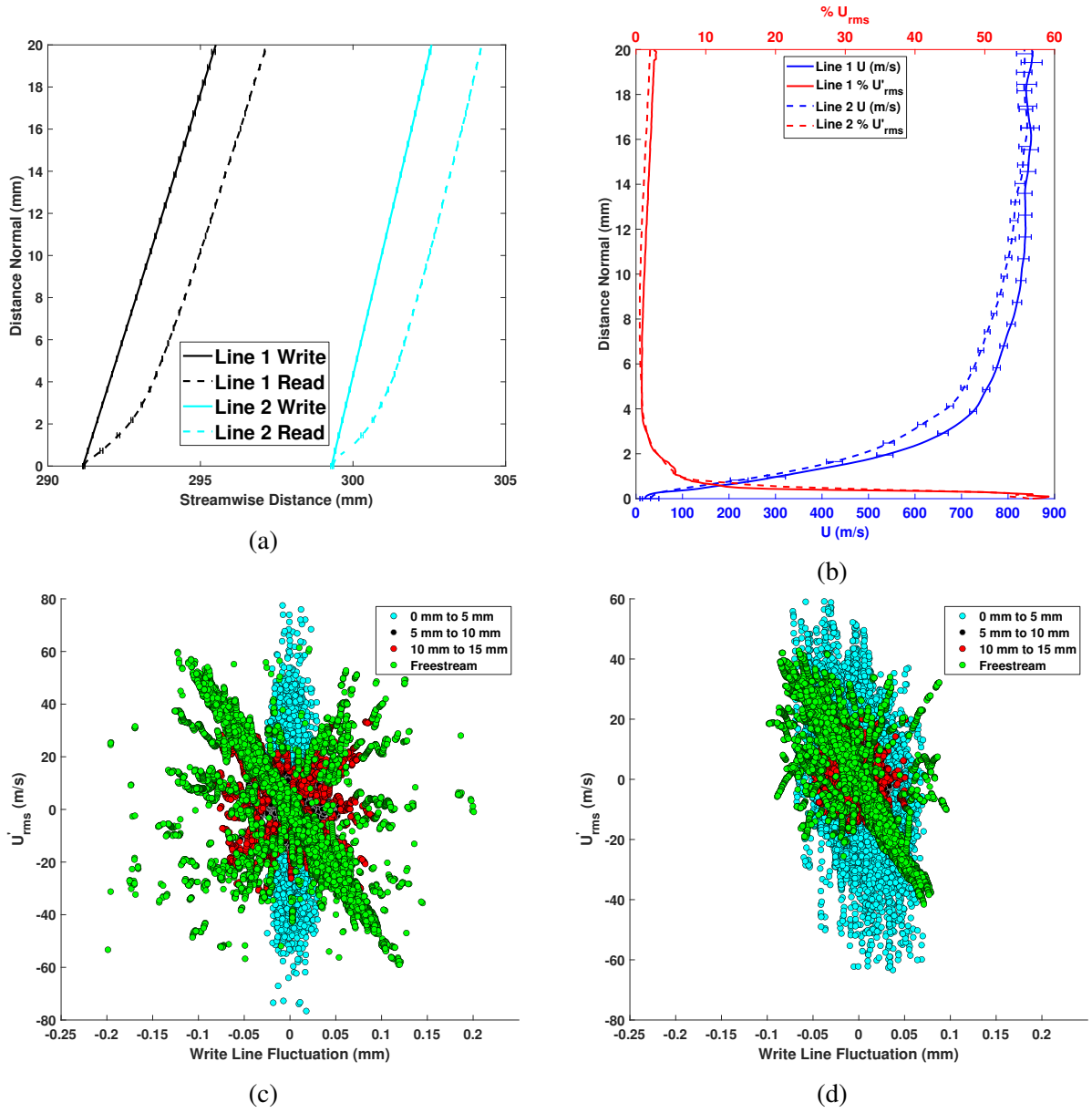

Figure 6.25: Streamwise LP3 velocimetry profiles. Figure a displays the write and read line positions. Figure b displays the velocity normal to the surface and the corresponding fluctuations. Figure c and d are the fluctuation correlation plots related to line 1 and 2, respectively.

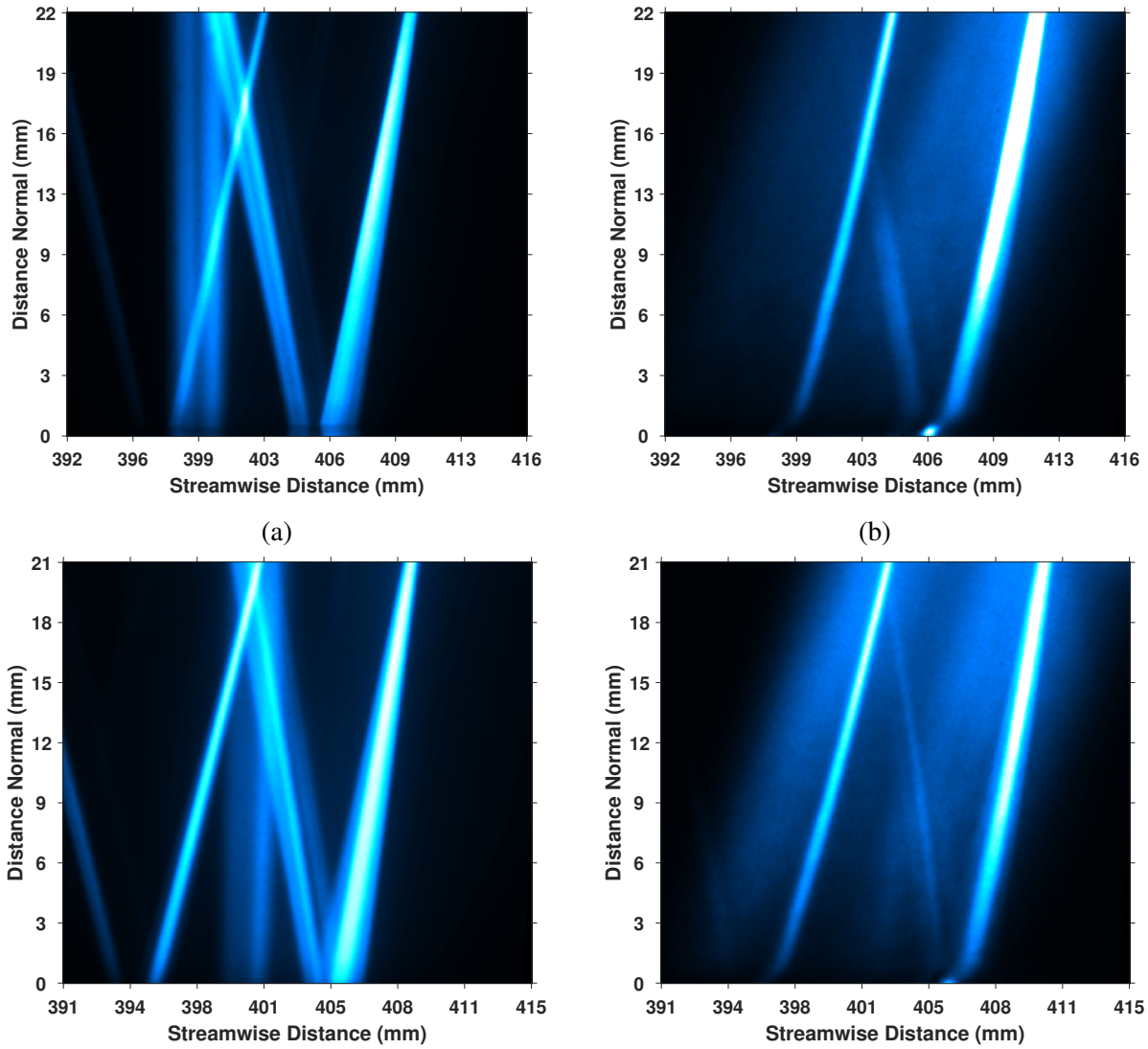

Figure 6.26: Representative fluorescent TW3 and TT3 flat plate MTV images. Figures a and b are the L3 write and read image, respectively. Figures c and d are the LP3 write and read images, respectively.

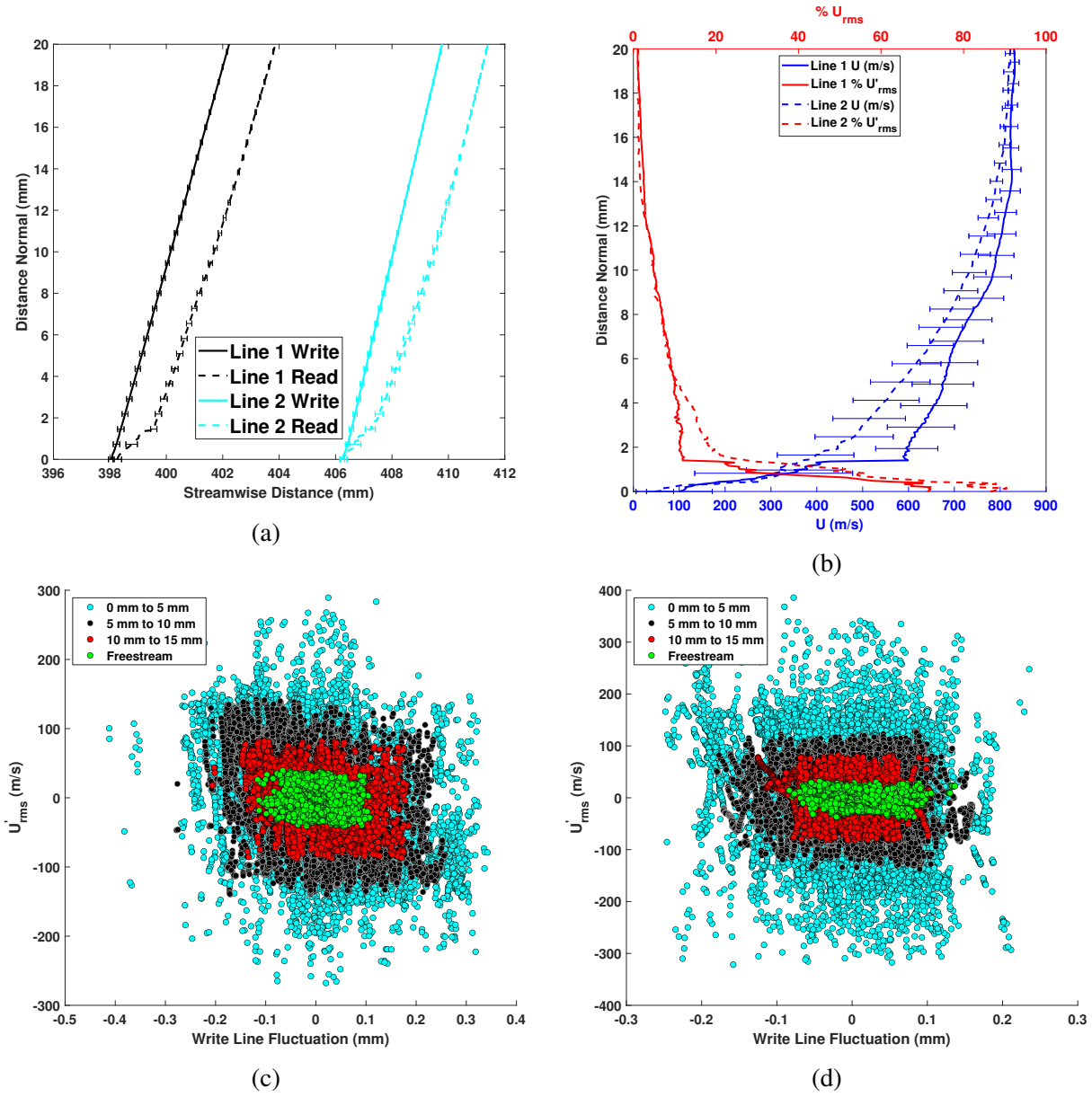

Figure 6.27: Streamwise TW3 velocimetry profiles. Figure a displays the write and read line positions. Figure b displays the velocity normal to the surface and the corresponding fluctuations. Figure c and d are the fluctuation correlation plots related to line 1 and 2, respectively.

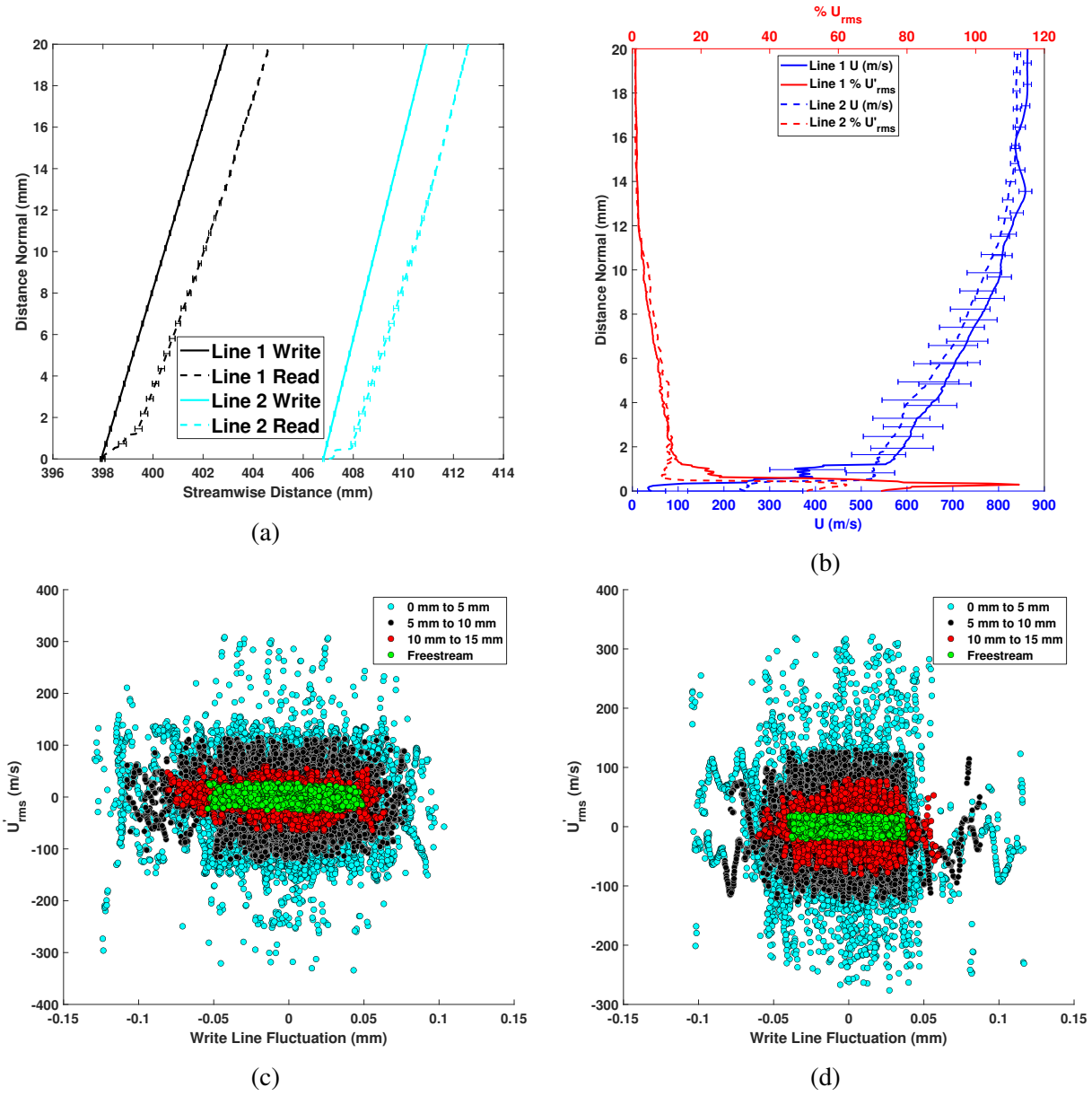

Figure 6.28: Streamwise TWP3 velocimetry profiles. Figure a displays the write and read line positions. Figure b displays the velocity normal to the surface and the corresponding fluctuations. Figure c and d are the fluctuation correlation plots related to line 1 and 2, respectively.

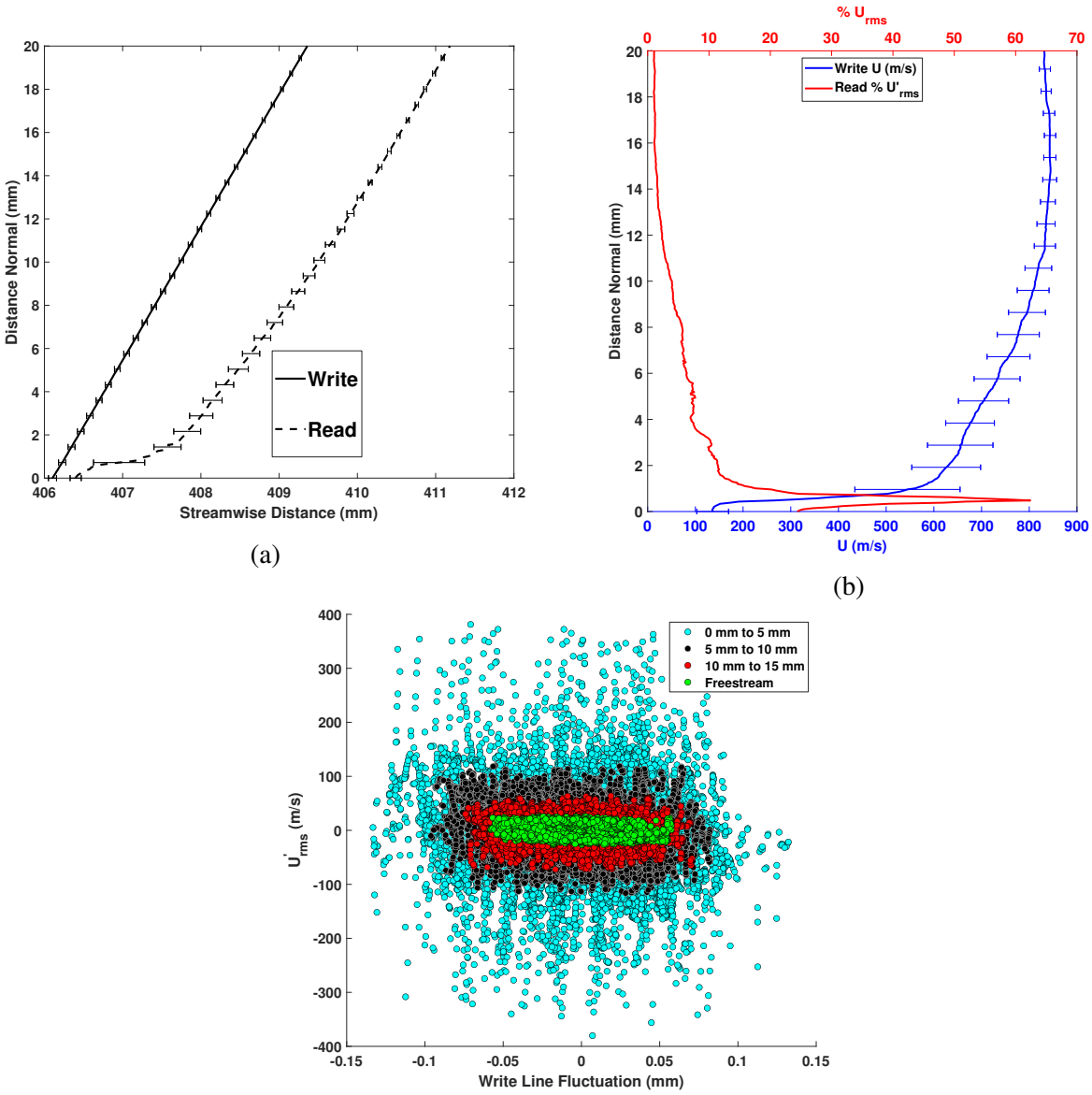

Figure 6.29: Streamwise TT3 velocimetry profiles. Figure a is the write and read line positions. Figure b displays the velocity normal to the surface and the corresponding fluctuations. Figure c is the fluctuation correlation plots related to the write line.

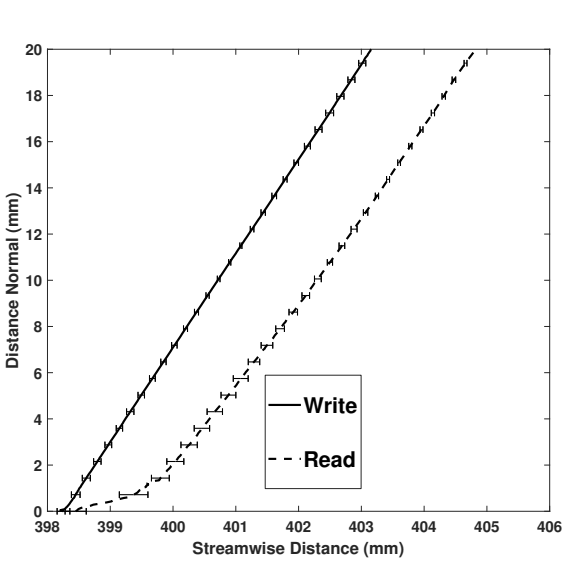

(a)

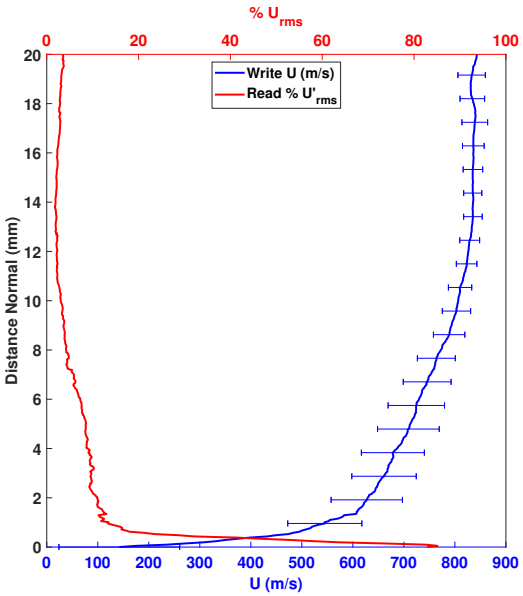

(b)

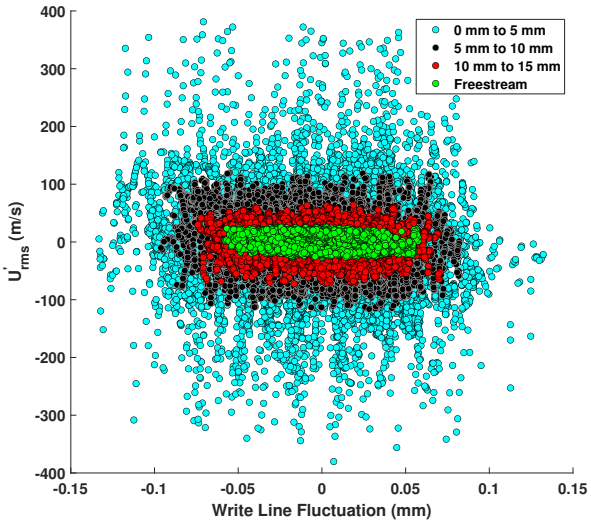

(c)

Figure 6.30: Streamwise TTP3 velocimetry profiles. Figure a is the write and read line positions. Figure b displays the velocity normal to the surface and the corresponding fluctuations. Figure c is the fluctuation correlation plots related to the write line.

6.5 Spanwise Flat Plate Velocimetry

Spanwise velocimetry measurements were performed to characterize the velocity profile across the plate. The goal was to identify any quantifiable differences across the spanwise direction of the plate when the trip insert was used. The spanwise velocity profiles for the 1st and 3rd locations of the plate were measured and collected at a single distance normal to the surface. The experiments will be referred to as L1, L3, T1, and T3 where T1 and T3 refer to a turbulent measurement at the 1st and 3rd locations. Spanwise velocimetry measurements with the plasma on were not performed. The tunnel conditions are the same as presented in Table 4.2.

Two sum frequency mixing systems were used for the spanwise velocimetry campaign. The two beams propagated through the side of the test section. The write beam was tuned to the *J* 4.5 of the Q_{21}/R_1 $A^2\Sigma^+$ ($v' = 0$) $\leftarrow$ $X^2\Pi_{1/2}$ ($v'' = 0$) transition. The read beam was tuned to the *J* 4.5 of the P_{21}/Q_1 $A^2\Sigma^+$ ($v' = 1$) $\leftarrow$ $X^2\Pi_{1/2}$ ($v'' = 1$) transition. The write beam was focused down to a line using a f = 30 mm 2" spherical lens. The beam waist was near the edge of the field of view of the camera. The write beam was 2 mm normal to the surface for the laminar cases and 3 mm normal to the plate for the turbulent cases. Due to the optical access at the 3rd location the write beam propagated over the plate 435 mm from the leading edge. The read beam was sheeted using a pair of cylindrical lens to produce a $\sim$1 cm wide 800 μm sheet. The write laser and read laser had a 4 μs delay between them. The beam power for each laser shot was collected and correlated to the respective acquired image.

A single camera was mounted above the test section and operated in the DIF mode. The camera was mounted above the test section and angled to 2.75° relative to the test section. The two images were delayed 4 μs and the two images were gated after the laser scatter. The gate width following the write beam was set to 3 ns and the read beam gate width was gated at 150 ns. A single ballast was pressurized to 180 PSIA with a mixture of 25% NO in N_2. The N_2/NO mixture was continuously seeded throughout the duration of the ACE tunnel run. Figure 6.31 displays the experiment configuration for the streamwise velocimetry campaign.

Representative spanwise L1 write and read images are shown in Figures 6.32a and 6.32b. The

(a) (b)

Figure 6.31: Spanwise velocimetry campaign. Figures a and b are the experimental configurations for the 1st and 3rd locations, respectively.

bright and dim regions in the write image was evidence of the non-uniformity in the NO seeding. The write line fluctuated 0.5 to 1.5 pixels which correlated to a 20 μm-75μm spatial fluctuation as shown in Figure 6.32c. Given the laminar behavior along the flat plate the measured fluctuations should be uniform in the spanwise direction. An IR thermography campaign performed by Casey Broslawski did not observe flow non-uniformities across the plate. The resulting velocity and fluctuation curves were unexpected because they were not uniform across the 40 mm span. The velocity at -20 mm was 620 m/s and increased to 635 m/s at 0 mm and then increased rapidly to 700 m/s at +20 mm. The write line was aligned 2 mm above the surface which would yield a velocity of 578 m/s with a relative velocity fluctuation of 6.5%. The error could be due to several experimental errors such as a slight angle between the write line and the plate parallel. Also in the write image the beam was diverging due to the spherical focusing lens. Therefore, the total population of the electronically excited NO $X^2\Sigma^+$ state was a function of the Gaussian beam distribution. The acquired fluorescence was a convoultion of a finite portion of the laminar boundary layer. The spanwise L1 beam varied from 0.5 mm to 2 mm in diameter. Using the velocity and the relative fluctuation curves from Section 6.4, the spanwise L1 velocimetry results

were rationalized. The streamwise L1 velocity at -20 mm correlated to a location 2.2 mm normal to the plate with a streamwise velocity fluctuation of 4.9%. This was supported well with the observed velocity fluctuation curve in Figure 6.32d. The L1 velocity at +20 mm correlated to a location 2.8 mm above the plate with a streamwise velocity fluctuation of 2.5%. The agreement between the spanwise and streamwise velocimetry measurements demonstrate the sensitivity of the MTV technique within the laminar boundary layer. The downstream L3 MTV images and velocimetry plots are shown in Figure 6.33. The write and read images reaffirmed the flow remained laminar in the spanwise direction as the flow traveled the length of the plate. The beam was thicker and varied from 1 mm to 3.5 mm in diameter. The velocity curve gradually increased from 200 m/s at -20 mm to 400 mm at +20 mm. The spanwise velocity gradient was attributed to the previously mentioned experimental errors. A 200 m/s spanwise velocity correlated to 0.5 mm above the surface with a relative streamwise velocity fluctuation of 24%. The 200 m/s spanwise velocity correlated to 1.2 mm above the surface with a relative streamwise velocity fluctuation of 8.2%. This observed spanwise fluctuations did not agree well with the streamwise fluctuations, but the fluctuation trend normal to the wall was consistent. The write beam was much thicker in the spanwise L3 location which convoluted a large portion of the 4 mm thick velocity boundary layer.

The spanwise turbulent experiments, T1 and T3, helped visualize how the trip inserts produce turbulence downstream. The T1 write and images are shown in Figures 6.34. There was an oscillatory pattern related to the spanwise S/N intensity due to the trip insert. The dim regions were directly downstream of the trip geometries *i.e.* the wakes and the bright regions were the troughs. This pattern was consistent in the read image where bands of NO fluorescence were observed in the trough region. The oscillatory pattern was indicative of wake formation around the individual trip geometries. The flow separated as it moved around the trip and produced wake-like structures downstream. This was clear in the average line positions shown in Figure 6.34c where the wake structures were clearly observed. The velocity and relative fluctuation curves shown in Figure 6.34d provide a clear illustration of the local velocity gradients introduced by the trip insert. The flow velocity was much higher downstream a trough relative to the flow downstream

of a wake. Sanchez-Gonzalez *et al.* observed a local minimum in the flow velocity directly behind a cylinder using the VENOM technique to characterize the flow around a cylinder.[93] They also observed a temperature increase downstream of the cylinder causing a decrease in the local number density which may account for the oscillating signal intensity observed here. The trough structures had a Gaussian like distribution with a local minimum in the center of the distribution. This local decrease in velocity was attributed to the counter rotating vortices produced by the trip geometry.[141] The interface between these two vortices introduced a local shear layer which has been shown to result in flow deceleration and instability growth. These local minimum are separated by $\sim$6 mm which was the distance between the center of each trip geometry. The relative velocity fluctuation curve also tracks with the presence of the wake structures. There were local relative fluctuation minimums a trough suggesting the flow between the trip geometries remained unaffected at the 1st location. The local fluctuation maximums were attributed to the counter rotating vortices actively mixing the local fluid elements. Comparing the curves in Figure 6.34d to the streamwise TW1 and TT1 velocimetry curves did not agree well. There was no discernible difference between the two streamwise velocity profiles. This may be due to the reasons mentioned earlier *i.e.* the write beam diameter and the write beam propagation angle. However, the spanwise velocimetry measurements clearly demonstrated the 1st location wake and trough flow differences. The downstream T3 write and read images are shown in Figures 6.35a and 6.35b, respectively. The oscillatory behavior in the signal intensity profile has disappeared indicating a considerable degree of 3-D mixing at the 3rd location. The read line position in Figure 6.35c does not contain any evidence of long-standing structure. Additionally the velocity profile was relatively consistent which was expected based on the streamwise turbulent velocity profiles. The T3 spanwise velocity of 650 m/s correlated to a location $\sim$3.8 mm above the surface and a relative velocity fluctuation of 10% which was in excellent agreement spanwise relative velocity fluctuation. The T3 velocimetry plots, Figure 6.35d suggests the flow was near fully turbulent, if not entirely turbulent at the 3rd location.

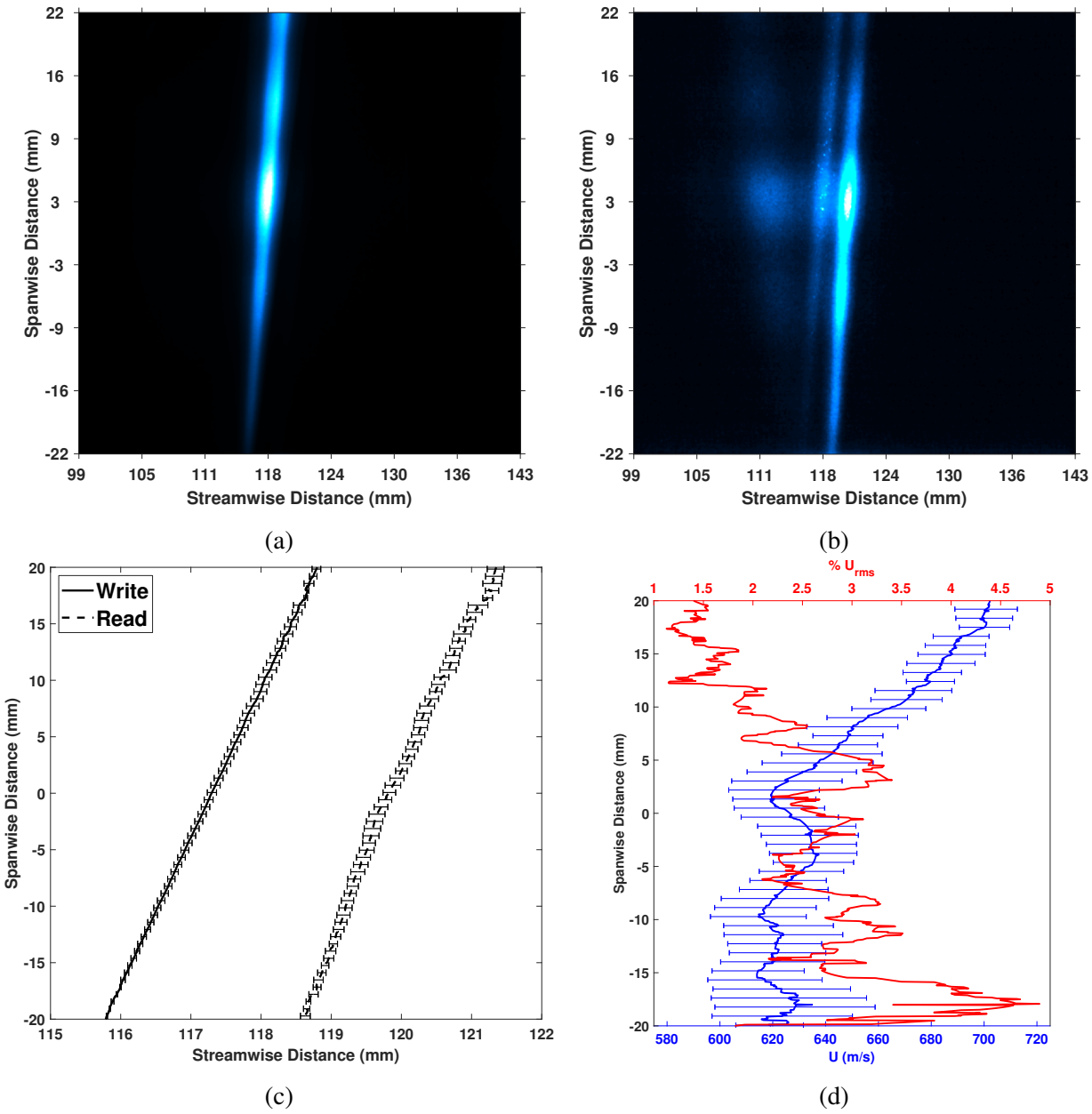

Figure 6.32: Spanwise L1 write and read velocimetry. Figures a and b are write and read images, respectively. Figure c depicts the average write and read line positions. Figure d illustrates the spanwise velocity and corresponding fluctuations.

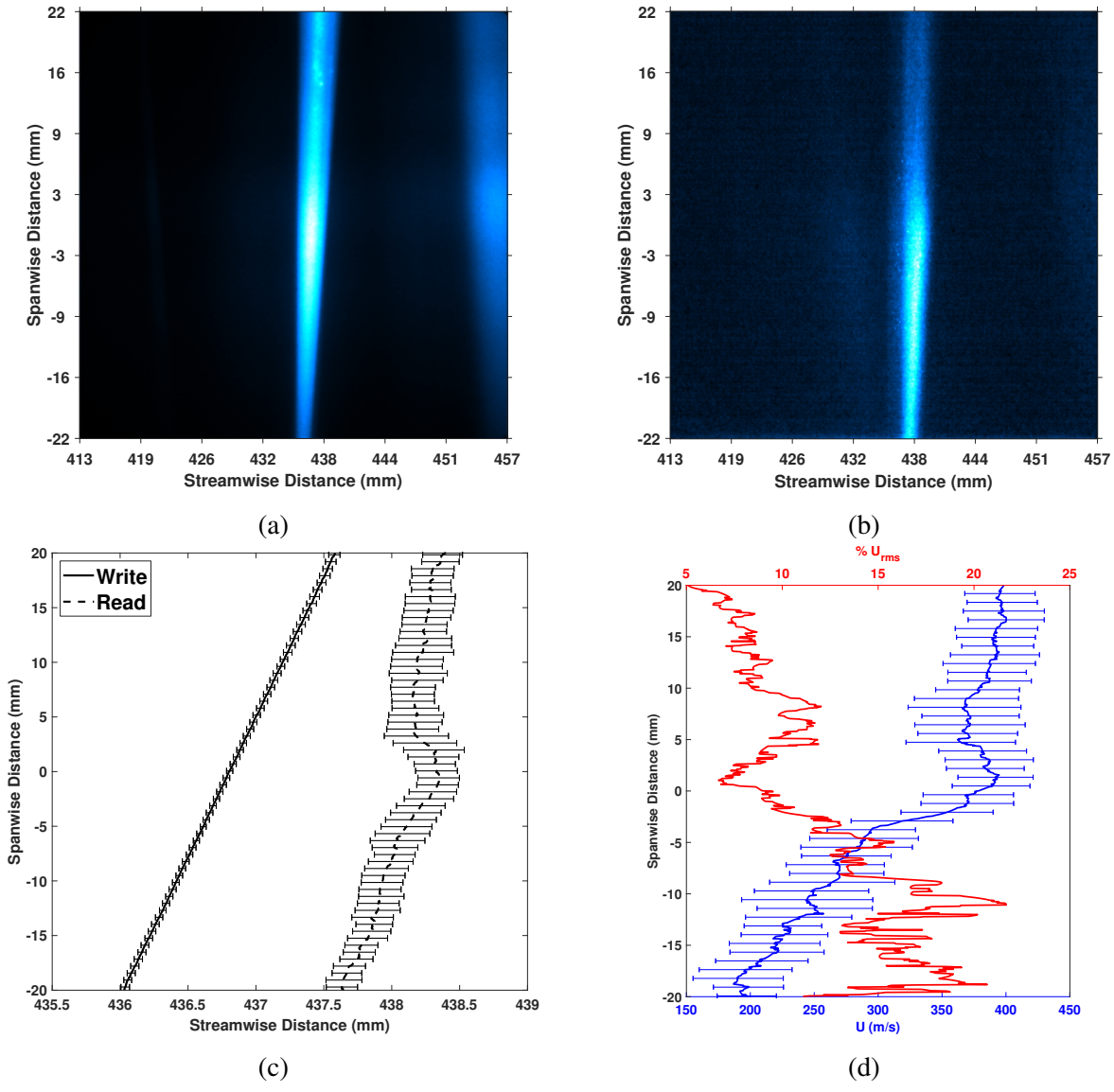

Figure 6.33: Spanwise L3 write and read velocimetry. Figures a and b are write and read images, respectively. Figure c depicts the average write and read line positions. Figure d illustrates the spanwise velocity and corresponding fluctuations.

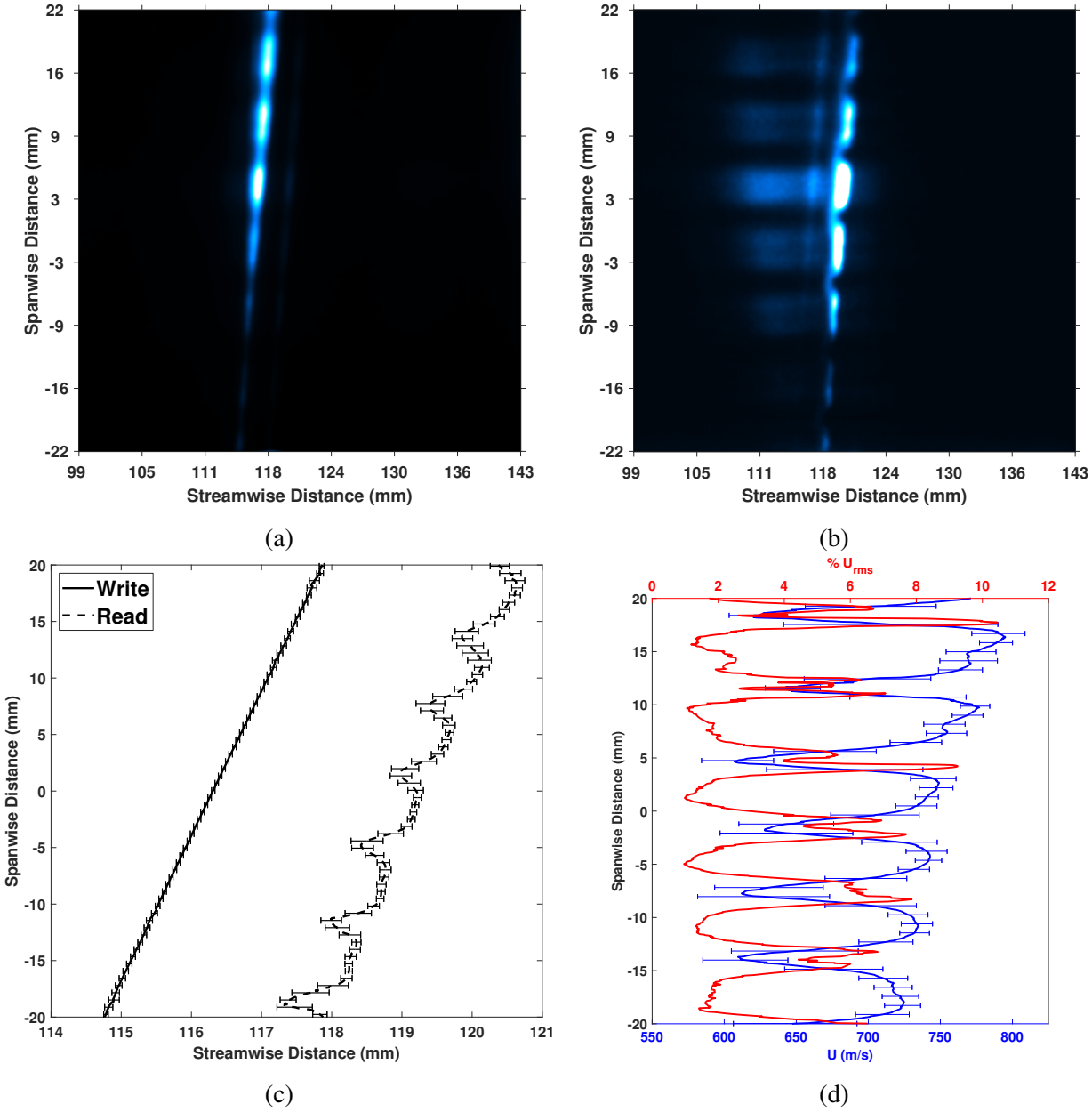

Figure 6.34: Spanwise T1 write and read velocimetry. Figures a and b are write and read images, respectively. Figure c depicts the average write and read line positions. Figure d illustrates the spanwise velocity and corresponding fluctuations.

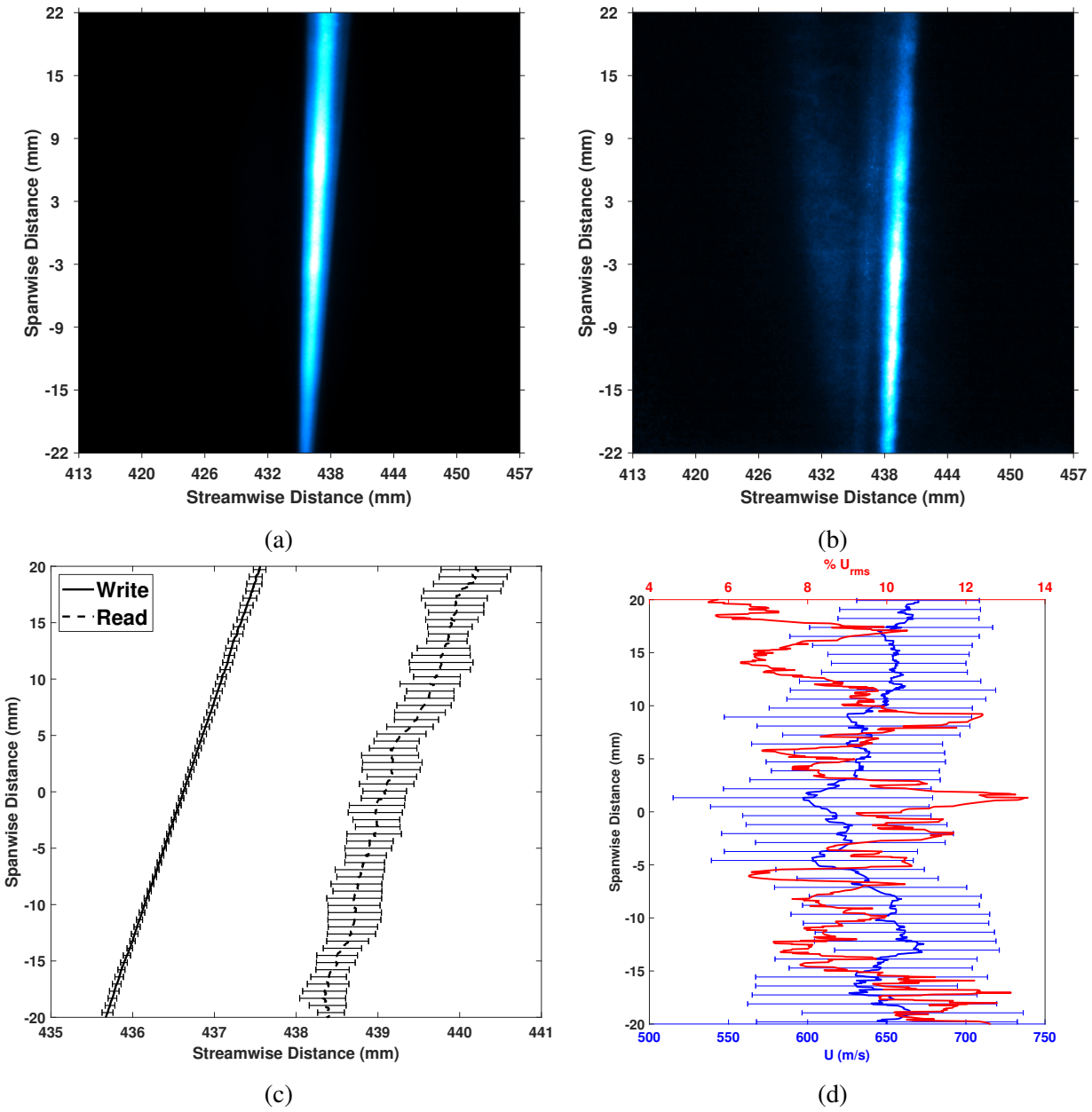

Figure 6.35: Spanwise T3 write and read velocimetry. Figures a and b are write and read images, respectively. Figure c depicts the average write and read line positions. Figure d illustrates the spanwise velocity and corresponding fluctuations.

7. CONCLUSION AND FUTURE RESEARCH OBJECTIVES

7.1 Increase the Magnitude of TNE introduced by the Plasma

The three laser diagnostic campaigns performed on the flat plate determined the hypersonic turbulent boundary was unaffected by the plasma along the leading edge of the model. This was attributed to the relatively small amount of TNE produced by the plasma. As stated in Section 5.2 the theoretical N_2 vibrational temperature was 420 K, causing the relative $N_{2,v=1}$ population to increase from 0.6 ppt ppm to 16 ppt. The 300 W RF plasma characterized by Fuller *et al.* produced a N_2 vibrational temperature of 1540 K yielding a relative $N_{2,v=1}$ population of 140 ppt.[135] The RF plasma may be a more efficient method of introducing a larger degree of vibrational excitation. The studies presented in Section 1.2.3 presented TNE influenced flow perturbations resulting from an RF plasma. In a study by Gulko *et al.* the $N_{2,v=1}$ population doubled when overlaying an RF pulse upon a ns pulsed DC plasma. They stated the RF pulsed plasma did not produce a large ion population, but instead had a greater number of electron impact scattering events.[142] They supported this claim by noting the RF plasma produced a smaller electric field which reduces the ion production and improved plasma uniformity. They noted a small rotational temperature perturbation on the order of $\sim$50 K. A separate study by Sun *et al.* studied the correlation between electric field strength and CH_4 vibrational excitation. They employed an RF plasma to a CH_4 pyrolytic chamber and characterized the products with gas chromatography.[143] Below 10 Td the total plasma energy was deposited exclusively into the CH_4 vibrational modes. However, above 10 Td the CH_4 ionization and dissociation channels became more significant and by 100 Td the vibrationally excited CH_4 was $\sim$2% of the total CH_4 population. Based on the studies presented here and in Section 1.2.3 it may be advantageous to implement an RF plasma along the leading edge of the model. It is an effective method of introducing vibrationally excited species without causing a large thermal perturbation. Another method may be to pulse the DC glow discharge plasma to reduce the strength of the electric field.

7.2 Minimization of the Rotational Thermal Perturbations

The thermal perturbations discussed in Section 4.4.2 were a result of a series of N_xO_y photodissociation reactions. These perturbations were mitigated by reducing the seeded NO concentration. However, the full scale VENOM measurements will require high concentrations of seeded NO in order to maximize the acquired $NO_{v=1}$ fluorescent signal. To optimize the fluorescent signal while minimizing the thermal perturbation a temporal rotational thermometry campaign should be performed. For the presented two-line PLIF rotational thermometry experiments the time delay between the two images was $\sim$500 ns which was too short for the NO to thermalize following the photodissociation processes. The relative gate between the two collected images should be increased at a single high concentration of seeded NO until the measured rotational temperature agrees with the known freestream temperature and expected wall temperature. However, it should be noted the flow will displace a greater distance with larger relative time delays. The experiment needs to be performed with the laminar insert to ensure large-scale turbulent structures do not cause errors in the convolution of the 2nd image with the 1st image. The campaign will be helpful in understanding the optimal time delay to perform a VENOM experiment without thermal perturbations.

Another method to mitigate thermal perturbations would be to employ Stimulated Raman Excited Fluorescence (SREF). This technique is capable of increasing the relative NO $X^2\Pi$ (v = 1) population without introducing high concentrations of NO within the ACE facility. Consider the mechanism proposed in Figure 7.1. The blue line, ω_1, is the write laser tuned to the NO $A^2\Sigma^+$ ($v' = 0$) $\leftarrow$ $X^2\Pi$ ($v'' = 0$). The stokes laser, ω_2, overlaps ω_1 temporally and spatially to drive the excited state population to the NO $X^2\Pi$ (v = 1) state. The stokes beam can be scanned at 236 nm to optimize the NO $X^2\Pi$ (v = 1) within the boundary layer. The read laser then probes the nascent NO $X^2\Pi$ (v = 1) population and the broadband emission, hν, can be collected. This generalized mechanism has been demonstrated in previous studies. Xiong *et al.* have demonstrated the improved sensitivity of the SREF technqiue on the Rhodamine 800 (Rh800) chromophore.[144] Within their biological imaging experiments the Rh800 fluorescent signature increased 100$\times$ relative to the

previous Raman spectroscopy experiments. A separate study demonstrated the use of stimulated Raman pumping within the NO $X^2\Pi$ ground state.[145] Their study used a 532 nm pump beam and a 591 nm stokes beam to increase the NO $X^2\Pi$ (v = 1) population. These two studies illustrate how the NO $X^2\Pi$ (v = 1) signal can be improved within ACE using higher order excitation schemes.

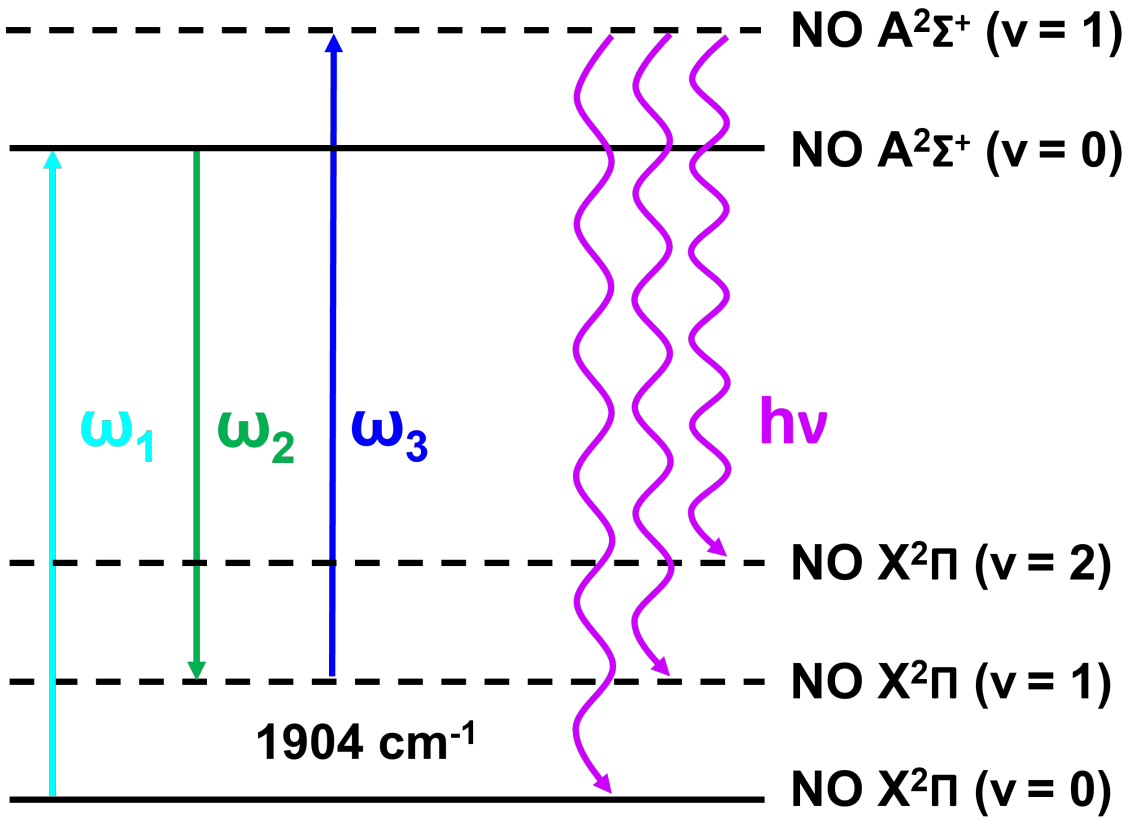

Figure 7.1: NO stimulated emission scheme.

7.3 Characterize the Origin of the Observed NO Vibrational Temperature

The two-line NO PLIF vibrational thermometry campaign characterized the mixing of the nascent NO $X^2\Pi$ (v = 1) state along the length of the plate. To expand the scope of understanding related to the vibrational decay mechanisms the origin of the NO vibrational temperature profile needs to be studied. OES needs to be performed on the plasma to observe any potential emission

related to the $X^2\Pi \leftarrow A^2\Sigma^+$ transition. Figure 7.2 illustrates the theoretical emission spectrum as a function of the calculated Franck-Condon factor. Evidence of NO $A^2\Sigma^+$ state relaxation would indicate a portion of the nascent NO $X^2\Pi$ (v = 1) profile was produced from an electron-impact excitation mechanism. In the study by Fuller *et.al.* they observed a small fraction of NO $A^2\Sigma^+$ state emission; however, they assumed the resulting NO $X^2\Pi$ (v = 1) population was negligible within their system.[17] If the NO $A^2\Sigma^+$ state is not observed in the OES experiments then the dominant production of the nascent NO $X^2\Pi$ (v = 1) population was produced through an inelastic electron scattering process.

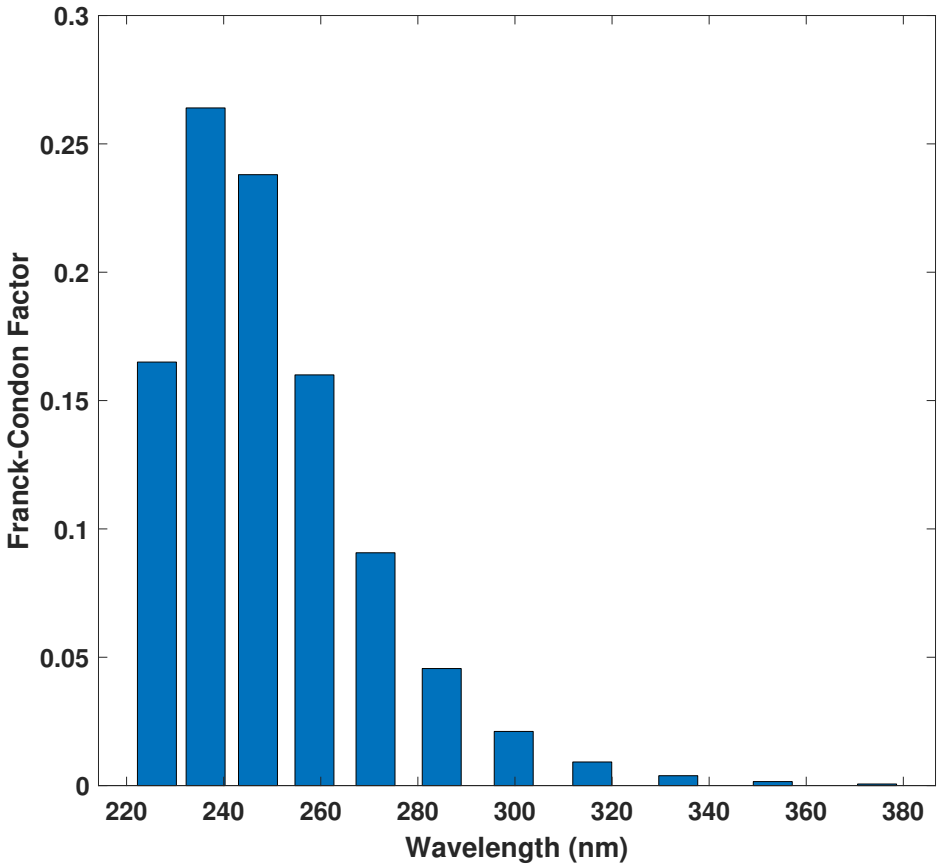

Figure 7.2: NO emission spectrum of the $X^2\Pi \leftarrow A^2\Sigma^+$ transition.

The second set of experiments should focus on characterizing the top-down distribution of the NO vibrational temperature. The plasma off experiments suggested there was vibrational decay

near the surface; however, this may be an artifact from the spatial distribution of the NO vibrational temperature within the ACE facility. The predicted NO vibrational temperature discussed in Section 5.1 applied to the ACE centerline. However, if there are spatial variations in the vibrational temperature within the test section then it will convolute with the measured NO vibrational temperature normal to the plate. Similar to the top-down rotational thermometry experiments, the vibrational temperature distribution needs to be characterized to fully understand the vibrational decay along the plate.

7.4 Acquisition of Coupled Flow Parameters Using the VENOM Technique

The implementation of various NO LIF techniques has been demonstrated as a viable diagnostic for the ACE facility. Rotational and vibrational temperature maps were acquired at various locations within the facility using the NO PLIF technique. The freestream velocity and the flat plate velocity profiles were measured using the MTV technique. These campaigns were critical in building towards the 2-D invisible ink VENOM technique which measures the coupled relationship between the temperature and velocity fluctuations *i.e.* $U'T'$ and $V'T'$. These two coupled quantities are a direct measurement of the turbulent heat flux within the turbulent boundary layer. The $U'T'$ quantity describes the turbulent energy exchange along the plate while $V'T'$ describes the energy exchange normal to the surface. These two quantities are more sensitive to the potential turbulent dampening and production compared to their individual components. Preliminary $U'T'$ measurements have been performed and appear to be viable. The probed J 1.5 $A^2\Sigma^+$ ($v' = 1$) $\leftarrow$ $X^2\Pi_{1/2}$ ($v'' = 1$) transition had too low of a S/N profile near the surface and as a result J 2.5 and 3.5 have been considered potential candidates for the probed low J transition. Figure 7.3 displays the temperature dependence of the NO rotational states. Above J 3.5 the temperature sensitivity begins to decrease for J 4.5 and 5.5. Prior to the $V'T'$ measurements, a Reynolds stress *i.e.* a $U'V'$ campaign needs to be performed. The $U'V'$ quantity relies on tracking the 2-D spatial displacement of a node within the flow.[93] The Reynolds stress is also a metric used to describe the degree of turbulent dampening and production as well as the identification of local vortices. The Reynolds stress parameter would be useful in mapping out the laminar boundary layer breakdown

downstream of the trip geometries. Additionally, it would validate and describe the shear layer produced by the counter rotating vortices discussed in section 6.5 that lead to turbulent transition.

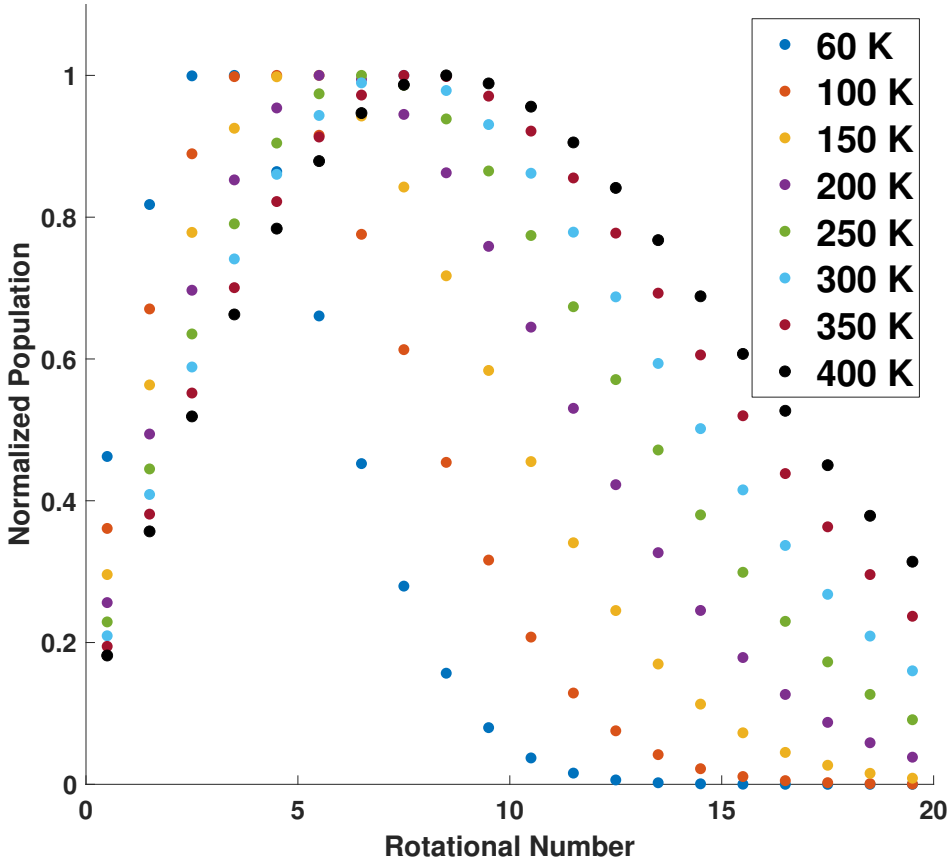

Figure 7.3: NO emission spectrum of the $A^2\Sigma^+ \leftarrow X^2\Pi$transition.

REFERENCES

[1] J. John D. Anderson, *Fundamentals of Aerodynamics*. 2nd ed., McGraw-Hill Inc., 1991.

[2] J. John D. Anderson, *Hypersonic and High Temperature Gas Dynamics*. International series of monographs on physics, McGraw-Hill Inc., 2006.

[3] J. A. Schetz, *Boundary Layer Analysis*. 1st ed., AIAA Inc., 2010.

[4] C. F. Dewey and J. F. Gross, "Exact similar solutions of the laminar boundary-layer equations," in *Advances in Heat Transfer*, 1st ed., Elsevier, 1967.

[5] T.-Y. Li and H. T. Nagamatsu, "Similar solutions of compressible boundary-layer equations," *Journal of the Aeronautical Sciences*, vol. 20, no. 9, pp. 653–655, 1953.

[6] S. P. Otta and A. P. Rothmayer, "Laminar subsonic, supersonic, and transonic boundary-layer flow past a flat plate," *AIAA Journal*, vol. 44, no. 1, pp. 102–107, 2006.

[7] J. A. Schetz, *Viscous Fluid Flow*. 3rd ed., McGraw Hill Inc., 2006.

[8] G. K. Batchelor, *An Introduction to Fluid Dynamics*. 1st ed., Cambridge University Press, 2000.

[9] S. B. Pope, *Turbulent Flows*. 1st ed., Cambridge University Press, 2000.

[10] O. Reynolds, "IV. on the dynamical theory of incompressible viscous fluids and the determination of the criterion," *Philosophical Transactions of the Royal Society of London. (A.)*, vol. 186, pp. 123–164, 1895.

[11] R. Bowersox and S. North, "Algebraic turbulent energy flux models for hypersonic shear flows," *Progress in Aerospace Sciences*, vol. 46, no. 2, pp. 49 – 61, 2010.

[12] R. Wolfgang, "Large-eddy simulations of the flow past bluff bodies : State-of-the art," *JSME International Journal Series B*, vol. 41, no. 2, pp. 361–374, 1998.

[13] U. Schumann, "Realizability of reynolds-stress turbulence models," *The Physics of Fluids*, vol. 20, no. 5, pp. 721–725, 1977.

[14] A. J. A. Favre, *Studies in Turbulence*. 1st ed., Springer, 1992.

[15] C. J. Roy and F. G. Blottner, "Review and assessment of turbulence models for hypersonic flows," *Progress in Aerospace Sciences*, vol. 42, no. 7, pp. 469–530, 2006.

[16] J. Huang, J. V. Bretzke, and L. Duan, "Assessment of turbulence models in a hypersonic cold-wall turbulent boundary layer," *Fluids*, vol. 4, no. 1, p. 37, 2019.

[17] T. J. Fuller, A. G. Hsu, R. Sanchez-Gonzalez, J. C. Dean, S. W. North, and R. D. Bowersox, "Radiofrequency plasma stabilization of a low-reynolds-number channel flow," *Journal of Fluid Mechanics*, vol. 748, no. 1, p. 663–691, 2014.

[18] M. J. Lighthill, "Viscosity effects in sound waves of finite amplitude," in *Surveys in Mechanics*, vol. 1, Cambridge University Press, 1956.

[19] S. Leonov, V. Bityurin, K. Savelkin, and D. Yarantsev, *Effect of electrical discharge on separation processes and shocks position in supersonic airflow*. 1st ed., AIAA Inc., 2012.

[20] S. Merriman, E. Ploenjes, P. Palm, and I. V. Adamovich, "Shock wave control by nonequilibrium plasmas in cold supersonic gas flows," *AIAA Journal*, vol. 39, no. 8, pp. 1547–1552, 2001.

[21] M. Samimy, J.-H. Kim, I. Adamovich, Y. Utkin, and J. Kastner, *Active Control of High Speed and High Reynolds Number Free Jets Using Plasma Actuators*. 1st ed., AIAA Inc., 2006.

[22] K. Fujii and H. G. Hornung, "Experimental investigation of high-enthalpy effects on attachment-line boundary-layer transition," *AIAA Journal*, vol. 41, no. 7, pp. 1282–1291, 2003.

[23] R. Miles, J. Forkey, and W. Lempert, *Filtered Rayleigh scattering measurements in supersonic/hypersonic facilities*. 1st ed., AIAA Inc., 1992.

[24] J. N. Forkey, N. D. Finkelstein, W. R. Lempert, and R. B. Miles, "Demonstration and characterization of filtered rayleigh scattering for planar velocity measurements," *AIAA Journal*, vol. 34, no. 3, pp. 442–448, 1996.

[25] J. George, T. P. Jenkins, and R. B. Miles, *Diagnosis of High Speed Flows using Filtered Rayleigh Scattering*. 1st ed., AIAA Inc., 2014.

[26] J. N. Forkey, *Development and demonstration of filtered rayleigh scattering: A laser based flow diagnostic for planar measurement of velocity, temperature and pressure*. PhD thesis, Princeton University, Princeton, NJ 08544, 1996.

[27] M. Alden, H. Edner, and S. Svanberg, "Coherent anti-stokes raman spectroscopy (CARS) applied in combustion probing," *Physica Scripta*, vol. 27, no. 1, pp. 29–38, 1983.

[28] F. Grisch, P. Bouchardy, M. Pealat, B. Chanetz, T. Pot, and M. C. Coet, "Rotational temperature and density measurements in a hypersonic flow by dual-line cars," *Applied Physics B*, vol. 56, no. 1, pp. 14–20, 1993.

[29] M. A. Woodmansee, R. P. Lucht, and J. C. Dutton, "Development of high-resolution N_2 coherent anti-stokes raman scattering for measuring pressure, temperature, and density in high-speed gas flows," *Applied Optics*, vol. 39, no. 33, pp. 6243–6256, 2000.

[30] A. C. Eckbreth, "Boxcars: Crossed-beam phase-matched cars generation in gases," *Applied Physics Letters*, vol. 32, no. 7, pp. 421–423, 1978.

[31] E. Fraval, P. Danehy, and F. P. Houwing, "Single-shot broadband coherent anti-stokes raman scattering measurements in a free piston shock tunnel nozzle expansion," 2001.

[32] J. C. McDaniel, B. Hiller, and R. K. Hanson, "Simultaneous multiple-point velocity measurements using laser-induced iodine fluorescence," *Opt. Lett.*, vol. 8, no. 1, pp. 51–53, 1983.

[33] B. Hiller and R. K. Hanson, "Simultaneous planar measurements of velocity and pressure fields in gas flows using laser-induced fluorescence," *Appl. Opt.*, vol. 27, no. 1, pp. 33–48, 1988.

[34] P. H. Paul, M. P. Lee, and R. K. Hanson, "Molecular velocity imaging of supersonic flows using pulsed planar laser-induced fluorescence of no," *Opt. Lett.*, vol. 14, no. 9, pp. 417–419, 1989.

[35] J. M. Seitzman, G. Kychakoff, and R. K. Hanson, "Instantaneous temperature field measurements using planar laser-induced fluorescence," *Opt. Lett.*, vol. 10, no. 9, pp. 439–441, 1985.

[36] J. Palmer and R. Hanson, "Planar laser-induced fluorescence temperature measurements in free jet flows with vibrational nonequilibrium," in *31st Aerospace Sciences Meeting*, vol. 46, AIAA, 1993.

[37] M. Havermann, J. Haertig, C. Rey, and A. George, *PIV Measurements in Shock Tunnels and Shock Tubes*, pp. 429–443. Springer Berlin Heidelberg, 2008.

[38] T. Sakurai, T. Handa, S. Koike, K. Mii, and A. Nakano, "Study on the particle traceability in transonic and supersonic flows using molecular tagging velocimetry," *Journal of Visualization*, vol. 18, no. 3, pp. 511–52, 2015.

[39] M. Hunter, S. Reid, D. D. C. Robie, and H. Reisler, "The monoenergetic unimolecular reaction of expansion-cooled no_2:no product state distributions at excess energies 0–3000 cm^{-1}," *The Journal of Chemical Physics*, vol. 99, no. 2, pp. 1093–1108, 1993.

[40] A. G. Hsu, R. Srinivasan, R. Bowersox, and S. North, "Two-component molecular tagging velocimetry utilizing no fluorescence lifetime and no2 photodissociation techniques in an underexpanded jet flowfield," *Applied Optics*, vol. 48, no. 22, pp. 4414–4423, 2009.

[41] A. G. Hsu, R. Srinivasan, R. D. W. Bowersox, and S. W. North, "Molecular tagging using vibrationally excited nitric oxide in an underexpanded jet flowfield," *AIAA Journal*, vol. 47, no. 11, pp. 2597–2604, 2009.

[42] R. Sanchez-Gonzalez, *Advanced Laser Diagnostics Development for the Characterization of Gaseous High Speed Flows. Doctoral Dissertation.* PhD thesis, Texas A & M University, 400 Bizzell St, College Station, TX 77843, 2012.

[43] R. Sanchez-Gonzalez, R. Srinivasan, R. W. Bowersox, and S. W. North, "Simultaneous velocity and temperature measurements in gaseous flow fields using the venom technique," *Optics Letters*, vol. 36, no. 2, pp. 196–198, 2011.

[44] R. Sánchez-González, W. D. Eveland, N. A. West, C. L. N. Mai, R. D. W. Bowersox, and S. W. North, "Low-temperature collisional quenching of NO $A^2\Sigma^+(v' = 0)$ by NO ($X^2\Pi$) and O_2 between 34 and 109 k," *The Journal of Chemical Physics*, vol. 141, no. 7, p. 074313, 2014.

[45] M. Semper, N. Tichenor, R. Srinvasan, S. North, and R. Bowersox, "On the design and calibration of an actively controlled expansion hypersonic wind tunnel," in *47th AIAA Aerospace Sciences Meeting including The New Horizons Forum and Aerospace Exposition*, vol. 799, AIAA, 2009.

[46] M. Semper, B. Pruski, and R. Bowersox, "Freestream turbulence measurements in a continuously variable hypersonic wind tunnel," in *50th AIAA Aerospace Sciences Meeting including the New Horizons Forum and Aerospace Exposition*, vol. 732, AIAA, 2012.

[47] Z. D. Buen, C. Broslawski, M. Smotzer, J. E. Kuszynski, S. W. North, and R. D. W. Bowersox, "Towards vibrationally excited nitric oxide monitoring (venom) in a laminar, hypersonic boundary layer," in *AIAA Scitech 2020 Forum*, vol. 1275, AIAA, 2020.

[48] A. Leidy, I. T. Neel, N. R. Tichenor, R. D. W. Bowersox, and J. D. Schmisseur, "High-speed schlieren imaging and hot-wire characterization of cylinder-induced hypersonic shock boundary layer interactions," in *2018 Fluid Dynamics Conference*, vol. 3703, AIAA, 2018.

[49] N. West, *Characterization of Benzene Laser-Induced Nonthermal Equilibrium via Nitric Oxide Laser Induced Fluorescence Temperature Measurements*. PhD thesis, Texas A & M University, 400 Bizzell St, College Station, TX 77843, 2018.

[50] P. A. Irwin, "Vortices and tall buildings: A recipe for resonance," *Physics Today*, vol. 63, no. 9, pp. 68–69, 2010.

[51] J. Suh, J. Yang, and F. Stern, "The effect of air–water interface on the vortex shedding from a vertical circular cylinder," *Journal of Fluids and Structures*, vol. 27, no. 1, pp. 1–22, 2011.

[52] M. M. Mendenhall, "Predicted vortex shedding from noncircular bodies in supersonic flow," *Journal of Spacecraft and Rockets*, vol. 18, no. 5, pp. 385–392, 1981.

[53] A. Roshko, "On the development of turbulent wake from vortex streets," *NACA Report. 1191*, 1954.

[54] C. H. K. Williamson, "Oblique and parallel modes of vortex shedding in the wake of a circular cylinder at low reynolds numbers," *Journal of Fluid Mechanics*, vol. 206, no. 1, p. 579–627, 1989.

[55] R. D. Blevins, *Flow-induced vibration*. 2nd ed., Van Nostrand Reinhold, 1990.

[56] M. Ardekani, "Hot-wire calibration using vortex shedding," *Measurement*, vol. 42, no. 5, pp. 722–729, 2009.

[57] D. Farivar, "Turbulent uniform flow around cylinders of finite length," *AIAA Journal*, vol. 19, no. 3, pp. 275–281, 1981.

[58] T. Kawamura, M. Hiwada, T. Hibino, I. Mabuchi, and M. Kumada, "Flow around a finite circular cylinder on a flat plate : Cylinder height greater than turbulent boundary layer thickness," *Bulletin of JSME*, vol. 27, no. 232, pp. 2142–2151, 1984.

[59] M. Zhao and L. Cheng, "Vortex-induced vibration of a circular cylinder of finite length," *Physics of Fluids*, vol. 26, no. 1, p. 015111, 2014.

[60] E. J. List, "Turbulent jets and plumes," *Annual Review of Fluid Mechanics*, vol. 14, no. 1, pp. 189–212, 1982.

[61] C. Lubert, "On some recent applications of the coanda effect to acoustics," vol. 11, p. 40006, 2010.

[62] T. B. Settersten, . D. Patterson, and C. D. Carter, "Collisional quenching of NO $A^2\Sigma^+(v' = 0)$ between 125 and 294 k," *The Journal of Chemical Physics*, vol. 130, no. 20, pp. 204–302, 2009.

[63] T. Imajo, K. Shibuya, K. Obi, and I. Tanaka, "Energy transfer and electronic quenching of the low-lying rydberg states of nitric oxide in nitric oxide/nitrogen mixtures," *The Journal of Physical Chemistry*, vol. 90, no. 22, pp. 6006–6011, 1986.

[64] G. D. Greenblatt and A. Ravishankara, "Collisional quenching of NO(A, $v' = 0$) by various gases," *Chemical Physics Letters*, vol. 136, no. 6, pp. 501–505, 1987.

[65] T. B. Settersten, B. D. Patterson, and W. H. Humphries, "Radiative lifetimes of NO $A^2\Sigma^+(v' = 0,1,2)$ and the electronic transition moment of the $A^2\Sigma^+ \rightarrow X^2\Pi$ system," *The Journal of Chemical Physics*, vol. 131, no. 10, p. 104309, 2009.

[66] M. C. Drake and J. W. Ratcliffe, "High temperature quenching cross sections for nitric oxide laser-induced fluorescence measurements," *The Journal of Chemical Physics*, vol. 98, no. 5, pp. 3850–3865, 1993.

[67] G. Nutt, S. Haydon, and A. McIntosh, "Measurement of electronic quenching rates in nitric oxide using two-photon spectroscopy," *Chemical Physics Letters*, vol. 62, no. 2, pp. 402–404, 1979.

[68] I. McDermid and J. B. Laudenslager, "Radiative lifetimes and electronic quenching rate constants for single-photon-excited rotational levels of NO ($A^2\Sigma^+$, $v' = 0$)," *Journal of Quantitative Spectroscopy and Radiative Transfer*, vol. 27, no. 5, pp. 483–492, 1982.

[69] J. Luque and D. Crosley, "LIFBASE: Database and simulation program (1.6)," 1999.

[70] G. Hancock and M. Saunders, "Vibrational distribution in NO ($X^2\Pi$) formed by self quenching of NO $A^2\Sigma^+(v' = 0)$," *Phys. Chem. Chem. Phys.*, vol. 10, no. 15, pp. 2014–2019, 2008.

[71] I. C. Hisatsune and L. Zafonte, "Kinetic study of some third-order reactions of nitric oxide," *The Journal of Physical Chemistry*, vol. 73, no. 9, pp. 2980–2989, 1969.

[72] J. Olbregts, "Termolecular reaction of nitrogen monoxide and oxygen: A still unsolved problem," *International Journal of Chemical Kinetics*, vol. 17, no. 8, pp. 835–848, 1985.

[73] R. Atkinson, D. L. Baulch, R. A. Cox, J. N. Crowley, R. F. Hampson, R. G. Hynes, M. E. Jenkin, M. J. Rossi, and J. Troe, "Evaluated kinetic and photochemical data for atmospheric chemistry: Volume I - gas phase reactions of O_x, HO_x, NO_x and SO_x species," *Atmospheric Chemistry and Physics*, vol. 4, no. 6, pp. 1461–1738, 2004.

[74] P. G. Ashmore and M. G. Burnett, "Concurrent molecular and free radical mechanisms in the thermal decomposition of nitrogen dioxide," *Trans. Faraday Soc.*, vol. 58, no. 1, pp. 253–261, 1962.

[75] E. Zimet, "Thermal decomposition of N_2O_4 and NO_2 by shock waves," *The Journal of Chemical Physics*, vol. 53, no. 2, pp. 515–518, 1970.

[76] W. Tsang and J. T. Herron, "Chemical kinetic data base for propellant combustion i. reactions involving NO, NO_2, HNO, HNO_2, HCN and N_2O," *Journal of Physical and Chemical Reference Data*, vol. 20, no. 4, pp. 609–663, 1991.

[77] M. Röhrig, E. L. Petersen, D. F. Davidson, and R. K. Hanson, "A shock tube study of the pyrolysis of NO_2," *International Journal of Chemical Kinetics*, vol. 29, no. 7, pp. 483–493, 1997.

[78] G. Guggenheim, "Dimerization of gaseous nitric oxide," *Molecular Physics*, vol. 10, no. 4, pp. 401–404, 1966.

[79] R. L. Scott, "Dimerization of gaseous nitric oxide," *Molecular Physics*, vol. 11, no. 4, pp. 399–401, 1966.

[80] S. E. Novick, P. B. Davies, T. R. Dyke, and W. Klemperer, "Polarity of van der waals molecules," *Journal of the American Chemical Society*, vol. 95, no. 26, pp. 8547–8550, 1973.

[81] L. Nxumalo and T. Ford, "IR spectra of the dimers of carbon dioxide and nitrous oxide in cryogenic matrices," *Journal of Molecular Structure*, vol. 327, no. 2, pp. 145–159, 1994.

[82] E. D. Glendening and A. M. Halpern, "Ab initio calculations of nitrogen oxide reactions: Formation of N_2O_2, N_2O_3, N_2O_4, N_2O_5, and N_4O_2 from NO, NO_2, NO_3, and N_2O," *The Journal of Chemical Physics*, vol. 127, no. 16, p. 164307, 2007.

[83] I. W. M. Smith and G. Yarwood, "Kinetic measurements on the system NO + $NO_2 \leftrightarrow$ N_2O_3 by time-resolved infrared laser absorption," *Chemical Physics Letters*, vol. 130, no. 1, pp. 24–28, 1986.

[84] B. Markwalder, P. Gozel, and H. van den Bergh, "Laser-induced temperature jump measurements in the kinetics of association and dissociation of the nitrogen oxide (N_2O_3) + M = NO_2 + NO + M system," *The Journal of Physical Chemistry*, vol. 97, no. 20, pp. 5260–5265, 1993.

[85] J. Brunning, M. J. Frost, and I. W. M. Smith, "Kinetic measurements on the system: $2NO_2$ = N_2O_4 at (224 ± 2) k using time-resolved infrared laser absorption," *International Journal of Chemical Kinetics*, vol. 20, no. 12, pp. 957–965, 1988.

[86] P. Borrell, C. J. Cobos, A. E. Croce De Cobos, H. Hippler, K. Luther, A. R. Ravishankara, and J. Tree, "Radical association reactions in gases at high pressures," *Berichte der Bunsengesellschaft für physikalische Chemie*, vol. 89, no. 3, pp. 337–339, 1985.

[87] P. Borrell, C. J. Cobos, and K. Luther, "Falloff curve and specific rate constants for the reaction nitrogen dioxide + nitrogen dioxide $\leftrightarrow$ nitrogen oxide (N_2O_4)," *The Journal of Physical Chemistry*, vol. 92, no. 15, pp. 4377–4384, 1988.

[88] B. Markwalder, P. Gozel, and H. van den Bergh, "Temperature-jump measurements on the kinetics of association and dissociation in weakly bound systems: N_2O_4 + M = NO_2 + NO_2 + M," *The Journal of Chemical Physics*, vol. 97, no. 8, pp. 5472–5479, 1992.

[89] A. L. L. East, "The 16 valence electronic states of nitric oxide dimer $(NO)_2$," *The Journal of Chemical Physics*, vol. 109, no. 6, pp. 2185–2193, 1998.

[90] A. J. Fairhall, M. M. Orlando, and J. A. Bartz, "355 nm photodissociation of N_2O_3 revealed by velocity-mapped ion imaging," *The Journal of Physical Chemistry A*, vol. 124, no. 3, pp. 472–478, 2020.

[91] R. Cattolica, "OH rotational temperature from two-line laser-excited fluorescence," *Appl. Opt.*, vol. 20, no. 7, pp. 1156–1166, 1981.

[92] R. K. Hanson, "Planar laser-induced fluorescence imaging," *Journal of Quantitative Spectroscopy and Radiative Transfer*, vol. 40, no. 3, pp. 343–362, 1988.

[93] R. Sánchez-González, R. D. W. Bowersox, and S. W. North, "Simultaneous velocity and temperature measurements in gaseous flow fields using the vibrationally excited nitric oxide monitoring technique: a comprehensive study," *Applied Optics*, vol. 51, no. 9, pp. 1216–1228, 2012.

[94] B. K. McMillin, J. L. Palmer, and R. K. Hanson, "Temporally resolved, two-line fluorescence imaging of NO temperature in a transverse jet in a supersonic cross flow," *Applied Optics*, vol. 32, no. 36, pp. 7532–7545, 1993.

[95] S. O'Byrne, P. Danehy, and A. Houwing, "PLIF temperature and velocity distributions in laminar hypersonic flat-plate flow," in *20^{th} International Congress on Instrumentation in Aerospace Simulation Facilities*, vol. 1, 2003.

[96] B. A. Thompson, P. Harteck, and R. R. Reeves Jr., "Ultraviolet absorption coefficients of CO_2, CO, O_2, H_2O, N_2O, NH_3, NO, SO_2, and CH_4 between 1850 and 4000 Å," *Journal of Geophysical Research (1896-1977)*, vol. 68, no. 24, pp. 6431–6436, 1963.

[97] J. Winner, F. Pan, M. H. McIlvoy, R. D. W. Bowersox, and S. North, "Temperature perturbation related to the invisible ink vibrationally excited nitric oxide monitoring (venom) technique: a simulation study," *Appl. Opt.*, vol. 58, no. 10, pp. 2702–2712, 2019.

[98] H. Zacharias, M. Geilhaupt, K. Meier, and K. H. Welge, "Laser photofragment spectroscopy of the NO_2 dissociation at 337 nm. A nonstatistical decay process," *The Journal of Chemical Physics*, vol. 74, no. 1, pp. 218–225, 1981.

[99] T. G. Slanger, W. K. Bischel, and M. J. Dyer, "Nascent no vibrational distribution from 2485 Å NO_2 photodissociation," *The Journal of Chemical Physics*, vol. 79, no. 5, pp. 2231–2240, 1983.

[100] H. Im and E. R. Bernstein, "Photodissociation of NO_2 in the region 217—237 nm: nascent no energy distribution and mechanism," *The Journal of Physical Chemistry A*, vol. 106, no. 33, pp. 7565–7572, 2002.

[101] M. Brouard, R. Cireasa, A. P. Clark, T. J. Preston, and C. Vallance, "The photodissociation dynamics of NO_2 at 308nm and of NO_2 and N_2O_4 at 226nm," *The Journal of Chemical Physics*, vol. 124, no. 6, p. 064309, 2006.

[102] J. Billingsley and A. B. Callear, "Investigation of the 2050 Å system of the nitric oxide dimer," *Trans. Faraday Soc.*, vol. 67, no. 1, pp. 589–597, 1971.

[103] O. Kajimoto, K. Honma, and T. Kobayashi, "Formation of electronically excited nitric oxide and energy partitioning in the 193-nm photolysis of the nitric oxide dimer," *The Journal of Physical Chemistry*, vol. 89, no. 13, pp. 2725–2727, 1985.

[104] Y. Naitoh, Y. Fujimura, K. Honma, and O. Kajimoto, "Photodissociation of the NO dimer at 193 nm. the rotational alignment of the NO ($A^2\Sigma$) fragments," *Chemical Physics Letters*, vol. 205, no. 4, pp. 423–428, 1993.

[105] Y. Naitoh, Y. Fujimura, O. Kajimoto, and K. Honma, "Photodissociation of the no dimer: rotational energy distribution and alignment of the NO ($B^2\Pi$) fragments," *Chemical Physics Letters*, vol. 190, no. 1, pp. 135–140, 1992.

[106] A. V. Demyanenko, A. B. Potter, V. Dribinski, and H. Reisler, "NO angular distributions in the photodissociation of $(NO)_2$ at 213 nm: Deviations from axial recoil," *The Journal of Chemical Physics*, vol. 117, no. 6, pp. 2568–2577, 2002.

[107] A. B. Potter, V. Dribinski, A. V. Demyanenko, and H. Reisler, "Exit channel dynamics in the ultraviolet photodissociation of the NO dimer: $(NO)_2 \rightarrow$ NO ($A^2\Sigma^+$) + NO ($X^2\Pi$)," *The Journal of Chemical Physics*, vol. 119, no. 14, pp. 7197–7205, 2003.

[108] "Equations, tables, and charts for compressible flow," *NACA Report. 1135*, 1951.

[109] K. Stetson and E. Thompson, "Laminar boundary layer stability experiments on a cone at mach 8. II- blunt cone," in *22nd Aerospace Sciences Meeting*, vol. 6, AIAA, 1984.

[110] A. Fedorov and A. Tumin, "Evolution of disturbances in entropy layer on blunted plate in supersonic flow," *AIAA Journal*, vol. 42, no. 1, pp. 89–94, 2004.

[111] M. T. Semper and R. D. W. Bowersox, "Tripping of a hypersonic low-reynolds-number boundary layer," *AIAA Journal*, vol. 55, no. 3, pp. 808–817, 2017.

[112] M. Lowson, "Pressure fluctuations in turbulent boundary layers," *NASA Technical Note D-3156*, 1965.

[113] A. L. Kistler and W. S. Chen, "The fluctuating pressure field in a supersonic turbulent boundary layer," *Journal of Fluid Mechanics*, vol. 16, no. 1, p. 41–64, 1963.

[114] M. Casassa, E. Heilweil, J. Stephenson, and R. Cavanagh, *Time-Resolved Measurements of Vibrational Relaxation at Surfaces*, vol. 26 of *Vibrations at Surfaces*. Elsevier, 1986.

[115] M. Head-Gordon and J. C. Tully, "Vibrational relaxation on metal surfaces: Molecular-orbital theory and application to CO/Cu (100)," *The Journal of Chemical Physics*, vol. 96, no. 5, pp. 3939–3949, 1992.

[116] F. Robben and L. Talbot, "Measurements of rotational temperatures in a low density wind tunnel," *The Physics of Fluids*, vol. 9, no. 4, pp. 644–652, 1966.

[117] J. J. Repetski and R. E. Mates, "Rotational temperature in an underexpanded jet," *The Physics of Fluids*, vol. 14, no. 12, pp. 2605–2610, 1971.

[118] P. V. Marrone, "Temperature and density measurements in free jets and shock waves," *The Physics of Fluids*, vol. 10, no. 3, pp. 521–538, 1967.

[119] H. Mori, T. Niimi, I. Akiyama, and T. Tsuzuki, "Experimental detection of rotational non-boltzmann distribution in supersonic free molecular nitrogen flows," *Physics of Fluids*, vol. 17, no. 11, pp. 103–117, 2005.

[120] A. Yakunchikov, V. Kosyanchuk, and A. Iuldasheva, "Rotational relaxation model for nitrogen and its application in free jet expansion problem," *Physics of Fluids*, vol. 32, no. 10, p. 102006, 2020.

[121] E. Josuyla and W. Bailey, "Vibrational relaxation and population depletion of nitrogen in hypersonic flows," in *40th AIAA Aerospace Sciences Meeting &; Exhibit*, vol. 200, 2002.

[122] E. Josyula and W. Bailey, "Multiquantum vibrational energy exchanges in nonequilibrium hypersonic flows," in *38th AIAA Thermophysics Conference*, vol. 5204, 2005.

[123] E. Josyula, W. F. Bailey, S. F. Gimelshein, R. R. Arslanbekov, and V. I. Kolobov, "Recent advances in modeling thermal and chemical nonequilibrium in continuum-rarefied gas flows," *AIP Conference Proceedings*, vol. 1084, 2008.

[124] P. C. Palma, P. M. Danehy, and A. F. P. Houwing, "Fluorescence imaging of rotational and vibrational temperature in shock-tunnel nozzle flow," *AIAA Journal*, vol. 41, no. 9, pp. 1722–1732, 2003.

[125] R. L. Zhang, J. L. Le, J. P. Cui, F. M. Yu, L. H. Han, S. Wang, and J. Liu, *Measurment and calculation of vibrational temperature behind strong shock waves*. Shock Waves, Springer Berlin Heidelberg, 2005.

[126] S. Kroll, P. Bengtsson, M. Alden, and D. Nilsson, "Is rotational cars an alternative to vibrational cars for thermometry?," *Appl. Phys. B*, vol. 51, no. 1, p. 25–30, 1990.

[127] S. Pendleton, C. Montello, A.and Carter, W. Lempert, and M. Gundersen, "Vibrational and rotational CARS measurements of nitrogen in afterglow of streamer discharge in atmospheric pressure fuel/air mixtures," *Journal of Physics D: Applied Physics*, vol. 45, no. 49, p. 495401, 2012.

[128] M. Weikl, Y. Cong, T. Seeger, and A. Leipertz, "Development of a simplified dual-pump dual-broadband coherent anti-stokes raman scattering system," *Applied Optics*, vol. 48, no. 4, pp. 43–50, 2009.

[129] F. Beyrau, T. Seeger, A. Malarski, and A. Leipertz, "Determination of temperatures and fuel/air ratios in an ethene–air flame by dual-pump cars," *Journal of Raman Spectroscopy*, vol. 34, no. 12, pp. 946–951, 2003.

[130] I. Nompelis, G. Candler, and M. Holden, "Effect of vibrational nonequilibrium on hypersonic double-cone experiments," *AIAA Journal*, vol. 41, no. 11, pp. 2162–2169, 2003.

[131] I. Boyd, W. Phillips, D. Levin, I. Boyd, and W. Phillips, "Sensitivity studies for prediction of ultra-violet radiation in nonequilibrium hypersonic bow-shock waves," in *35th Aerospace Sciences Meeting and Exhibit*, vol. 131, AIAA, 1997.

[132] J. Méolans, "Thermal slip boundary conditions in vibrational nonequilibrium flows," *Mechanics Research Communications*, vol. 30, no. 6, pp. 629–637, 2003.

[133] G. Candler, J. D. Kelley, S. O. Macheret, M. N. Shneider, and I. V. Adamovich, "Vibrational excitation, thermal nonuniformities, and unsteady effects on supersonic blunt bodies," *AIAA Journal*, vol. 40, no. 9, pp. 1803–1810, 2002.

[134] A. C. de Gavelle de Roany, C. Flament, J. W. Rich, V. V. Subramaniam, and W. R. Warren, "Strong vibrational nonequilibrium in supersonic nozzle flows," *AIAA Journal*, vol. 31, no. 1, pp. 119–128, 1993.

[135] A. Hsu, *Application of advanced laser and optical diagnostics towards non-thermochemical non-equilibrium systems*. PhD thesis, Texas A & M University, 400 Bizzell St, College Station, TX 77843, 2009.

[136] M. Y. Song, J. S. Yoon, H. Cho, V. Karwasz, G. P.and Kokoouline, Y. Nakamura, and J. Tennyson, "Cross sections for electron collisions with NO, N_2O, and NO_2," *Journal of Physical and Chemical Reference Data*, vol. 48, no. 4, p. 043104, 2019.

[137] S. O'Byrne, P. Danehy, and A. Houwing, "Investigation of hypersonic nozzle flow uniformity using NO fluorescence," *Shock Waves*, vol. 15, no. 2, pp. 81–87, 2006.

[138] N. Bachchan and R. Hillier, "Effects of hypersonic inlet flow non-uniformities on stabilising isolator shock systems," in *AIAA Atmospheric Flight Mechanics Conference and Exhibit*, vol. 4716, AIAA, 2004.

[139] P. M. Danehy, S. O'Byrne, A. Frank, P. Houwing, J. S. Fox, and D. R. Smith, "Flow-tagging velocimetry for hypersonic flows using fluorescence of nitric oxide," *AIAA Journal*, vol. 41, no. 2, pp. 263–271, 2003.

[140] B. E. Hedlund, A. W. Houpt, G. S., and S. B. Leonov, "Measurement of plasma induced flow perturbations affecting a Mach 4.5 corner separation zone," in *55th AIAA Aerospace Sciences Meeting*, vol. 154, 2017.

[141] J. F. Garten, S. Arendt, D. C. Ftitts, and J. Werne, "Dynamics of counter-rotating vortex pairs in stratified and sheared environments," *Journal of Fluid Mechanics*, vol. 361, no. 1, p. 189–236, 1998.

[142] I. Gulko, E. R. Jans, C. Richards, S. Raskar, X. Yang, D. C. M. van den Bekerom, and I. V. Adamovich, "Selective generation of excited species in ns pulse/RF hybrid plasmas for plasma chemistry applications," *Plasma Sources Science and Technology*, vol. 29, no. 10, p. 104002, 2020.

[143] J. Sun and Q. Chen, "Kinetic roles of vibrational excitation in rf plasma assisted methane pyrolysis," *Journal of Energy Chemistry*, vol. 39, no. 1, pp. 188–197, 2019.

[144] H. Xiong, L. Shi, Y. Shen, R. Long, Z. Zhao, and W. Min, "Stimulated raman excited fluorescence spectroscopy and imaging," *Nature Photonics*, vol. 13, no. 1, pp. 412–417, 2019.

[145] N. Chai, R. P. Lucht, W. D. Kulatilaka, S. Roy, and J. R. Gord, "Electronic-resonance-enhanced coherent anti-stokes raman scattering of nitric oxide: saturation and stark effects," *The Journal of Chemical Physics*, vol. 133, no. 8, p. 084310, 2010.